Dissertation

submitted to the

Combined Faculty of Natural Sciences and Mathematics

of the Ruperto Carola University Heidelberg, Germany

for the degree of

Doctor of Natural Sciences

Presented by

M.Sc. Dominik Pfister

born in: Leonberg, Germany 08th July 1988

Oral examination: 04th June 2019

Deciphering TCR signaling in metabolically activated T-cells in NASH and liver cancer development

Referees:

Professor Doktor Ralf Bartenschlager

Professor Doktor Mathias Heikenwälder

Table of contents

1 Abbreviations

µl	microliter
µm	micrometer
ab	antibody
Acc	acceleration
ACK buffer	ammonium-chloride-potassium buffer
ADP	adenosine diphosphate
a-Gal	glycolipid alpha-galactosyl ceramide
Akt	protein kinase B
ALT	alanine aminotransferase
ANOVA	analysis of variance
AP1	activator protein-1
APC	antigen presenting cells
APT	antiplatelet treatment
ASH	alcoholic steatohepatitits
Asp	Aspirin
AST	Aspartate Aminotransferase
BMI	body mass index
Ca^{2+}	Calcium 2+ ion
CBM	CARMA1/Bcl10/MALT1
CD	cluster of differentiation
CD-HFD	choline-deficient, high-fat diet
cDNA	complementary DNA
Clo	Clopidogrel
ColIV	collagen IV
COX	cyclooxygenase
CTL	cytotoxic T lymphocyte
CTLA-4	cytotoxic T lymphocyte antigen-4
DAG	diacylglycerol
DAMP	damage-associated molecular pattern
DNA	deoxyribonucleic acid
Dcc	decceleration
ER	endoplasmic reticulum
f.c.	final concentration
FACS	flow cytometry activated cell sorting
FasL	Fas ligand
FFA	free fatty acid
FGF21	fibroblast growth factor 21
FOV	field of view
GPIbα	glycoprotein Ib alpha
GPVI	glycoprotein VI
GzmA	granzyme A
GzmB	granzyme B
h	hour

H&E	hematoxylin-eosin
HBSS	Hank's Balanced Salt Solution
HBV	hepatitis B virus
HCC	hepatocellular carcinoma
HCV	hepatitis C virus
HFD	high fat diet
HRP	horse-radish peroxidase
hURI	human unconventional prefoldin RPB5 interactor
i.p.	intraperitonal
i.v.	intra venous
ICAM	intercellular adhesion molecule
ICC	intrahepatic cholangiocarcinoma
ICOS	Inducible T-cell co-stimulator
IDO	Indolamin-2,3-Dioxygenase
IFNy	interferon gamma
IL	interleukin
IP_3	inositol trisphosphate
IPGTT	intraperitonal glucose tolerance test
irAEs	immune-related adverse effects
ITAM	Immunoreceptor tyrosine-based activation motif
Itga2b	integrin alpha-IIb
ITIM	Immunoreceptor tyrosine- based inhibitory motif
KC	Kupffer cell
LAG-3	lymphocyte-activation gene 3
LAT	linker-of-the-activation-of-T-cells
Lck	lymphocyte cell-specific protein-tyrosine kinase
LFA-1	Lymphocyte function-associated antigen 1
LS	low sugar
LSEC	liver sinusoidal endothelial cell
Ly6G	lymphocyte antigen 6 complex locus G6D
MAP kinase	mitogen-activated protein kinase
MCD	methionine-choline deficient diet
mDC	myeloid dendritic cell
MHC	major histocompatibility complex
min	minutes
ml	milliliter
NAFLD	non-alcoholic fatty liver disease
NAS	NAFLD activity score
NASH	non-alcoholic steatohepatitis
ND	normal diet
NFAT	nuclear factor of activated T cells
NF-κB	nuclear factor 'kappa-light-chain-enhancer' of activated B-cells
NK	natural killer cells
NKT	natural killer T-cells
o.n.	overnight

OCT	optimal cutting temperature
PAMP	pathogen-associated molecular pattern
PBS	phosphate buffered saline
PCR	Polymerase chain reaction
PD-1	programmed death receptor 1
pDC	plasmacytoid dendritic cell
PDK1	3-phosphoinositide- dependent protein kinase 1
PD-L1	programmed death receptor ligand 1
$PI(4,5)P_2$	phospholipid phosphatidylinositol 4,5 bisphosphate
PI3 kinase	Phosphoinositide 3-kinase
PKCθ	protein kinase C θ
PLT	platelet
Prf	perforin
PSC	Primary Sclerosing Cholangitis
Rag-1	recombination-activating gene 1
RIPA	Radioimmunoprecipitation assay
ROS	reactive oxygen species
rpm	rounds per minute
RPMI medium	Roswell Park Memorial Institute medium
RT	room temperature
SEM	standard error of the mean
SLP-76	Src homology 2 domain–containing leukocyte phosphor-protein
STAT	signal transducer and activator of transcription
TCR	t-cell receptor
TGF- β	transforming growth factor ß
TIGIT	T cell immunoreceptor with Ig and ITIM domain
TIM-3	mucin-domain containing-3
TLR	Toll-like receptor
TNF-a	tumor necrosis factor alpha
tSNE	t-distributed stochastic neighbor embedding
VCAM	vascular cell adhesion molecule
VLA-4	very late antigen-4
VWF	von Willebrand factor
WD	western-style diet
WD-HTF	western-style diet with trans fats
β2m	β2-Microglobulin

2 Summary

Due to the consumption of high caloric food combined with an increased sedentary lifestyle, the incidence of overweight and obesity is growing rapidly in western cultures, like the USA, Europe and notably also in developing countries (e.g. India, China) - as a consequence of adaptation to the western lifestyle[1–3]. Thus, obesity-related pathologies like metabolic syndrome have become a major issue in modern medicine, and thus far therapeutic options are limited[3–5].

The liver - the major metabolic organ of the body - is particularly affected by constant high caloric food intake. Consequently, the liver undergoes dramatic changes, including the development of fatty liver disease, termed non-alcoholic fatty liver disease (NAFLD). In 25% of all NAFLD cases, progression to a more severe pathology termed non-alcoholic steatohepatitis (NASH) can be observed. Immune cell activation in NASH leads to liver fibrosis and subsequently to hepatocellular carcinoma (HCC)[3,6]. Today, more than 90 million people in the USA and 30 million people in Europe are affected by NAFLD. Although chronic viral infections with Hepatitis B or C are the leading etiology causing HCC, it has become clear that NASH is an increasingly important factor for HCC development, a notion supported by the fact that HCC is currently the fastest rising cancer in the USA, with a similar trend in Europe. At the same time, knowledge about the key mechanisms causing NASH and NASH-triggered HCC are scarce and therefore efficient therapies to treat this diseases are lacking[3,7,8].

The group of Professor Heikenwälder generated a mouse model of NASH and NASH-driven HCC in the context of a chronic metabolic syndrome[6]. Mice fed a long-term choline-deficient high fat diet (CD-HFD) develop obesity, steatosis, fibrosis, NASH and NASH-triggered HCC, recapitulating most of the key features found in human patients. In this model, activated $CD8^+$ and NKT-cells drive NASH and HCC through cytokine-mediated crosstalk with hepatocytes. Remarkably, a similar T-cell activation, cytokine and immune cell pattern was found in NASH patients - establishing the clinical relevance of the CD-HFD mouse model.

Aim 1: Deciphering TCR signaling in metabolically activated T-cells in NASH and liver cancer development

In this scientific context, I investigated the role of T-cells in greater detail and T-cell receptor (TCR) dependent signaling in NASH development and NASH-induced HCC. By utilizing different dietary (high fat diet (HFD), CD-HFD and western-style diet with trans-fat (WD-HTF), genetic mouse models (C57Bl6, $TCR\beta\delta^{-/-}$, OT-1, $Prf1^{-/-}$, $J\alpha18^{-/-}$, $CD1d^{-/-}$) and interventional antibody (α-CD8, α-PD-1, α-NK1.1) -based strategies in dietary mouse models, I shed new light on the key mechanisms of NASH pathology and its progression towards HCC.

The data of this PhD thesis indicates that from early time points onwards, activation of subsets of $CD8^+$ T-cells correlate with NASH pathology of different severity. Further, with progression of NASH towards advanced stages, $CD8^+$ T-cells of animals fed NASH-inducing diets (CD-HFD or WD-HTF) expressed increasing amounts of early activation marker CD69 and activation/exhaustion marker PD-1. Also, PD-1^+ $CD8^+$ T-cells expressed different TCR variable β chains (TCR vβ), indicating that distinct exhausted repertoires develop over the course of NASH. Next, I showed that NASH pathology is dependent on a functional TCRαβ repertoire with intact TCRαβ effector function, but less on natural killer T-cell (NKT) cell-dependent mechanisms. Consistent with TCRαβ dependency in NASH development, I demonstrated a differential role of $CD8^+$ T-cells depending on the progression state of NASH pathology, with a protective function of CD8+ T-cells in early states of NASH. However, in advanced NASH $CD8^+$ T-cells drive hepatic immune-related adverse effects (irAEs), resulting in liver damage and tumor formation potentially involving a TNF-a-mediated mechanism.

Aim 2: Platelet GPIbα is a mediator and potential interventional target for NASH and subsequent liver cancer

After deciphering the role of T-cells in NASH and NASH-induced hepatocarcinogenesis, I investigated alternative ways to target hepatic inflammation in NASH without targeting potentially inflammation-driving immune cell populations directly. Thus, I investigated the key mechanisms of cell-immune cell interactions driving early NASH pathogenesis and identified platelets and platelet activation as major contributors to NASH pathology and subsequent HCC development. Further, I deciphered that platelets could be targeted by antiplatelet therapy (therapeutic Ticagrelor), thereby ameliorating NASH pathology and potentially subsequent hepatocarcinogenesis. I could show that platelet interaction with Kupffer cells and CD44-hyaluronan are key mechanisms of NASH progression and that GPIbα is an interventional target for NASH therapy.

I published these results as a co-first author in *Nature Medicine* in April 2019 (https://doi.org/10.1038/s41591-019-0379-5)[9].

3 Zusammenfassung

Aufgrund des Konsums an hoch-kalorischen Essen kombiniert mit einem wachsendem bewegungsarmen Lebensstils steigt in westlichen Kulturen, wie der USA, Europa, aber auch in Schwellenländern, wie Indien und China, die Anzahl an Übergewicht und Fettleibigkeit[1–3]. Daher sind Krankheiten, welche mit Übergewicht in Verbindung gebracht werden, wie das metabolische Syndrom, eine der großen Herausforderungen der modernen Medizin, da therapeutische Optionen rar sind[3–5].

Die Leber, als das zentrale Organ des Metabolismus, ist von dem konstanten Überfluss an hoch-kalorischem Essen besonders betroffen. Unter diesen Umständen verändert sich die Leber dramatisch. Sie entwickelt sich zur Fettleber. Ohne übermäßigen Alkoholkonsum wird dieses Leberkrankheitsstadium „Nicht-alkoholische Fettleber Erkrankung“ genannt (englisch: non-alcoholic fatty liver disease (NAFLD)). In etwa 25% aller Fälle kommt es zu einer weiteren Verschlimmerung dieser Lebererkrankung, welche dann als „Nicht-alkoholische Steatohepatitis“ bezeichnet wird (englisch: non-alcoholic steatohepatitis (NASH)). In dieser NASH kommt es zur Immunzellaktivierung, welche zur Leberfibrose und schlussendlich zum hepatozellulären Karzinom (englisch: hepatocellular carcinoma (HCC)) führt[3,6]. Zum jetzigen Zeitpunkt sind mehr als 90 Millionen Menschen in den USA und mehr als 30 Millionen Menschen in Europa an NAFLD erkrankt. Das führt dazu, dass obwohl chronische virale Infektionen, wie Hepatitis B oder C, die führenden Ätiologien der Hepatokarzinogenese sind, Hepatokarzinogenese als Resultat einer zugrundeliegenden NASH sich über den Zeitraum der nächsten Jahre zu einem ernstzunehmenden Faktor entwickeln wird. Das wird zum Beispiel unterstützt, dass HCC heutzutage der Krebs ist, dessen Häufigkeit am rasantesten in der USA und Europa wächst. Gleichzeitig ist aber der heutige Wissenschaftsstand begrenzt in Bezug auf das Verständnis der Mechanismen der NASH und der NASH induzierten HCC Entstehung. Deshalb fehlen effiziente therapeutische Maßnahmen[3,7,8].

Das Labor von Professor Heikenwälder hat ein präklinisches Mausmodell entwickelt mit metabolischen Syndrom, NASH und NASH induzierte Hepatokarzinogenese[6]. In diesem Model werden Mäuse über einen langen Zeitraum mit Choline defizienter Hoch-Fett Diät (CD-HFD) gefüttert, was zu Übergewicht, Steatose, Fibrose und schlussendlich zu einer NASH Pathologie mit resultierender Hepatokarzinogenese führt. Dieses Model rekapituliert somit die wichtigsten Merkmale humaner NASH. In diesem CD-HFD Maus Model wird NASH durch eine $CD8^+$ und NKT-Zellen Zytokin-vermittelten Interaktion mit den Hepatozyten induziert. Ein besonderes Augenmerk ist auch darauf zu richten, dass in NASH Patienten ein ähnliches T-Zell Aktivierungsprofil mit analogen Zytokin-vermittelten Mechanismen gefunden wird, was die klinische Relevanz unseres Mausmodels unterstreicht.

Ziel 1: Entschlüsselung des TCR Signalings in metabolisch aktivierten T-Zellen in NASH und Leberkrebs Entstehung

In diesem wissenschaftlichen Kontext wurde in dieser PhD Thesis die Rolle von T-Zellen detaillierter als zuvor, sowie T-Zell Rezeptor (englisch: T-cell receptor (TCR)) abhängigen Mechanismen untersucht, welche zu der NASH Entstehung und der NASH induzierten Hepatokarzinogenese wichtig sind. Dazu wurden verschiedene Diäten (Hoch-Fett Diät (HFD), CD-HFD, Western-Stil Diät mit Trans-Fetten (englisch: western-style diet with trans-fat (WD-HTF))), genetische Maus Modelle (C57Bl6, TCRβδ$^{-/-}$, OT-1, Prf1$^{-/-}$, Jα18$^{-/-}$, CD1d$^{-/-}$) und Antikörper basierte Strategien (α-CD8, α-PD-1, α-NK1.1) in den Diät-Maus Modellen verwendet. Dies ermöglichte es, neues Licht auf Mechanismen der NASH Pathologie Entstehung und deren Progression zum hepatozellulären Karzinom zu entschlüsseln.

Die gewonnenen Daten deuten darauf hin, dass nur in NASH induzierenden Diäten, wie der CD-HFD oder der WD-HTF, von einem frühen Zeitpunkt an CD8$^+$ T-Zellen aktiviert werden und diese daraufhin mehr frühe Aktivierungsmarker CD69 und den Aktivierungs-/Erschöpfungsmarker PD-1 über den Verlauf der NASH Pathologie exprimieren. Weiter deuten meine Daten darauf hin, dass es zu einer differenziellen TCR variablen Ketten β (TCR vβ) Expressionen in PD-1$^+$ CD8$^+$ T-Zellen kommt, was auf verschiedene erschöpfte TCR Repertoires im Verlauf der NASH schließen lässt. Auch konnte ich zeigen, dass die Entstehung und Progression der NASH Pathologie nur mit einem natürlichen TCRαβ Repertoires mit intakter TCRαβ Effektor Funktion möglich ist. Mechanismen, die mit Natürlichen Killer T-Zellen (NKT) in Verbindung gebracht werden, scheinen eine eher untergeordnete Rolle in unseren verwendeten NASH Modellen zu spielen. Zusätzlich zu der Abhängigkeit von einem natürlichen und intakten TCRαβ Repertoire für die NASH Entstehung konnte ich zeigen, dass CD8$^+$ T-Zellen je nach Progressionsstand der NASH Pathologie eine unterschiedliche Rolle haben. Zum Beispiel in frühen Stadien der NASH scheinen CD8$^+$ T-Zellen einen eher protektiven Charakter zu haben. Wohingegen in fortgeschrittenen Stadien der NASH CD8$^+$ T-Zellen für immun-abhängigen schädlichen Effekte (englisch: immune-related adverse effects (irAEs)) verantwortlich sind, welche zu Leberschädigung, stärkerem Leberschaden und Tumor Entstehung über einen möglicherweise TNF-a vermittelten Mechanismus führen.

Ziel 2: Platelet GPIbα ist ein Mediator und potentielles Ziel für eine medikamentöse Therapie in NASH und Leberkrebs

Auf der Suche, um den Kreislauf der hepatischen chronischen Entzündung in NASH durchbrechen zu können, habe ich bei der Erstellung dieser Thesis Schlüssel-Mechanismen untersucht, die verantwortlich für die NASH Pathogenese sind. Ich habe Zell-Immunzellen

Interaktion analysiert. Dabei habe ich Blutplättchen (Platelets) und Platelet Aktivierung als verantwortliche Mechanismen identifiziert, welche NASH treiben und somit Lebertumor Entstehung möglich machen. Platelets konnten mit anti-Platelet Therapie (therapeutischen Einsatz von Ticagrelor) gezielt beeinflusst werden und somit NASH Pathologie Progression verhindert oder NASH Pathologie verbessert werden. Weiter konnte ich zeigen, dass Platelet Interaktion mit Kupfferzellen und CD44-Hyaluron wichtige Mechanismen des Fortschreitens von NASH sind. Weiter, konnte ich GPIbα als ein therapeutisches Zielmolekül für die NASH Therapie identifizieren.

Diese Ergebnisse konnte ich als ein Erstautor in *Nature Medicine* im April 2019 publizieren (https://doi.org/10.1038/s41591-019-0379-5)[9].

4 Introduction

4.1 General Introduction

4.1.1 The liver

The liver is the central metabolic organ of the mammalian system, which links the absorbance of external substances through the gastrointestinal tract to the portal vein or lymph tract. Consequently, the liver serves a barrier and filter function. Further, the liver breaks down digestible ingredients of ingested food to useable micro- and macronutrients. Next, the liver enriches the circulating blood with nutrients for peripheral organs, as well as detoxifying potential harmful substances[10]. The liver therefore serves as a crucial homeostatic organ balancing peaks of nutritional overload and subsequent energy excess after eating against times of fasting to keep a constant level of metabolites like glucose and fats bound to the different lipoproteins in the circulating blood[10]. Also, the liver is a self-regenerative organ, able to regenerate completely by compensatory growth mechanism even after loss of up to 75% of its original mass[10,11].

The liver`s functional structure is composed of a unique fenestrated architecture, which increases the interaction surface with surrounding fluids for maximal exchange rates of metabolites, proteins and fats[10]. The liver`s main cell type is the hepatocyte, which is capable of storing, synthesizing and producing the molecules needed for a functional mammalian system, like cholesterol, bile salts, phospholipids, proteins and stabilizing carbohydrates levels[10]. The second hepatic cell type is the cholangiocytes, which in addition to the hepatocytes, produce some of the bile acids needed for food resorption. Further, there are a plethora of cells of the endothelium, the liver sinusoidal endothelial cells (LSECs) and leukocytes, both resident as well as patrolling cells (e.g. Kupffer cells (KC), yδ T-cells, natural killer (NK), natural killer T (NKT) cells and myeloid lineage cells like dendritic cells). The liver has traditionally been considered to have a gatekeeper function, digesting food, detoxifying potential harmful substances from the periphery and handling danger signals derived from the intestine, like bacterial components. Therefore, the liver has a remarkably anti-inflammatory microenvironment, allowing the liver to train and form the immunological responses and thus the immunological landscape. In conclusion, the liver has a central role as a metabolic organ, as well as in shaping the hormonal and immunological landscape[10].

4.1.2 Hepatocellular carcinoma

Although remarkable progress in terms of survival, response and treatment options for nearly every known cancer type has been achieved in the last decade, a few entities are opposing this trend of progress in anti-cancer diagnosis and successful therapies. One of these entities is hepatocellular carcinoma, which is the primary cancer type of the liver[3]. This leads to high mortality rates, which are still increasing, despite modern medical advances[12]. Depending on the stage and thereby the severity of liver cancer, this results in a low median 5 year survival rate between 4-17.2%[3,4,13]. Primary liver cancer, the 5th most common cancer type detected, can be grouped into multiple entities. A relatively small proportion of liver cancer arises from non-epithelial tumors and pediatric hepatoblastoma, 10-15% result from cholangiocarcinoma (**Figure 1a**), but the main burden, accounting for 80-90% of all liver cancer, comes from hepatocellular carcinoma (HCC) (**Figure 1b**)[3]. A ratio of 3:1 of primary liver cancer in males/females indicate that men are especially prone to developing liver tumors[14,15].

While the underlying mechanisms for HCC induction is strongly dependent on geographical region in worldwide incidences, in 90% of HCCs the underlying mechanisms for induction is a chronic inflammation of various origins, leading to different degrees of fibrosis and cirrhosis[3]. Viral infections are still the leading cause of chronic liver inflammation, but due to lifestyle changes, alcohol and dietary-induced liver inflammation are gaining importance as HCC etiologies in areas of the world traditionally having low HCC rates (**Figure 1c**). However, chronic inflammation in regenerative organs like the liver lead to a hepatic environment of constant cell death and increased compensatory proliferation through increased activation of liver progenitor cells and non-parenchymal cells[3]. This chronic cycle of death and regeneration is termed “chronic necroinflammation”[3]. The high turnover of cells in a chronic necroinflammatory environment results in DNA damage, epigenetic modifications and an overall genetic instability, paired with increased senescence of cells and intracellular stress, leading overall to the fibrosis and scarring of liver tissue, which is the soil of tumorigenesis (**Figure 1c**)[3].

4.1.3 Underlying aspects of chronic inflammation for hepatocellular carcinoma development

The current understanding of liver cancer development suggests that chronic inflammation leads to constant stress on hepatocytes and liver-associated cells, resulting in chromosomal aberrations, cell death, necroinflammation, an inflammatory cytokine milieu and compensatory proliferation of hepatocytes and progenitor cells, as well as immune cell activation[3,16]. Further, this inflammatory environment leads to activation of hepatic stellate cells, inducing enhanced production of extracellular matrix mostly consisting of collagen, resulting in scarring of the liver

and increased liver stiffness. Scarring of liver tissue leads to cirrhosis, and combined with an impaired immune surveillance, results in a pro-oncogenic hepatic environment, which induces aberrant cells, lesions and liver cancer formation[17].

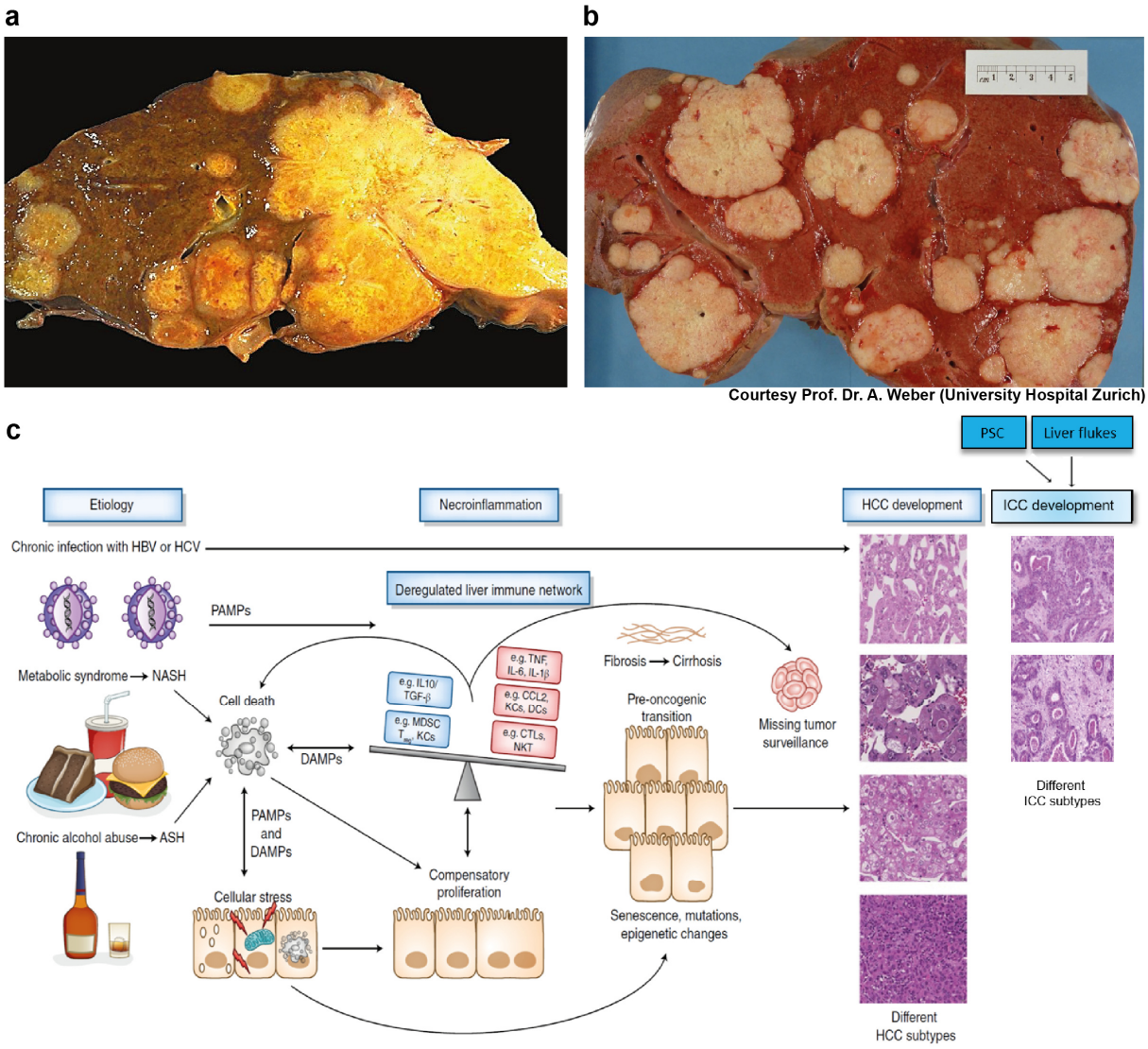

Figure 1: Chronic inflammatory stimuli drive necroinflammation and subsequent hepatocarcinogenesis (adapted from Ringelhan et al.[3])
(a) Examples of resected ICC and (b) HCC in collaboration with Achim Weber. (c) Chronic inflammatory stimuli of various origin (virus, metabolic excess, alcohol abuse) deregulate the liver immune network, induce cell death and compensatory proliferation. This necroinflammation drives genetic instability and fibrosis leading to hepatocarcinogenesis. Also intrahepatic cholangiocarcinoma (ICC) develops in the background of chronic inflammatory stimuli (primary sclerosing cholangitis (PSC) and liver flukes).

The multitude of variables influencing liver cancer formation is also represented by the complexity and different mutational backgrounds of liver cancer found in patients, making therapeutic approaches difficult and patient-specific[3].

The liver cancer`s underlying chronic inflammation can arise via different etiologies, with viral infections of HBV and HCV currently being the most common. However, with the epidemic rise of metabolic syndrome and obesity all over the world, metabolically-induced liver cancer is continually rising[18–20].

Despite increasing alcohol abuse leading to alcoholic liver disease and alcoholic steatohepatitis (ASH), an increasing contributor to liver inflammation is correlated to over nutrition combined with a sedentary lifestyle with or without extensive alcohol abuse (less than two alcoholic beverages per day)[21,22]. This liver pathology, termed non-alcoholic fatty liver disease (NAFLD) and its more severe form non-alcoholic steatohepatitis (NASH) are the most prevalent causes of dietary-induced HCC[23].

Further, epidemiologic studies show that in adipose patients with a body mass index (BMI)>30 kg/m^2 and a high caloric intake combined with a sedentary lifestyle the cancer incidence massively increases by up to six-fold[20,24].

4.1.4 Dietary steatohepatitis as a driver of hepatic carcinogenesis

Thus, I wanted to focus on dietary-induced pathologies and HCC, due to the exorbitantly rising burdens of overweight, obesity and metabolic-related disease like e.g. Type II diabetes in western cultures like the USA and Europe, but also in developing countries in the past 30 years[1–3,25].

NAFLD is characterized by a reversible increase in liver fat deposition in hepatocytes, resulting in micro- and macro-steatosis, systemic increase of fatty acids (e.g. triglycerides, cholesteric derivatives), insulin resistance and therefore development of metabolic syndrome on the background of non-significant alcohol intake (**Figure 2a**)[21,22,25]. Although reversible, the prevalence of NAFLD is high, affecting people on an epidemic scale. For example, in the United States approximately 20-30% of the adult population are diagnosed positive for NAFLD and an alarmingly incidence of 10% of children positive for NAFLD, as well[25,26]. Further, NAFLD is on a steady rise with 15% of the US population affected in 2005 to 25% affected after only 5 more years, in 2010 (**Figure 2b**)[25]. Similar rates of 20-30% of NAFLD prevalence were reported on a global scale, affecting an epidemic scale of more than 1 billion people[25,27,28].

Depending on the population (e.g. ethnicity, gender) and region of individual studies, progression to the more severe pathology, NASH, can be observed in 15-26% of all NAFLD cases. For example, in a US cohort between 3-4% of the adult population was affected, which nearly doubled from 2005 to 2010 (**Figure 2b**) [25,27]. What exactly drives NAFLD to NASH progression is not understood, but there are indications that there are multiple hits or drivers of pathogenesis. Hits including further metabolic reprogramming, lipid toxicity and increasing

endoplasmic reticulum (ER) stress as a result of the underlying NAFLD and metabolic syndrome. However, one of the defining features of NASH is an immune cell-meditated mostly liver-associated inflammatory component ("sterile inflammation") fueling the previously described chronic necroinflammation and subsequent fibrosis, which is one of the defining mechanisms of HCC development[3,29].

Chronic necroinflammation, including the frequently induced fibrosis, leads to the activation of damage-associated molecular patterns (DAMPs), pathogen-associated molecular patterns (PAMPs), Toll-like receptors (TLRs), together with increased levels of reactive oxygen species (ROS), toxic metabolites (e.g. high cholesterol and free fatty acids levels) and increasing concentrations of cytotoxic cytokines (e.g. TNF-a). This inflamed environment affects not only hepatocytes and stellate cells, but immune cells, both innate, e.g. dendritic and Kupffer cells, and adaptive immune cells like cluster of differentiation (CD) 4^+ or $CD8^+$ T-cells, in particular (**Figure 3**)[6,22,26,29,30]. The exact sequence of progression as a result of the chronic necroinflammation from NASH to HCC is not fully understood. On an immunological level, selective loss of $CD4^+$ T-cells by cytotoxic fatty acids induces less macrophage-mediated clearance of senescent hepatocytes, as well as a potential tolerance break due to decreased numbers of regulatory T-cells[31,32]. In addition, $CD8^+$ subsets drive liver damage in established NASH in a CD-HFD-based mouse model (**Figure 3**)[6,33]. Further, $CD8^+$ T-cells express programmed death receptor 1 ($PD\text{-}1^+$) in HFD-induced NAFLD, indicating an exhausted T-cell phenotype[34]. Further, IgA^+ B-cell-mediated suppression of anti-tumoral $CD8^+$ subsets together with a change of NKT cell polarization and disruption of the immune-tolerant liver environment by M1/M2 shifting of myeloid cells were found to correlate with tumor promotion (**Figure 3**)[3,35–37]. On a molecular level, there is an intense "cross-talk" between immune cells and hepatocytes responsible for HCC induction/development. In general, dysregulation or activation of TLR through DAMPs and PAMPs, canonical and non-canonical NF-κB signaling lead to tumor induction, with mediators including molecules such as TNF-a, lymphotoxin β, interferon gamma (IFNy), ROS, IL-1β, IL-6, , IL-10, TGF-β and alarmins including IL-33[3,13,20,21].

In summary, a high global prevalence of underlying inflammatory conditions, lack of therapeutic strategies and predictions of a global increase in HCC rates, makes HCC one of the most dangerous cancer entities besides hormonal carcinogenesis. As a result, a diagnosed HCC, regardless of the underlying cause, is for the individual patient essentially a death sentence.

4.1.5 Mouse models of non-alcoholic steatohepatitis

Due to the complexity of non-alcoholic steatohepatitis-induced hepatocarcinogenesis, modelling key mechanisms and facets of the underlying disease, NAFLD and NASH, in animal models is challenging[38,39]. Aspects of an appropriate model must include systemic obesity, insulin resistance, hepatic steatosis and steatohepatitis, as well as forms of fibrosis that lead subsequently to HCC development[38–40].

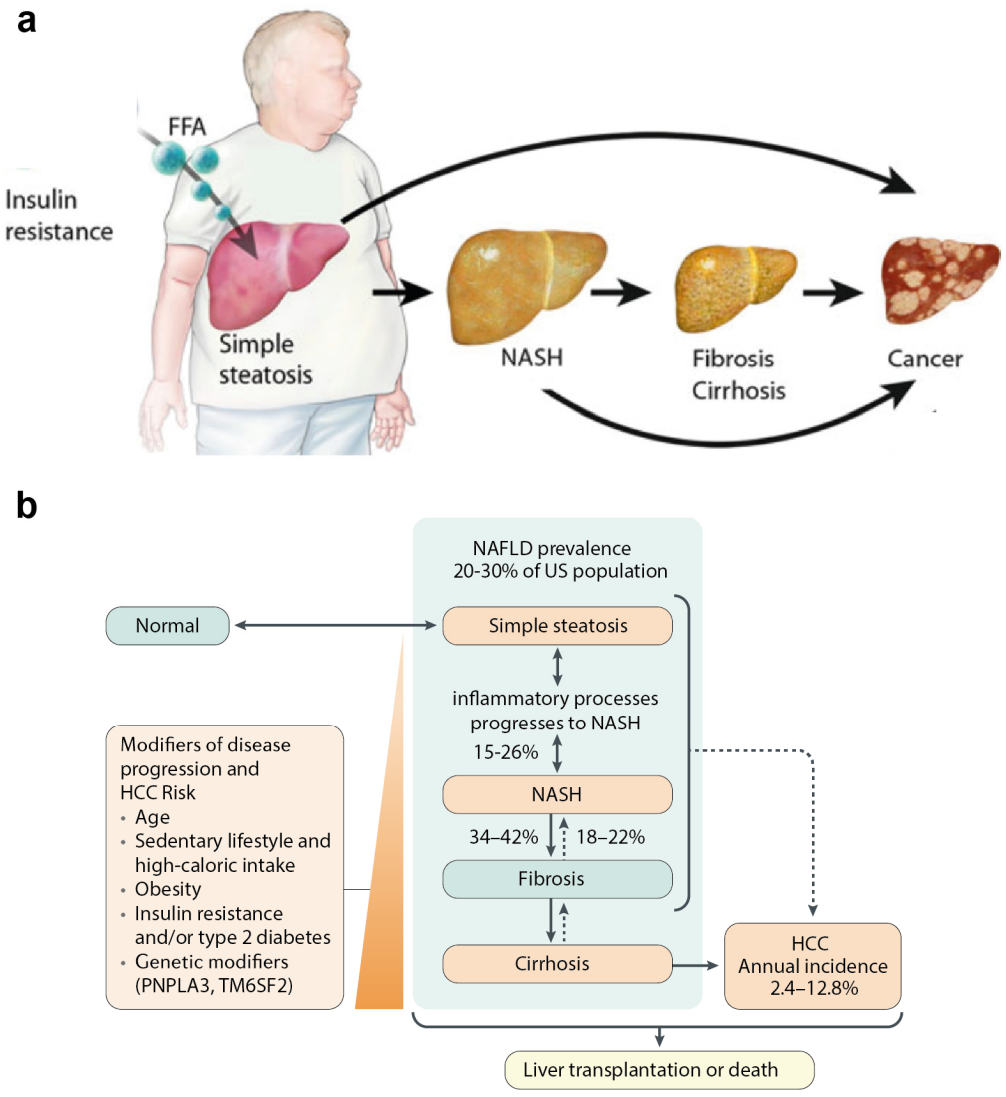

Figure 2: Hepatocarcinogenesis in the background of a non-alcoholic fatty liver disease (adapted from Dannenberg and Berger[41] and Anstee et al.[42])
(a) Sedentary life-style and nutrient excess lead to obesity, insulin resistance and free fatty acids (FFA) influx to the liver, inducing simple steatosis. Simple steatosis progresses to non-alcoholic steatohepatitis (NASH), which progresses to fibrosis and cirrhosis in the context of necroinflammation. Liver cancer can develop not only from fibrotic/cirrhotic, but also from steatotic or NASH livers lacking fibrosis. (b) Overview of incidence rates for progression from normal liver, to simple steatosis, NASH, fibrosis, cirrhosis and liver cancer.

In principle, three different experimental approaches to model NAFLD in different severity states with varying probabilities of progression to HCC can be done (**Table 1**, adapted from

Anstee et al.[42]). The first approach employs the use of chemical carcinogens (e.g. carbon tetrachloride or diethylnitrosamine with or without high-fat diets)[43,44]. The second approach uses genetically altered mouse models (e.g. leptin-deficient ob/ob mouse strains or unconventional prefoldin RPB5 interactor (URI) with or without high-fat diets)[45,46].

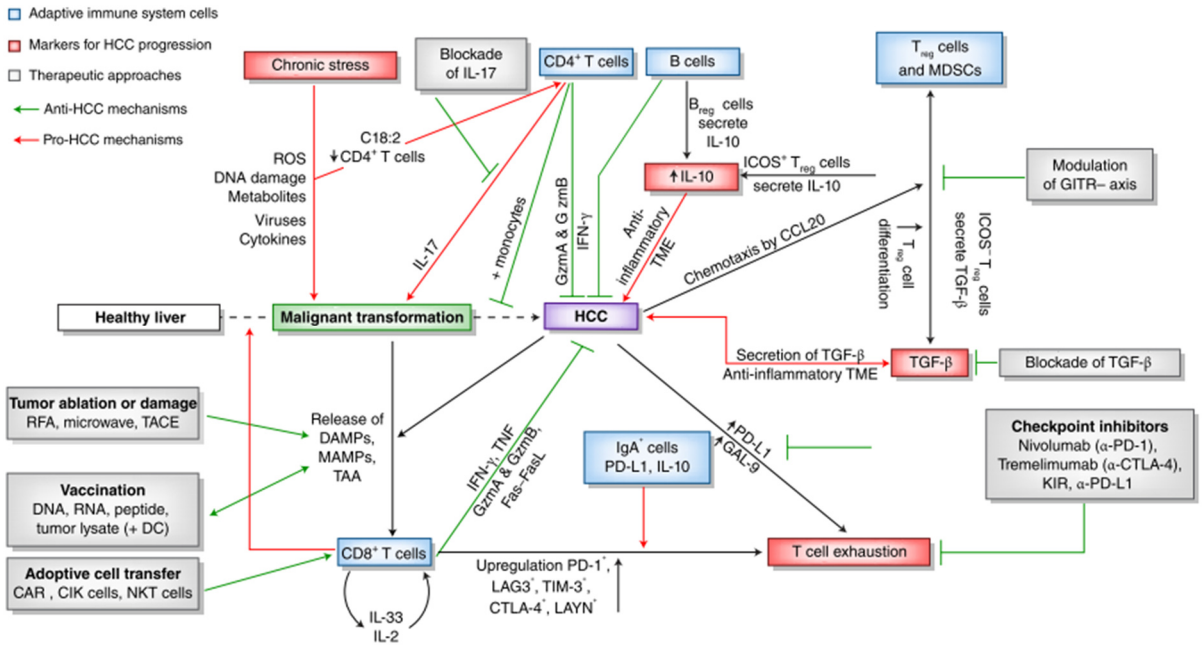

Figure 3: Immune cell mediated contribution driving or counteracting HCC development with therapeutically approaches (adapted from Ringelhan et al.[3])
Network of immune cell driving or inhibiting development of HCC by direct or cytokine mediated mechanisms. In particular chronic stress drive malignant transformation of hepatocytes by cytotoxic or pro-inflammatory polarized $CD4^+$ and $CD8^+$ T-cells (red arrows). Anti-inflammatory mechanisms by B-cells, regulatory T-cells and M2 polarized myeloid cells inhibit effect anti-tumor surveillance in concert with increased IL-10 and TGF-β levels, as well as T-cell exhaustion. In grey boxes are potential clinical approaches for therapy by blocking exhaustion signals on T-cells, increase cytotoxic cells by adoptive transfer or vaccination, or physical based tumor destruction methods like microwave or transarterial chemoembolization (TACE). TAA, tumor-associated antigen; RFA, radiofrequency ablation; CAR, chimeric antigen receptor; CIK cells, chemokine-induced killer cells; Breg cells, regulatory B cells; TME, tumor microenvironment; GITRL, ligand for GITR[3].

The third approach uses dietary mouse models that involve feeding different styles of diets either to wild type or to genetically modified mice (e.g. methionine/choline-deficient [MCD] feeding; liver specific c-myc transgenic mice fed a MCD; high-fat diet [HFD] feeding; overexpression of urokinase plasminogen activator leading to constant endoplasmic reticulum stress mostly in hepatocytes (MUP-uPA transgenic) mice fed a HFD; long-term “western-style” diets, which include increased fructose and cholesterol levels or choline-deficient high-fat diets) (**Table 1**, adapted from Anstee et al.[42])[6,31,37,47].

Wild type mouse models, which rely on feeding of specific diets alone, are an ideal method of modelling the initiation, establishment and progression of NAFLD, NASH and HCC, as they do

not rely on genetic alterations, which are not observed in human disease. Further, the rather slow pace of disease development by long-term diet feeding allow for in depth investigation at stages of earliest steps of disease initiation, progression to NAFLD, early or advanced NASH[9].

Table 1: Overview of animal models of NAFLD, NASH and HCC development (adapted from Anstee et al.[42])

Model	NAFLD	NASH	Metabolic Syndrome	HCC	Comments
WD/CCL4[48]	+	+	+	+	Steatosis: + Fibrosis: ++ Weight loss HCC development
DEN/HFD[49]	+	+	+	+	Steatosis: + Fibrosis: - Obesity HCC development
Ob/ob[39]	+	-	+	-	no spontaneous NASH or HCC
URI-IL17 / HFD/ CD-HFD[46]	+	+	+	+	Steatosis: + Fibrosis: +/- Obesity HCC development
Methionine-choline deficient diet [MCD][50]	+	+	Weight loss, cachexia	-	steatosis, fibrosis and cachexia, but HCC development is infrequent
MYC-ON mice/MCD[31]	+	+	-	+	Steatosis: + Fibrosis: + HCC development
High-fat diet [HFD][50]	+	-	+	+ / -	steatosis and obesity but not fibrosis HCC incidence is very low
MUP-uPA mice/HFD[51]	+	+	+	+	Steatosis: + Fibrosis: + Obesity HCC development
High-fat/ cholesterol high fructose diet [WD][47]	+	+	+	+	Steatosis: + Fibrosis: ++ Obesity HCC development
Choline deficient High-fat diet [CD-HFD][6]	+	+	+	+	steatosis, fibrosis, obesity, metabolic syndrome HCC development

Thus, models using choline-deficient high fat diet feeding (CD-HFD) were utilized within the framework of the current PhD thesis due to its representation of NASH phenotype observed in the clinics and its ability to reproduce the whole spectrum of disease initiation leading to NAFLD and NASH ending in dietary induced hepatocarcinogenesis without genetic drivers. This CD-HFD model induces systemic obesity, metabolic syndrome, liver steatosis and liver inflammation after 6 months of diet feeding and subsequent liver tumor development in 25% of all CD-HFD fed mice after 12 months (**Figure 4**, adapted from Wolf et al.[6]). In particular, a cytokine-mediated (e.g. LIGHT) cross-talk between NKT, adaptive immune cells of the CD8 lineage and hepatocytes cause liver steatosis, inflammation and subsequent HCC by hepatocellular LTβR and canonical NF-κB signaling NASH to tumor transition (**Figure 4**, adapted from Wolf et al.[6]).

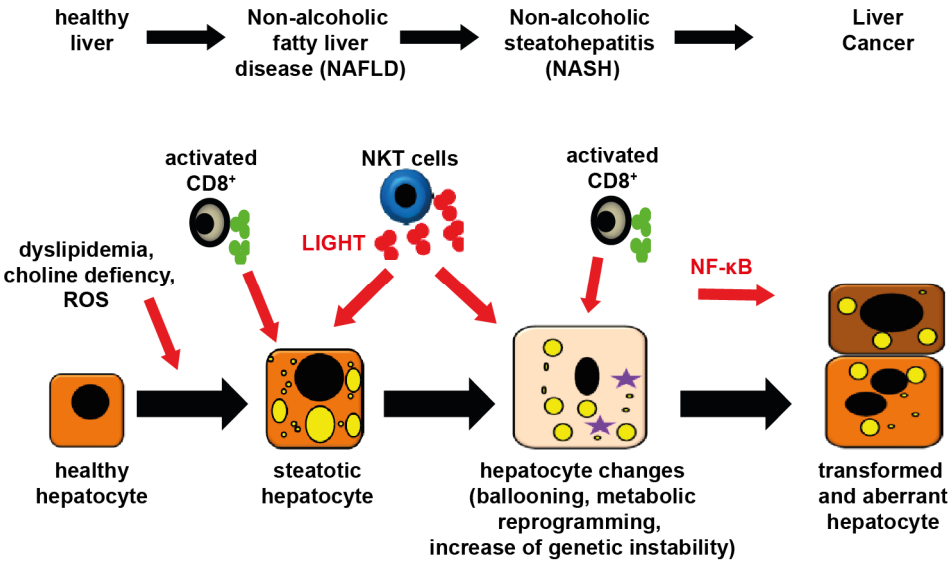

Figure 4: Mechanistic underpinnings of the CD-HFD mouse model (adapted from Wolf et al.[6])
Chronic CD-HFD feeding induces dyslipidemia, choline deficiency and ROS formation together with NKT cells and LIGHT driving the transformation of healthy hepatocytes to steatotic hepatocytes. Steatotic hepatocytes change and get metabolically reprogrammed by chronic exposure to inflammation mediated by activated CD8+ T-cells and NKT cells and nutrient excess of the CD-HFD. Thus, necroinflammation with chronic cell death and compensatory proliferation induces genetic instability, which transforms hepatocytes in NF-κB mediated processes to drive hepatocarcinogenesis.

4.2 Understanding drivers of chronic liver inflammation – T-cells

4.2.1 T-cells

Due to the known role played by T-cells in dietary liver inflammation, a more thorough analysis of how they mediate cytotoxicity should be performed. In general, the T-cell lineage can be subdivided into two major classes of T-cells, first invariant T-cells including natural killer T-cells and T-cell receptor (TCR) γδ T-cells and second, classical TCRαβ T-cells, which can be subdivided into $CD4^+$ T-cells and $CD8^+$ T-cells[52].

Depending on the microenvironment, T-cells have different roles. Generally speaking, invariant T-cells are the patrolling, organ-specific cells, the first responders to tissue damage and detection of foreign proteins from e.g. bacteria[53]. These invariant T-cells are therefore considered to be innate-like T-cells and have a bridging role between the innate and adaptive immune system[54].

$CD4^+$ T-cells are the so-called helper T-cells, whose function is to mediate cellular immunity (TH1 polarization) by e.g. granzyme A/B (GzmA/B) or indirectly by interaction with monocytes to clear senescent cells[3]. Further, TH2-polarized $CD4^+$ T-cells influence immune reactions either in a promoting manner (e.g. supporting humoral B-cell-mediated immune responses through IL-4), or a dampening manner (e.g. anti-inflammatory, regulating role of T regulatory cells through IL-10)[52]. An additional subset of $CD4^+$ T-cells are the TH17 cells, which mainly produce IL-17 and are important in chronic inflammation and autoimmunity.

In contrast, $CD8^+$ T-cells, although capable of fulfilling regulatory and anti-inflammatory functions in certain contexts (e.g. intestinal barrier function), are more efficient and prone to being cytotoxic T lymphocytes (CTLs). Classical $CD8^+$ T-cells are considered efficient killer cells, patrolling the body constantly checking cells for foreign peptide structures presented in a major histocompatibility complex (MHC) I TCR-interacting fashion[52]. Upon detection of foreign antigens (e.g. on virus-infected cells), CTLs inject granzymes through perforin into the target cells. In parallel, cytotoxic cytokines like IFNy or TNF-a get released, inducing a strong local inflammatory reaction.

4.2.2 TCR signaling

The classical αβ TCR is a cell membrane-anchored protein complex orientated toward the outside of the cell, building a complex with the CD3 chains, which point to the inside. Through this difference in orientation, signal transduction from extracellular signals to the inside is achieved. Upon TCR stimulation by interaction of the specific TCR with its mutual antigen presented by MHC molecules, a multi-layered and feedback-controlled signal cascade starts, leading either to T-cell activation or, when co-stimulation is insufficient to T-cell anergy induction, a state in which T-cells become unresponsive to additional TCR stimuli[52,55,56].

For signal transduction, CD3 chains possess different amounts of biochemically exposed tyrosines for immunoreceptor tyrosine-based activation motifs (ITAMs), which upon phosphorylation by e.g. lymphocyte cell-specific protein tyrosine kinase (Lck) recruit different kinases (e.g. ZAP-70). ZAP-70 recruitment leads to a phosphorylation cascade of linker-of-the-activation-of-T-cells (LAT) and cytosolic adapter protein Src homology 2 domain–containing leukocyte phosphor-protein of 76 kDa (SLP-76), which unleash MAP kinase pathways upon phosphorylation for effective TCR signaling amplification and transduction.

Further, Lck leads to PI3 kinase activity combined with phospholipase C, which regulates intracellular Ca^{2+} levels by the $PI(4,5)P_2$ – IP_3 – DAG signaling pathway (phospholipid phosphatidylinositol 4,5 bisphosphate - inositol trisphosphate – diacylglycerol). Downstream of PI3K, other kinases (e.g. PKCθ) amplify on the one hand further TCR signals and on the other hand induce the formation of the CBM (CARMA1/Bcl10/MALT1) complex. Depending on the activated pathway, different transcription factors get used (e.g. nuclear factor of activated T cells (NFAT), activator protein-1 (AP1), NF-κB, signal transducer and activator of transcriptions (STATs)). Upon their simultaneous activation and interaction, T-cells get activated (e.g. NFAT activated together with AP-1) and produce IL-2 or T-cells become anergic (e.g. NFAT activated without AP-1)[52,55].

Further, a process called inside-out signaling leads upon TCR stimulation to actin cytoskeletal changes and enhanced integrin binding (e.g. lymphocyte function–associated antigen-1 (LFA-1), very late antigen-4 (VLA-4) and their cognate ligands intercellular adhesion molecule (ICAM) and vascular cell adhesion molecule (VCAM))[55].

However, all these changes upon TCR stimulation and activation are controlled on multiple levels in a context-specific manner, e.g. by specific phosphatases like CD45, SH2 domain–containing protein- tyrosine phosphatase (SHP1, SHP2 and PP2A) recruited to phosphorylated ITIMs (immunoreceptor tyrosine- based inhibitory motifs e.g. in T cell immunoreceptor with Ig and ITIM domains, short TIGIT), or HPK1 binding to SLP76[55]. An example of this dual regulation is CD45, which can either dephosphorylate Lck`s inhibitory domains and allowing Lck activation, or by dephosphorylating Lck`s active sites and limiting its signaling potential[55].

In conclusion, there are multiple pathways and interaction sites translating TCR stimuli into T-cell phenotypic changes, thus allowing them to distinguish between specific, acute and chronic, as well as weak and strong TCR stimuli.

4.2.3 T-cell exhaustion

For an effective T-cell response, a TCR stimulus alone is not sufficient, but induces T-cell anergy. Therefore, simultaneous co-stimulatory signals parallel to TCR stimuli are important (**Figure 5**). One of the prominent examples is the receptor interaction of CD28 on T-cells and CD80 or CD86 on antigen presenting cells (APCs), inducing T-cell intracellular PI3K signaling, leading to PDK1 (3-phosphoinositide- dependent protein kinase 1), Akt and NF-κB activation through the CBM complex. Other co-stimulatory receptors are CD2, CD5, CD137, OX40, Inducible T-cell co-stimulator (ICOS) and the previously described LFA-1. Upon effective T-cell activation the activation chemokine IL-2, the survival factor Bcl-xl and proteins involved in increasing metabolic capacities (e.g. Glut1 increasing glucose uptake and glycolysis) are increased[55–58].

Prolonged and chronic TCR activation leads to an exhausted T-cell phenotype, characterized by first a decreased response to antigen stimuli by downregulation of CD3 or a decreased response to survival signals like IL7 or IL15 by reduced expression of CD122, the β-chain of the IL-2 and IL-15 receptor, and CD127, which is the α-chain of the IL-7 receptor. Second, poor T-cell effector function (e.g. decreased production of IL-2, IFNy, and TNF-a; decreased cytolytic capacity by Fas ligand or the GzmB/perforin axis) is observed, and third, expression of inhibitory receptors like lymphocyte-activation gene 3 (LAG-3), mucin-domain containing-3 (TIM-3), cytotoxic T lymphocyte antigen-4 (CTLA-4) and PD-1 are increased (**Figure 5**)[55–58]. For example, LAG-3 interaction with MHC II affects cell cycle progression; CTLA-4 affects co-stimulation of T-cells by competing with CD28 as a high affinity binding partner to CD80/CD86, and trans-endocytosis of CD80/CD86; PD-1/PD-L1 interaction recruits T-cell internal phosphatases, thereby limiting TCR dependent signaling. Further, chemokines like IL-10 or TGF-β, activation of amino acids (e.g. tryptophan), depleting enzymes like indolamin-2,3-dioxygenase (IDO) or immunoregulatory cells (e.g. T_{regs} or M2 polarized myeloid cells) contribute to an exhausted phenotype or induce further T_{reg} formation[55–58]. Therefore, a non-effective clearance of a TCR stimulus and prolonged T-cell activation, like in HBV infections or chronic hepatitis, leads to T-cell exhaustion and eventually to chronic inflammatory conditions.

4.3 Platelets –mediators of chronic liver inflammation

In order to understand early mediators of chronic dietary-induced liver inflammation in greater detail and to potentially therapeutically intervene with these inflammatory mechanisms, previous work in the group of Mathias Heikenwälder investigated the role of platelets[59]. It has become evident that platelets play a more prominent role in mediating inflammatory processes than initially appreciated. Reports of other disease entities like thrombosis, obesity, atherosclerosis, metastasis, cancer and stroke suggested that platelets could potentially mediated adverse effects in a chronic liver inflammation[9,60–63].

In the background of virus-induced liver inflammation, platelets were identified as a crucial factor mediating cytotoxic T-cell responses[64–66]. Further, platelets contributed to hepatitis B-mediated HCC development, aggressivity and subsequent survival of infected mice. Thus, antiplatelet therapy by Aspirin-Clopidogrel was beneficial in this mouse model of hepatitis B by reducing hepatic T-cell migration and accumulation, inducing prolonged survival of infected mice[67].

Therefore, a growing body of literature implicates platelets as key mediators of damage and inflammation, rather than as a bystander effector cell contributing to inflammation.

4.3.1 Platelet biology

Platelets derive from the megakaryocytes in the bone marrow by fragmentation and have a relatively short life time of approximately 7 days[60,68]. Platelets lack a nucleus but have characteristics of whole cells. Traditionally, platelets are involved in wound closing, thus blood clotting, wound healing, angiogenesis, but also promoting local leukocyte recruitment by changing the local cytokine/chemokine environment[9,59,60].

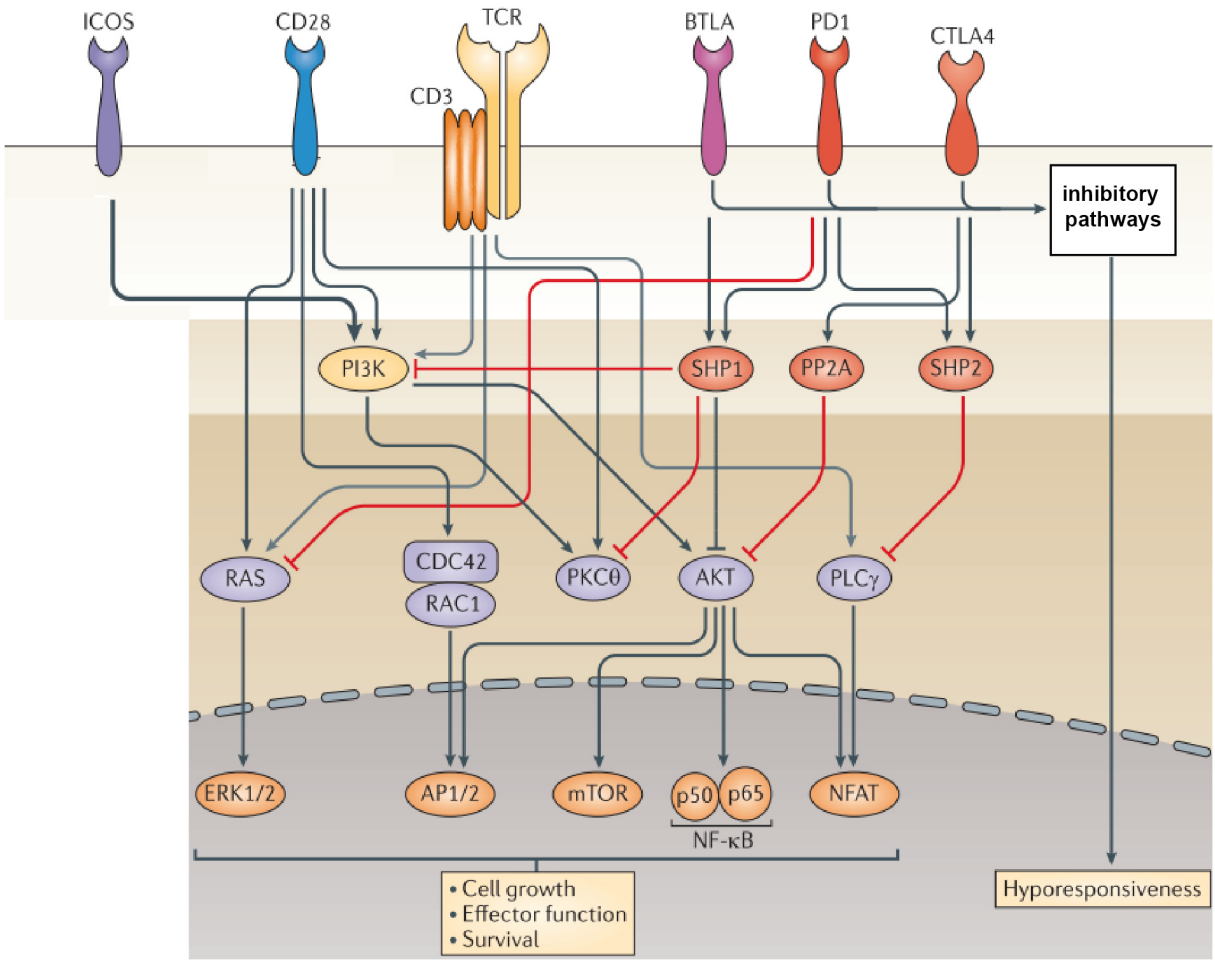

Figure 5: Important factors of co-stimulation or inhibition of TCR signaling (adapted from Chen et al.[58])
Intracellular signaling network downstream of TCR and co-stimulatory (ICOS and CD28) or co-inhibitory (PD-1 and CTLA-4) receptors on T-cells indicating interaction and cross-talk determining T-cell reaction (activation, inhibition or anergy/hyporesponsiveness) in a context and TCR stimulus dependent manner.

Platelets have different surface receptors mediating signals upon different interactions with the specific ligands triggering specific actions (**Figure 6**)[69]. Depending on the trigger, platelets have a repertoire of reactions. This includes, for example, influencing local blood flow parameters by platelet activation and subsequent aggregation, platelet-mediated cell apoptosis by Fas/FasL interaction, limited transcriptional activity of megakaryocyte-derived RNA, and platelet cargo release[9,60]. Cargo release of the platelet granules is a particularly

powerful mediator of the local cytokine/chemokine environment. For example, platelets release cytokines like immune cell-interacting TGF-β and blood flow-modulating serotonin - not only in a direct manner, but also by guiding inflammatory cells "laying" paths of exosomes[59,60]. Under non-pathological conditions these processes execute mainly local defense mechanisms during injury and angiogenesis; however, chronic inflammatory situations reverse these mechanisms and promote chronic inflammation[59,60,66,67].

However, similar to van-der-Waals forces in fatty acid binding interaction or the working behaviour of ants, a lot of small interactions can have a large systemic effect. Therefore, one should not underestimate the impact of local platelet activation/aggregation and cargo release, because platelet abundance in healthy individuals of 1.5-3.0E11 platelets/L is increased to pathological levels greater than 4E11 platelets/L in diseased patients of different entities[59,60].

4.3.2 Antiplatelet treatments

Different antiplatelet treatments are in clinical use modifying platelet functions in a specific manner (**Figure 6**)[69]. Antiplatelet treatments are in general considered safe, for example prolonged low-dose Aspirin (Asp) treatment, which inhibits irreversible cyclooxygenase (COX)-1 and thereby inhibiting platelet function lifelong, are commonly used for treatment of patients with risk for cardiovascular disease or atherosclerosis[69,70]. The limitation of Aspirin as a relative weak antiplatelet drug can be overcome when combined with additional antiplatelet drugs, like Clopidogrel (Clo) [69,71]. This is called dual antiplatelet therapy. Clopidogrel inhibits irreversible the $P2Y_{12}$ receptor on platelets and thereby the adenosine diphosphate (ADP)-induced platelet aggregation, which is a consequence of ADP release of activated platelets at sides of injury, like artherosclerotic plaques (**Figure 6**)[69,71]. To circumvent the irreversibility of platelet function inhibition by either Asp or Clo or combined Asp-Clo, reversible platelet function inhibitors like Ticagrelor were developed[72]. Similar to Clo, Ticagrelor inhibits the $P2Y_{12}$ receptor on platelets and thereby the adenosine diphosphate (ADP)-induced platelet aggregation, but in a reversible manner (**Figure 6**)[69,72]. Other prominent $P2Y_{12}$ receptor inhibitors are Prasugrel, which inhibits platelet function irreversible but in a more rapid and consistent way compared to Clo; or Cangrelor, which inhibits platelet function reversible, but in contrast to Ticagrelor Cangrelor has the disadvantage of intravenous administration for long-term treatments[69,73,74]. Next, Abciximab, Eptifibatide, or Tirofiban are FDA approved antiplatelet treatments targeting αIIbβ3 and thereby platelet aggregation, but also have the disadvantage of intravenous administration (**Figure 6)**[69].

In summary, antiplatelet treatments have minimal risks besides prolonged bleeding times, are relatively cheap and are therefore administered on a regular basis for different pathologies increasing clinical outcome for patients.

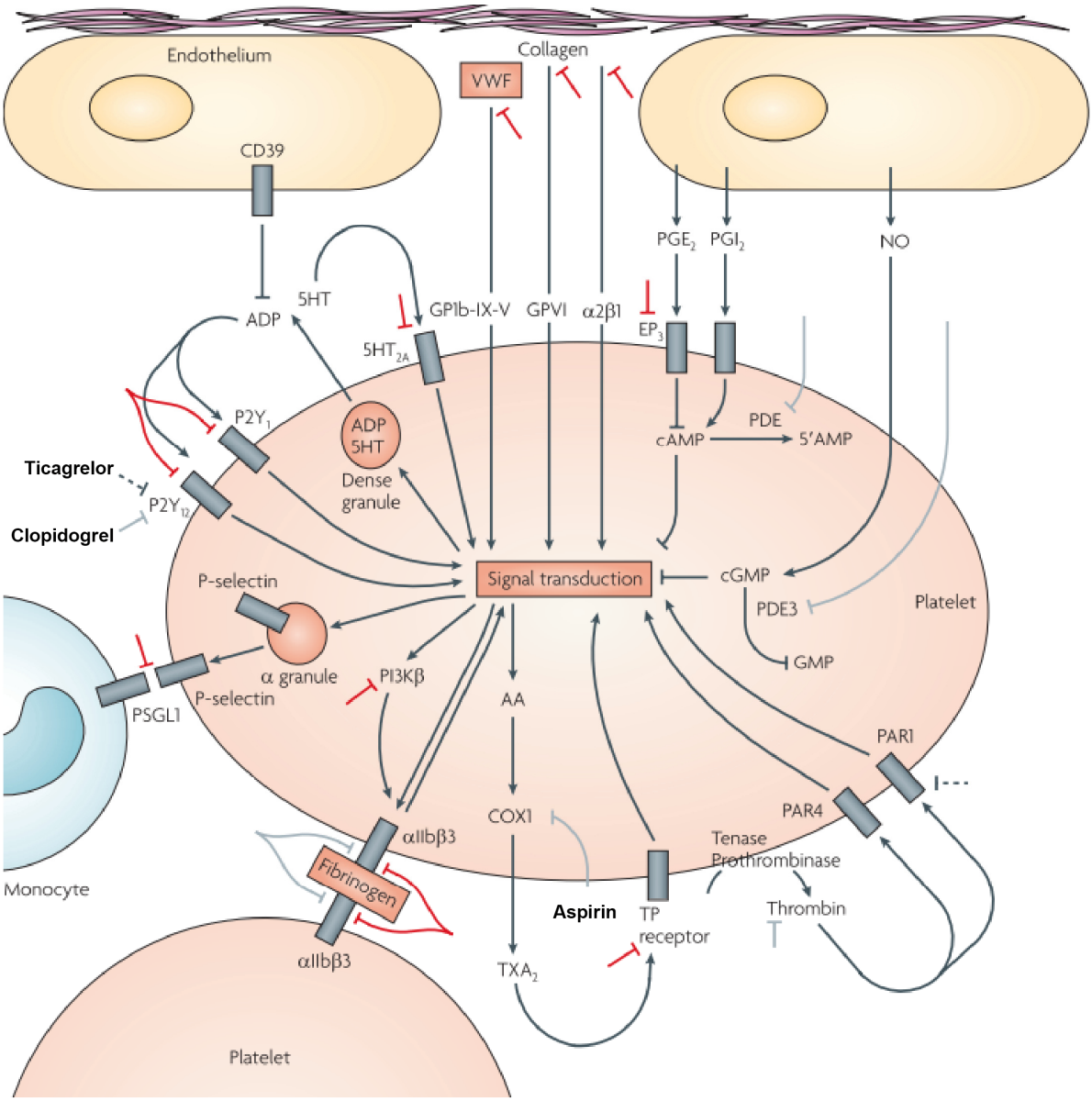

Figure 6: Platelet receptors/ligand interaction and potential interventional antiplatelet treatments (adapted from Michelson[69])

Receptors and respective ligands on platelet surface. Receptors playing an important role in binding to collagen are platelet surface glycoprotein VI (GPVI), integrin α2β1, as well as von Willebrand factor (VWF) binding to platelet surface glycoprotein 1b (GP1b)-IX-V complex. Further, thrombin is a potent activator of platelets by proteinase-activated receptor 1 (PAR1) and PAR4. Platelet- platelet aggregation is mediated by fibrinogen or with high local blood pressure/shear forces by VWF-integrin αIIbβ3 interaction.

Platelet–monocyte interaction is mediated by platelet surface P-selectin after platelet degranulation its cognate receptor, P-selectin glycoprotein ligand 1 (PSGL1). Antiplatelet treatments used in Malehmir*, Pfister* et al.[9] are dual therapy with Aspirin-Clopidogrel and monotherapy with Ticagrelor. Other potential platelet targeted therapies are indicated in blue (approved therapies) and red (investigational therapies) (adapted from Malehmir[59] and Michelson[69]).GPVI: glycoprotein VI, VWF: von Willebrand factor, GP1b: glycoprotein 1b, PAR1: proteinase-activated receptor 1, P2Y1: P2Y purinoceptor 1, 5HT2A: 5-hydroxytryptamine 2A, 5-HT: 5- hydroxytryptamine, TP: thromboxane prostanoid, TXA2: thromboxane A2, COX1: cyclooxygenase 1, PSGL1: P-selectin glycoprotein ligand 1, UFH: unfractionated heparin, AA: arachidonic acid; EP3, prostaglandin E2 receptor EP3 subtype; NO, nitric oxide; PDE, phosphodiesterase; PG, prostaglandin; PI3Kβ, phosphoinositide 3-kinase β-isoform, adapted from[69].

5 Hypothesis and aims

In the frame of this PhD thesis two main questions were addressed. First, what is the role of T-cells and TCR-associated signaling in NASH development and NASH-induced HCC. Second, how could the knowledge of hepatic inflammation driving NAFLD and NASH be used to understand mechanisms triggering inflammation as well as focusing to intervene therapeutically with the progression of NAFLD and NASH.

Aim 1: Deciphering TCR signaling in metabolically activated T-cells in NASH and liver cancer development

The first aim of this PhD thesis was to decipher the role of T-cells and TCR-associated signaling in NASH development and NASH-induced HCC by utilizing different genetic mouse models, genetic therapeutic and interventional antibody-based strategies.

To address the hypothesis that specific dietary-activated subsets of $CD8^+$ and NKT cells contribute mechanistically to the development of NASH and subsequently to HCC in a potentially antigen-mediated manner in a dietary mouse model, the following questions, aims and milestones were defined:

1. Is the dietary activation of T-cells a consequence of NAFLD or of NASH-promoting mechanisms? Do different subsets of T-cells influence pathology development?
2. Are there changes in the T-cell compartment upon progression of NASH pathology?
3. Are T-cells and TCR-dependent mechanisms essential to induce NASH pathology and subsequent HCC development?
4. Characterization of T-cell subsets at different stages of NASH pathology by antibody-mediated manipulation.
5. Does suppression of T-cell exhaustion in NASH prevent liver cancer formation?

This study should allow an in-depth analysis of the role and the origin of T-cells in metabolic syndrome-induced hepatitis, NASH and HCC. Thus, it was envisaged, that the data would deepen current knowledge about the role of T-cells in NASH development and identify potential novel therapeutic targets, as well as allowing reevaluation of currently used and approved clinical antibodies (e.g. α-PD-1) in the context of NASH and NASH-triggered HCC diseases.

Aim 2: Platelet GPIbα is a mediator and potential interventional target for NASH and subsequent liver cancer

The second aim of this PhD thesis was to investigate if anti-platelet treatment (APT) could be used therapeutically to ameliorate NASH, as well as to decipher the role of platelets as

mediators of hepatic inflammation in NASH development by utilizing different therapeutic and interventional antibody-based strategies.

To address the hypothesis that platelets are mediators of hepatic inflammation in NASH development and could be a potential interventional target the following questions, aims and milestones were defined:

1. Is intrahepatic platelet abundance a result of NAFLD with induced insulin resistance or NASH diet feeding?
2. Do therapeutic APT strategies have comparable beneficial effects to preventive APTs in established NASH?
3. When do platelets home the liver during NASH diet feeding, and which other immune cells co-localize with platelets?
4. What are the potential mechanisms of hepatic platelet homing in early NASH development and established NASH?
5. Does therapeutic use of GPIbα antibody have other beneficial effects besides reduction of intrahepatic platelets?
6. Does long-term CD-HFD feeding induce hepatocarcinogenesis in hIL4rα/GPIbα-Tg mice?

This study allowed an in-depth analysis of the role of platelets in metabolic syndrome-induced hepatitis, NASH and HCC. Thus, the data deepened current knowledge about the role of platelets as markers of early liver damage in NASH development and identified platelet GPIbα as a potential interventional target in the context of NASH and NASH-triggered HCC diseases[9].

6 Methods

6.1 Mice, diets and treatments

Adapted from Malehmir*, Pfister* et al.[9]: 4-6 weeks old male C57BL/6J mice were purchased from Charles River, and all strains of genetically-altered mice were on a C57BL/6J background. Control mice were matched by genetic background, age and sex.

Mice were housed at the at the University Hospital Zurich (USZ), the Biomedical Services Unit at University of Birmingham or University of Newcastle, the University of Calgary and German Cancer Research Center (DKFZ). Animals were maintained under specific pathogen-free conditions and experiments were performed in accordance to German Law (G129/16, G7/17, 55.2-1-54-2532-39-2015, G-91/14 and AZ:84-02.04.2014.A010). Further, experiments were performed in accordance to the UK Animals Scientific Procedures Act of 1986, with project license approval granted by the UK Home Office (project license P3F79C606) and the University of Calgary Animal Care Committee (protocol AC16-0148) in accordance with the Canadian Council for Animal Care Guidelines.

6-8 week-old male mice were fed ad libitum: normal diet (ND), high fat diet (HFD) (Research Diets; D12451), choline-deficient high-fat diet (CD-HFD) (Research Diets; D05010402), western diet with trans-fat (WD-HTF) (Research Diets; D09100301 - 40 kcal % fat (Primex shortening), 20 kcal % fructose, 2% cholesterol).

For interventional studies, male mice were fed CD-HFD for the indicated timeframes and treated with CD8 depleting antibody (Bioxcell, 2.43), NK1.1 depletion antibody (Bioxcell, PK136) or anti-PD-1 (Bioxcell, RMP1-14). At the end of the experiment, animals were sacrificed, and the liver, fat and serum harvested for analysis[9].

Adapted from Malehmir*, Pfister* et al.[9]: For therapeutic anti-platelet treatments, cohorts of mice fed CD-HFD or WD-HTF were treated with Ticagrelor (40µg/ ml drinking water; ~3mg/kg/day).
For studies deciphering early platelet homing mechanisms, 5-week-old male mice were fed ND, CD-HFD or WD-HTF for 3.5 weeks and subsequently treated for 2.5 weeks.
Mice were treated intravenously in 100µl PBS either 20µg/mouse anti-CD44 blocking antibody (clone KM81, Cedarlane, CL8944AP) or 100µg/mouse anti-CD44 non-blocking antibody (clone IM7, Bioxcell, BE0039). For further deciphering of the role of early platelet homing by the CD44-hyaluronan axis, mice were treated intraperitoneally 20U/g murine hyaluronidase (HYAL) in 100µl PBS.
For Kupffer cell depletion experiments mice were treated with 100µl/ mouse Clodrosome (liposomal clodronate), or as a control 100µl/mouse Encapsome (Control Liposomes).

For interventional GPIbα blocking experiments mice were treated intravenously in 100µl PBS either 100µg/mouse anti-GPIbα or 100µg/mouse Fab-Rat IgG (kindly provided by Bernhard Nieswandt, University of Wurzburg).
In late treatment regimes, mice were fed CD-HFD for 6 months and treated with the same protocol for Kupffer cell depletion or interventional GPIbα blocking experiments for indicated time points[9].

Adapted from Malehmir*, Pfister* et al.[9]: For deciphering of the role of granulocytes in early phases of NASH, an osmotic pump experiment was performed in collaboration with Caroline L. Wilson, Jack Leslie and Derek A. Mann from Newcastle University. In this experiment, 5-week-old male mice were fed a CD-HFD for 12 weeks. Four weeks after the diet started, mini pumps (Alzet, model 2004) were implanted subcutaneously into the mice to deliver 30µg per day of Ly6G (clone 1A8, Bioxcell, BP0075) neutrophil-depleting antibody or Rat IgG2a (clone 2A3, Bioxcell, BE0089) for 8 more weeks. At the end of the experiment, animals were sacrificed, and the liver, fat and serum harvested for analysis[9].

6.2 Measurement of liver triglycerides

Adapted from Malehmir*, Pfister* et al.[9]: Liver triglycerides were measured by crushing 20 - 50 mg of tissue in liquid with a pestle and adding 250µl 0.9% NaCl. After incubation on heat block for 10min, RT, 450rpm, 250µl ethanolic 0.5KOH was added, samples were vortexed and incubated for 30min, 71°C, 450rpm. 500µl 0.15M MgSO4 was added, and samples were vortexed. After centrifugation for 10min, RT, 13,000g supernatants were collected and analyzed by using optical densitometry O.D. 505 with 1:4 diluted liver samples by GPO-PAP from Roche Diagnostics[9].

6.3 Intraperitoneal glucose tolerance test

Adapted from Malehmir*, Pfister* et al.[9]: After overnight fasting, mice were i.p. injected with 5µl/gr body weight of a 20% glucose solution, blood glucose was measured using “Accu-chek Performa Glucometer” at the indicated time intervals, by puncturing the lateral tail vein[9].

6.4 Intraperitoneal insulin tolerance test

Adapted from Malehmir*, Pfister* et al.[9]: After mild fasting for 6 h, blood glucose concentrations were determined for each mouse before insulin (1U/g lean mass determined by EchoMRI analysis) administration using “Accu-chek Performa Glucometer”. Mice were i.p. injected with insulin and blood glucose was measured at the indicated time intervals by puncturing the lateral tail vein[9].

6.5 Western blot analysis

Adapted from Malehmir*, Pfister* et al.[9]: Liver homogenates were prepared using radioimmunoprecipitation assay (RIPA) buffer supplemented according to the manufacturer's manual with complete protease inhibitor cocktail (Roche #11697498001) and phosphatase inhibitor (Sigma-Aldrich) in a gentleMACS™ Dissociator (Miltenyi Biotec). Protein concentrations were determined using the Pierce BCA Protein Assay Kit (Thermo Scientific) according to the manufacturer's manual. 10µg of proteins were separated under reducing conditions (2.5% β-mercaptoethanol) by 10% gels and electrophoresis and blotted by wet blotting for 1.5h onto nitrocellulose membranes (Bio Rad). Membranes were blocked in 5% milk/PBS-T for 1h at RT. Primary antibodies (**Table 2**, all Cell Signaling) were incubated at 4°C overnight under shaking conditions. Incubation with the secondary antibody (Anti-Rabbit IgG (H+L) – HRP, 1:5000, W4011 Promega) was performed for 1h. Detection was performed by Clarity Western ECL Substrate (Bio Rad) with a ChemiDoc imaging system (BioRad).

Table 2: Antibodies for Westernblot analysis

Name	Clone	Cat #
P-p38MAPK (Thr180/ Tyr182)	D3F9	4511
p38 MAPK	D13E1	8690
P-p65	Ser536	3033
p65	D14E12	8242
COX2	D5H5	12282
GAPDH	14C10	2118

6.6 Isolation and staining of lymphocytes for flow cytometry and FACS

Adapted from Malehmir*, Pfister* et al.[9]: Mice were transcardially perfused with PBS, and livers were dissected. Livers were incubated for up to 35min in 37°C with digestion buffer (Collagen IV 1:10 (60 U f.c.) and DNase I 1:100 (25µg/ml f.c.)) and subsequently passed through a 100µm filter. Livers were Washed with RPMI1640 (#11875093) medium and subsequently centrifuged for 7min/300g/4°C. Lymphocyte enrichment was achieved by a 2-step Percoll gradient (20ml 25% Percoll/HBSS underlay with 20ml 50% Percoll/HBSS) and centrifugation for 15min/1800g/4°C (Acc:1 Dcc:0). Leukocytes were collected, washed with HBSS, centrifuged for 10min/700g/4°C, counted and transferred to a 15ml Falcon for a final washing step with FACS buffer (PBS supplemented with v/v 0.4% 0.5M EDTA pH= 8 and w/v 0.5% albumin fraction V (#90604-29-8)).

Isolation of splenic lymphocytes was done by passing spleens through a 100µm mesh and subsequent washing. Afterwards, an erythrocyte lysis using ACK-buffer 1x 2ml for 5 min RT and then a wash was performed.

Isolation of blood-derived lymphocytes was done by collection of blood in FACS buffer and performing erythrocyte lysis two times using ACK-buffer 1x 2ml for 5 min RT and then washing.

For T-cell re-stimulation, cells were incubated for 2h, 37°C, 5% CO_2 in RPMI 1640 supplemented with v/v 2% fetal calf serum using 1:500 Biolegend´s Cell Activation Cocktail (with Brefeldin A) (#423304) and 1:1000 Monensin Solution (1,000X) (#420701).

Staining was performed using Live/Dead discrimination by using DAPI or ZombieDyeNIR according to the manufacturer´s instructions. After washing (~400g, 5min, 4°C), cells were stained in 25µl of titrated antibody master mix for 20min at 4°C and washed again (antibodies shown in **Table 3**). Samples for flow cytometric activated cell sorting (FACS) were then sorted. Samples for flow cytometry were fixed using eBioscience IC fixation (#00-8222-49) or Foxp3 Fix/Perm kit (#00-5523-00) according to the manufacturer´s instruction. Intracellular staining was performed in eBioscience Perm buffer (#00-8333-56).

Cells were analyzed using BD FACSFortessa, Sony spectral analyzer SP6800 and data were analyzed using FlowJo. For sorting, a FACS Aria II and a FACSAria FUSION in collaboration with the DKFZ FACS core facility were used.

The 24-color flow cytometric analysis was done in collaboration with Nicolas Nunez and Burkhard Becher from the University of Zurich[75].

Table 3: Flow cytometry antibodies

Fluorochrome	Name	Clone	Cat #
Alexa700	CD4	RM4-5	100536
Alexa700	CD45	30-F11	103128
Alexa700	CD86	GL-1	105023
Alexa647	FOXP3	150D	320014
APC	CD11b	M1/70	101212
APC	CD11c	N418	117309
APC	CD3	17A2	100236
APC	CD44	IM7	103012
APC	IFNy	XMG1.2	505810
APC	CD366	RMT3-23	119706
APC	NK1.1	PK136	108710
APC/Cy7	CD19	6D5	115530
APC/Fire	NK1.1	PK136	108751
APC/Fire	CD19	6D5	115557

APC/Fire	CD3	17A2	100247
FITC	CD11b	M1/70	101205
FITC	CD19	6D5	115505
FITC	CD25	3C7	558689
FITC	CD45	I3/2.3	147710
FITC	KLRG1 (MAFA)	2F1/KLRG1	138409
FITC	IL-10	JES5-16E3	505006
FITC	Ly- 6C	HK 1.4	128005
FITC	TCR γδ	UC7-13D5	107504
FITC	CD206 (MMR)	C068C2	141704
FITC	NK1.1	PK136	108706
PE	CD274	10F.9G2	124307
PE	CD278	7E.17G9	117405
PE	CD69	H1.2F3	104508
PE	F4/80	BM8	123110
PE	Granzyme B	NGZB	12-8898-80
PE	IL-17A	TC11-18H10.1	506904
PE	mCD1d/α- GalCer/PE	Immudex	YD8002-PE
PE	TCR γδ	eBioGL3	12-5711-82
PE	CD223 (LAG-3)	C9B7W	125208
PE	TNF-α	MO6-XT22	506306
PE	Perforin	S16009A	154306
PE/Cy7	CD3	17A2	100220
PE/Cy7	Ly-6G (PE/Cy7)	1A8	127618
PE/Cy7	NK1.1	PK136	108713
PE/Cy7	F4/80	BM8	123114
PE/Dazzle	CD11c	N418	117348
PE/Dazzle	CD279	RMP1-30	109116
PE/Dazzle	CD335	29A1.4	137630
PE/Dazzle	CD62L	MEL-14	104448
PE/Dazzle	TNF-α	MP6-XT22	506346
PE/Dazzle	CD11c	N418	117647
PerCP/Cy5.5	CD8a	53-6.7	100734
PerCP/Cy5.5	I-A/I-E	M5/114.15.2	107625
PerCP/Cy5.5	LY-6C	HK1.4	128012
	CD16/32	93	101302

6.7 Electron microcopy

Adapted from Malehmir*, Pfister* et al.[9]: In collaboration with Marco Prinz from the Universitätsklinikum Freiburg electron microscopy was performed. For this, sections from epon-embedded, glutaraldehyde-fixed liver samples were cut and stained with toluidine blue.

After trimming and ultrathin cutting of liver, tissues were treated with uranyl acetate and lead citrate as described previously[76]. For analysis analySIS Docu System (Soft Imaging System) was used[9].

6.8 Isolation of RNA and quantitative real-time PCR.

Adapted from Malehmir*, Pfister* et al.[9]: Total RNA from whole liver homogenates was isolated from frozen liver tissues according to the manufacturer's protocol using RNeasyMini Kit (Qiagen)[9]. The quantity and quality of the RNA was analyzed by Nanodrop analyzer (Thermo Scientific). For cDNA production 1µg of RNA was used by using Quantitect Reverse Transcription Kit (Qiagen) according to the manufacturer's protocol[9]. qRT-PCR was performed in duplicates in a in 384-well plate using Fast Start SYBR Green Master Rox (Roche) with custom made primers purchased from Eurofins with a 7900 HT qRT-PCR system (Applied Biosystems, Life Technologies Darmstadt, Germany)[9].

6.9 Measurement of serum parameters

Adapted from Malehmir*, Pfister* et al.[9]: Serum was isolated from the heart blood after sacrifice, and parameters were measured by using either a Fuji DRI-CHEM NX500i machine with commercially available test application from FUJIFILM for ALT, AST, cholesterol and triglycerides, or analyzing parameters on a Cobas Reader in collaboration with the Institute for Clinical Chemistry and Pathobiochemistry, TUM, Munich[9].

6.10 Histology, immunohistochemistry, scanning and automated analysis

Adapted from Malehmir*, Pfister* et al.[9]: Tissues were fixed in 4% paraformaldehyde and paraffin-embedded in collaboration with Ruth Hillermann and Olga Seelbach at the Technical University of Munich (TUM) or in collaboration with Danijela Heide, Jenny Hetzer, Corinna Gropp, Katharina Kessler and Nathalie Klaumünzer at the DKFZ, Department of Chronic Inflammation and Cancer (Heidelberg). Briefly, 2µm sections from FFPE and cryo-preserved tissues were prepared and stained with Hematoxylin/Eosin or IHC antibodies on a Bond MAX (Leica) (**Table 4**). For Sudan Red staining, cryo sections (5µm) were cut and stained with Sudan Red (0.25% Sudan IV in ethanolic solution). Slides were scanned with SCN400 slide scanner (Leica) and analyzed either using for area based stainings Tissue IA image analysis software by Leica Biosystems Version 4.0.6, or macro-based analysis by ImageJ. NAFLD activity scoring (NAS) was performed on murine livers and cross-validated by pathological expertise[9].

Table 4: IHC antibodies

Target	Dilution	Clone	Cat #
MHCII	1:500	M5/114.15.2	NBP1-43312
CD3	1:250	ab16669	ab16669
F4/80	1:50	BM8	123105
Collagen IV	1:50	CL50451AP-1	007CL50451AP
Ki-67	1:200	RM-9106-S1	RM-9106-S1
Ly6G	1:600	1A8	551459
CD42b	1:200	SP219	ab183345

6.11 Intravital microscopy

Adapted from Malehmir*, Pfister* et al.[9]: In collaboration with Moritz Peiseler, Bas Surewaard and Paul Kubes from the University of Calgary, multichannel spinning-disk confocal microscopy was performed. After anesthetization of mice by i.p. administration of ketamine (200mg/kg body weight; Bayer Animal Health) and xylazine (10mg/kg body weight; Bimeda-MTC), fluorescently conjugated antibodies and proteins to mark cells/structures of interest (**Table 5**), as well as additional anesthetics were administered by tail vein catheterization[9]. Exact mouse fixation and intravital microscopy setup are described in Malehmir*, Pfister* et al.[9]. Briefly, the mouse was placed on a heating plate to maintain 37°C and the liver was fixed to restrict movement by breathing and subsequent artefacts, before acquiring videos by an inverted spinning-disk confocal microscope (IX81; Olympus) with motorized drive and stage, controlled by Volocity software (Perkin Elmer).

In vivo image analysis was performed by Volocity software (Perkin Elmer) and is described in detail in Malehmir*, Pfister* et al.[9]:

Table 5: Antibodies used for intravital microscopy

Fluorochrome	Target	Dilution	Clone	Cat #
AF750	F4/80	2µg/mouse	BM8	AbLab, custom made
AF647	CD49b	3µg/mouse	HMa2	103511
PE	Ly6G	3µg/mouse	1A8	127607
FITC	CD3e	2µg/mouse	145-2c11	11-0031-82
AF555 (self-labeled)	HAPB			Sigma- Aldrich

6.12 Immunofluorescence microscopy

Adapted from Malehmir*, Pfister* et al.[9]: In collaboration with Donato Inverso from the DKFZ Heidelberg immunofluorescence microscopy was performed. Briefly, after perfusion of mice, livers were harvested, fixed for 16h, dehydrated in 30% sucrose, embedded in OCT and cut

into 25µm slices. After permeabilization and blocking with PBS containing 0.3% Triton X-100 (Sigma-Aldrich) and 10% FBS, samples were stained with primary antibodies (**Table 6**). Stained slides were covered with fluorescence mounting medium (DAKO), pictures were taken with an inverted Leica microscope (TCS STED CW SP5, Leica Microsystems) and 3D reconstruction from z-stacks was performed by using Imaris (Bitplane) software[9].

Table 6: Antibodies used for immunofluorescence microscopy

Target	Dilution	Clone	Cat #
CD41	1:100	MWReg-30	133906
F4/80	1:100	BM8	17-4801-82
B220	1:100	RA3-6B2	103226
CD11b	1:100	M1/70	101212
collagen IV	1:200		10808
CD3	1:100		A0445229-2

6.13 Statistical analyses

Adapted from Malehmir*, Pfister* et al.[9]: Mouse data are presented as the mean±SEM. Pilot experiments and previously published results were used to estimate the sample size, such that appropriate statistical tests could yield significant results. Statistical analysis was performed using GraphPad Prism software version 7.03 (GraphPad Software). Data were analyzed by one way analysis of variance (ANOVA) with post hoc tests. When comparing multiple groups I used Tukey`s multiple comparison test, when I compared only two experimental groups I used Dunnett´s multiple comparison test. Multiple parameters were analyzed by two way ANOVA with Tukey`s or when comparing to one experimental group Sidak`s multiple comparison test post hoc test. Analysis of two samples was performed by two-tailed Student's t test, and statistics for HCC incidence were calculated using Fisher's exact test. Statistical significance is indicated as follows:*$p < 0.05$, **$p < 0.01$, ***$p < 0.001$ and ****$p < 0.0001$[9].

7 Results

7.1 Aim 1: Deciphering TCR signaling in metabolically activated T-cells in NASH and liver cancer development

7.1.1 NASH - a chronic disease with a defined T-cell phenotype

Recent publications suggest a role of T-cell receptor (TCR)-dependent cells in the progression from a healthy mouse liver to a NAFL phenotype, NASH and eventually HCC induction[6,31,36]. Therefore, I sought to investigate whether in mouse models of NAFLD or NASH, TCR-dependent cells are changed in their number, their activation and exhaustion status in early stages of pathology development, highlighting potential initiators and drivers of disease.

Wildtype (WT) mice fed for 3 months an NAFLD-inducing high-fat diet (HFD) or a NASH-inducing choline-deficient high fat (CD-HFD), developed significantly more body weight compared to normal chow diet (ND) mice (**Figure 7a**). Only CD-HFD fed mice developed liver damage (**Figure 7b**), which was not associated with an increase of hepatic triglycerides (**Figure 7c**). Further, markers of NASH pathology like macrovesicular steatosis and immune cell infiltration could be observed by H&E (**Figure 7d**) and in NAFLD activity scoring (NAS) (**Figure 7e**). No TCR-dependent cell increase was seen (**Figure 7f**); however, the hepatic immune cell compartment was polarized towards $CD3^+$ and $CD8^+$ T-cells, while $CD4^+$ T-cells remained unchanged (**Figure 7g**). Further, in CD-HFD fed mice an increase of activated memory ($CD44^+CD69^+$) $CD8^+$ T-cells was observed. The $CD8^+$ T-cells were positive for interferon gamma (IFNy) and expressed markers of exhaustion (PD-1) (**Figure 7g + h**).

Thus, I concluded that $CD8^+$ T-cell activation and subsequent $CD8^+$ T-cell exhaustion marker expression are specifically associated with a NASH-inducing diet, but not an NAFLD-inducing HFD alone.

Next, I sought to characterize the changes in TCR-dependent cells over the progression of NASH pathology.

3, 6 or 12-month CD-HFD mice showed significantly increased body weight (**Figure 8a**) and liver damage (**Figure 8b**) compared to ND fed mice. Further, the progression of pathology was associated with increased absolute numbers of hepatic $CD45^+CD3^+$ and $CD3^+CD8^+$ T-cells, but not $CD3^+CD4^+$, after 6 and 12 months of diet (**Figure 8c**). Further, these $CD8^+$ T-cells expressed markers of exhaustion (PD-1) and activation (CD69) (**Figure 8d, e, f**). In line with more liver damage, immune cell infiltration and activation, H&E stainings and NAS evaluation indicated a progression of NASH pathology over time (**Figure 9a**).

In a second model of NASH based on 6 months of a Western-style diet (high cholesterol and high fructose) with high trans fats (WD-HTF) feeding, mice had a significantly increased body weight and liver damage (**Figure 9b**). Further, markers of NASH pathology (**Figure 9c**) and a similar T-cell polarization for activation and exhaustion to previously reported data (**Figure 8a-d)** for CD-HFD fed mice (**Figure 9d**) were observed.

Thus I concluded that prolonged NASH diet feeding leads to a phenotype of increased liver damage, progressive NASH development and $CD8^+$ T-cell activation, as well as $CD8^+$ T-cell exhaustion.

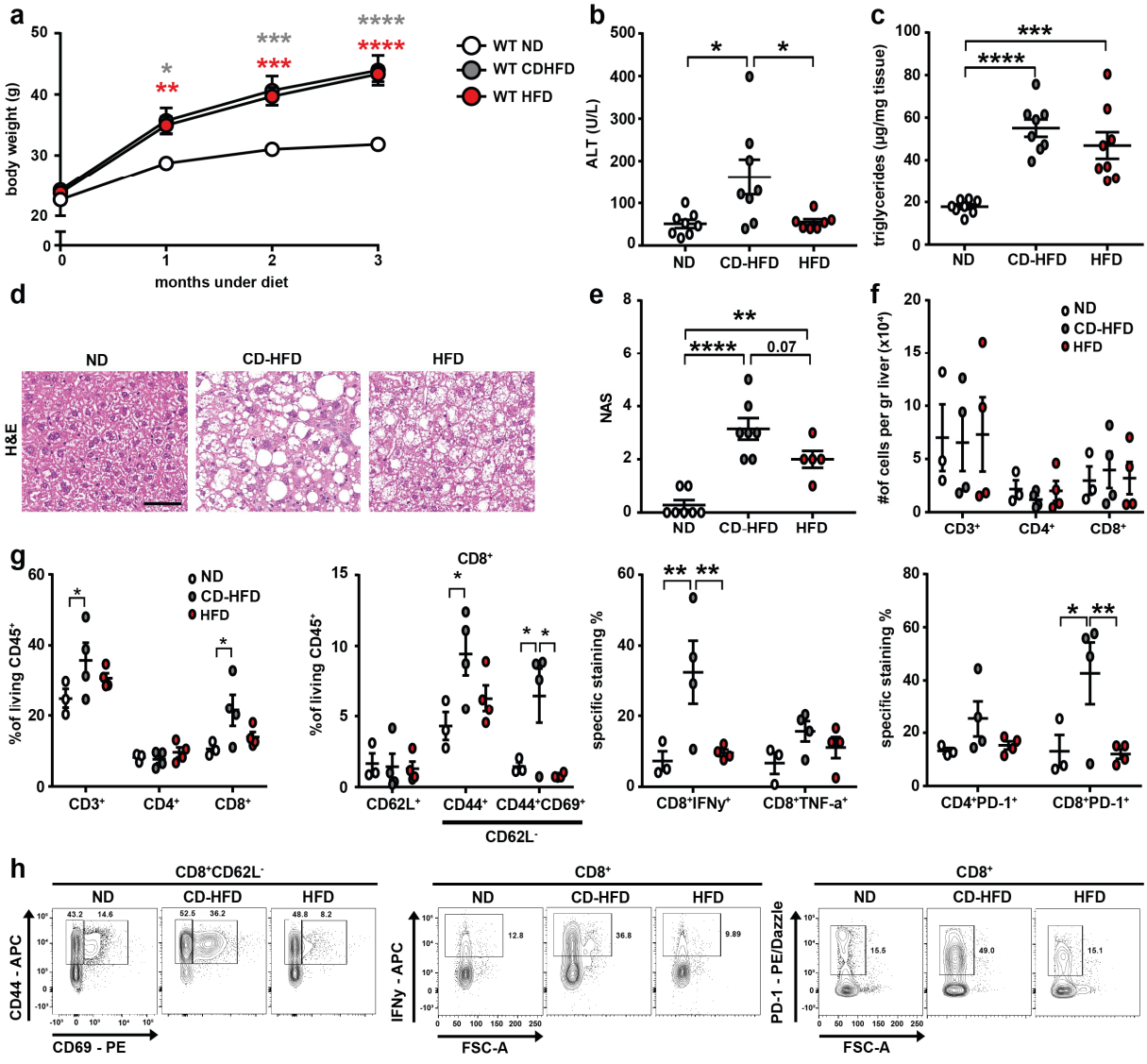

Figure 7: Early phases of NASH induction are correlated with activated $CD8^+$ T-cells

(a) Body weight development of 3 months ND, HFD or CD-HFD fed mice. (n= 8 mice/group). Asterisks indicate significance of groups compared to ND fed mice. (b) ALT of mice shown in a. (ND n= 8 mice; CD-HFD n= 8 mice; HFD n= 7 mice). (c) Hepatic triglycerides of mice shown in a. (n= 8 mice/group). (d) H&E staining, with (e) NAS evaluation of mice shown in a. (ND n= 7 mice; CD-HFD n= 7 mice; HFD n= 5 mice). Scale bar: 50 µm. (f) Quantification in absolute numbers and (g) relative to CD45 of hepatic lymphocytes by flow cytometry of mice shown in a. (n= 4 mice/group). (h) Representative flow cytometry plots of data shown in g. (n= 4 mice/group). All data are

shown as mean ± SEM. All data were analyzed by one way ANOVA and Tukey`s multiple comparison test. *p<0.05; **p<0.01; ***p<0.001; ****p<0.0001.

Increased hepatic T-cell accumulation and higher CD69 and PD-1 expression indicated a specific T-cell reaction in a chronic model of dietary liver challenge; therefore, I investigated possible T-cell clonal outgrowth, potential antigen-driven T-cell activation and subsequent T-cell expansion.

Flow cytometric analysis of 15 TCR variable beta (TCR vβ) chains of hepatic isolated $CD4^+$ and $CD8^+$ T-cells showed, with one exception, preferential expression of TCR vβ 7 after 12 months CD-HFD feeding and no significant differences between ND or CD-HFD fed mice after 3, or 6 months (**Figure 10a, b, c**).

Lymphocytes isolated from blood showed only small differences compared to changes observed in the liver in relative T-cell lymphocyte composition, $CD4^+$ or $CD8^+$ T-cell expression of markers for activation or exhaustion, or TCR vβ representation in ND or CD-HFD fed mice after 3, 6, or 12 months (**Figure 11a-e**). However, in blood, two TCR vβ chains, namely TCR vβ4 after 6 months and TCR vβ 3 after 12 months, showed significant differences between ND and CD-HFD fed mice (**Figure 11d, e**).

Next, I investigated whether specific T-cell subsets are activated and subsequently express markers of exhaustion. Thus, I focused on hepatic $CD8^+PD\text{-}1^+$ T-cells. Indeed, several TCR vβ chains were significantly overrepresented in $CD8^+PD\text{-}1^+$ T-cells compared to the whole population of ND or CD-HFD-associated $CD8^+$ T-cells (**Figure 12a-c**). Further, in 3, 6 and 12 months CD-HFD fed mice, different TCR vβ chains are significantly or close to significantly overrepresented in the $CD8^+PD\text{-}1^+$ population, potentially indicating that different clones emerge at different progression states of NASH pathology (**Figure 12a-c**).

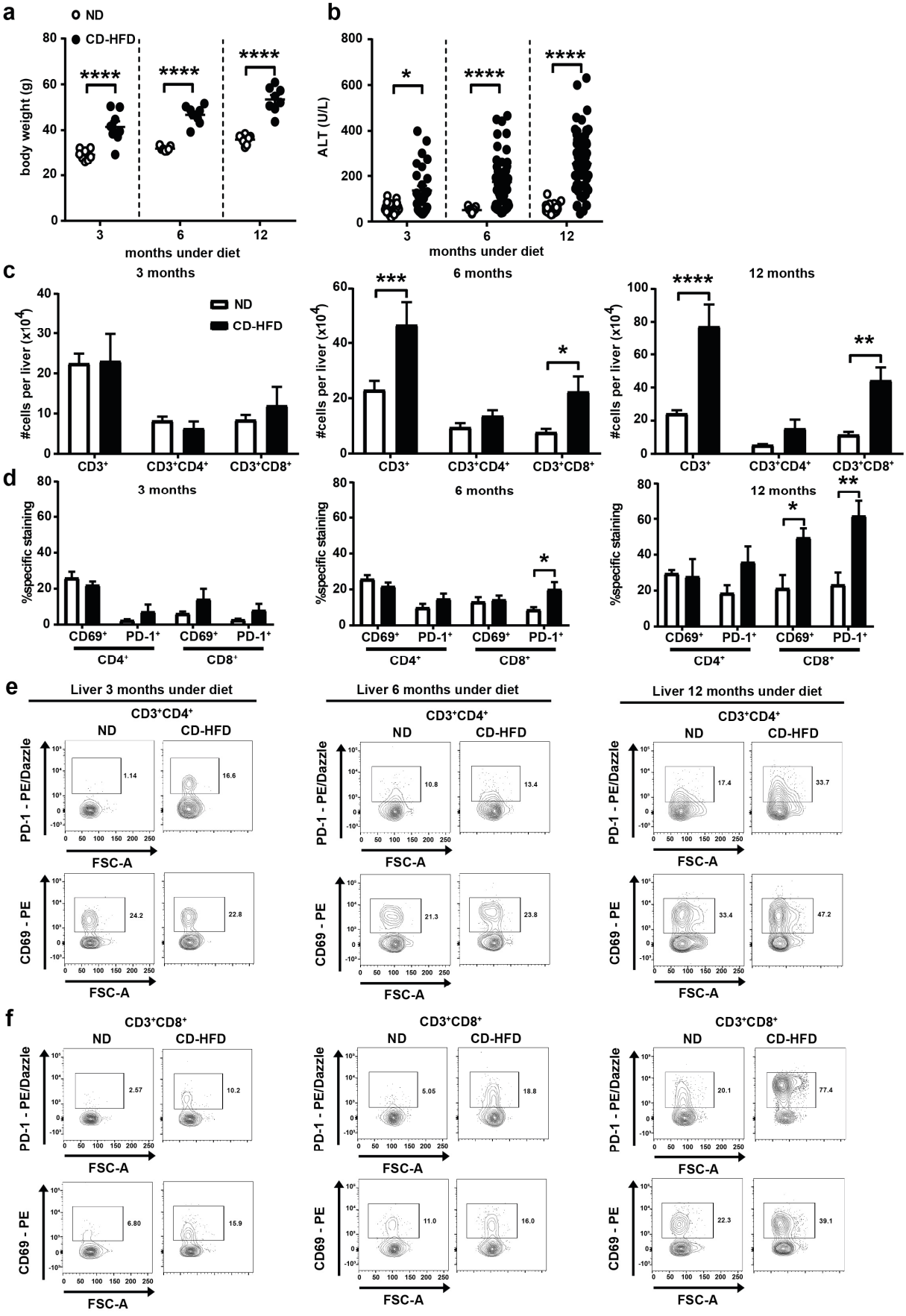

Figure 8: NASH: a progressive disease

(a) Body weight development over 12 months of CD-HFD feeding. (n= 8 mice/group; but ND 6 months n= 7 mice/group). (b) ALT development over time. (3 months ND n= 20 mice, 3 months CD-HFD n= 27 mice; 6 months

ND= 31 mice, 6 months CD-HFD n= 58 mice; 12 months ND= 18 mice, 12 months CD-HFD n= 69 mice). (c) Absolute quantification of hepatic lymphocytes by flow cytometry (3 months n= 7 mice/group; 6 months ND n= 13 mice, CD-HFD n= 10 mice; 12 months n= 4 mice/group). (d) Polarization of hepatic lymphocytes by flow cytometry (3 months n= 4 mice/group; 6 months ND n= 11 mice, CD-HFD n= 16 mice; 12 months ND n= 4 mice, CD-HFD n= 3 mice). (e) Representative flow cytometry plots of $CD3^+CD4^+$ and (f) $CD3^+CD8^+$ lymphocytes of mice shown in d. All data are shown as mean ± SEM. Data were analyzed by two way ANOVA and Sidak`s multiple comparison test or two-tailed Student T test. *p<0.05; **p<0.01; ***p<0.001; ****p<0.0001.

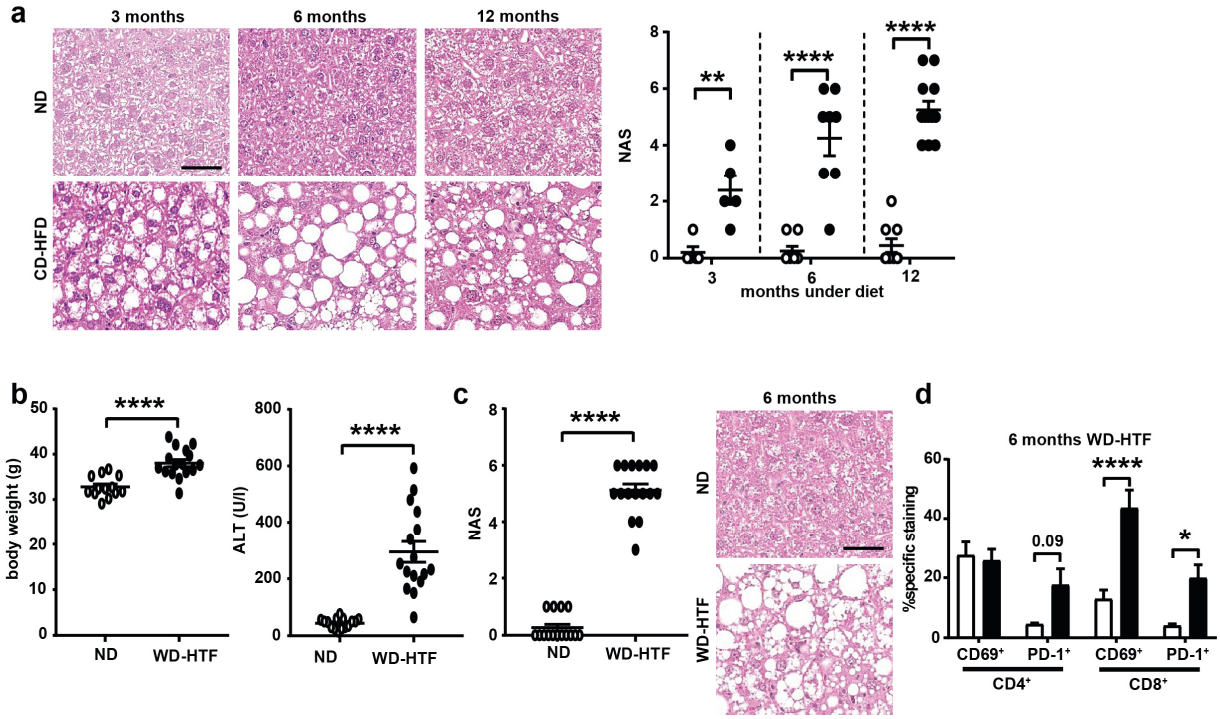

Figure 9: Corroboration of NASH being a progressive disease

(a) H&E staining and NAS evaluation (3 months n= 5 mice/group; 6 months n= 8 mice/group; 12 months ND n= 9 mice, CD-HFD n= 12 mice). Scale bar: 50 µm. (b) Body weight and ALT concentrations of mice fed 6 months ND or WD-HTF (body weight: ND n= 13 mice, WD-HTF n= 16 mice; ALT: ND n= 15 mice, WD-HTF n= 16 mice). (c) H&E staining and NAS evaluation (ND n= 15 mice, WD-HTF n= 16 mice). Scale bar: 50 µm. (d) Polarization of hepatic lymphocytes by flow cytometry (ND n= 3 mice, WD-HTF n= 8 mice). All data are shown as mean ± SEM. Data were analyzed by two way ANOVA and Sidak`s multiple comparison test or two-tailed Student T test. *p<0.05; **p<0.01; ***p<0.001; ****p<0.0001.

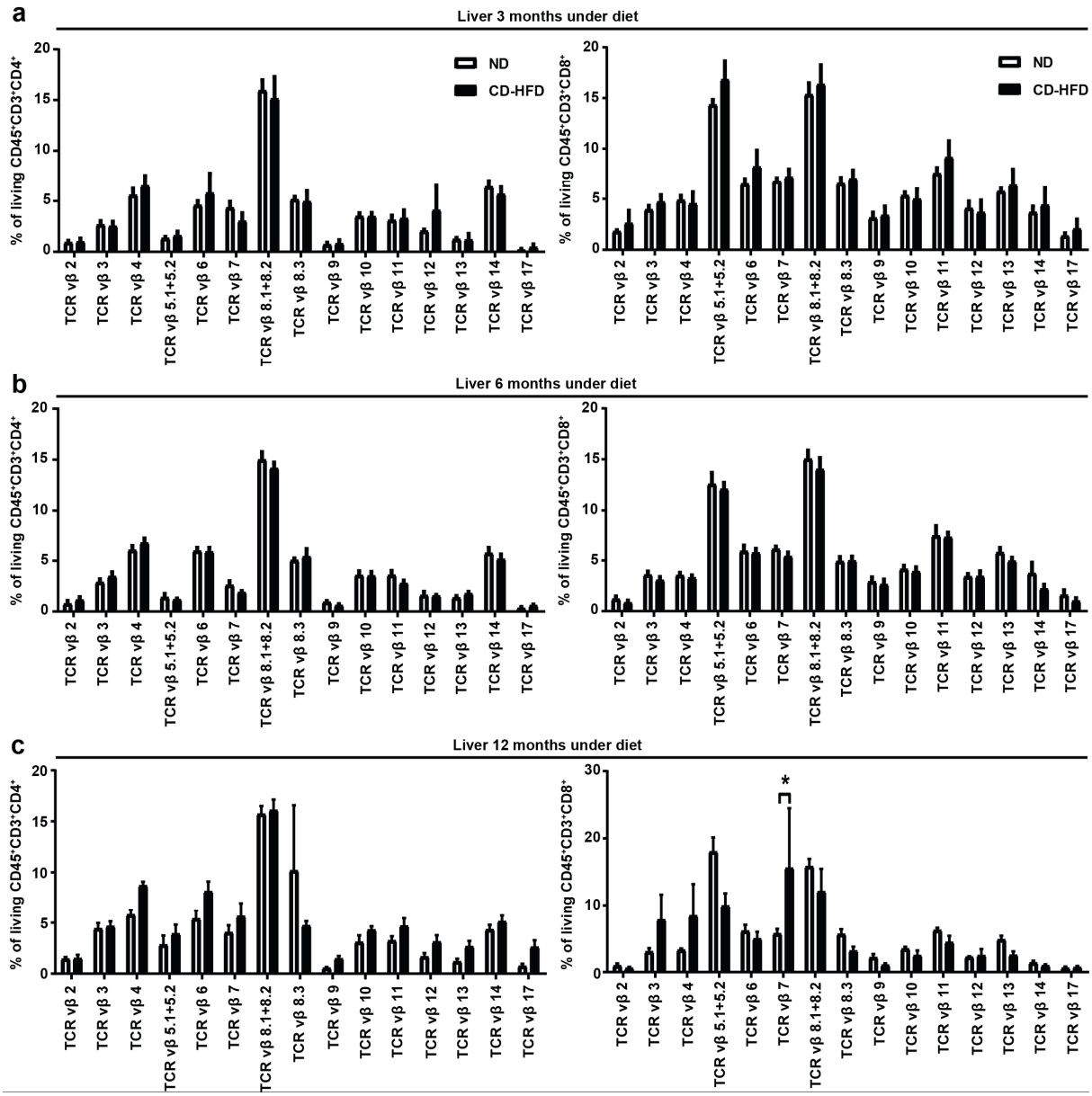

Figure 10: Hepatic T-cell clonal distribution

(a) Flow cytometric analysis for TCR vβ expression of hepatic T-cells of 3, or (b) 6, or (c) 12 months ND or CD-HFD fed mice (n= 4 mice/group). All data are shown as mean ± SEM. Data were analyzed by two way ANOVA and Sidak`s multiple comparison test. *p<0.05.

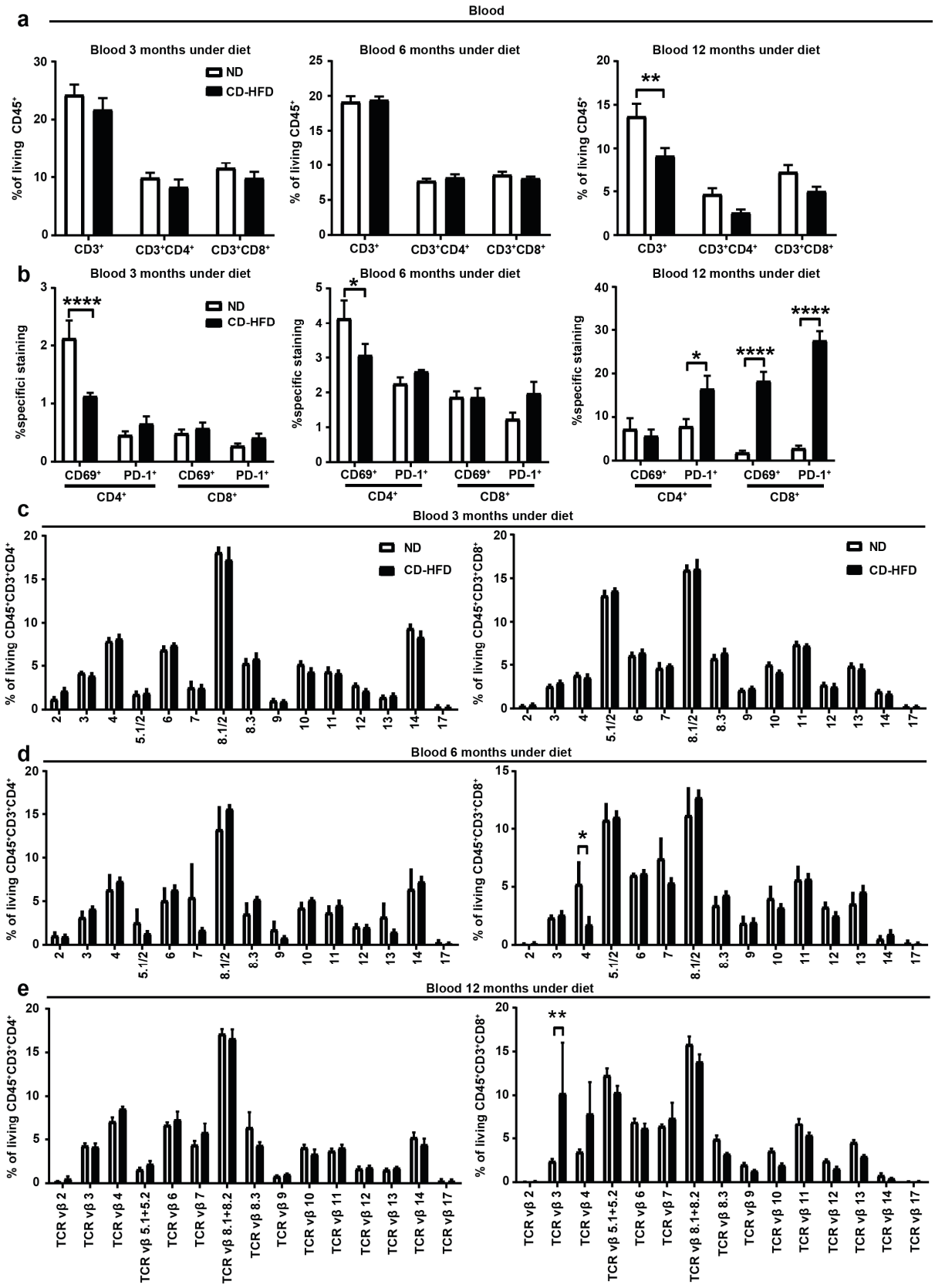

Figure 11: NASH is associated with strong immunological changes in the liver, but to a lesser degree in blood

(a) T-cells isolated from the blood of 3, 6 or 12 months ND or CD-HFD fed mice and (b) the expression of activation or exhaustion marker (n= 4 mice/group). (c) Analysis for TCR vβ expression of blood isolated T-cells of 3, or (d) 6, or (e) 12 months ND or CD-HFD fed mice (n= 4 mice/group). All data are shown as mean ± SEM. Data were analyzed by two way ANOVA and Sidak`s multiple comparison test. *p<0.05; **p<0.01; ***p<0.0001; ****p<0.0001.

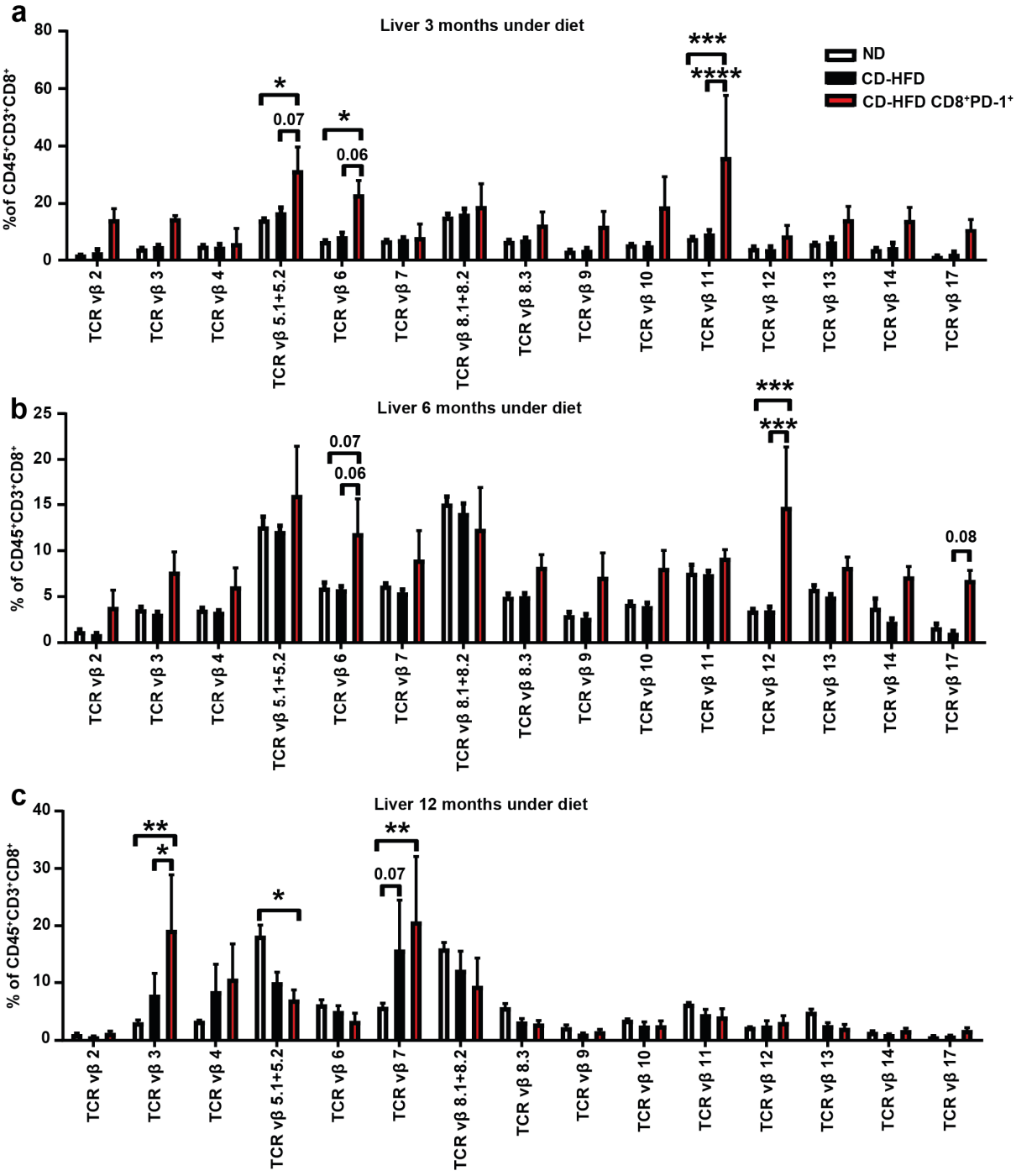

Figure 12: Accumulation of clones positive for CD8⁺PD-1⁺ in progression of NASH pathology
(a) Analysis for TCR vβ expression of hepatic whole population CD8⁺ T-cells or CD8⁺PD-1⁺ T-cells of 3, or (b) 6, or (c) 12 months ND or CD-HFD fed mice (n= 4 mice/group). All data are shown as mean ± SEM. Data were analyzed by two way ANOVA and Sidak`s multiple comparison test. *p<0.05; **p<0.01; ***p<0.0001; ****p<0.0001.

7.1.2 Dependency on a natural TCR repertoire and TCR-mediated effector function for NASH development

After I observed differential representation of TCR vβ chains during the progression from healthy liver to NAFLD and further to NASH in hepatic $CD8^+PD\text{-}1^+$ T-cells, I next investigated the dependency on TCR abundance for NASH development, in general.

$TCR\beta\delta^{-/-}$, lacking invariant innate-like TCRδ chain-dependent, as well as classical adaptive TCRβ-dependent T-cells, were fed CD-HFD for 6 months. CD-HFD fed $TCR\beta\delta^{-/-}$ mice did have significantly less body weight (**Figure 13a**), were metabolically less impaired by intraperitoneal glucose tolerance test (IPGTT) (**Figure 13b**) and had significantly less liver damage compared to CD-HFD WT mice (**Figure 13c**). Further, CD-HFD $TCR\beta\delta^{-/-}$ lacked histopathological signs of NASH on H&E staining, had no $CD3^+$ cells, no Kupffer cell cluster formation and lacked fibrosis development (**Figure 13d, e**).

Thus, I concluded that TCRβδ cells and therefore TCR abundance are essential for NASH development.

Next, I investigated whether a natural TCR repertoire is necessary for inducing NASH pathology. To this end, OT-1 mice, which have transgenic expression of a chicken ovalbumin reactive TCR and thus a strongly CD8 polarized T-cell compartment, were put under 6 months CD-HFD. CD-HFD fed OT-1 mice did have significantly less body weight (**Figure 14a**), were metabolically equally impaired by IPGTT (**Figure 14b**) and had significantly less liver damage compared to CD-HFD fed WT mice (**Figure 14c**). Further, CD-HFD fed OT-1 lacked histopathological signs of NASH on H&E staining, had more $CD3^+$ cells and no Kupffer cell cluster formation (**Figure 14d, e**).

Thus, I concluded, that without a natural TCR repertoire, mice lacked liver pathological signs of NASH development and therefore a natural TCR repertoire is essential for driving NASH.

Next, I sought to decipher in which way a natural functional TCR repertoire influences the induction of NASH. To this end, I fed CD-HFD to perforin knockout mice ($Prf1^{-/-}$), lacking systemically the pore forming protein perforin and thus have a TCR effector function impairment.

6 months CD-HFD fed $Prf1^{-/-}$ mice developed body weight comparable to WT CD-HFD fed mice (**Figure 15a**), were metabolically not impaired by IPGTT (**Figure 15b**) and had significantly less liver damage compared to CD-HFD WT mice (**Figure 15c**). Further, after 6 months of CD-HFD feeding, $Prf1^{-/-}$ mice lacked or had ameliorated histopathological signs of NASH on H&E staining, had fewer hepatic $CD3^+$ cells, less Kupffer cell cluster formation and

comparable levels of fibrosis and Ki-67 proliferating cells to WT ND (**Figure 15d, e**). Further, activated hepatic $CD8^+CD62L^-CD44^+CD69^+$ were significantly reduced in $Prf1^{-/-}$ CD-HFD fed mice, as well as hepatic $CD8^+PD\text{-}1^+$ T-cells (**Figure 15f, g**). These $CD8^+$ T-cells were previously identified to be drivers of NASH pathology[6]. Further, in the frame of this thesis, accumulation of hepatic $CD8^+C69^+$ and $CD8^+PD\text{-}1^+$ T-cells correlated with progression of NAFLD and NASH pathology.

Thus, I concluded that early phases of NASH development are dependent on TCR effector function.

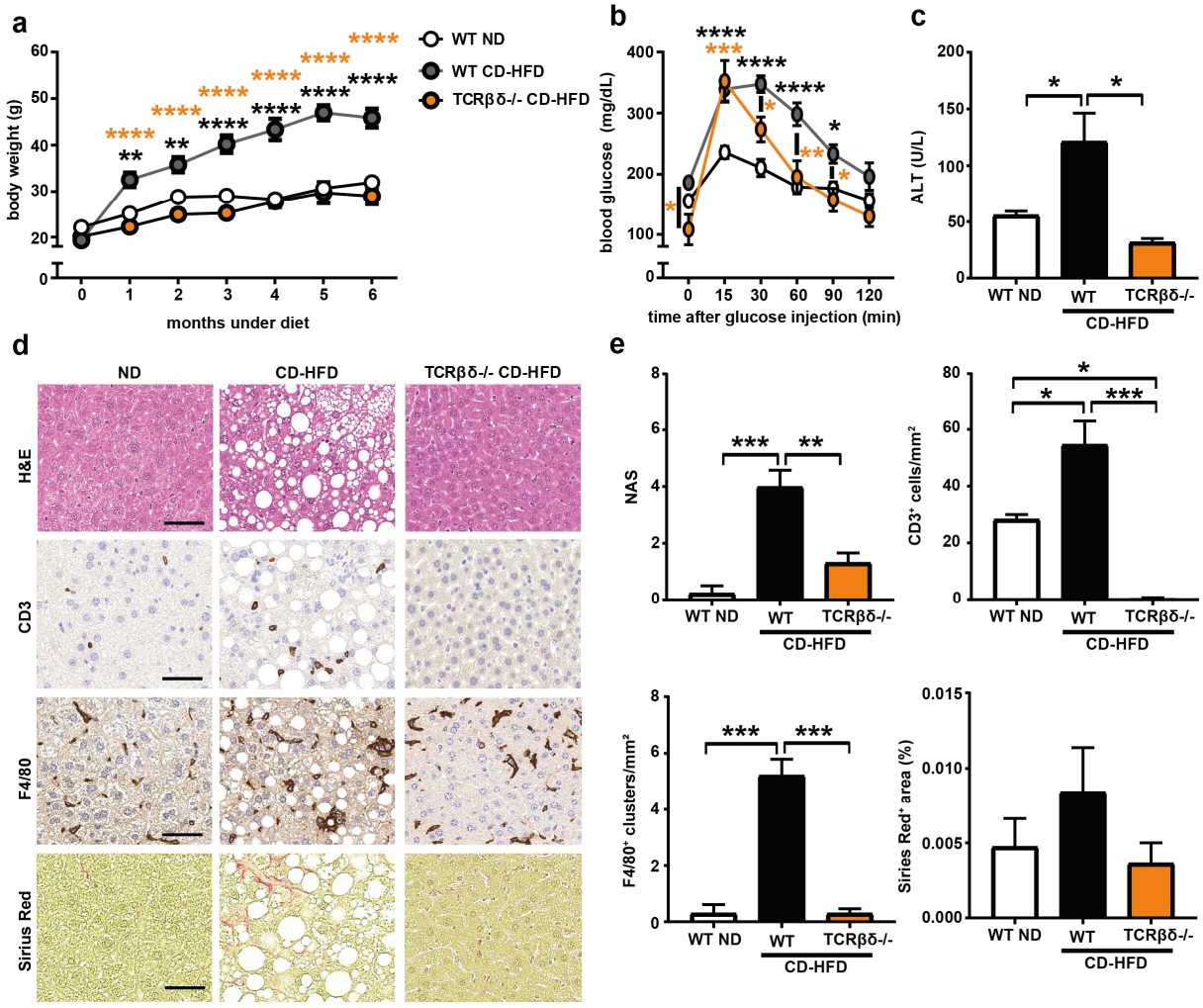

Figure 13: NASH development is dependent on TCR abundance

(a) Body weight development of WT ND, WT CD-HFD or $TCR\beta\delta^{-/-}$ CD-HFD fed mice (ND n= 4 mice; CD-HFD n= 6 mice; $TCR\beta\delta^{-/-}$ CD-HFD n= 6 mice). Asterisks indicate significance of groups compared to WT CD-HFD fed mice. (b) IPGTT of mice shown in a (ND n= 6 mice; CD-HFD n= 8 mice; $TCR\beta\delta^{-/-}$ CD-HFD n= 3 mice). (c) ALT of mice shown in a. (ND n= 4 mice; CD-HFD n= 4 mice; $TCR\beta\delta^{-/-}$ CD-HFD n= 3 mice). (d) H&E, CD3, F4/80 and Sirius Red staining with (e) NAS evaluation and quantification of mice shown in a. (H&E: ND n= 4 mice; CD-HFD n= 4 mice; $TCR\beta\delta^{-/-}$ CD-HFD n= 3 mice; CD3: ND n= 5 mice; CD-HFD n= 5 mice; $TCR\beta\delta^{-/-}$ CD-HFD n= 3 mice; F4/80 and Sirius red: n= 3 mice/group). Scale bar: 50 µm. All data are shown as mean ± SEM. All data were analyzed by one or two way ANOVA and Tukey`s multiple comparison test. *p<0.05; **p<0.01; ***p<0.001; ****p<0.0001.

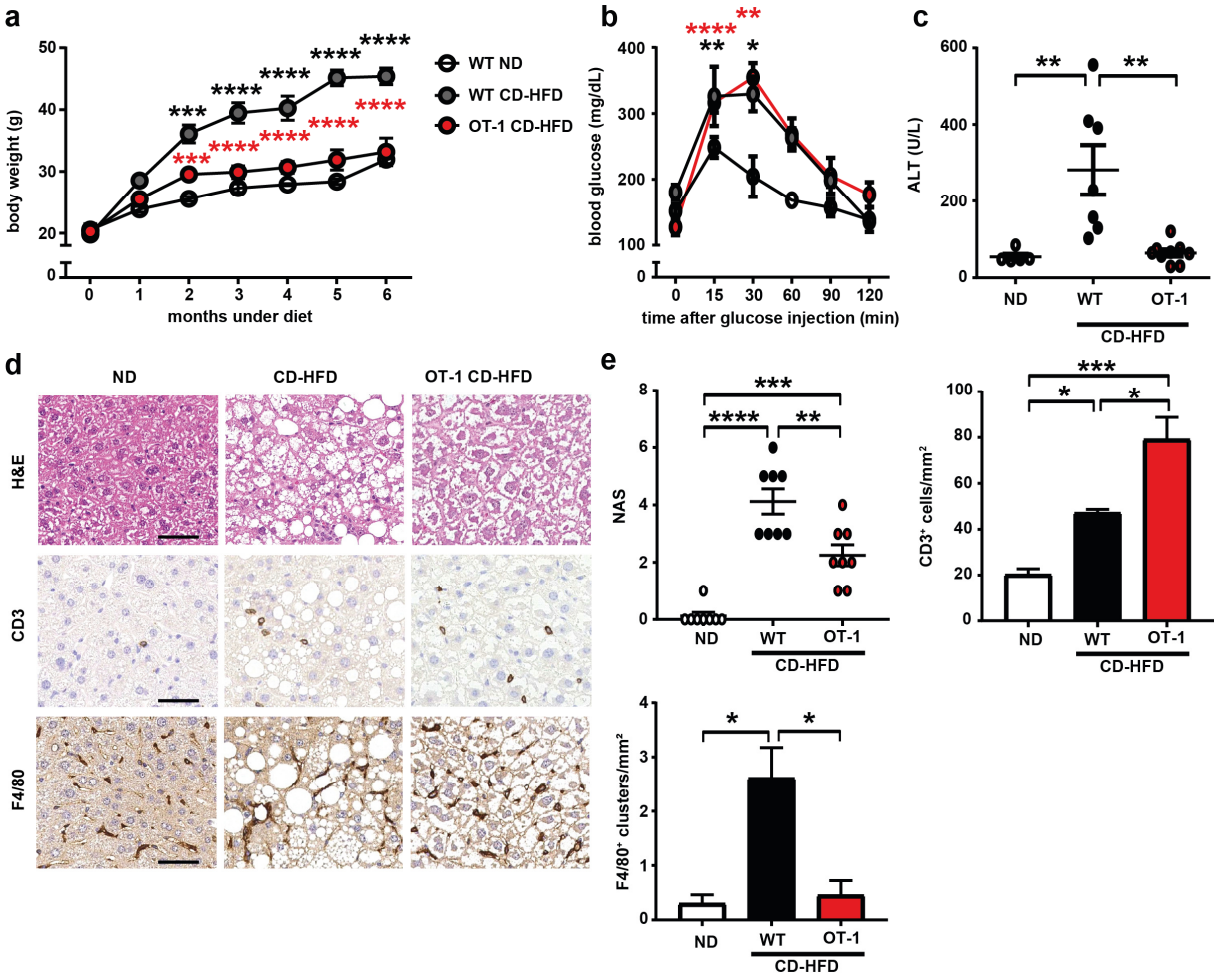

Figure 14: A natural TCR repertoire is essential for NASH development
(a) Body weight development of WT ND, WT CD-HFD or OT-1 CD-HFD fed mice (ND n= 3 mice; CD-HFD n= 6 mice; OT-1 CD-HFD n= 10 mice). Asterisks indicate significance of groups compared to WT CD-HFD fed mice. (b) IPGTT of mice shown in a (ND n= 3 mice; CD-HFD n= 3 mice; OT-1 CD-HFD n= 6 mice). (c) ALT of mice shown in a. (ND n= 5 mice; CD-HFD n= 7 mice; OT-1 CD-HFD n= 9 mice). (d) H&E, CD3 and F4/80 staining with (e) NAS evaluation and quantification of mice shown in a. (H&E: n= 8 mice/group; CD3 and F4/80: n= 3 mice/group). Scale bar: 50 µm. All data are shown as mean ± SEM. All data were analyzed by one or two way ANOVA and Tukey`s multiple comparison test. *p<0.05; **p<0.01; ***p<0.001; ****p<0.0001.

Due to the fact that some CD-HFD fed Prf1$^{-/-}$ mice developed histopathological signs of NAFLD and trends for increased ALT, indicative of liver damage, I investigated the lack of perforin in 12 months long-term CD-HFD feeding, a time point at which WT mice develop tumors with an incidence of 25%[6].

12 months CD-HFD fed Prf1$^{-/-}$ mice developed body weight comparable to WT CD-HFD fed mice (**Figure 16a**), had no difference in liver damage compared to CD-HFD fed WT mice (**Figure 16b**) and had histopathological signs of established NASH on H&E staining (**Figure 16c, d**). Further, 12 months CD-HFD fed Prf1$^{-/-}$ developed tumors with an incidence comparable to WT CD-HFD fed mice (**Figure 16d, e**).

Thus, I concluded the delay of NASH pathology initiation by an impaired TCR effector function does not translate to a significantly lower tumor incidence in long-term CD-HFD feeding experiments.

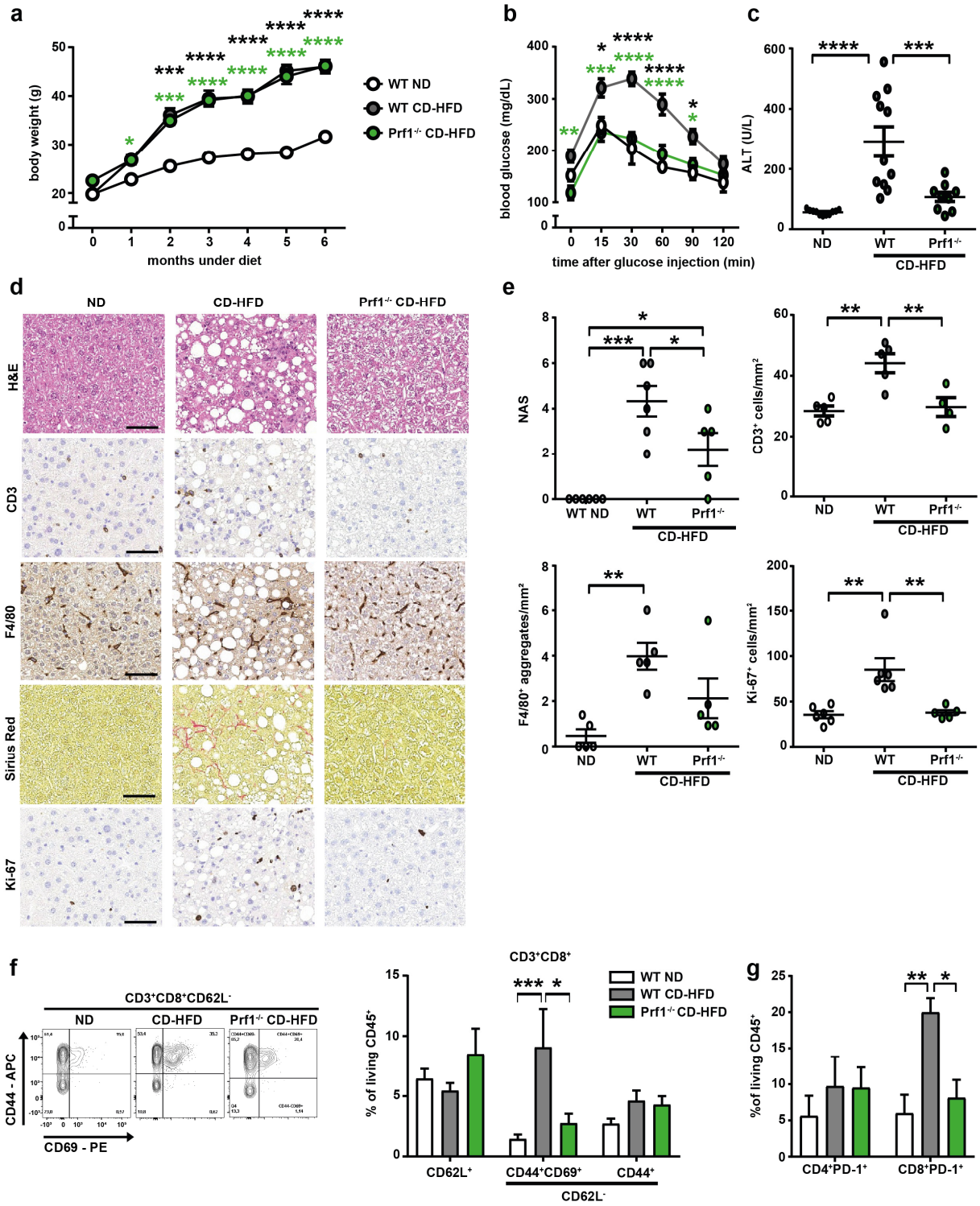

Figure 15: Lack of TCR effector function delays NASH development

(a) Body weight development of 6 months WT ND, WT CD-HFD or Prf1$^{-/-}$ CD-HFD fed mice (ND n= 6 mice; CD-HFD n= 9 mice; Prf1$^{-/-}$ CD-HFD n= 18 mice). Asterisks indicate significance of groups compared to WT ND fed mice. (b) IPGTT of mice shown in a (ND n= 3 mice; CD-HFD n= 9 mice; Prf1$^{-/-}$ CD-HFD n= 6 mice). (c) ALT of mice

shown in a. (ND n= 11 mice; CD-HFD n= 18 mice; Prf1$^{-/-}$ CD-HFD n= 9 mice). (d) H&E, CD3, F4/80, Sirius Red and Ki-67 staining with (e) NAS evaluation and quantification of mice shown in a. (H&E: ND n= 6 mice, CD-HFD n= 6 mice, Prf1$^{-/-}$ CD-HFD n= 5 mice; CD3: ND n= 5 mice, CD-HFD n= 5 mice, Prf1$^{-/-}$ CD-HFD n= 4 mice; F4/80: n= 5 mice/group; Ki-67: ND n= 6 mice, CD-HFD n= 6 mice, Prf1$^{-/-}$ CD-HFD n= 5 mice). Scale bar: 50 µm. (f) Flow cytometry plots and (g) quantification of mice shown in a (ND n= 9 mice, CD-HFD n= 9 mice, Prf1$^{-/-}$ CD-HFD n= 5 mice). (g) Flow cytometric quantification of mice shown in a (ND n= 6 mice, CD-HFD n= 6 mice, Prf1$^{-/-}$ CD-HFD n= 5 mice). All data are shown as mean ± SEM. All data were analyzed by one or two way ANOVA and Tukey`s multiple comparison test. *p<0.05; **p<0.01; ***p<0.001; ****p<0.0001.

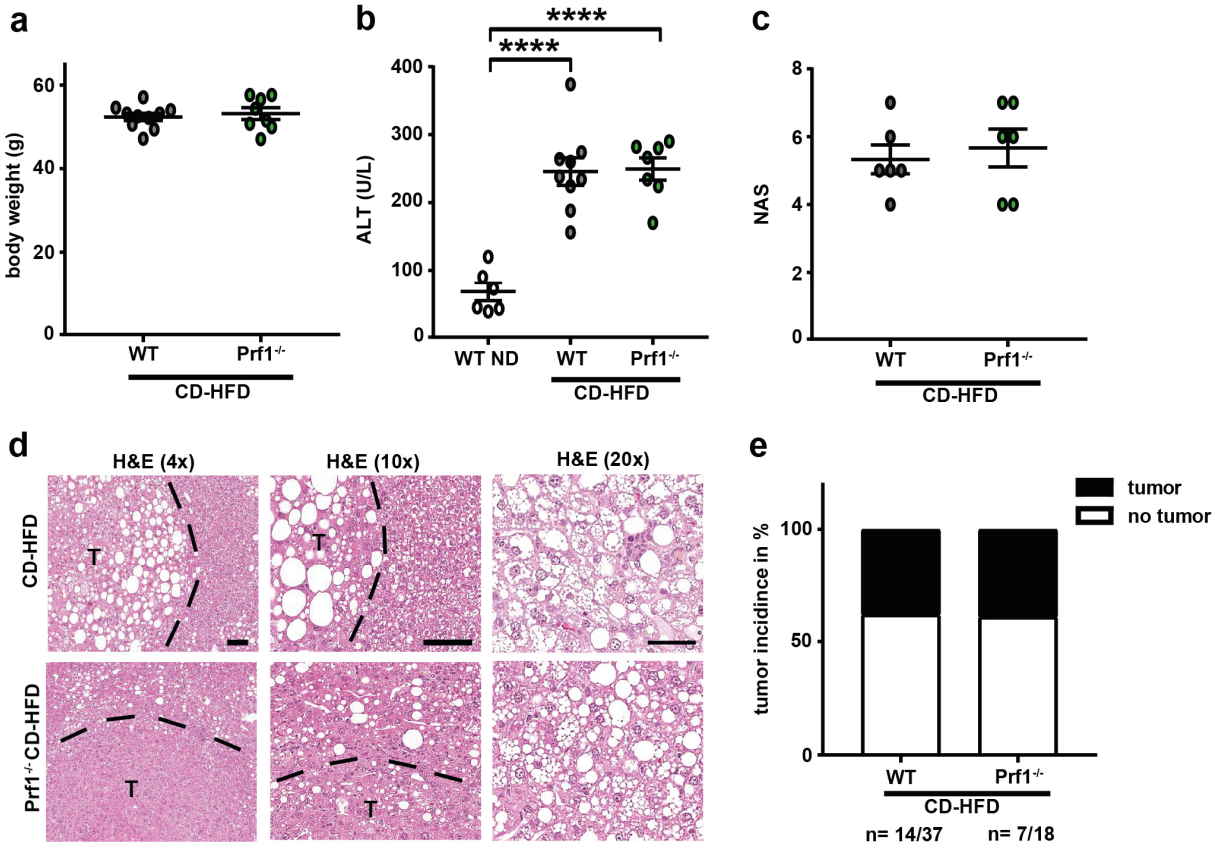

Figure 16: Impaired TCR effector function has no influence on dietary tumor formation
(a) Body weight development of 12 months WT or Prf1$^{-/-}$ CD-HFD fed mice (CD-HFD n= 10 mice; Prf1$^{-/-}$ CD-HFD n= 8 mice). (b) ALT of mice shown in a, with WT ND as a baseline of aged animals. (ND n= 6 mice; CD-HFD n= 9 mice; Prf1$^{-/-}$ CD-HFD n= 7 mice). (c) NAS evaluation and (d) H&E staining of mice shown in a. (n= 6 mice/group). Scale bar: 50µm. (e) Tumor incidence of mice groups shown in a (CD-HFD n= 14 tumors in 37 mice, Prf1$^{-/-}$ CD-HFD n= 7 tumors in 18 mice). All data are shown as mean ± SEM. All data were analyzed by one way ANOVA and Tukey`s multiple comparison test, by two-tailed Student T test, or by Fisher`s exact test. *p<0.05; **p<0.01; ***p<0.001; ****p<0.0001.

To determine whether T-cell effector impairment is the main driver of the observed delay of NASH in the systemic Prf1$^{-/-}$ mice, I investigated the role of natural killer T-cells (NKT) in NASH development and subsequent tumor formation. NKT type I cells mainly mediate cytotoxicity by using perforin.

To this end, I used Jα18$^{-/-}$ mice lacking the Jα281 TCR and therefore lacking NKT type I cells reactive to the glycolipid alpha-galactosyl ceramide (α-Gal), and fed these mice CD-HFD for 6 or 12 months.

After 6 months of CD-HFD feeding, Jα18$^{-/-}$ and WT control mice had no significant differences in body weight development (**Figure 17a**) and were metabolically significantly less impaired compared to WT CD-HFD fed mice by IPGTT (**Figure 17b**). CD-HFD fed Jα18$^{-/-}$ had liver damage similar to WT CD-HFD fed mice (**Figure 17c**) and no difference in histological evaluation of NASH pathology (**Figure 17d**). The lack of α-Gal NKT cells was confirmed by flow cytometric analysis (**Figure 17e**).

Next, I investigated whether the lack of NKT type I cells has any influence on tumor formation despite the underlying NASH pathology. Upon 12 months CD-HFD feeding to WT and Jα18$^{-/-}$ mice, Jα18$^{-/-}$ mice developed higher body weight (**Figure 17f**), similar liver damage (**Figure 17g**) and a similar histological evaluation of NASH by H&E staining (**Figure 17h, i**). Further, 12 months CD-HFD fed Jα18$^{-/-}$ mice developed tumors (**Figure 17j**).

Thus, I concluded lack of NKT type I cells cannot prevent NASH development and subsequent cannot prevent tumor formation upon long-term CD-HFD feeding.

To further test the potential role of the NKT compartment in NASH pathology, I next investigated whether a lack of all NKT cells would affect NASH pathology and subsequent tumor formation.

Thus, I used in collaboration with Manfred Kopf from the ETH Zurich CD1d$^{-/-}$ mice, lacking the antigen presenting protein CD1d and therefore have no invariant T-cells, namely NKT type I and NKT type II. In contrast to NKT type I cells, NKT type II cells` effector function is the release of cytokines. NKT type II cells, which are increased in dietary situations[6], an effect which I also observed (**Figure 17e**), can concert their activity with other immune cells, like, for example, the previously described hepatic C69^{+}CD8^{+} and PD-1^{+}CD8^{+} T-cells.

After 6 months of CD-HFD feeding, CD1d$^{-/-}$ and heterozygous control CD1d$^{+/-}$ mice had no significant difference in body weight (**Figure 18a**), no difference in liver damage (**Figure 18b**) and no difference in histopathological evaluation of NASH (**Figure 18c**). Further, WT and CD1d$^{-/-}$ 12 months CD-HFD fed mice developed the similar body weight (**Figure 18d**), similar liver damage (**Figure 18e**) and similar histological evaluation of NASH by H&E staining (**Figure 18f**). Both WT and CD1d$^{-/-}$ 12 months CD-HFD fed mice developed tumors (**Figure 18g**).

Thus, I concluded that lack of NKT type I and type II cells cannot prevent NASH development and lead subsequently to tumor formation upon long-term CD-HFD feeding.

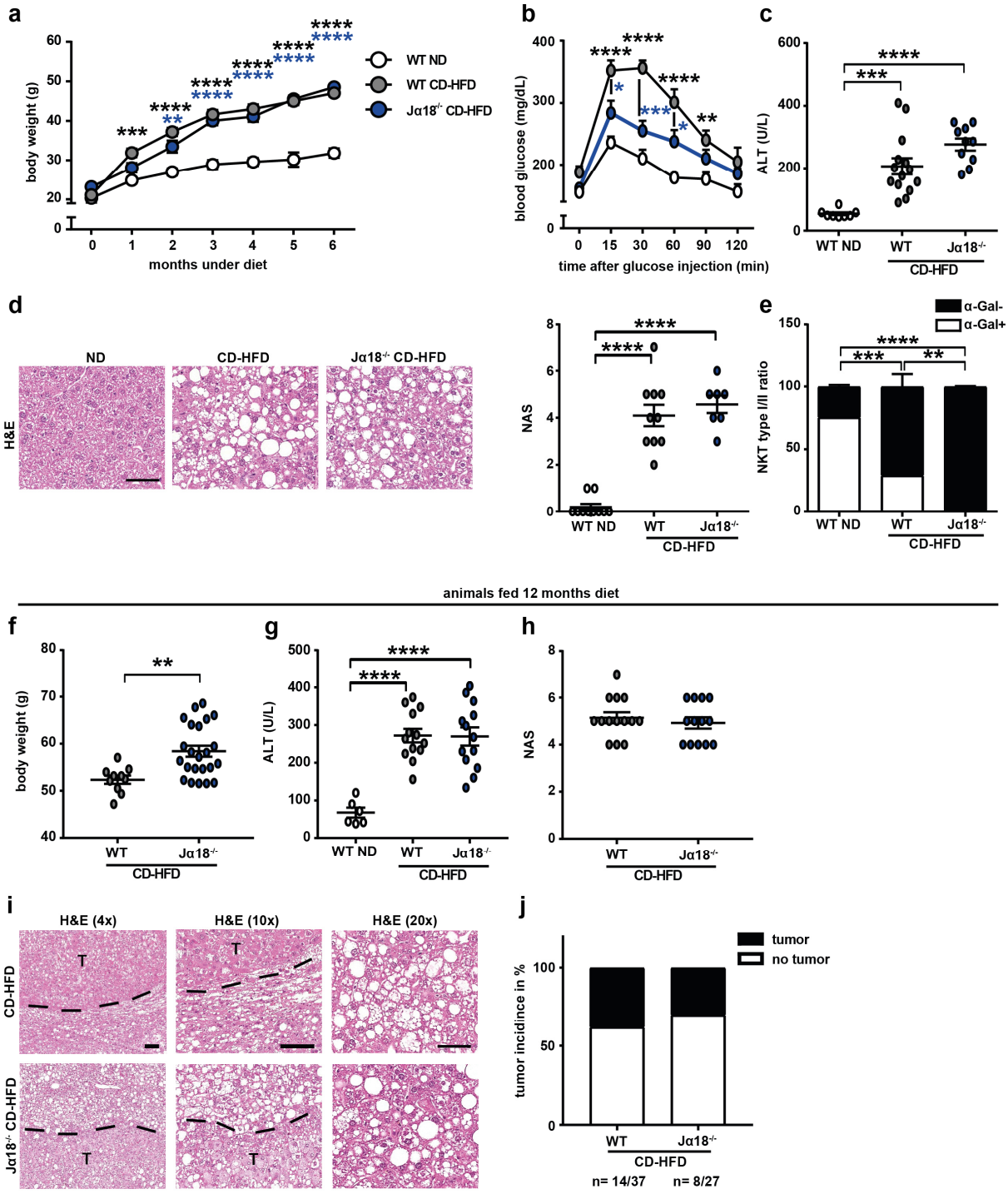

Figure 17: Lack of NKT type I cannot prevent NASH development and subsequent tumor formation

(a) Body weight development of 6 months WT ND, WT or Jα18$^{-/-}$ CD-HFD fed mice (WT ND n= 9 mice; WT CD-HFD n= 14 mice; Jα18$^{-/-}$ CD-HFD n= 15 mice). (b) IPGTT of mice shown in a (WT ND n= 5 mice; WT CD-HFD n= 8 mice; Jα18$^{-/-}$ CD-HFD n= 3 mice). (c) ALT of mice shown in a (WT ND n= 8 mice; WT CD-HFD n= 14 mice; Jα18$^{-/-}$ CD-HFD n= 10 mice). (d) H&E staining and NAS evaluation of mice shown in a. (n= 7 mice/group). Scale bar: 50µm. (e) Flow cytometric analysis of hepatic NKT type I/II ratio (n= 6 mice/group). (f) Body weight of WT or Jα18$^{-/-}$ 12 months CD-HFD fed mice (WT CD-HFD n= 10 mice; Jα18$^{-/-}$ CD-HFD n= 23 mice). (g) ALT of mice shown in f. WT ND shown as a baseline for aged mice (WT ND n= 6 mice; WT CD-HFD n= 13 mice; Jα18$^{-/-}$ CD-HFD n= 13 mice). (h) NAS evaluation and (i) H&E staining of mice shown in f. (WT CD-HFD n= 14 mice; Jα18$^{-/-}$ CD-HFD n= 13 mice). Scale bar: 50µm. (j) Tumor incidence of mice groups shown in f (WT CD-HFD n= 14 tumors in 37 mice; Jα18$^{-/-}$ CD-HFD n= 8 tumors in 27 mice). All data are shown as mean ± SEM. All data were analyzed by one or two way ANOVA and Tukey`s multiple comparison test, by two-tailed Student T test, or by Fisher`s exact test. *p<0.05; **p<0.01; ***p<0.001; ****p<0.0001.

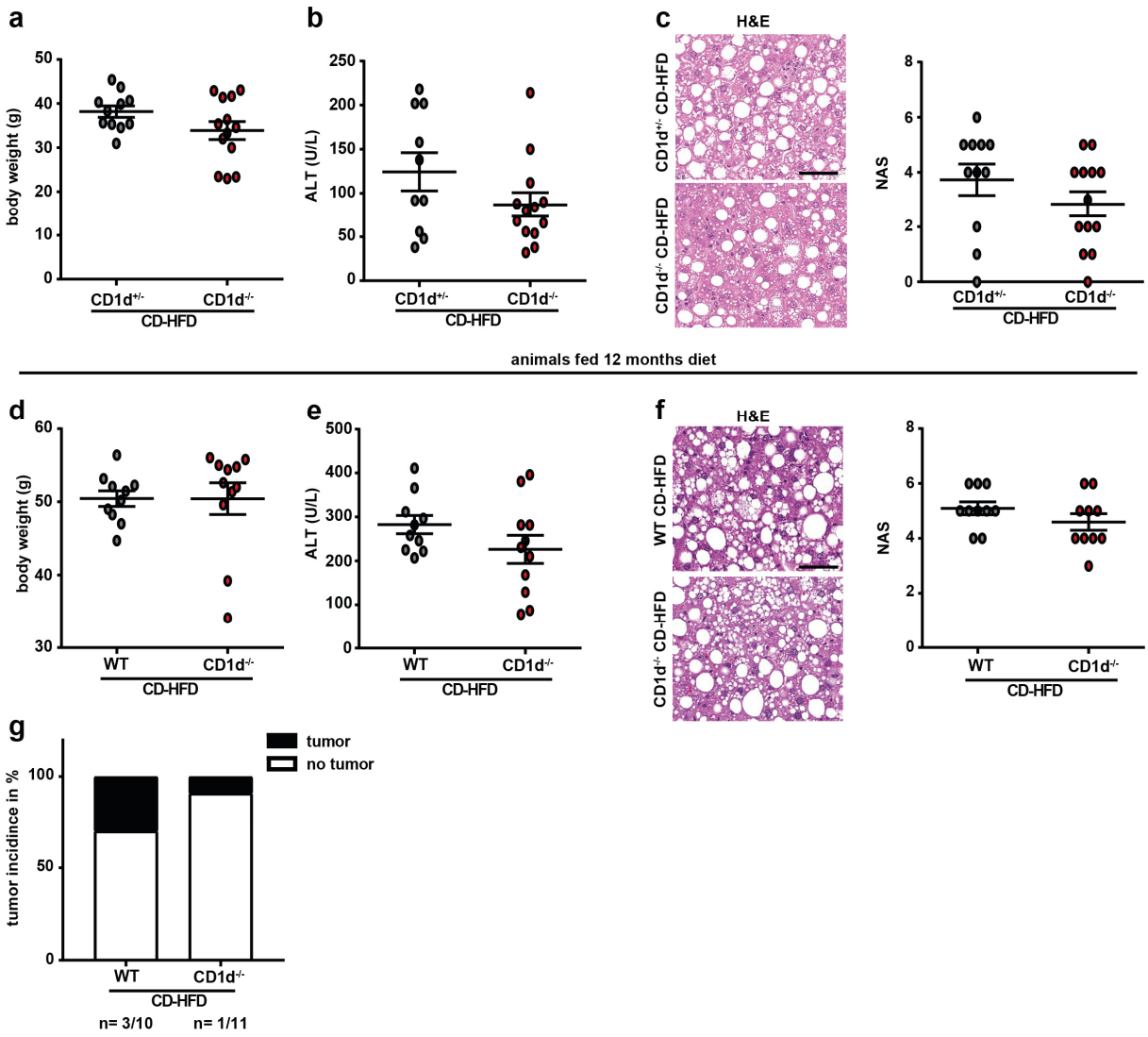

Figure 18: Lack of invariant NKT type I and II cannot prevent NASH development and subsequent tumor formation

(a) Body weight development of CD1d$^{+/-}$ or CD1d$^{-/-}$ 6 months CD-HFD fed mice (CD1d$^{+/-}$ CD-HFD n= 11 mice; CD1d$^{-/-}$ CD-HFD n= 13 mice). (b) ALT of mice shown in a. (CD1d$^{+/-}$ CD-HFD n= 10 mice; CD1d$^{-/-}$ CD-HFD n= 13 mice). (c) H&E staining and NAS evaluation of mice shown in a. (CD1d$^{+/-}$ CD-HFD n= 11 mice; CD1d$^{-/-}$ CD-HFD n= 13 mice). Scale bar: 50µm. (d) Body weight development of WT or CD1d$^{-/-}$ 12 months CD-HFD fed mice (WT CD-HFD n= 10 mice; CD1d$^{-/-}$ CD-HFD n= 11 mice). (e) ALT of mice shown in d. (WT CD-HFD n= 10 mice; CD1d$^{-/-}$ CD-HFD n= 11 mice). (f) H&E staining and NAS evaluation of mice shown in d. (n= 10 mice/group). Scale bar: 50µm. (g) Tumor incidence of mice groups shown in d (WT CD-HFD n= 3 tumors in 10 mice; CD1d$^{-/-}$ CD-HFD n= 1 tumor in 11 mice). All data are shown as mean ± SEM. All data were analyzed by two-tailed Student T test, or Fisher's exact test.

7.1.3 Differential role of T-cells during NASH and subsequent tumor development

My data so far indicated that the progression process of NAFLD to NASH development is strongly correlated to an activated and exhausted CD8$^+$ T-cell phenotype and a natural TCR repertoire with intact TCR effector function. To decipher the contribution of CD8$^+$ T-cells at different progression states of NASH pathology with the observed phenotype, I put WT mice

on CD-HFD for 4 months and treated these mice either with CD8 depleting antibody or checkpoint inhibition PD-1 blocking antibody with continuous CD-HFD diet for 8 weeks.

After 6 months of ND or CD-HFD feeding and 8 weeks of treatment, the CD-HFD fed mouse groups had no significant difference in body weight (**Figure 19a**), but CD8 depleted mice had significantly increased liver damage compared to control-treated CD-HFD fed mice (**Figure 19b**). The different treatment groups developed no difference in histopathological evaluation of NASH (**Figure 19c, d**). To define the immune compartments in more detail, analysis by flow cytometry showed an absolute cell number increase of α-PD-1 treated mice both in $CD3^+$ and $CD8^+$ T-cells, while CD8 depleted mice showed a significant reduction in $CD8^+$ T-cells (**Figure 19e**). Further, the composition of all living $CD45^+$ cells changed significantly between treatments, namely CD8 depleted mice showed a significant decrease in $CD3^+$ and $CD8^+$ T-cells, while other immune cells were left unchanged in terms of relative abundance (**Figure 19f, h**). In contrast, α-PD-1 treated mice had a significant increase in CD8+ T-cells and a decrease in $CD19^+$ B-cells, while other immune cells were again left unchanged in terms of relative abundance (**Figure 19f, h**). Both treatments resulted in more $CD8^+$ T-cells expressing $PD\text{-}1^+$ cells compared to CD-HFD fed control mice (**Figure 19g**). However, CD8 depletion reduced naive $CD62L^+$, as well as memory $CD62L^-CD44^+$ or activated memory $CD62L^-CD44^+CD69^+$ $CD8^+$ T-cells (**Figure 19i**). Treatment by α-PD-1 increased significantly $CD62L^-CD44^+CD8^+$ T-cells (**Figure 19i**). Focusing on potentially cytotoxic molecules mediating liver damage, compared to CD-HFD fed control mice, the T-cells populations of remaining $CD8^+$ T-cells upon CD8 depletion and the α-PD-1 treated $CD8^+$ T-cells, had more GzmB-positive $CD8^+$ T-cells (**Figure 19j**). Nevertheless, fewer of the remaining $CD8^+$ T-cells upon CD8 depletion were positive for IFNy, and no significant differences between the groups for TNF-a was detected (**Figure 19j**). To test if more cells express $GzmB^+$ or if individual T-cells express higher levels of GzmB+ per cell, indicative of high cytotoxic potential, I analyzed the levels of GzmB expression in $CD4^+$ and $CD8^+$ T-cells. Indeed, upon α-PD-1 treatment, $CD4^+$ and $CD8^+$ T-cells express higher levels of GzmB (**Figure 19k**). Further, the remaining $CD8^+$ T-cells upon CD8 depletion expressed high levels of GzmB, as well (**Figure 19k**). Next, I investigated potential side effects of both treatments. First, potential compensatory reactions of $CD4^+$ T-cells upon CD8 depletion or second, overreaction or reactivation upon α-PD-1 treatment of $CD4^+$ T-cells. However, both treatments had, aside from the increase of GzmB expression upon α-PD-1 treatment (**Figure 19k**), no significant effect on $CD4^+$ T-cells (**Figure 19h, l**). Also the ratio of type I to type II NKT cells was not changed compared to CD-HFD control mice (**Figure 19m**). Alternatively, innate immune system cells could play an important role in mediating the observed effects of higher liver damage. However, KC, $CD11b^+$, and myeloid dendritic cells (mDCs) showed no increase in MHC II expression, a marker of myeloid

activation (**Figure 19n**). However, upon CD8 depletion more plasmacytoid dendritic cells (pDCs) express MHC II compared to control CD-HFD fed mice (**Figure 19n**).

Thus, I concluded CD8 depletion and α-PD-1 treatment worked effectively in mice in an 8 week treatment scheme and that CD8 depletion induces liver damage in NASH development at the stages of 4 to 6 months of CD-HFD feeding.

7.1.4 Immunological profiling of hepatic tumor-associated lymphocytes

To focus more on the potential translational aspects of this study, I investigated advanced NASH to HCC time points, because most patients will be diagnosed in advanced stages of NASH. Therefore, understanding the role of T-cells in this progressed pathology state of NASH is important and may have strong clinical implications.

Thus, I fed WT mice CD-HFD for 10 months to induce an advanced liver pathology and treated these mice with CD8 depleting antibody for 8 weeks while continuously feeding CD-HFD diet.

After 12 months of ND or CD-HFD feeding followed by 8 weeks of treatment, the CD-HFD fed mouse groups had no significant difference in body weight (**Figure 20a**). CD8 depleted mice had a no difference in ALT levels (**Figure 20b**) and were metabolically equally impaired by IPGTT compared to control-treated CD-HFD fed mice (**Figure 20c**). In contrast, CD8 depleted mice had weaker signs of NASH pathology, ameliorated fibrogenesis and reduced tumor burden (**Figure 20d, e, f**). To define the immune compartment in more detail, analysis by flow cytometry showed an absolute cell number decrease in CD8 depleted mice for hepatic $CD45^+$, $CD3^+$, $CD8^+$ and $CD19^+$ cells (**Figure 20g, h**). Further, the composition of all hepatic $CD45^+$ cells changed, namely I saw reduced $CD3^+$ and $CD8^+$ T-cells in α-CD8 treated mice (**Figure 20h, i**). I could not observe differences in the $CD4^+$ T-cell compartment in terms of abundance (**Figure 20g, h, i**), polarization (**Figure 20j**) or effector molecules between α-CD8 treated and control mice (**Figure 20k**). Further, MHC II^+ innate immune cells were unchanged (**Figure 20l**).

Thus, I concluded that CD8 depletion in advanced stages of NASH pathology reduced $CD8^+$ T-cells numbers, ameliorated liver pathology and tumor formation, but did not decrease ALT levels.

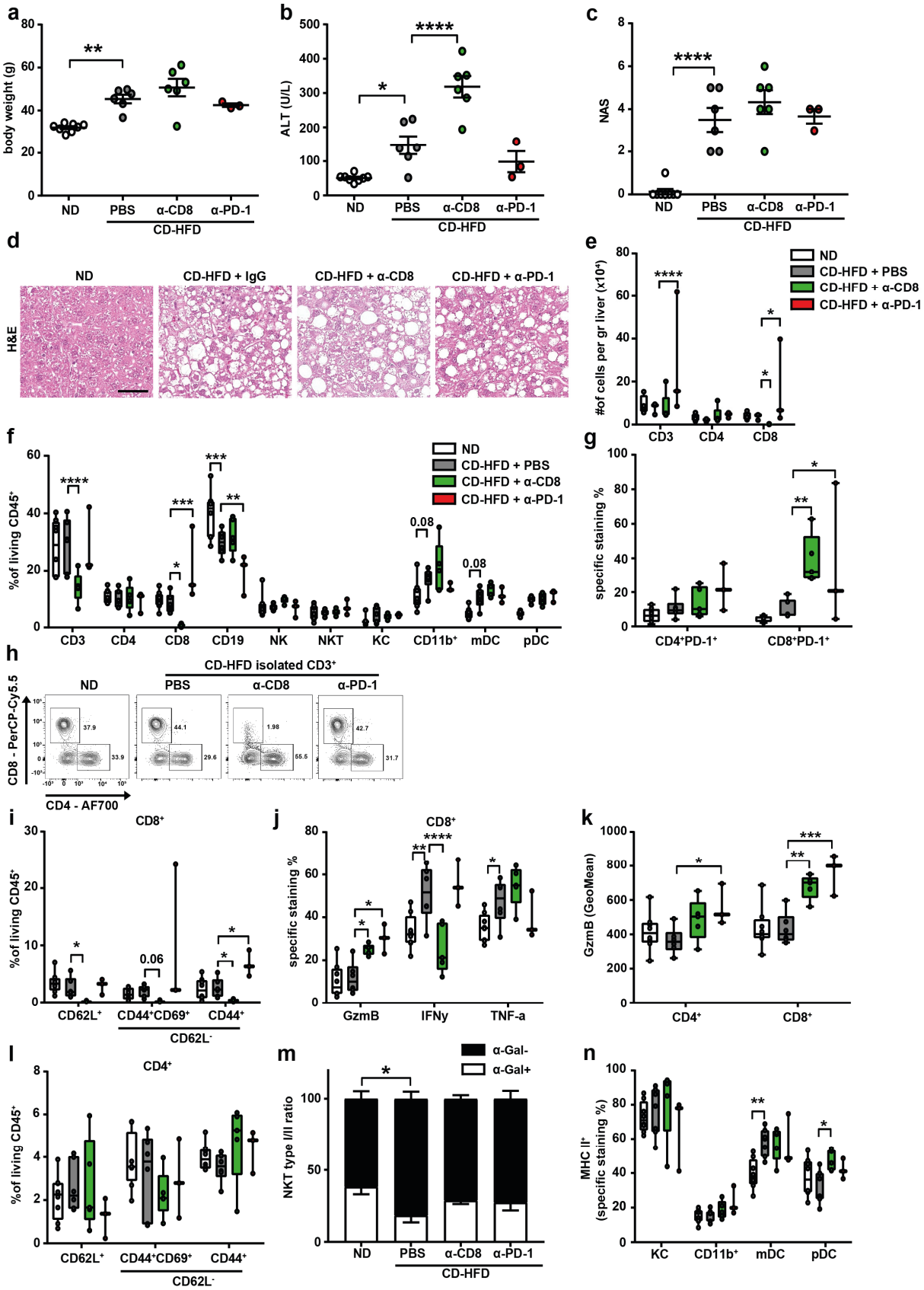

Figure 19: Functional antibody-mediated treatments fail to rescue NASH

(a) Body weight of 6 months ND, or CD-HFD fed mice, treated 2x per week for 8 weeks with either PBS, α-CD8 or α-PD-1 antibodies (ND n= 8 mice; PBS + CD-HFD n= 6 mice; α-CD8 + CD-HFD n= 6 mice; α-PD-1 + CD-HFD n= 3 mice). (b) ALT of mice shown in a (ND n= 8 mice; PBS + CD-HFD n= 6 mice; α-CD8 + CD-HFD n= 6 mice; α-PD-1 + CD-HFD n= 3 mice). (c) NAS evaluation and (d) H&E staining of mice shown in a. (ND n= 8 mice; PBS + CD-

HFD n= 6 mice; α-CD8 + CD-HFD n= 6 mice; α-PD-1 + CD-HFD n= 3 mice). Scale bar: 50µm. (e) Absolute flow cytometric analysis of hepatic T-cells (ND n= 4 mice; PBS + CD-HFD n= 3 mice; α-CD8 + CD-HFD n= 5 mice; α-PD-1 + CD-HFD n= 3 mice). (f) Flow cytometric analysis of hepatic $CD45^+$ cells (ND n= 8 mice; PBS + CD-HFD n= 6 mice; α-CD8 + CD-HFD n= 5 mice; α-PD-1 + CD-HFD n= 3 mice). (g) Flow cytometric analysis of hepatic $CD3^+$ T-cells (ND n= 8 mice; PBS + CD-HFD n= 6 mice; α-CD8 + CD-HFD n= 5 mice; α-PD-1 + CD-HFD n= 3 mice). (h) Flow cytometric plots of $CD3^+$ T-cells. (i) Flow cytometric analysis of hepatic $CD3^+CD8^+$T-cells for T-cell activation and (j) positive cells for effector molecules (ND n= 8 mice; PBS + CD-HFD n= 6 mice; α-CD8 + CD-HFD n= 5 mice; α-PD-1 + CD-HFD n= 3 mice). (k) Flow cytometric analysis for GzmB expression in hepatic $CD3^+$ T-cells (ND n= 8 mice; PBS + CD-HFD n= 6 mice; α-CD8 + CD-HFD n= 5 mice; α-PD-1 + CD-HFD n= 3 mice). (l) Flow cytometric analysis of hepatic $CD3^+CD4^+$T-cells for T-cell activation (ND n= 8 mice; PBS + CD-HFD n= 6 mice; α-CD8 + CD-HFD n= 5 mice; α-PD-1 + CD-HFD n= 3 mice). (m) Flow cytometric analysis of hepatic NKT type I/II ratio (ND n= 8 mice; PBS + CD-HFD n= 6 mice; α-CD8 + CD-HFD n= 5 mice; α-PD-1 + CD-HFD n= 3 mice). (n) Flow cytometric analysis of hepatic innate immune system cells (ND n= 8 mice; PBS + CD-HFD n= 6 mice; α-CD8 + CD-HFD n= 5 mice; α-PD-1 + CD-HFD n= 3 mice). All data are shown as mean ± SEM. All data were analyzed by one or two way ANOVA and Tukey`s multiple comparison test or when comparing only to one group or Sidak`s multiple comparison test. *p<0.05; **p<0.01; ***p<0.001; ****p<0.0001.

Next, I tried to determine by immunological phenotyping why CD8 depletion abrogates tumor formation but not liver damage.

Upon CD8 depletion, fewer hepatic naive, memory effector and memory CD8+ T-cells were detected **(Figure 21a)**. These remaining $CD8^+$ cells, as well as the $CD4^+$ T-cell compartment, had similar exhaustion marker expression **(Figure 21b)**. More of the non-depleted CD8+ T-cells expressed Fas ligand (FasL) and expressed higher amounts of GzmB compared to control mice **(Figure 21c, d)**. Other cell types which could potentially mediate liver damage are NK and NKT cells. CD8 depleted mice had no difference in their expression for effector molecules in NK cells **(Figure 21e)**, but fewer NKT cells expressed IFNy without changes in TNF-a or perforin expression **(Figure 21f)**. The NKT type I to type II ratio was not significantly changed upon CD8 depletion **(Figure 21g)**.

Of note, I depleted mice by α-CD8 and α-NK1.1 antibodies, to address a potential role of a concerted $CD8^+$ $NK1.1^+$ cell mechanism in driving liver damage. However, CD8/NK1.1 depleted mice had no difference in body weight **(Figure 21h)**, liver damage **(Figure 21i)**, NAS evaluation **(Figure 21j)** and no tumors could be detected upon successful antibody mediated depletion.

Thus, I concluded although low in numbers the remaining hepatic $CD8^+$ T-cells expressed FasL and higher GzmB - markers of potential cytotoxic mediation. Similar to the previously reported data of knockout mice for NK and NKT cells, I could not detect an amelioration of advanced NASH pathology with α-CD8/NK1.1 co-treatment.

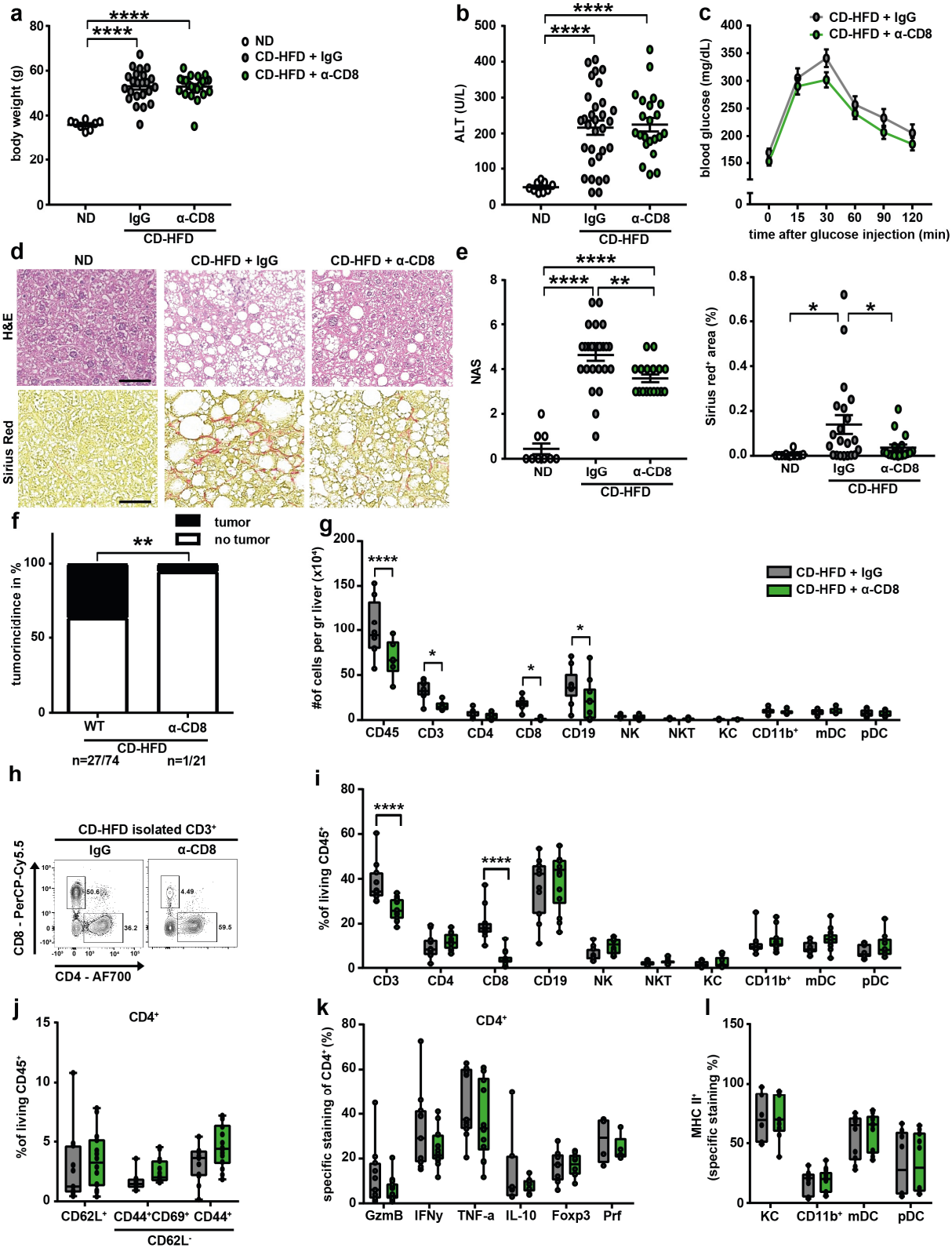

Figure 20: CD8+ T-cells drive tumorigenesis in advanced stages of NASH pathology

(a) Body weight of 12 months ND, or CD-HFD fed mice, treated 2x per week for 8 weeks with IgG or α-CD8 antibodies (ND n= 8 mice; control CD-HFD n= 23 mice; α-CD8 + CD-HFD n= 22 mice). (b) ALT of mouse groups shown in a (ND n= 9 mice; control CD-HFD n= 31 mice; α-CD8 + CD-HFD n= 22 mice). (c) IPGTT of mouse groups shown in a (control CD-HFD n= 8 mice; α-CD8 + CD-HFD n= 10 mice). (d) H&E and Sirius Red staining with (e) NAS evaluation and Sirius Red quantification of mouse groups shown in a (H&E: ND n= 11 mice; control CD-HFD n= 28 mice; α-CD8 + CD-HFD n= 23 mice; Sirius Red: ND n= 12 mice; control CD-HFD n= 21 mice; α-CD8 + CD-HFD n= 17 mice). Scale bar: 50μm. (f) Tumor incidence of mouse groups shown in a (control CD-HFD n= 27 tumors

in 74 mice; α-CD8 + CD-HFD n= 1 tumor in 21 mice). (g) Absolute flow cytometric analysis of hepatic immune cells (control CD-HFD n= 10 mice; α-CD8 + CD-HFD n= 14 mice). (h) Flow cytometric plots of $CD3^+$ T-cells. (i) Flow cytometric analysis of hepatic $CD45^+$ cells (control + CD-HFD n= 11 mice; α-CD8 + CD-HFD n= 14 mice). (j) Flow cytometric analysis for polarization of hepatic $CD4^+$ T-cells (control + CD-HFD n= 11 mice; α-CD8 + CD-HFD n= 14 mice). (k) Flow cytometric analysis for effector molecules of hepatic $CD4^+$ T-cells (control + CD-HFD n= 11 mice; α-CD8 + CD-HFD n= 14 mice). (l) Flow cytometric analysis of hepatic innate immune system cells (control + CD-HFD n= 10 mice; α-CD8 + CD-HFD n= 14 mice). All data are shown as mean ± SEM. All data were analyzed by one way ANOVA and Tukey`s multiple comparison test, or two way ANOVA and Sidak`s multiple comparison test, or for tumor incidence Fisher's exact test. *p<0.05; **p<0.01; ***p<0.001; ****p<0.0001.

Next, I investigated the effects of interfering with the inhibitory axis of T-cell signaling by PD-1/PD-L1 for $PD\text{-}1^+$ cells in advanced stages of NASH pathology by administering α-PD-1 blocking antibody.

Thus, I fed WT mice CD-HFD for 10 months to induce a strong liver pathology and treated these mice with α-PD-1 blocking antibody for 8 weeks while continuously feeding CD-HFD diet. After 12 months CD-HFD feeding with 8 weeks of treatment the CD-HFD fed mouse groups had no significant difference in body weight (**Figure 22a**). Treatment with α-PD-1 increased AST and ALT levels significantly (**Figure 22b**), but affected glucose tolerance only mildly compared to control-treated CD-HFD fed mice (**Figure 22c**). Further, compared to control, CD-HFD fed mice and α-PD-1 treated mice had increased NAS, similar levels of fibrosis and increased tumor burden (**Figure 22d, e, f**). To decipher the immune compartment in more detail, analysis by flow cytometry showed no difference in absolute cell numbers (**Figure 22g**), nor in the composition of all hepatic $CD45^+$ cells upon α-PD-1 treatment (**Figure 22h**). Nevertheless, α-PD-1 treatment increased the amount of hepatic effector memory $CD8^+$ T-cells (**Figure 22i**). Further, analysis of three independent experiments indicated that, upon α-PD-1 treatment, more $CD8^+$ T-cells are positive for the effector molecules GzmB and IFNy (**Figure 22j**). Also, α-PD-1 treatment correlated with more $PD\text{-}1^+CD8^+$ T-cells and trends toward higher numbers of $PD\text{-}1^+CD4^+$ T-cells (**Figure 22k**), but no differences in $FasL^+$ T-cells (**Figure 22l**).

Thus, I concluded that α-PD-1 treatment in advanced stages of NASH pathology likely induced immune-related adverse events (irAEs) leading to increased liver damage, tumor or lesion formation and increased effector function markers on $CD8^+$ T-cells.

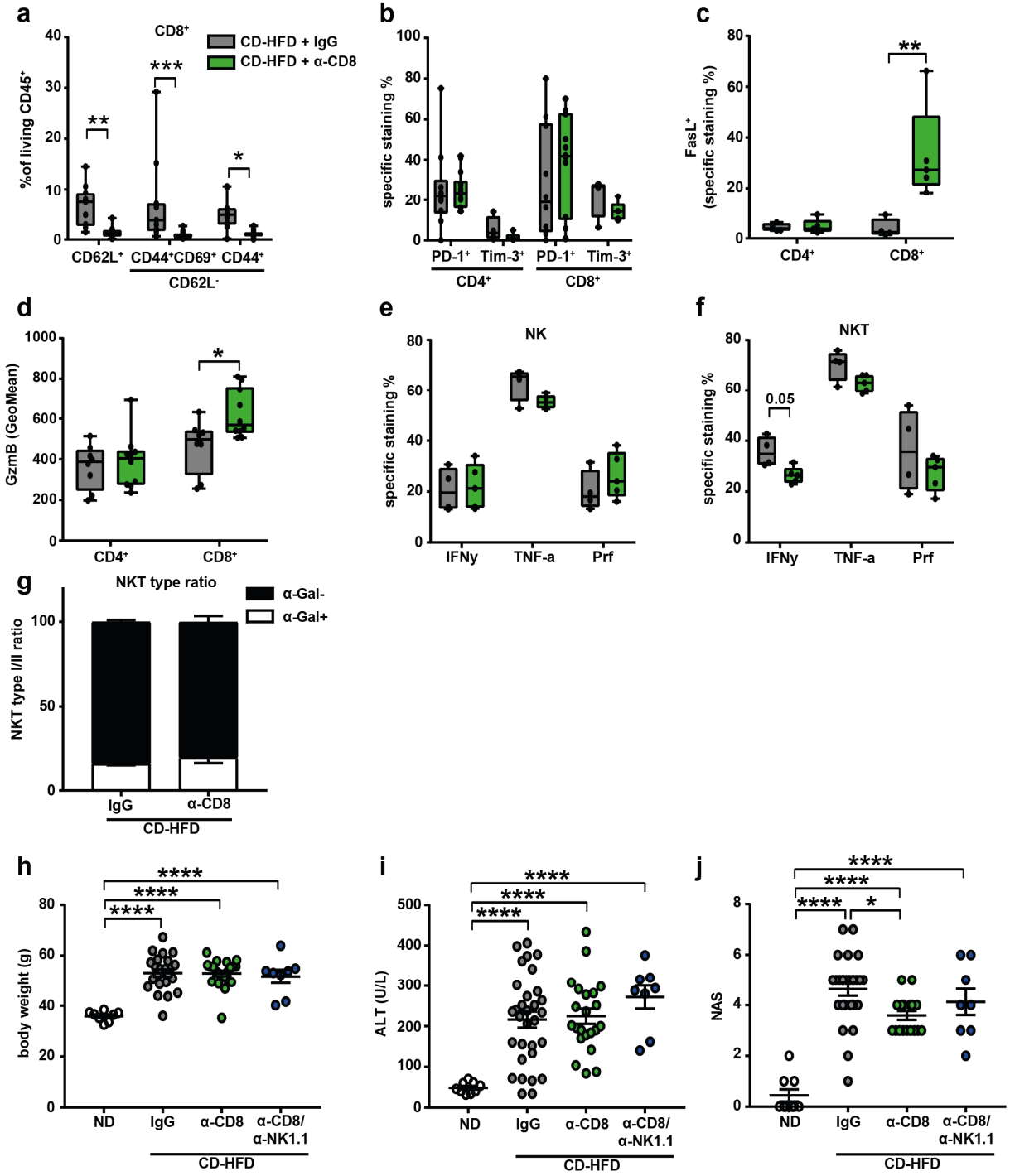

Figure 21: Understanding high ALT in CD8 depleted mice with advanced NASH

(a) Flow cytometric analysis for polarization of hepatic CD8+ T-cells isolated from mice 12 months fed ND, or CD-HFD and treated 2x per week for 8 weeks with IgG or α-CD8 antibodies (control + CD-HFD n= 11 mice; α-CD8 + CD-HFD n= 14 mice). (b) Flow cytometric analysis of markers of hepatic T-cell exhaustion (control + CD-HFD n= 4 mice; α-CD8 + CD-HFD n= 5 mice). (c) Flow cytometric analysis of FasL T-cell polarization (control + CD-HFD n= 4 mice; α-CD8 + CD-HFD n= 5 mice). (d) Flow cytometric analysis for GzmB expression in hepatic CD3+ T-cells (control + CD-HFD n= 8 mice; α-CD8 + CD-HFD n= 10 mice). (e) Flow cytometric analysis for effector molecules of hepatic NK and (f) NKT cells (control + CD-HFD n= 4 mice; α-CD8 + CD-HFD n= 5 mice). (g) Flow cytometric analysis of hepatic NKT type I/II ratio (control + CD-HFD n= 6 mice; α-CD8 + CD-HFD n= 9 mice). (h) Body weight of 12 months fed ND, or CD-HFD fed mice, treated 2x per week for 8 weeks with IgG, α-CD8, or α-CD8/α-NK1.1 antibodies (ND n= 8 mice; control CD-HFD n= 23 mice; α-CD8 + CD-HFD n= 22 mice; α-CD8/α-NK1.1 + CD-HFD n= 8 mice). (i) ALT of mouse groups shown in h (ND n= 9 mice; control CD-HFD n= 31 mice; α-CD8 + CD-HFD n= 22 mice; α-CD8/α-NK1.1 + CD-HFD n= 8 mice). (j) NAS evaluation of mouse groups shown in h (H&E: ND n= 11 mice; control CD-HFD n= 28 mice; α-CD8 + CD-HFD n= 23 mice; α-CD8/α-NK1.1 + CD-HFD n= 8 mice). All data

are shown as mean ± SEM. All data were analyzed by one way ANOVA and Tukey`s multiple comparison test, or two way ANOVA and Sidak`s multiple comparison test. *p<0.05; **p<0.01; ***p<0.001; ****p<0.0001.

To decipher the mechanisms underlying increased liver damage and tumorigenesis as a result of α-PD-1 treatment in advanced stages of NASH pathology, I investigated cell types typically able to express PD-1 like $CD4^+$ T-cells, NK and NKT cells, but also innate immune system cells potentially concerting cytotoxicity together with the $CD8^+$ T-cell compartment.

In both the main T-cell compartments, $CD4^+$ as well as $CD8^+$, GzmB expression was downregulated (**Figure 23a**). Upon α-PD-1 treatment less hepatic naïve $CD4^+$ T-cells, but no significant enlargements of the memory effector and memory $CD4^+$ T-cell compartments compared to CD-HFD control mice were detected (**Figure 23b**). Analysis of effector molecules of the CD4 lineage revealed only a significant difference in IL-10 expression (**Figure 23c**). Similar to the CD8 depletion experiment, I considered NK and NKT cells as potential mediators of liver damage. However, after analysis of three experimental cohorts, no difference in the numbers of NK or NKT cells for effector molecules could be detected (**Figure 23d, e**). In addition, the NKT type I to type II ratio was not significantly changed upon α-PD-1 treatment **(Figure 23f)**. Analysis of innate immune cells expressing MHC II revealed more KC, mDCs and pDCs expressing MHC II upon α-PD-1 treatment (**Figure 23f**).

Thus, I concluded, first that cytotoxic capacity by the GzmB axis decreases in the T-cell compartment after α-PD-1 treatment. Second, $CD4^+$ T-cells are potentially more Th2 polarized, possibly as a means of coping with the increased liver damage through increased IL-10 expression. Further, NK and NKT cells seem to play a minor role, but a strong activation of the innate immune cell compartment correlate with α-PD-1 treatment.

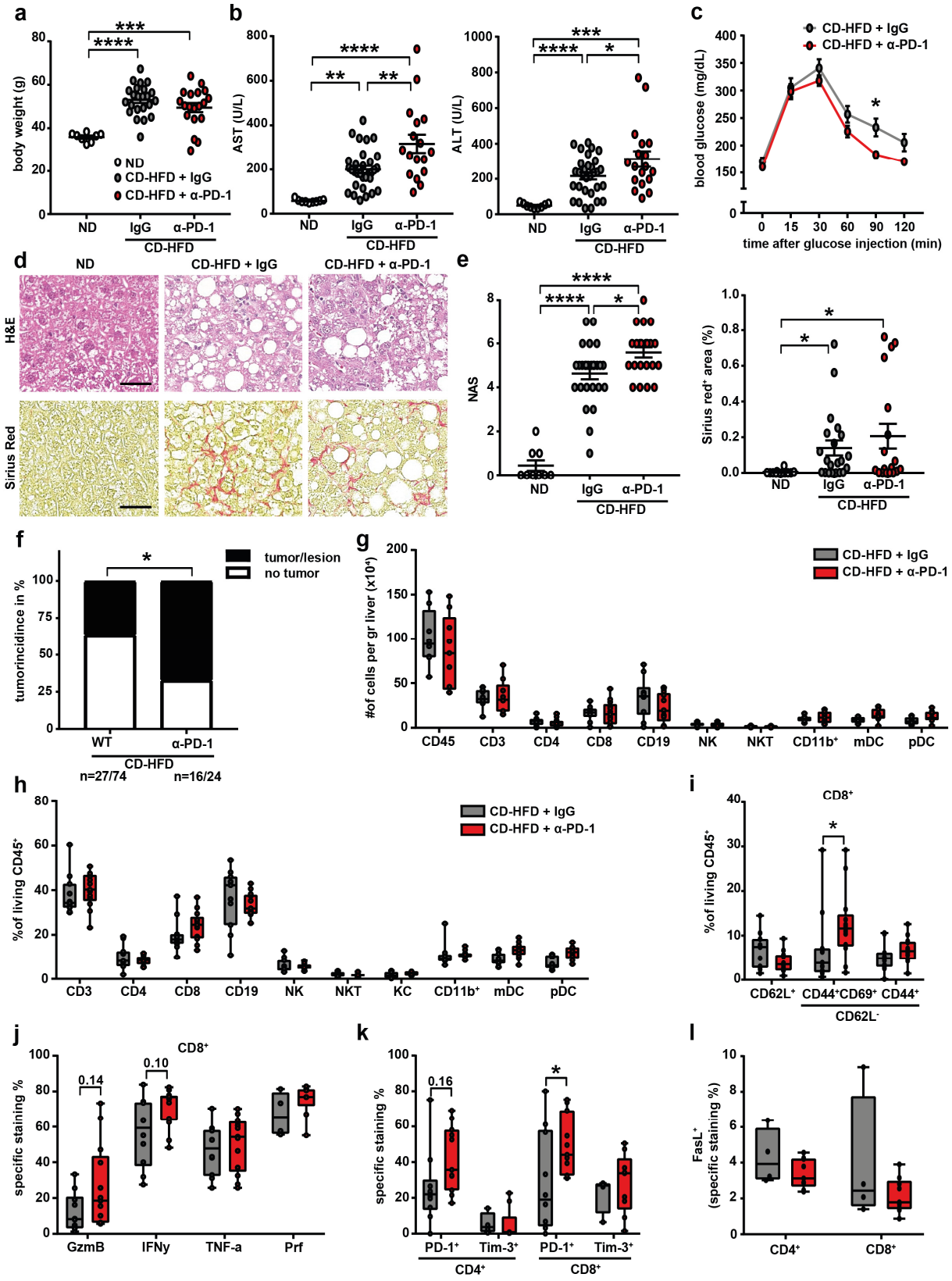

Figure 22: Blocking inhibitory PD-1/PD-L1 drives liver damage and tumorigenesis in advanced stages of NASH pathology

(a) Body weight of 12 months ND, or CD-HFD fed mice, treated 2x per week for 8 weeks with IgG or α-PD-1 antibodies (ND n= 8 mice; control CD-HFD n= 23 mice; α-PD-1 + CD-HFD n= 19 mice). (b) AST and ALT of mouse groups shown in a (ND n= 9 mice; control CD-HFD n= 31 mice; α-PD-1 + CD-HFD n= 17 mice). (c) IPGTT of mouse groups shown in a (control CD-HFD n= 8 mice; α-PD-1 + CD-HFD n= 10 mice). (d) H&E and Sirius Red staining with (e) NAS evaluation and Sirius Red quantification of mouse groups shown in a (H&E: ND n= 11 mice; control

CD-HFD n= 28 mice; α-PD-1 + CD-HFD n= 24 mice; Sirius Red: ND n= 12 mice; control CD-HFD n= 21 mice; α-PD-1 + CD-HFD n= 18 mice). Scale bar: 50µm. (f) Tumor incidence of mouse groups shown in a (control CD-HFD n= 27 tumors in 74 mice; α-PD-1 + CD-HFD n= 16 tumors/lesions in 24 mice). (g) Absolute flow cytometric analysis of hepatic immune cells (control CD-HFD n= 10 mice; α-PD-1 + CD-HFD n= 13 mice). (h) Flow cytometric analysis of hepatic CD45$^+$ cells (control + CD-HFD n= 11 mice; α-PD-1 + CD-HFD n= 13 mice). (i) Flow cytometric analysis for polarization of hepatic CD8$^+$ T-cells (control + CD-HFD n= 11 mice; α-PD-1 + CD-HFD n= 13 mice). (j) Flow cytometric analysis for effector molecules of hepatic CD8$^+$ T-cells (control + CD-HFD n= 11 mice; α-PD-1 + CD-HFD n= 13 mice; for Prf: control + CD-HFD n= 4 mice; α-PD-1 + CD-HFD n= 4 mice). (k) Flow cytometric analysis of markers of hepatic T-cell exhaustion (control + CD-HFD n= 4 mice; α-PD-1 + CD-HFD n= 9 mice). (l) Flow cytometric analysis of FasL T-cell polarization (control + CD-HFD n= 4 mice; α-CD8 + CD-HFD n= 9 mice). All data are shown as mean ± SEM. All data were analyzed by one way ANOVA and Tukey`s multiple comparison test, or two way ANOVA and Sidak`s multiple comparison test, or for tumor incidence Fisher's exact test. *p<0.05; **p<0.01; ***p<0.001; ****p<0.0001.

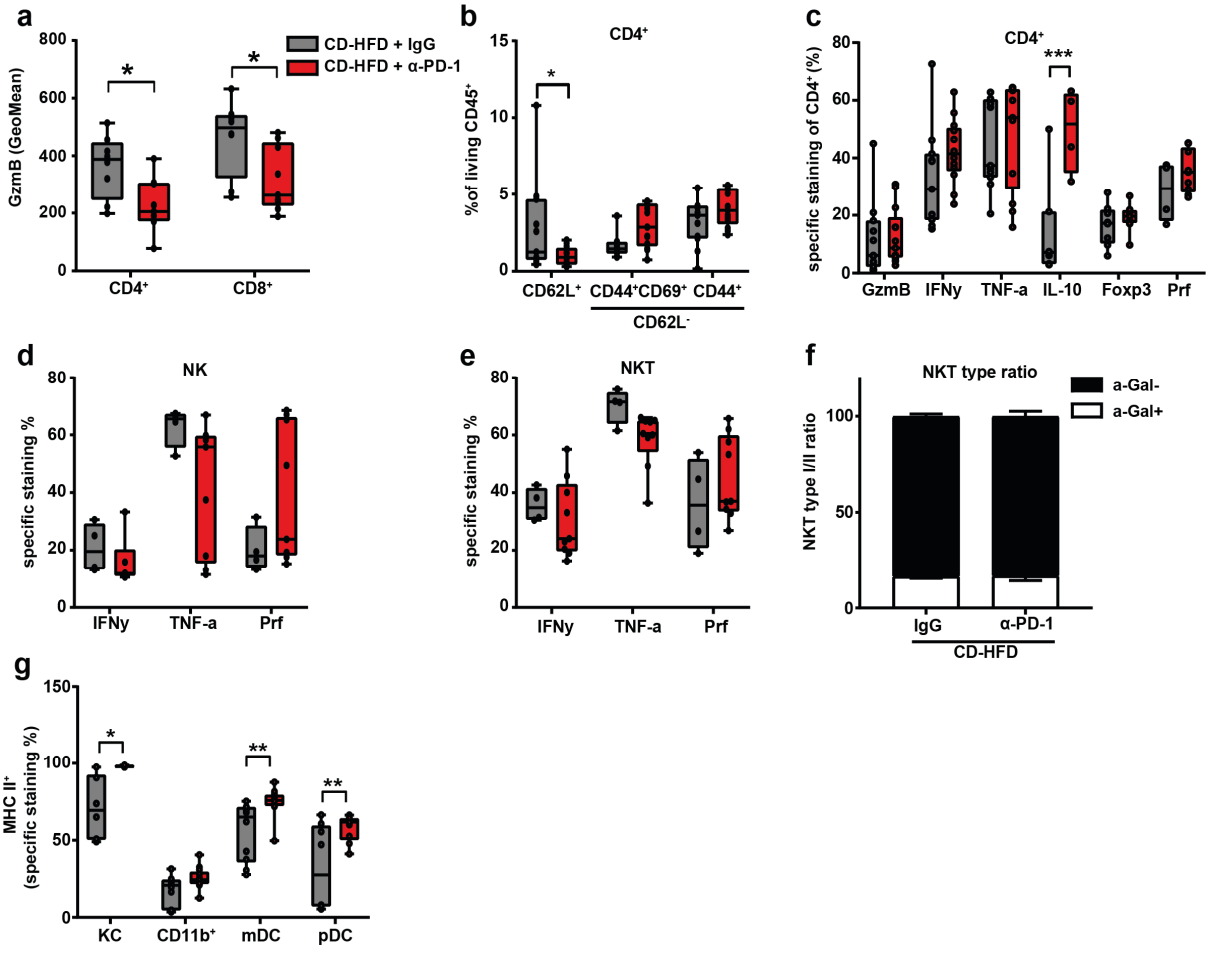

Figure 23: Deciphering tumor driving mechanism of PD-1 checkpoint blockade in advanced stages of NASH
(a) Flow cytometric analysis for GzmB expression in hepatic CD3$^+$ T-cells isolated from 12 months CD-HFD fed mice, treated 2x per week for 8 weeks with IgG or α-PD-1 antibodies (control + CD-HFD n= 8 mice; α-PD-1+ CD-HFD n= 9 mice). (b) Flow cytometric analysis for polarization of hepatic CD4$^+$ T-cells (control + CD-HFD n= 11 mice; α-PD-1+ CD-HFD n= 13 mice). (c) Flow cytometric analysis for effector molecules of hepatic CD4$^+$ T-cells (control + CD-HFD n= 8 mice; α-PD-1+ CD-HFD n= 13 mice). (d) Flow cytometric analysis for effector molecules of hepatic NK and (e) NKT cells (control + CD-HFD n= 4 mice; α-PD-1+ CD-HFD n= 9 mice; for perforin: control + CD-HFD n= 4 mice; α-PD-1+ CD-HFD n= 4 mice). (f) Flow cytometric analysis of hepatic NKT type I/II ratio (control + CD-HFD n= 6 mice; α-PD-1+ CD-HFD n= 13 mice). (g) Flow cytometric analysis of hepatic innate immune system cells (KC: control + CD-HFD n= 6 mice; α-PD-1 + CD-HFD n= 4 mice; CD11b$^+$: control + CD-HFD n= 10 mice; α-PD-1 + CD-HFD n= 13 mice; mDCs: control + CD-HFD n= 10 mice; α-PD-1 + CD-HFD n= 13 mice; pDCs: control + CD-HFD n= 8 mice; α-PD-1 + CD-HFD n= 9 mice). All data are shown as mean ± SEM. All data were analyzed by two way ANOVA and Sidak`s multiple comparison test. *p<0.05; **p<0.01; ***p<0.001; ****p<0.0001.

7.1.5 Deciphering mechanisms of immune cell mediated hepatocarcinogenesis

To understand the tumor- and hepatic damage-promoting role of PD-1 blocking, I phenotyped the hepatic immune compartment in depth in collaboration with Nicolas Nunez and Burkhard Becher from the University of Zurich using a 24 multicolor flow cytometric analysis[75].

First, I defined in collaboration with Nicholas Nunez clusters of marker expression of living $C45^+$ cells by t-distributed stochastic neighbor embedding (tSNE) analysis of randomly chosen 5000 events of 12 month ND or CD-HFD with IgG, or α-CD8, or α-CD8/α-NK1.1 or α-PD-1 treatment for 8 weeks (**Figure 24a**). By this approach, I in collaboration with Nicholas Nunez could define the hepatic immune compartment (B-cells, $CD4^+$ or $CD8^+$ or $CD4^-CD8^-$ or regulatory T-cells, myeloid cells, NK cells and other leukocytes) (**Figure 24b**) and their frequency among $CD45^+$ cells (**Figure 24c**). Further, I in collaboration with Nicholas Nunez assigned relative expression of markers to the individual populations of the defined hepatic immune cell compartment (**Figure 24d**). I found differences in the $CD8^+$ T-cell compartment of 12 month CD-HFD fed mice with IgG control treatment compared to α-PD-1 checkpoint inhibition. $CD8^+$ T-cells increased in absolute numbers (mean difference -31; 95% CI -50 to -13; p= 0.0007) and as a frequency of $CD45^+$ cells (mean difference -9.07; 95% CI -14.27 to -3.88; p= 0.0004).

Thus, I focused on deciphering the effects of α-PD-1 treatment on $TCR\beta^+$ cells. After I defined clusters of marker expression of $TCR\beta^+$ cells in collaboration with Nicholas Nunez, tSNE analysis was performed on randomly chosen 5000 events among the treated groups described earlier (**Figure 24e**). I in collaboration with Nicholas Nunez assigned cells by tSNE analysis to different T-cell compartments (naïve or conventional $CD4^+$; naïve or conventional $CD8^+$; $CD4^-CD8^-$ T-cells and regulatory T-cells) (**Figure 24f**). Next, I in collaboration with Nicholas Nunez quantified the different T-cell compartments as frequency among $CD45^+$ cells (**Figure 24g**). I in collaboration with Nicholas Nunez observed no differences in the $CD4^+$ and regulatory T-cell compartments between mice fed 12 months ND or CD-HFD treated with IgG or α-PD-1 in the frequency among $CD45^+$ cells. However, I discovered differences in the conventional $CD8^+$ T-cell and $CD4^-CD8^-$ T-cell compartment between mice fed 12 months ND or CD-HFD treated with IgG in the frequency among $CD45^+$ cells (conventional $CD8^+$ T-cells: mean difference 21; 95% CI -13 to 29; p< 0.0001 and $CD4^-CD8^-$ T-cells: mean difference -11; 95% CI -19 to -3.1; p= 0.0049). Further, I saw trends for an decrease of conventional $CD8^+$ T-cells in IgG control compared to α-PD-1 treated mice (mean difference -5.1; 95% CI -12 to 1.9; p= 0.1855).

Therefore I decided to investigate the $CD8^+$ T-cell compartment in more detail in order to decipher the reported immune-related adverse effects (irAEs), higher liver damage, and tumor formation after α-PD-1 treatment.

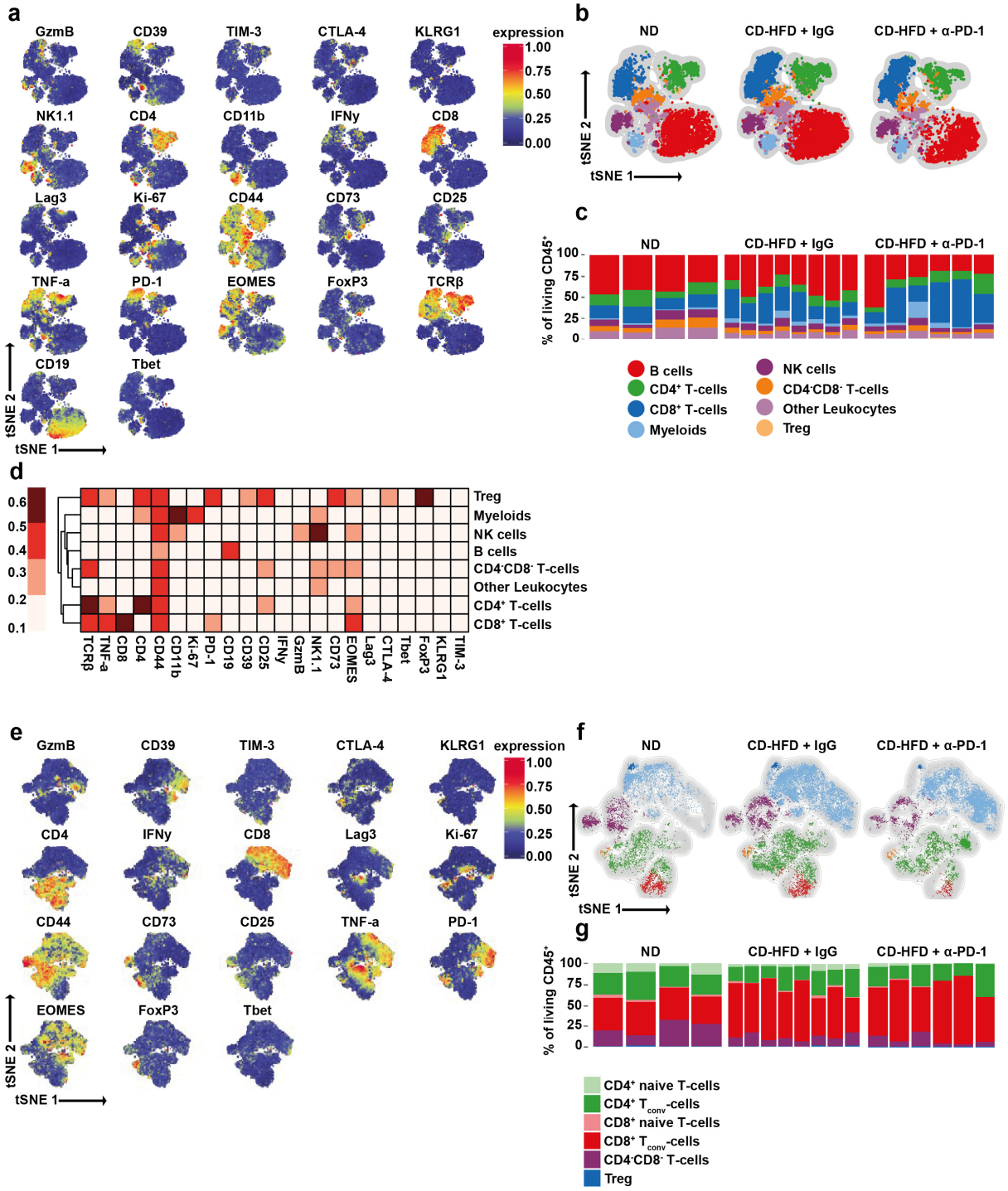

Figure 24: CD8 T-cells are the effector cells of immune-related adverse events upon PD-1 checkpoint blockade in advanced NASH

(a) Unbiased analysis of 5000 randomly chosen events of a 24 color flow cytometric analysis to define distinct marker expression of mice 12 months fed ND or CD-HFD with IgG, or α-CD8, or α-CD8/α-NK1.1 or α-PD-1 treatment for 8 weeks. (ND n= 4 mice; IgG + CD-HFD n= 8 mice; α-PD-1+ CD-HFD n= 6 mice; α-CD8 + CD-HFD n= 7 mice; α-CD8/α-NK1.1 + CD-HFD n= 7 mice). (b) Flowsom generated tSNE plots for definition of immune cell compartments of 12 months fed ND or CD-HFD with IgG or α-PD-1 treatment for 8 weeks. (c) Phenotypic composition of the immune cell compartment of individual mice shown in b (ND n= 4 mice; IgG + CD-HFD n= 8 mice; α-PD-1+ CD-HFD n= 6 mice). (d) Heatmap of marker expression of immune cell populations defined in b. (e) Unbiased analysis of 5000 randomly chosen TCRβ$^+$ cells of a 24 color flow cytometric analysis to define distinct marker expression of mice 12 months fed ND or CD-HFD with IgG, or α-CD8, or α-CD8/α-NK1.1 or α-PD-1 treatment for 8 weeks. (ND n= 4 mice; IgG + CD-HFD n= 8 mice; α-PD-1+ CD-HFD n= 6 mice; α-CD8 + CD-HFD n= 7 mice; α-CD8/α-NK1.1 + CD-HFD n= 7 mice). (f) Flowsom generated tSNE plots for definition of TCRβ$^+$ cell

compartments of 12 months fed ND or CD-HFD with IgG or α-PD-1 treatment for 8 weeks. (g) Phenotypic composition of the TCRβ$^+$ cell compartment of individual mice shown in b (ND n= 4 mice; IgG + CD-HFD n= 8 mice; α-PD-1+ CD-HFD n= 6 mice). All data are shown as mean ± SEM. All data were analyzed by two way ANOVA and Dunnett`s multiple comparison test. *p<0.05; **p<0.01; ***p<0.001; ****p<0.0001.

Next, I in collaboration with Nicholas Nunez defined clusters of marker expression for TCRβ$^+$ CD8$^+$ T-cells by tSNE analysis of randomly chosen 5000 events among the 12 month ND or CD-HFD treated with IgG as control or α-PD-1 for 8 weeks (**Figure 25a**). To identify subsets reactive to or changed upon α-PD-1 treatment, I in collaboration with Nicholas Nunez sub-clustered the CD8$^+$ T-cell compartment into 30 sub-clusters by tSNE analysis (**Figure 25b**) and quantified their abundance relative to CD45$^+$ cells (**Figure 25c**). Cluster 3 (mean difference 9.2; 95% CI 5.4 to 13; p= 0.0001) and Cluster 10 (mean difference -18; 95% CI -22 to -15; p= 0.0001) were changed in CD-HFD fed mice treated with IgG compared to α-PD-1 treated mice. Next, I in collaboration with Nicholas Nunez assigned the relative expression of investigated molecules to the 30 individual clusters of the hepatic CD8$^+$ T-cell compartment (**Figure 25d**). I in collaboration with Nicholas Nunez divided the 30 sub-clusters into two main populations, one associated with a memory phenotype including the decreased Cluster 3 upon α-PD-1 treatment. The other main population was positive for TNF-a and PD-1, including Cluster 10, which was increased by α-PD-1 treatment (**Figure 25e**). Compared to IgG control, the TNF-a$^+$PD-1$^+$ CD8$^+$ T-cell population was increased (mean difference -23.5; 95% CI -46.82 to -0.19; p= 0.0482) upon α-PD-1 treatment (**Figure 25f**). Further, compared to the CD8$^+$ memory T-cell population, the TNF-a$^+$PD-1$^+$ CD8$^+$ T-cell population expressed, in general, higher amounts of markers associated with activation (EOMES, Tbet), cytotoxicity (TNF-a, IFNy, GzmB) and exhaustion (PD-1, Tim-3) (**Figure 25g**).

Further, in collaboration with Nicolas Nunez I applied a representation learning approach (CellCnn)[77] to the flow cytometric data set. Using this method, I in collaboration with Nicholas Nunez could identify differential marker expression in the CD8$^+$ T-cell compartment in a tSNE analysis (**Figure 25h**). Next, I in collaboration with Nicholas Nunez selected CD8$^+$ T-cells negative for PD-1 and TNF-a (**Figure 25i**). Similar to Nicolas Nunez and my 30 sub-cluster approach (**Figure 25a-f**), I in collaboration with Nicholas Nunez determined that double-negative PD-1$^-$TNF-a$^-$ CD8$^+$ T-cells were significantly increased in mice fed 12 months CD-HFD and treated with IgG as a control compared to α-PD-1 treated animals (**Figure 25j**). Consequently, I confirmed by manual gating a significant increase of TNF-a$^+$PD-1$^+$ CD8$^+$ T-cells upon α-PD-1 treatment (**Figure 25k, l**).

Of note, I did not observe an increase of TNF-a or PD-1 expression per CD8$^+$ T-cell in a mean fluorescence based analysis, comparing IgG control with α-PD-1 treated animals.

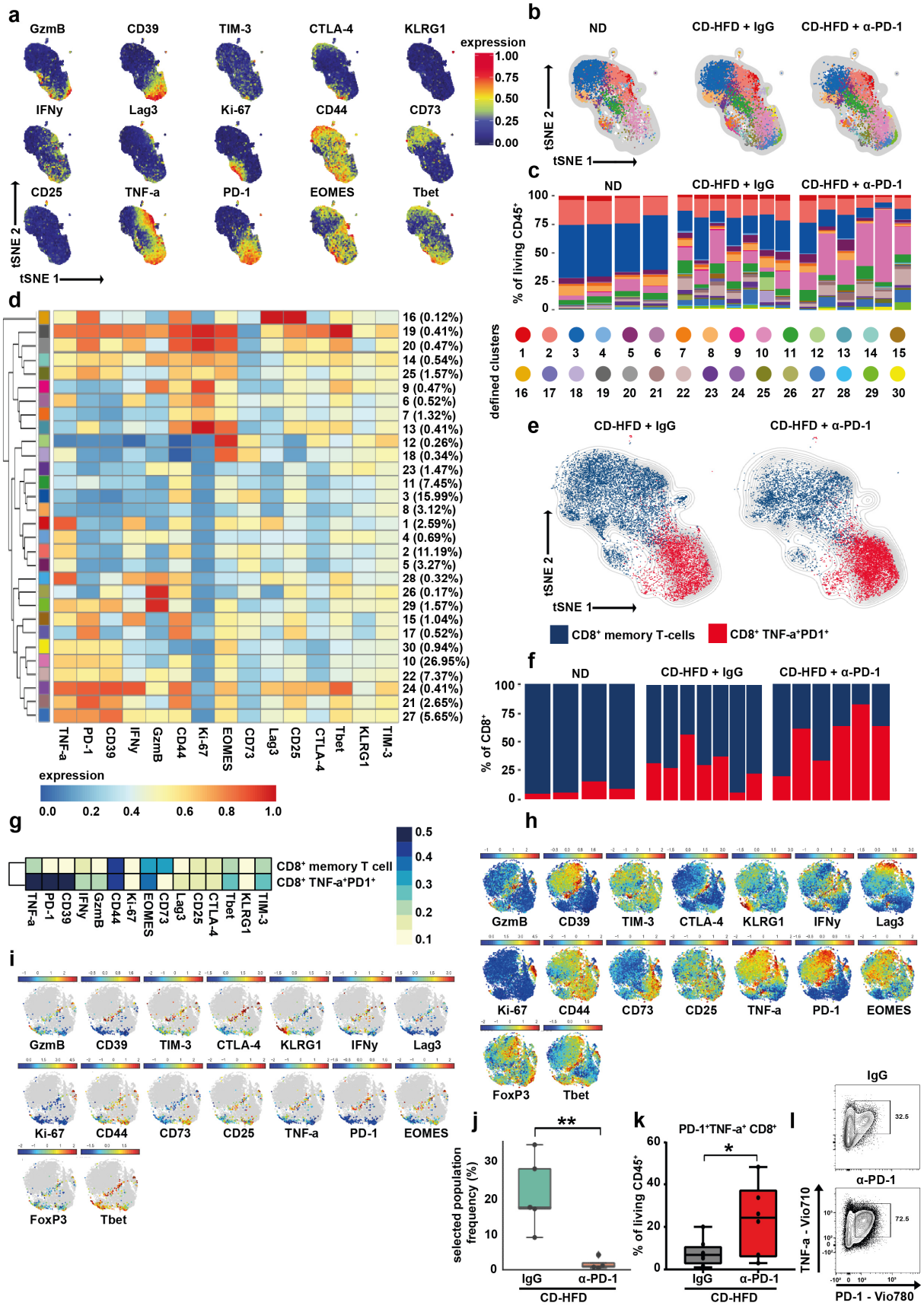

Figure 25: PD-1+TNF-a+ CD8 T-cells are potential disease-driving effector cells upon PD-1 checkpoint blockade in advanced NASH

(a) Unbiased analysis of 5000 randomly chosen TCRβ⁺ CD8⁺ cells of a 24 color flow cytometric analysis to define distinct marker expression of mice 12 months fed ND or CD-HFD with IgG, or α-CD8, or α-CD8/α-NK1.1 or α-PD-1 treatment for 8 weeks. (ND n= 4 mice; IgG + CD-HFD n= 7 mice; α-PD-1+ CD-HFD n= 6 mice; α-CD8 + CD-HFD

n= 7 mice; α-CD8/α-NK1.1 + CD-HFD n= 7 mice). (b) Flowsom generated tSNE plots and unbiased clustering for 30 clusters of 12 months fed ND or CD-HFD with IgG or α-PD-1 treatment for 8 weeks. (c) Phenotypic composition for the 30 clusters of individual mice defined in in b (ND n= 4 mice; IgG + CD-HFD n= 7 mice; α-PD-1+ CD-HFD n= 6 mice). (d) Heatmap of marker expression and abundance relative to living $CD45^+$ for the 30 clusters defined in b. (e) Flowsom generated tSNE plots for definition of $CD8^+$ cell compartments (memory T-cells and $TNF\text{-}a^+PD\text{-}1^+$) of 12 months fed CD-HFD with IgG or α-PD-1 treatment for 8 weeks. (f) Phenotypic composition of $CD8^+$ T-cells (ND n= 4 mice; IgG + CD-HFD n= 7 mice; α-PD-1+ CD-HFD n= 6 mice). (g) Heatmap of marker expression of $CD8^+$ T-cells defined in e. (h) An unbiased analysis: CellCNN analysis of marker expression represented in tSNE plots of $CD8^+$ T-cells of mice 12 months fed ND or CD-HFD with IgG, or α-CD8, or α-CD8/α-NK1.1 or α-PD-1 treatment for 8 weeks. (ND n= 4 mice; IgG + CD-HFD n= 7 mice; α-PD-1+ CD-HFD n= 6 mice; α-CD8 + CD-HFD n= 7 mice; α-CD8/α-NK1.1 + CD-HFD n= 7 mice). (i) CellCNN based analysis by tSNE of $CD8^+$ T-cells for population selected for markers associated with no or low activation. (j) Quantification of population represented in i (IgG + CD-HFD n= 5 mice; α-PD-1+ CD-HFD n= 4 mice). (j) Quantification by manual gaiting for $PD\text{-}1^+TNF\text{-}a^+$ $CD8^+$ T-cells population for confirmation of defined population in i(IgG + CD-HFD n= 8 mice; α-PD-1+ CD-HFD n= 6 mice). (l) Representative flow cytometric plots of populations quantified in k. All data are shown as mean ± SEM. All data were analyzed two-tailed Student T-test or Mann-Whitney. *p<0.05; **p<0.01; ***p<0.001; ****p<0.0001.

Thus, I concluded with three different approaches that hepatic irAEs in 12 month CDHFD treated with α-PD-1 are correlated with higher abundance and frequency of $TNF\text{-}a^+PD\text{-}1^+$ $CD8^+$ T-cells.

7.2 Aim 2: Platelet GPIbα is a mediator and potential interventional target for NASH and subsequent liver cancer

7.2.1 New targets for breaking through the cycle of chronic hepatic inflammation in NASH

After deciphering the role of T-cells in NASH and NASH induced hepatocarcinogenesis, I searched for an alternative way to target hepatic inflammation in NASH, without targeting potentially inflammation driving immune cell populations directly. Such an approach promised less adverse effects by not changing the immunological landscape drastically. Thus, it could unravel a more subtle manipulation of parameters responsible for NASH development, NASH pathology progression and subsequent tumor induction.

Platelets were described in the literature as potential mediators of adverse effects in chronic liver inflammation, mainly in the background of chronic virus associated inflammation[9,60–66]. Further, previous work of Mohsen Malehmir in the group of Mathias Heikenwälder demonstrated that hepatic platelet numbers, as well as platelet aggregates are increased in CD-HFD induced NASH compared to healthy controls fed a normal chow diet[59].

As a follow up to this study, I investigated whether increased hepatic platelet numbers and aggregates are a result of hepatic steatosis and insulin resistance, resembling non-alcoholic fatty liver disease (NAFLD), or if hepatic inflammation resembling non-alcoholic steatohepatitis (NASH) is a key mediator driving hepatic platelet accumulation.

To this end, I fed WT mice either NAFLD-inducing diets, HFD-45% or a HFD with low sugar (HFD-60% + LS), and compared them to WT animals fed a NASH-inducing diets - choline deficient high fat diet (CD-HFD) or western-style diet with trans fats (WD-HTF).

Adapted from my written and experimental contribution in Malehmir*, Pfister* et al.[9]: Wildtype (WT) mice fed for 6 months an NAFLD-inducing high fat diet (HFD-45%) developed macrovesicular steatosis by H&E and subsequently an increase in NAS, but no significant difference of hepatic platelet numbers (**Figure 26a, b**), despite significantly increased body weight compared to normal chow diet (ND) fed control mice (**Figure 26c**). To corroborate these results, I fed WT mice for 5 months a second NAFLD-inducing HFD with low sugar (HFD-60% + LS). These HFD-60% + LS fed mice developed macrovesicular steatosis by H&E, subsequently an increase in NAS, but again no significant difference of hepatic platelet numbers (**Figure 26d, e)**, despite significantly increased body weight and insulin resistance compared to ND fed control mice (**Figure 26f, g**). In contrast, WT mice fed 6 months an NASH-inducing CD-HFD developed histopathological features of NASH (macrovesicular steatosis, hepatic immune cell infiltration and hepatocytic damage), together with a significant increase of hepatic platelet numbers compared to ND fed mice (**Figure 26h, i**). Mice fed WD-HTF developed similar to CD-HFD fed mice a phenotype of NASH and hepatic platelet accumulation compared to ND fed mice (**Figure 26j, k**). Further, in collaboration with Marco Prinz from the Universitätsklinikum Freiburg using electron microscopy I could demonstrate that platelets found in CD-HFD liver have an activated phenotype (**Figure 26l)** (adapted from Malehmir*, Pfister* et al.[9]).

Thus, I concluded that increased hepatic platelet numbers and their activation status can only be found in livers of NASH-inducing diet-fed mice. Thus, antiplatelet treatment (APT) could be a therapeutic or interventional option for mice developing NASH.

7.2.2 Therapeutic use of antiplatelet treatments in established NASH

Mohsen Malehmir demonstrated that preventive use of APT like Aspirin-Clopidogrel (Asp-Clo), or Ticagrelor, but not the use of nonsteroidal anti-inflammatory drug (NSAID) Sulindac prevented NASH and subsequent HCC development[59]. Therefore, I investigated if not only the preventive but also the therapeutic use of APT in NASH could ameliorate NASH pathology.

Adapted from my written and experimental contribution in Malehmir*, Pfister* et al.[9]: Therefore, WT mice fed 4 months of NASH-inducing diet were administered the platelet-specific APT Ticagrelor with continuous NASH diet for 2 months (**Figure 27a**). WT mice fed for 6 months CD-HFD with 2 months of Ticagrelor treatment had reduced hepatic platelet numbers and ameliorated NASH pathology by H&E compared to untreated CD-HFD fed mice (**Figure 27b**).

Therapeutic Ticagrelor treated mice were metabolically equally impaired by IPGTT, but had reduced ALT levels compared to untreated CD-HFD fed mice (**Figure 27c**).

To corroborate these results, WT mice fed for 6 months WD-HTF with 2 months of Ticagrelor treatment also had reduced hepatic platelet numbers and a trend towards ameliorated NASH pathology by H&E compared to untreated WD-HTF fed mice (**Figure 27d**). Like CD-HFD fed mice, therapeutic Ticagrelor-treated WD-HTF fed mice were metabolically equally impaired by IPGTT but had reduced ALT levels compared to untreated WD-HTF fed mice (**Figure 27e**). In collaboration with Suchira Gallage, I investigated the effects of APT on fibrosis development. Therapeutic Ticagrelor-treated WD-HTF fed mice showed ameliorated fibrogenesis (**Figure 27f**) (adapted from Malehmir*, Pfister* et al.[9]).

Thus, I concluded that in established NASH pathology, APT using Ticagrelor can ameliorate NASH pathology or abrogate NASH progression in two murine models of NASH.

7.2.3 Platelets - more than a bystander in NASH development

Next, I investigated, when the platelets home to the liver upon NASH diet feeding and with which other cell type platelets co-localize indicating potential interaction with each other.

Adapted from my written and experimental contribution in Malehmir*, Pfister* et al.[9]: In collaboration with Moritz Peiseler, Bas Surewaard and Paul Kubes from the University of Calgary I performed intravital microscopy to track intrahepatic platelets live in living mice, in order to understand the dynamics of intrahepatic platelet recruitment and platelet-cell interaction during the initial events of NAFL preceding NASH. Intravital microscopy of WT mice fed CD-HFD for 4, 5, 6 or 8 weeks showed, that platelets home the liver at this early time points of diet feeding in a progressive manner (**Figure 28a, d**), with no significant increase of hepatic CD3+ T-cells at this early time points (**Figure 28b, c**). Additionally, sinusoidal diameter is decreased (**Figure 28e**) and in collaboration with Suchira Gallage I showed, that hepatocytes start to increase in size at this early time points of CD-HFD feeding (**Figure 28f**). Further, pathological features of NASH start to develop (**Figure 28g**) and I observed a trend for an increase of hepatic triglycerides in CD-HFD fed mice (**Figure 28h**).

I observed, in collaboration with Donato Inverso from the DKFZ Heidelberg using confocal microscopy, a significant increase of platelet aggregate size attached to Kupffer cell (KC) in established NASH (**Figure 28i**). Further, in collaboration with Moritz Peiseler, Bas Surewaard and Paul Kubes I found, that there is an induction of the extracellular matrix component hyaluronan colocalizing with hepatocytes, Kupffer cells and, to a lesser degree, on liver sinusoidal endothelial cells (LSECs) (**Figure 28j**) (adapted from Malehmir*, Pfister* et al.[9]).

Thus, I concluded, that platelets were the first non-resident cell type to home to the liver at earliest time points of borderline NASH development with sinusoidal diameter decrease and hepatocyte size increase. Further, my data indicated, that KCs and increased hyaluronan abundance may play key roles correlating with platelet attachment and recruitment in early phases NASH development[9].

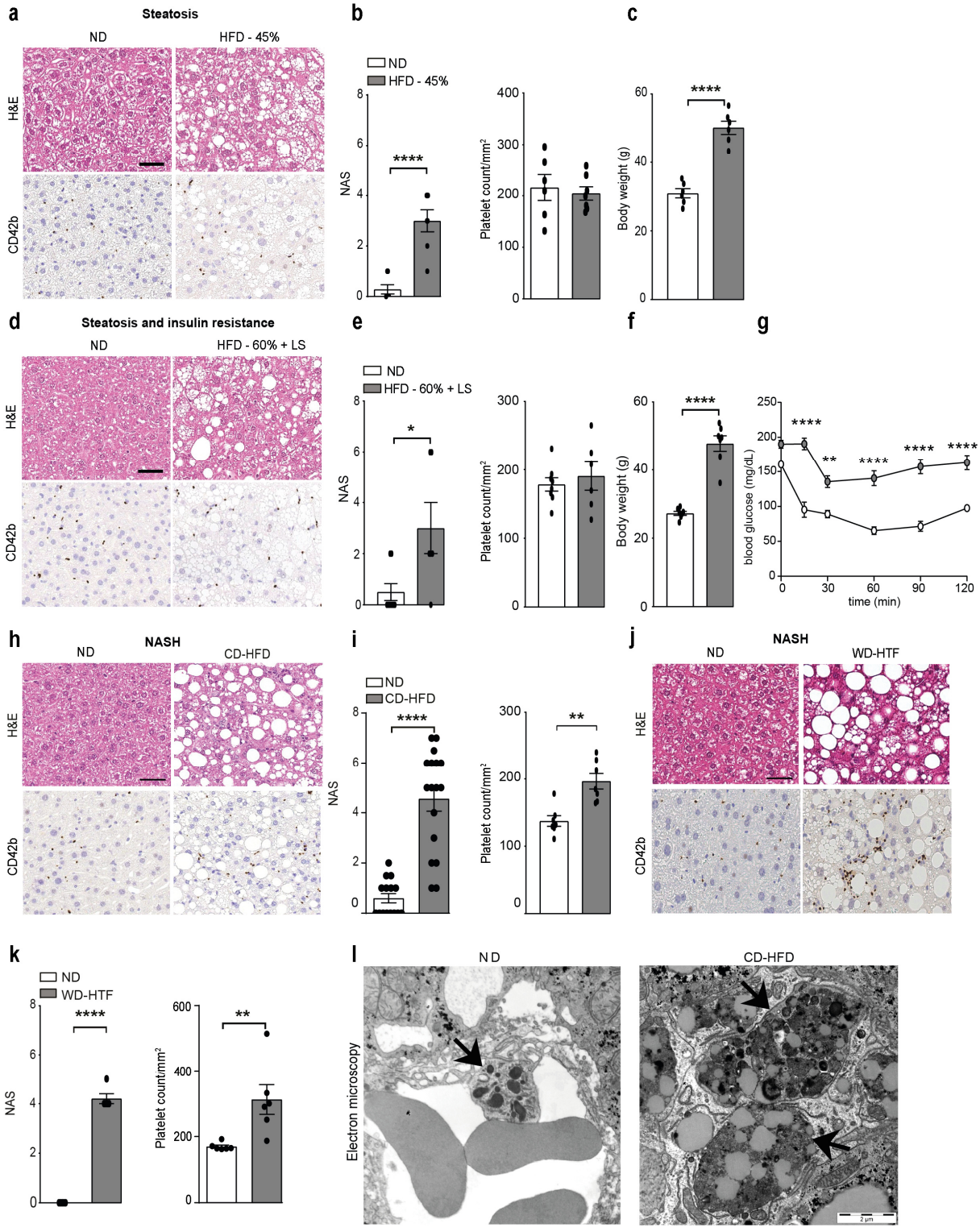

Figure 26: NASH diets induce hepatic platelet number and aggregation (adapted from Malehmir*, Pfister* et al.[9])

Adapted from my written contribution in Malehmir*, Pfister* et al.[9]: "(a) H&E, CD42b staining and (b) NAS evaluation and quantification of 6 months ND or HFD-45% fed mice (ND n= 6 mice; HFD-45% n= 7 mice). Scale bar: 50 µm. (c) Body weight (n= 6 mice/group) of mice shown in a. (d) H&E, CD42b staining and (e) NAS evaluation and quantification of 5 months ND or HFD-60%-fed (60% kcal and low sucrose (LS)) mice (ND n= 8 mice; HFD n= 6 mice). (f) Body weight of mice shown in d (n= 7 mice/group). (g) Insulin tolerance test of mice shown in d (ND n=6 mice; HFD-60%+LS n=7 mice). (h) H&E, CD42b staining and (i) NAS evaluation and quantification of 6 months ND or CD-HFD fed mice (NAS: ND n=15 mice; CD-HFD n=17 mice; CD42b: n= 7 mice/group). Scale bar: 50 µm. (j) H&E, CD42b staining and (k) NAS evaluation and quantification of 6 months ND or WD-HTF fed mice (NAS: n=5 mice/group; CD42b: n= 6 mice/group). Scale bar: 50 µm. (l) Representative electron microscopy images of activated platelets in livers from 6 months ND or CD-HFD fed mice. (ND, left panel) Platelet adhering to an endothelial cell showing an inactivated appearance of tubular system, alpha granules, dense bodies and glycogen. (CD-HFD, right panel) Platelets close to fatty hepatocytes outside the vessels, showing signs of activation (compact dense granulae, closed canalicular system, enlarged size) (n= 4 mice/group). All data are represented as mean ± SEM. Data were analyzed by two way ANOVA and Sidak`s multiple comparison test or two-tailed Student T test. *: $P < 0.05$. **: $P < 0.01$. ***: $P < 0.001$. ****: $P < 0.0001$"[9].

Although I did not find any increase of granulocytes or granulocyte-platelet interaction, literature indicated granulocytes as early responders of injury[78]. Therefore, in collaboration with Caroline L. Wilson, Jack Leslie and Derek A. Mann from Newcastle University I investigated the role of granulocytes using osmotic pumps for a constant depletion.

Adapted from my written and experimental contribution in Malehmir*, Pfister* et al.[9]: WT mice fed 4 weeks CD-HFD were put under granulocyte depleting conditions with continuous NASH diet for 8 weeks (**Figure 29a**). Despite the granulocyte depletion being successful (**Figure 29b**), no significant difference in body weight (**Figure 29c**), NASH pathology by H&E, hepatic platelet number (**Figure 29d, e**) or ALT levels was detected (**Figure 29f**) (adapted from Malehmir*, Pfister* et al.[9]).

Thus, I concluded, that granulocytes played not a significant role in the CD-HFD model for early development of NASH pathology and borderline NASH.

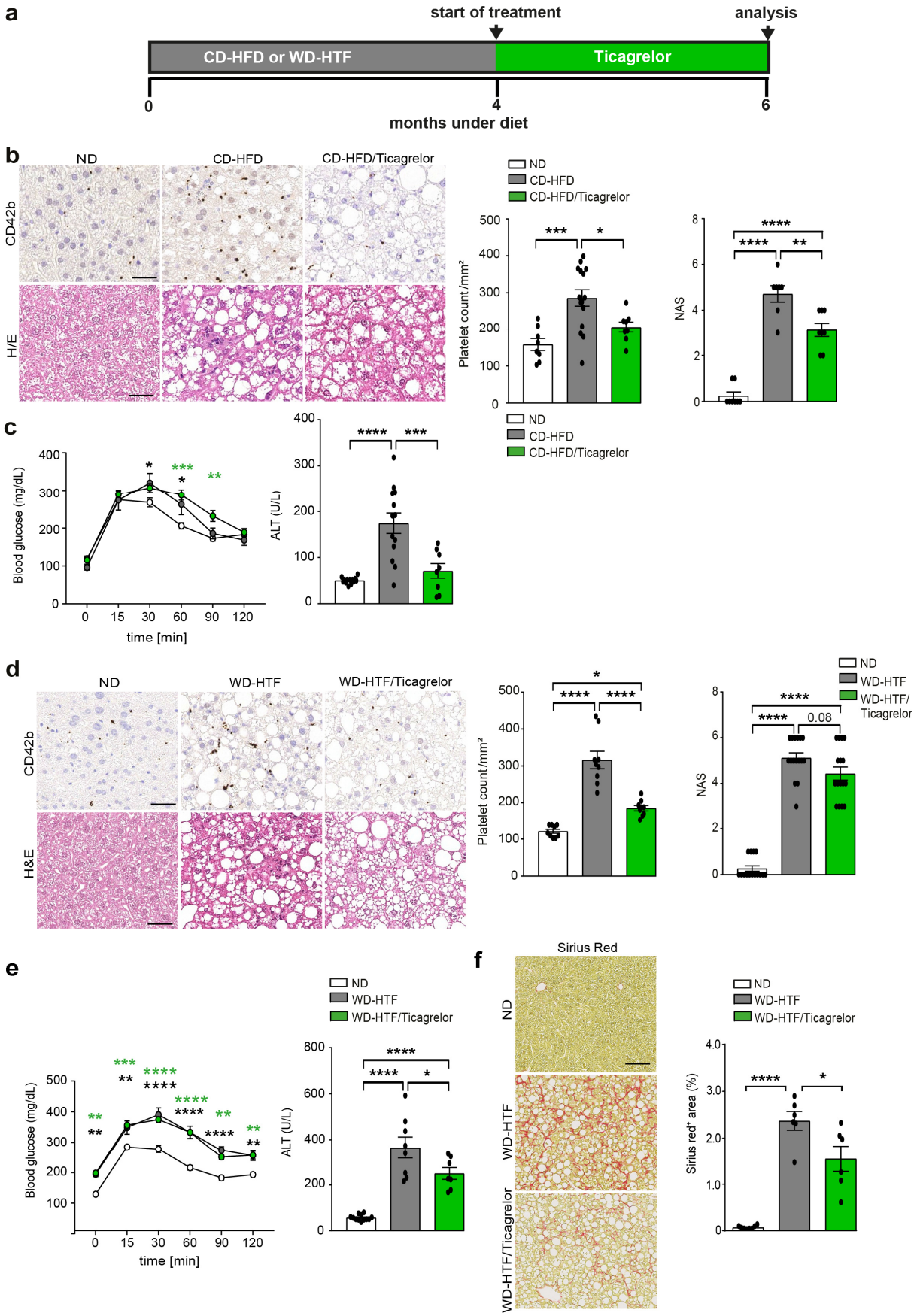

Figure 27: Therapeutic anti-platelet treatment with Ticagrelor ameliorates NASH progression (adapted from Malehmir*, Pfister* et al.[9])

Adapted from my written contribution in Malehmir*, Pfister* et al.[9]: "(a) Experimental setup for therapeutic anti-platelet treatments with Ticagrelor in 6 months ND, CD-HFD or WD-HTF fed mice. (b) H&E, CD42b staining and

(b) NAS evaluation and quantification of 6 months ND, CD-HFD or therapeutic CD-HFD/Ticagrelor fed mice (CD42b: ND n=8 mice; CD-HFD n=15 mice; CD-HFD/Ticagrelor n=8 mice; NAS: ND n=8 mice; CD-HFD n=7 mice; CD-HFD/Ticagrelor n=8 mice). Scale bar: 50 µm. (c) IPGTT and ALT from mice shown in b (IPGTT: ND n=8 mice; CD-HFD n=7 mice; CD-HFD/Ticagrelor n=8 mice; ALT: ND n=13 mice; CD-HFD n=13 mice; CD-HFD/Ticagrelor n=8 mice). Statistics: ND vs CD-HFD (black asterisks), ND vs therapeutic CD-HFD/Ticagrelor (green asterisks). (d) H&E, CD42b staining and (b) NAS evaluation and quantification of 6 months ND, WD-HTF or therapeutic WD-HTF/Ticagrelor fed mice (CD42b: n=9 mice/group; NAS: ND n=15 mice; WD-HTF n=16 mice; WD-HTF/Ticagrelor n=16 mice). Scale bar: 50 µm. (e) IPGTT and ALT from mice shown in d (IPGTT: n=8 mice/group; ALT: ND n=12 mice; WD-HTF n=8 mice; WD-HTF/Ticagrelor n=7 mice). Statistics: ND vs WD-HTF (black asterisks), ND vs therapeutic WD-HTF /Ticagrelor (green asterisks). (f) Sirius Red staining and quantification of mice shown in d (ND n=8 mice; WD-HTF n=6 mice; WD-HTF/Ticagrelor n=6 mice). Scale bar: 50 µm. All data are shown as mean ± SEM. Data were analyzed by one way or two way ANOVA with Tukey's or Sidak`s multiple comparison test.*: P < 0.05. **: P < 0.01. ***: P < 0.001. ****: P < 0.0001" [9].

7.2.4 Deciphering mechanisms of hepatic platelet homing in early NASH development

After exclusion of a role of granulocytes in early time points of NASH development, I focused on the functional role of platelet-KCs and platelet-hyaluronan interactions to decipher mechanisms leading to platelet attachment and recruitment in early phases NASH development.

Adapted from my written and experimental contribution in Malehmir*, Pfister* et al.[9]: WT mice fed 3.5 weeks CD-HFD were put under different treatment conditions with continuous CD-HFD diet for 2.5 weeks. Either I depleted KCs using clodronate liposome (CLL), I abrogated hyaluronan-platelet interaction using hyaluronidase (HYAL), or I treated with both together, CLL and HYAL. Further, hyaluronan can interact with CD44, which is highly expressed on platelets[66]. Thus, I investigated the role of CD44 binding using antibody mediated targeting of the CD44 binding sides, either with CD44/hyaluronan binding sides blocking (clone KM81) or non-blocking antibodies (clone IM7)[66] (**Figure 30a**).

In collaboration with Moritz Peiseler, Bas Surewaard and Paul Kubes from the University of Calgary I performed intravital microscopy to track the intrahepatic platelet response to the respective treatments. I successfully depleted KCs in mice treated with CLL (**Figure 30b, c**). 6 weeks CD-HFD-fed mice with 2.5 weeks of treatment of either CLL or HYAL showed reduced NAS (**Figure 30c**) and reduced intrahepatic platelet abundance compared to control CD-HFD fed mice (**Figure 30b, d**). Mice treated with HYAL, but not CLL, had reduced ALT levels compared to untreated CD-HFD fed mice (**Figure 30e**). Combined treatment of HYAL and CLL did not further reduce intrahepatic platelet numbers compared to single treatments (**Figure 30f, g**). Mice treated with α-CD44 binding/hyaluronan-blocking antibody (clone KM81), but not with α-CD44 binding/hyaluronan-non-blocking antibody (clone IM7) had reduced ALT levels (**Figure 30h**) and reduced NAS compared to untreated CD-HFD fed mice (**Figure 30i, j**).

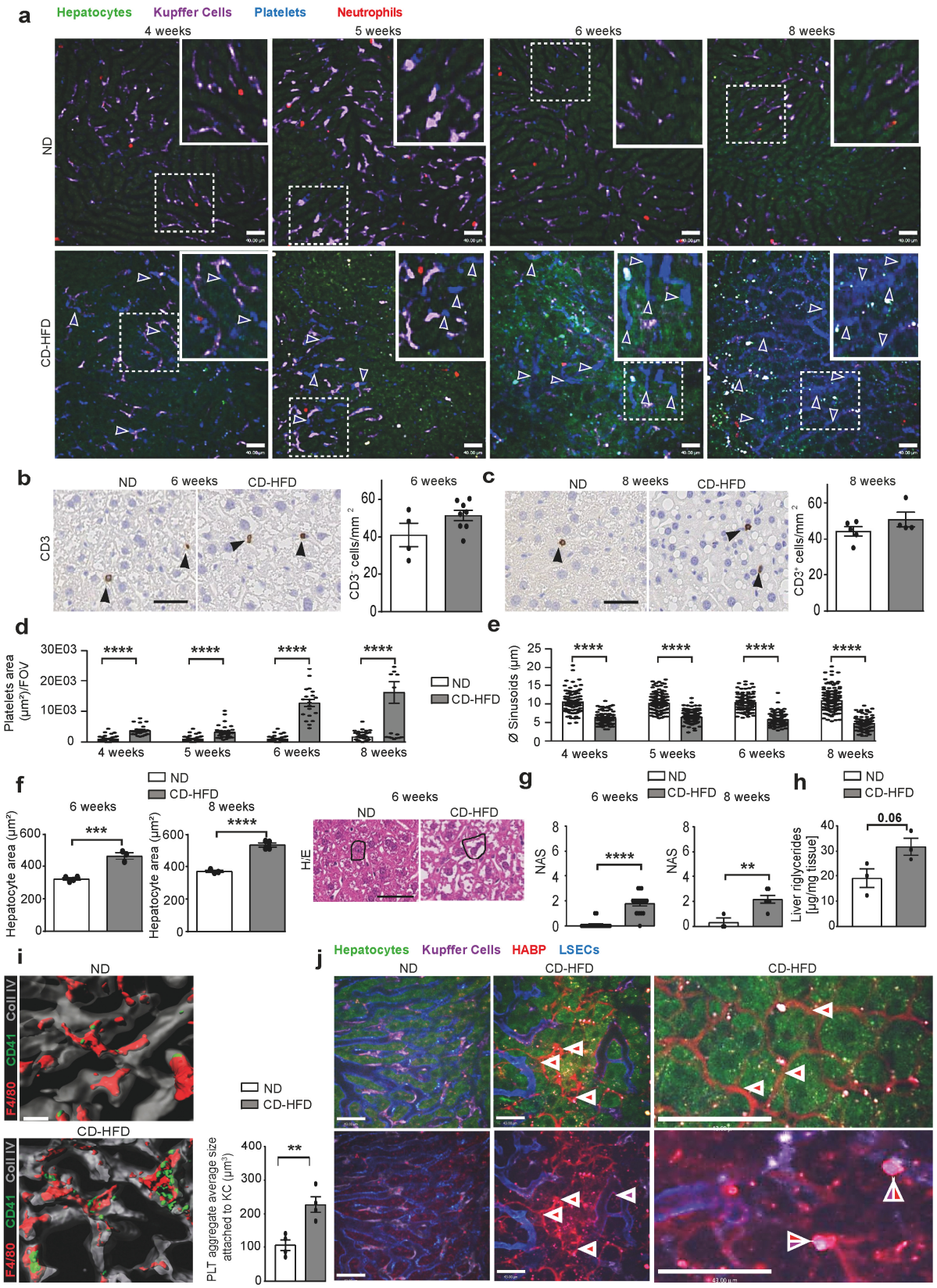

Figure 28: Platelets home to the liver in early phases of NASH pathogenesis (adapted from Malehmir*, Pfister* et al.[9])

Adapted from my written contribution in Malehmir*, Pfister* et al.[9]: "(a) Intravital microscopy of livers of 4, 5, 6 and 8 weeks ND or CD-HFD fed mice. Analysis of Kupffer cells (violet), platelets (blue) and granulocytes (red), (4 weeks: ND n= 2 mice; CD-HFD n= 2 mice; 5 weeks: ND n= 2 mice; CD-HFD n= 2 mice; 6 weeks: ND n= 4 mice; CD-HFD

n= 4 mice; 8 weeks: ND n= 3 mice; CD-HFD n= 3 mice). Scale bars: 40 µm. (b) CD3 staining and quantification of 6 weeks (ND n= 4 mice; CD-HFD n= 8 mice) or (c) 8-weeks ND or CD-HFD fed mice (ND n= 5 mice; CD-HFD n= 4 mice). Scale bar: 50 µm. (d) Quantification of platelet area by intravital microscopy of mice shown in a (ND: 4 weeks n= 2 mice and 40 FOV; 5 weeks n= 2 mice and 40 FOV; 6 weeks n= 4 mice and 40 FOV; 8 weeks n= 2 mice and 40 FOV; CD-HFD: 4 weeks n= 2 mice and 20 FOV; 5 weeks n= 2 mice and 20 FOV; 6 weeks n= 4 mice and 30 FOV; 8 weeks n= 2 mice and 19 FOV). (e) Analysis of liver sinusoid diameter by intravital microscopy of mice shown in a (ND: 4 weeks n= 2 mice and 101 sinusoids; 5 weeks n= 2 mice and 150 sinusoids; 6 weeks n= 4 mice and 100 sinusoids; 8 weeks n= 2 mice and 150 sinusoids; CD-HFD: 4 weeks n= 2 mice and 100 sinusoids; 5 weeks n= 2 mice and 150 sinusoids; 6 weeks n= 4 mice and 100 sinusoids; 8 weeks n= 2 mice and 100 sinusoids). (f) Hepatocyte swelling measurement by H&E of mice shown in b and c (6 weeks: ND n= 4 mice; CD-HFD n= 3 mice; 8 weeks: ND n= 3 mice; CD-HFD n= 4 mice). Scale bar: 50 µm. (g) NAS evaluation of 6 or 8 weeks ND- or CD-HFD fed mice (6 weeks: ND n= 19 mice; CD-HFD n= 18 mice; 8 weeks: ND n= 3 mice; CD-HFD n= 6 mice). (h) Liver triglycerides of 6 weeks ND or CD-HFD fed mice (n= 3 mice/group). (i) 3D confocal images and quantification of platelet (green)/Kupffer cells (red) interaction of 6 months ND or CD-HFD fed mice (n= 4 mice/group). Liver endothelium (gray). Scale bar: 20 µm. (j) Left, representative images of intravital microscopy of 6 weeks ND or CD-HFD fed mice. Right, representative high-magnification images of intravital microscopy. Analysis of Kupffer cells (violet, violet arrowhead), HABP (red, red arrowhead) and LSECs (blue) (ND n= 4 mice; CD-HFD n= 4 mice). Scale bar: 43 µm. All data are shown as mean ± SEM. All data were analyzed using two-tailed Student T test. *p<0.05; **p<0.01; ***p<0.001; ****p<0.0001"[9].

Further, in mice with established NASH fed 6 months CD-HFD a short treatment of CLL for 2.5 weeks led to a significant reduction of NAS and platelet accumulation (**Figure 30k, l**) (adapted from Malehmir*, Pfister* et al.[9]).

Thus, I concluded that KC, hyaluronan and CD44 are important players in the early and advanced stages of NASH development and NASH progression[9].

Adapted from my written and experimental contribution in Malehmir*, Pfister* et al.[9]: To corroborate my findings in the CD-HFD model with a second model of NASH, I fed WT mice 3.5 weeks WD-HTF and depleted KCs using CLL with continuous WD-HTF diet for 2.5 weeks (**Figure 31a**).

In collaboration with Moritz Peiseler, Bas Surewaard and Paul Kubes from the University of Calgary I performed intravital microscopy of 6 or 8 weeks ND or WD-HTF fed mice (**Figure 31b**). I corroborated my results from the CD-HFD model with respect to increased and progressive hepatic platelet abundance (**Figure 31b, c**) in borderline NASH by H&E (**Figure 31d, e**) and increased hepatic liver triglycerides (**Figure 31f**) in 6 or 8 weeks WD-HTF fed mice compared to ND fed mice (adapted from Malehmir*, Pfister* et al.[9]).

Thus, I concluded that similar to the CD-HFD model, platelets were the first non-resident cell type to home to the liver at earliest time points of borderline NASH in the WD-HTF model. Further, my data indicated that KCs may play key roles correlating with platelet attachment and recruitment in early phases NASH development in the WD-HTF model[9].

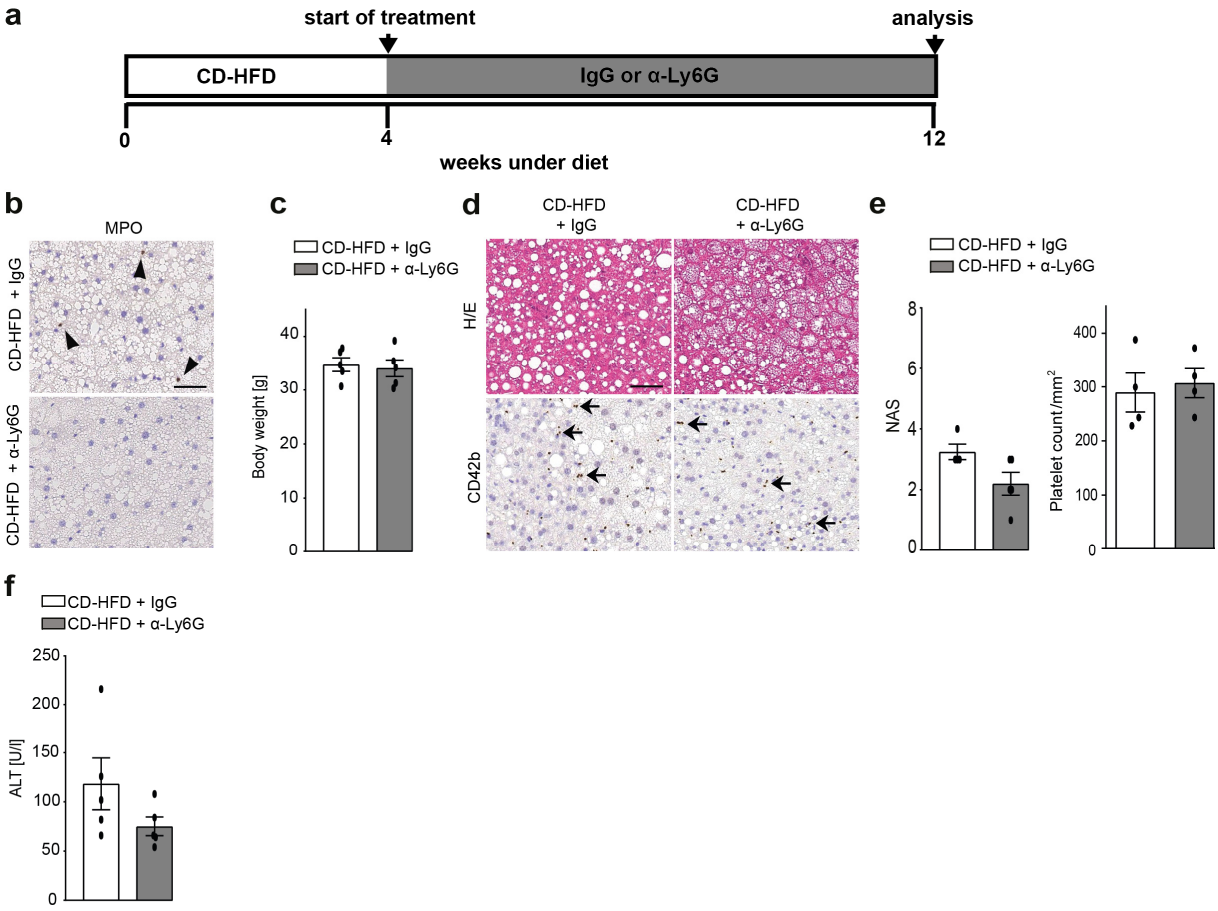

Figure 29: Granulocyte abundance does not delay NASH development (adapted from Malehmir*, Pfister* et al.[9])

Adapted from my written contribution in Malehmir*, Pfister* et al.[9]: "(a) Experimental setup for α-Ly6G depletion in 12 weeks ND or CD-HFD fed mice. (b) Myeloperoxidase (MPO) of 12 weeks CD-HFD + IgG or CD-HFD + α-Ly6G fed mice (n=4 mice/group). Scale bar: 50 µm. (c) Body weight, (d) H&E, CD42b staining, (e) NAS evaluation and quantification and (f) ALT of mice shown in b (body weight and ALT: n=5 mice/group; CD42b: CD-HFD + IgG n=4 mice, CD-HFD + α-Ly6G n=4 mice; NAS: CD-HFD +IgG n=4 mice, CD- HFD +α-Ly6G n=5 mice). Scale bar: 50 µm. All data are shown as mean ± SEM and were analyzed using two-tailed Student T test. *p<0.05; **p<0.01; ***p<0.001; ****p<0.0001"[9].

7.2.4 GPIbα – an interventional target on platelets for amelioration of NASH pathology and NASH induced hepatocarcigonesis

Adapted from my written and experimental contribution in Malehmir*, Pfister* et al.[9]: My data indicated that intrahepatic interaction of platelets with KCs, involving hyaluronan/CD44 binding, contributed to NASH development and progression. Further, previous work of Mohsen Malehmir from the group of Mathias Heikenwälder demonstrated by using different genetic mouse model under CD-HFD, that platelet cargo (Nbeal2$^{-/-}$) but not platelet aggregation (Itga2b$^{-/-}$), nor specific platelet activation (GPVI$^{-/-}$) is important to abrogate or ameliorate NASH pathology[59].

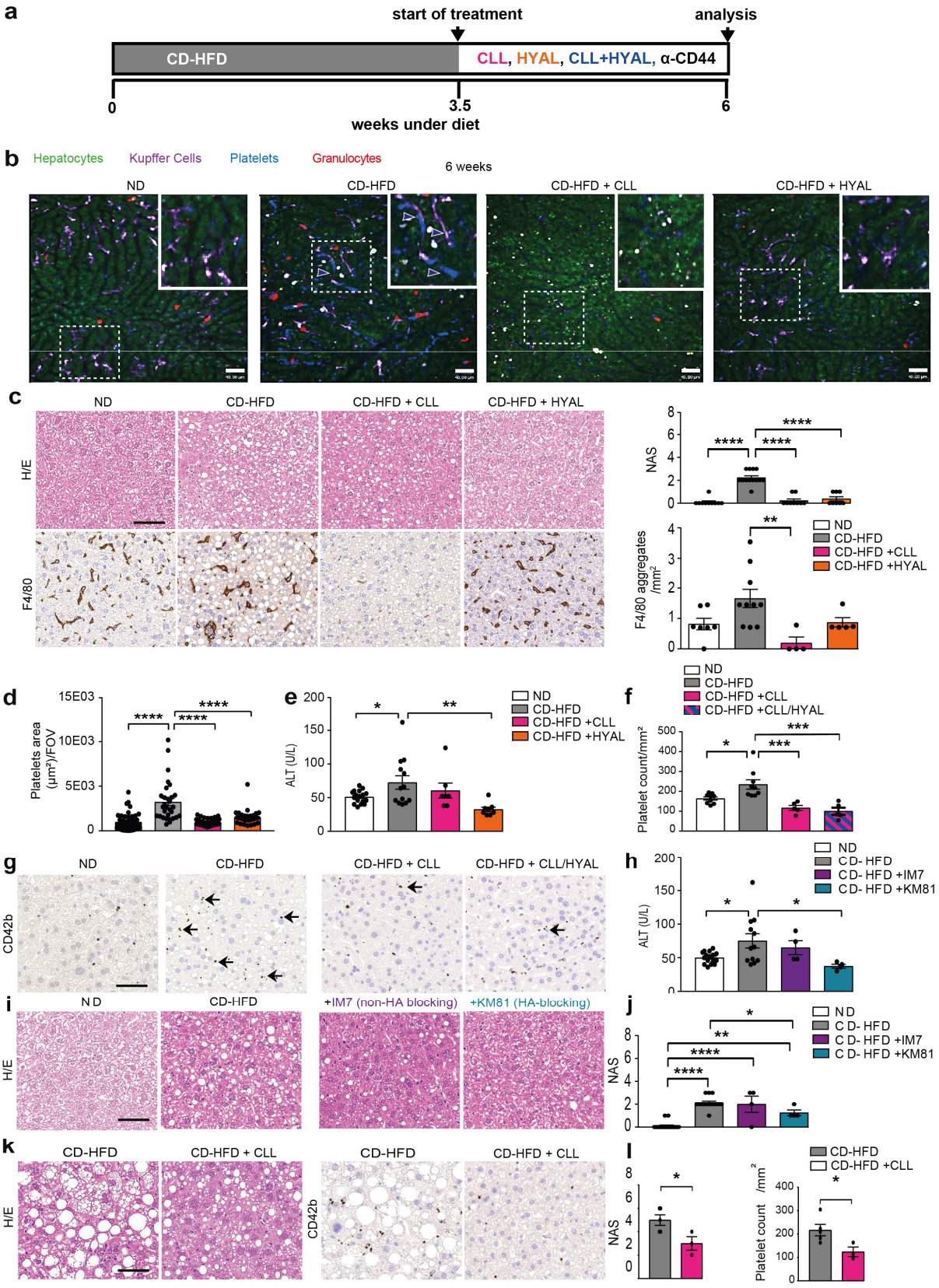

Figure 30: Intrahepatic platelet accumulation depends on Kupffer cells and CD44-hyaluronan interaction in early phases of NASH pathogenesis (adapted from Malehmir*, Pfister* et al.[9])

Adapted from my written contribution in Malehmir*, Pfister* et al.[9]: "(a) Experimental setup for various treatments (clodronate liposome (CLL), hyaluronidase (HYAL) or both (HYAL+CLL), or α-CD44 antibodies) in 6 weeks ND or CD-HFD. (b) Representative images of intravital microscopy after treatment (CLL or HYAL) of 6 weeks ND, CD-HFD, CD-HFD + CLL or CD-HFD + HYAL fed mice. Analysis of Kupffer cells (violet), platelets (blue, blue arrowhead)

and granulocytes (red) (n= 4 mice/group). Scale bar: 40 µm. (c) H&E and F4/80 staining with quantification and NAS evaluation of 6 week ND, CD-HFD, CD-HFD + CLL or CD-HFD + HYAL fed mice (H&E: ND n= 10 mice; CD-HFD n= 14 mice; CD-HFD + CLL n= 9 mice; CD-HFD + HYAL n= 8 mice; F4/80: ND n= 7 mice; CD-HFD n= 10 mice; CD-HFD + CLL n= 4 mice; CD-HFD + HYAL n= 5 mice). Scale bar: 50 µm. (d) Quantification of platelet area by intravital microscopy of mice shown in b (ND n= 4 mice and 40 FOV; CD-HFD n= 4 mice and 30 FOV; CD-HFD + CLL n= 4 mice and 40 FOV; CD-HFD + HYAL n= 4 mice and 30 FOV). (e) ALT levels of mice shown in b (ND n= 17 mice; CD-HFD n= 13; CD-HFD + CLL n= 7 mice; CD-HFD + HYAL n= 8 mice). (f) CD42b quantification and (g) CD42b staining of 6 weeks ND, CD-HFD, CD-HFD + CLL or CD-HFD + CLL/HYAL fed mice (ND n=9 mice, CD-HFD n=9, CD-HFD+CLL and CD-HFD+CLL/HYAL n=5 mice/group). Scale bar: 50 µm. (h) ALT, (i) H&E and (j) NAS evaluation after anti-CD44 antibody treatment (anti-CD44 antibody blocking (KM81) or non-blocking (IM7) HA-binding site) in 6 weeks ND, CD-HFD, CD- HFD + IM7 (non-HA blocking) or CD-HFD + KM81 (HA-blocking) fed mice (ALT: ND n= 16 mice; CD-HFD n= 12 mice; CD-HFD + IM7 n= 4 mice; CD- HFD + KM81 n= 4 mice; NAS: ND n= 19 mice; CD-HFD n= 15 mice; CD-HFD + IM7 n= 4 mice; CD-HFD + KM81 n= 4 mice). Scale bar: 50 µm. (k) H&E, CD42b staining and (l) NAS evaluation and quantification after CLL treatment in 6-months CD-HFD or CD-HFD + CLL fed mice (NAS: CD-HFD n= 5 mice; CD-HFD + CLL n= 3 mice; CD42b: CD-HFD n= 5 mice; CD-HFD + CLL n= 3). Scale bars: 50 µm. All data are shown as mean ± SEM. All data were analyzed using one way ANOVA with Tukey's multiple comparison test or two-tailed Student T test.*: P < 0.05. **: P < 0.01. ***: P < 0.001. ****: P < 0.0001"[9].

However, Mohsen Malehmir`s work and literature indicated that GPIbα on platelets is important for platelet attachment, as well as activation and thus potentially for NASH development[59,60].

Therefore, in collaboration with Donato Inverso from the DKFZ, Heidelberg, using confocal microscopy I showed that in 6 months CD-HFD fed mice increased amounts of GPIbα$^+$ platelets colocalized with KCs and decreased amounts of GPIbα$^+$ platelets with LSECs compared to ND fed mice (**Figure 32a, b**). Therefore, I treated 6 months CD-HFD fed mice with established NASH therapeutically using GPIbα blocking Fab fragments for 5 weeks. After 5 weeks of GPIbα blocking treatment with continuous CD-HFD diet, the mice had ameliorated NASH pathology by H&E, reduced intrahepatic platelet numbers (**Figure 32c**), less liver damage (**Figure 32d**) and reduced hepatic liver triglycerides (**Figure 32e**). Further, in collaboration with Suchira Gallage I observed a trend for ameliorated fibrosis (**Figure 32f, g**). Of note, in anti-GPIbα-treated mice, intrahepatic CD3 T-cell and KCs levels remained unchanged (**Figure 32h, i**).

Next, in collaboration with Moritz Peiseler, Bas Surewaard and Paul Kubes from the University of Calgary I tested whether blocking GPIbα in early NASH development would have an effect. Thus, mice fed 6 weeks CD-HFD with 2.5 weeks of GPIbα blocking antibody were analyzed by intravital microscopy. However, no differences in intrahepatic platelet abundance could be observed (**Figure 32j**).

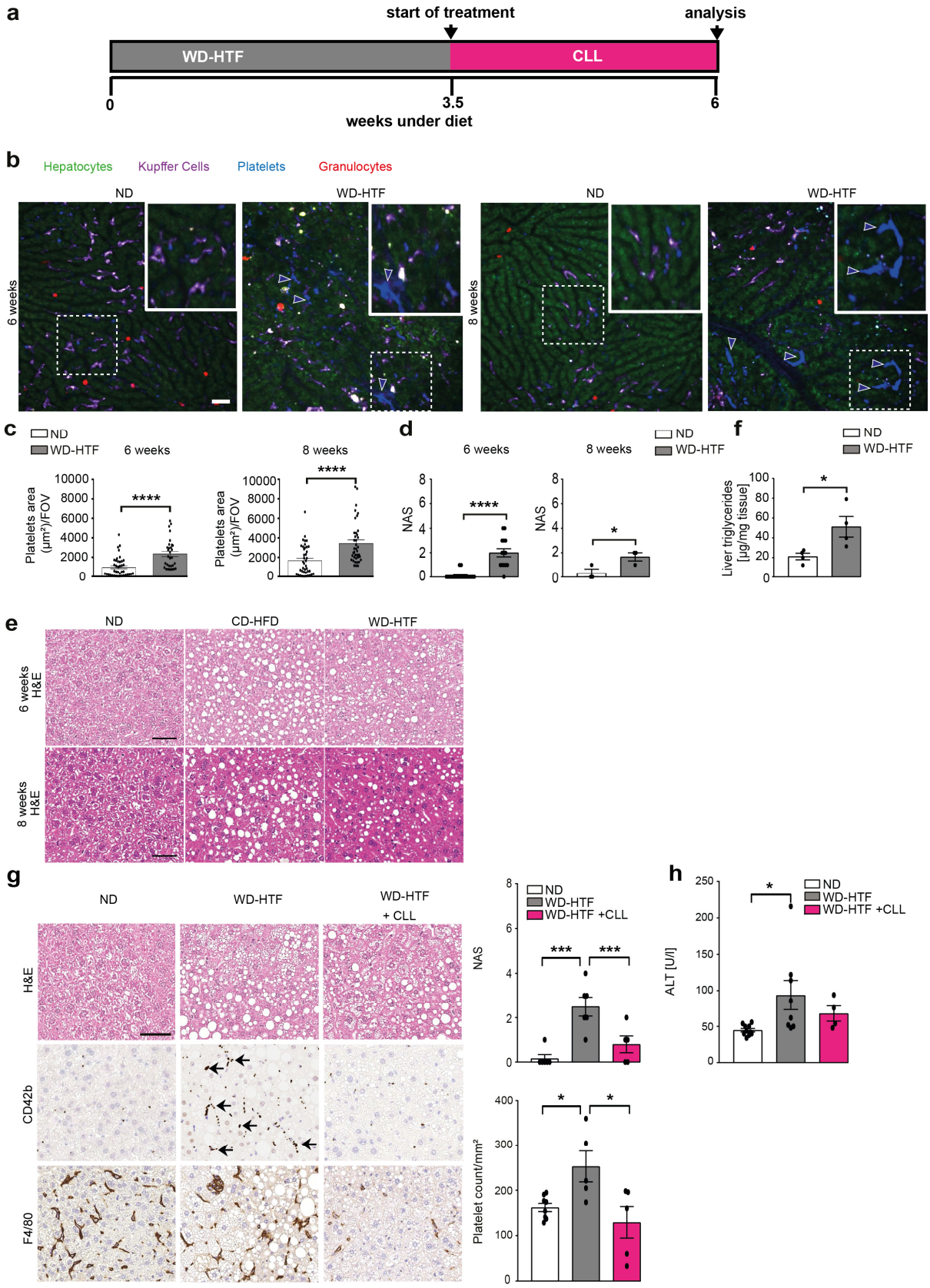

Figure 31: Corroboration of platelet phenotype with a second model of NASH diet (adapted from Malehmir*, Pfister* et al.[9])

Adapted from my written contribution in Malehmir*, Pfister* et al.[9]: "(a) Experimental setup for CLL treatment in 6 weeks ND or WD-HTF fed mice. (b) Intravital microscopy of livers of 6 and 8 weeks ND or WD-HTF fed mice. Analysis of Kupffer cells (violet), platelets (blue) and granulocytes (red) (n=4 mice/group), scale bar: 40 µm. (c) Quantification of platelet area by intravital microscopy of mice shown in b (n=4 mice/group). (d) NAS evaluation by

(e) H&E staining of mice shown in b (6 weeks: ND n=19 mice, WD-HTF n=10 mice; 8 weeks: n=3 mice/group). (f) Liver triglycerides of 6 weeks fed ND or WD-HTF mice (n=4 mice/group). (g) H&E, CD42b, F4/80 staining, quantification and NAS evaluation (NAS: ND n=6 mice, WD-HTF n=5 mice/group; WD-HTF + CLL n=5 mice/group; CD42b: ND n=10 mice, WD-HTF n=5 mice/group; WD-HTF + CLL n=5 mice/group) and (h) ALT levels in 6 weeks fed ND or WD-HTF mice (ND n=10 mice, WD-HTF, n=8 mice WD-HTF+CLL n=4 mice). Scale bar: 50 µm. All data are shown as mean ± SEM. Data were analyzed using two-tailed Student T test or one way ANOVA with Tukey`s multiple comparison test. *p<0.05; **p<0.01; ***p<0.001; ****p<0.0001"[9].

Previous work by Mohsen Malehmir from the group of Mathias Heikenwälder demonstrated that mice with a ligand-binding ectodomain of GPIbα replacement by the α-subunit of the human IL-4 receptor (hIL4rα/GPIbα-Tg)[79] were protected from NASH pathology upon 6 months of CD-HFD feeding[9,59]. As a follow up, I investigated whether hIL4rα/GPIbα-Tg, despite being protected from NASH after 6 months of CD-HFD feeding, would develop tumors after 12 months of CD-HFD feeding. 12 months CD-HFD fed hIL4rα/GPIbα-Tg mice had reduced liver damage (**Figure 32k**) and no macroscopic (**Figure 32l**) or microscopic tumor development (**Figure 32m**), resulting to a significantly reduced tumor burden compared to CD-HFD fed WT mice (**Figure 32n**) (adapted from Malehmir*, Pfister* et al.[9]).

Thus, I concluded that GPIbα on platelet is a mediator of platelet-KC interaction, a potential interventional target for NASH by Fab-mediated GPIbα blocking and therefore a potential target reducing NASH induced hepatocarcinogenesis.

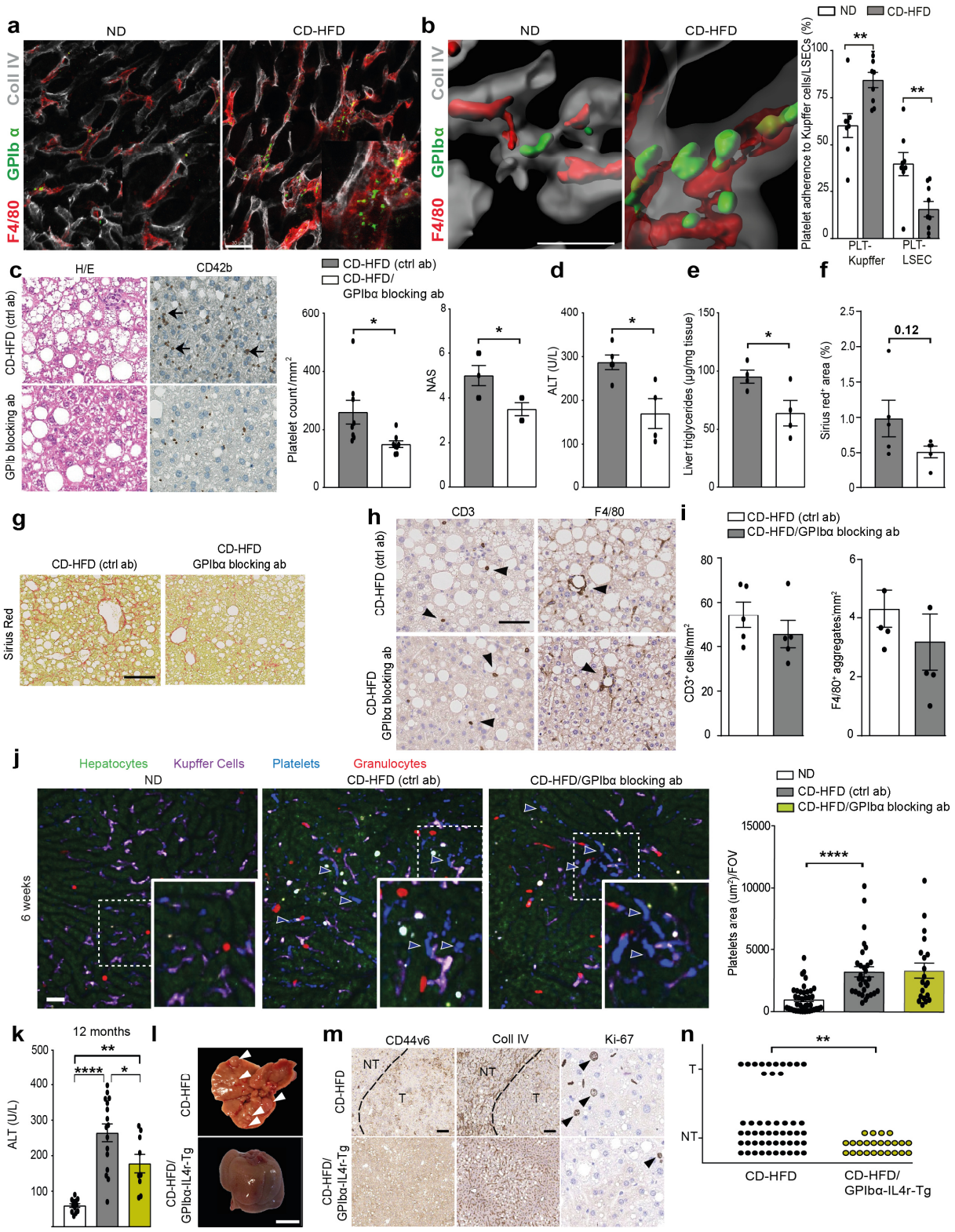

Figure 32: Antibody mediated blockade of GPIbα ameliorates established NASH pathology, but not NASH development and dysfunctional GPIbα abrogates hepatocarcinogenesis (adapted from Malehmir*, Pfister* et al.[9])

Adapted from my written contribution in Malehmir*, Pfister* et al.[9]: "(a) 3D confocal images of GPIbα (green) and Kupffer cells (red) interaction of 6 months ND or CD-HFD fed mice (n= 4 mice/group). Liver endothelium (gray). Scale bar: 30 µm. (b) High-magnification 3D confocal images and quantification of GPIbα (green)/Kupffer cells (red) and GPIbα (green)/LSECs (gray) interaction in 6 months ND or CD-HFD fed mice (ND n= 4 mice and 2 FOV/mouse; CD-HFD n= 4 mice and 2 FOV/mouse). Scale bar: 3 µm. For visualization of intravascular events, the transparency of the sinusoidal rendering was set to 50%. (c) H&E, CD42b staining, NAS evaluation and quantification after 5

weeks of GPIbα blocking or control antibody (ab) in 6 months CD-HFD fed mice (CD42b: CD-HFD + control ab n= 8 mice; CD-HFD + GPIbα blocking ab n= 8 mice; NAS: CD-HFD + control ab n= 5 mice; CD-HFD + GPIbα blocking ab n= 4 mice) Scale bar: 50 µm. Platelet aggregates are indicated by arrows. (d) ALT, (e) liver triglycerides, (f) quantification of (g) Sirius red–positive areas of mice shown in c (ALT: CD-HFD + control ab n= 5 mice; CD-HFD + GPIbα blocking ab n= 4 mice; liver triglycerides: CD-HFD + control ab n= 4 mice; CD-HFD + GPIbα blocking ab n= 4 mice; Sirius red: CD-HFD + control ab n= 5 mice; CD-HFD + GPIbα blocking ab n= 4 mice). Scale bar: 50 µm. (h) CD3, F4/80 staining and (i) quantification of mice shown in c (n= 5 mice/group). Scale bar: 50 µm. (j) Intravital microscopy of Kupffer cells (violet), granulocytes (red), platelets (blue) and quantification of platelet area per FOV of livers of 2.5 weeks treatment in 6 weeks ND, CD-HFD + ctrl ab or CD-HFD +GPIbα blocking antibody fed mice (FOV n=5 fields/mouse, ND n= 8 mice, CD-HFD n= 6 mice, CD-HFD + GPIbα blocking antibody n= 4 mice), scale bar: 40 µm. (k) ALT of 12 months ND, CD-HFD or CD-HFD/hIL4rα/GPIbα-Tg mice (ND n= 12 mice; CD-HFD n= 16 mice; CD-HFD/hIL4rα/GPIbα-Tg n= 9 mice). (l) Macroscopical images of tumors of mice shown in k; tumor nodules are indicated by arrowhead) (CD-HFD: n= 13 tumors in 52 mice; CD-HFD/hIL4rα/GPIbα-Tg: n= 0 tumors in 24 mice). Scale bar: 750 µm. (m) Tumor characterization by CD44v6, Collagen IV (Coll IV) and Ki67 staining of mice shown in k. Arrowheads indicate positive hepatocytes, dashed line indicates tumor (T) border. Scale bar: 200 µm (CD44v6 and Coll IV), 50 µm (Ki67). (n) Tumor incidence (T = tumor; NT = non-tumor) of 12 months CD-HFD-fed or CD-HFD/hIL4rα/GPIbα-Tg mice (CD-HFD: n= 13 tumors in 52 mice; CD-HFD/hIL4rα/GPIbα-Tg: n= 0 tumors in 24 mice). All data are shown as mean ± SEM. Data were analyzed using two-tailed Student T test, one way ANOVA with Tukey`s multiple comparison test or Fisher's exact test. *$p < 0.05$, **$p < 0.01$, ***$p < 0.001$ and ****$p < 0.0001$"[9].

8 Discussion

8.1 Aim 1: Deciphering TCR signaling in metabolically activated T-cells in NASH and liver cancer development

In the frame of this PhD thesis, I report several findings that help decipher the role of TCR-dependent cell-mediated mechanisms driving liver pathogenesis in metabolic disease, NAFLD, NASH and dietary-induced tumor burden.

I identified that only NASH-inducing CD-HFD, but not NAFLD-inducing HFD, led to liver damage in systemically obese mice, which correlated with an increase of activated and memory $CD8^+$ T-cells positive for IFNy and PD-1 - an effect, which increased over time and thus correlated with progression of disease. Further, these effects were corroborated using a second model of mouse NASH, WD-HTF. Over the past decade, a variety of metabolic disease models recapitulating to different degrees NAFLD or NASH with or without tumor induction have been published[40]. In line with recent models of not only NAFLD but NASH, I could identify a hepatic T-cell phenotype in the CD-HFD model, as well as a WD-HTF-based model[6,31,33,46,47,51]. Unfortunately, relating these results to two relatively recent publications is difficult, because the studies utilizing the genetic model of c-myc overexpression plus methionine-choline deficient diet (MCD), as well as a genetic model with inducible human URI reported data focused on intrahepatic $CD4^+$ T-cells, without considering in depth the potential role of the CD8 compartment[31,46]. Of note, the role of the $CD4^+$ compartment is important, especially differential polarization of these cells, like the Th17 compartment, as well as the selective loss of regulatory $CD4^+$ T-cells in driving pathologies resembling NASH[80]. Nevertheless, in a model of hepatocellular damage combined with HFD and DEN injection, Shalapour et al. reported comparable results to my observed phenotypes of hepatic immune cell abundance and density, CD45 polarization, activation and effector molecule expression in the $CD8^+$ T-cell compartment[51]. Further, studies in patients have linked inflamed livers with increased peripheral $IFNy^+$ $CD8^+$ T-cells, as well as higher hepatic infiltration and increased production of IFNy by these cells in NASH[81,82]. In addition, obesity was linked with PD-1 expressing $CD8^+$ T-cells in mice, macaques and human[83].

Next, I found, that progression of NASH disease is correlated with differential TCR vβ hepatic expression in PD-1^+CD8 T-cells, as well as a dependency for NASH development on a natural TCR repertoire and a functional TCR effector function, but not NKT type I or type II cells.

Studies about hepatic TCR repertoires are scarce, with most of the studies focusing on adipose tissue T-cells. In these studies, activated $CD8^+$ T-cells together with reduced regulatory T-cells contribute to inflammatory macrophage influx, insulin resistance and glucose intolerance in

models of NAFLD[84–86]. However, similar to my results showing that the hepatic TCR repertoire of the whole population of hepatic $CD4^+$ and $CD8^+$ T-cells between ND and CD-HFD is not changed, a study by McDonnell et al. reported no significant change of hepatic CD8+ T-cell clonality by deep sequencing of the TCRβ chains in an NAFLD model[87]. However, referring to the differences I observed in my comparison between NAFLD- and NASH-inducing diets (e.g. activation and expression of exhaustion marker of $CD8^+$ T-cells, increased ALT levels), the inflammatory part in the liver is strongly reduced or might not be present in these models of NAFLD. Other NASH studies in the context of tumor development need to be scrutinized, because they might overlook TCR repertoire changes induced by NASH pathology, due to potential strong reactions against tumor-associated antigens that might mask NASH-associated TCR repertoires. Future single-cell RNA sequencing-based approaches combined with flow cytometric analysis could pave the way for a more in-depth understanding of NASH-induced TCR repertoire changes. To the best of my knowledge, no study has thus far reported TCR repertoires which could explain my observed changes of the hepatic PD-1^+ expressing T-cells, which could drive liver inflammation in a oligo-clonal manner in the context of progressing NASH pathology.

In line with my results that there is a need for functional TCRs for NASH development, as well as a natural TCR repertoire, studies addressed NAFLD or NASH development in TCR-deficient mice (e.g. Rag-$1^{-/-}$, nude mice, $\beta2m^{-/-}$) and concluded that there was a lack of hepatic fat deposition, as well as, depending on the study, glucose intolerance[6,88]. Further, an impaired CD8 compartment led to decreased liver damage in an HFD ischemia reperfusion model[89]. These data indicate a mostly TCRαβ dependency for NASH development; however, the exact role of TCRγδ is so far not well-characterized and should be characterized in greater detail[90,91]. The use of single knockouts for TCRβ and TCRδ under NASH-inducing diets could shed new light on this issue.

Additionally, active and functional TCR effector function is important for driving NASH pathology, either directly by TCR MHC interaction or by similar mechanisms. Mauro et al. reported a mechanism of PI3K activation of $CD4^+$ T-cells by palmitate on the background of a HFD, which could potentially activate $CD8^+$ T-cells in a similar fashion[92]. In contrast to Revelo et al. using Prf$1^{-/-}$ under HFD and therefore NAFLD conditions, Prf$1^{-/-}$ under long-term CD-HFD performed significantly better in glucose tolerance test and had ameliorated liver pathology[93]. However, lack of perforin in my hands could only delay but not abrogate NASH pathology and subsequent tumor development, shedding new light on the role of perforin dependency in NASH. Potentially, secondary mechanisms besides T-cell activation may drive liver disease progression. In line, the study of Revelo et al. reported higher levels of IFNy-producing $CD8^+$ T-cells in adipose tissue in Prf$1^{-/-}$ mice, leading to higher fat tissue inflammation, adipose tissue fibrosis and a potential feedback loop to the liver, inducing steatosis and insulin resistance[94].

Another potential side effect of using global perforin knockout mice is a reduction of perforin-positive dendritic cells, a regulatory DC compartment associated with protection from metabolic syndrome and autoimmunity[95]. To this end, the use of specifically TCR signaling impaired mice (e.g. conditional SLP76 knockout) or mice with perforin knockouts in specific cell types, rather than the whole-body TCR effector impaired Prf1$^{-/-}$ could shed new light on the specific TCR dependency in NASH development. One remaining question is still unanswered. What activates the T-cells in the first place, and is it antigen-dependent (e.g. classical versus non-classical antigen presentation) or antigen-independent (e.g. metabolic or cytokine microenvironment)?

NKT cells are widely accepted to play an important role in energy, adipose tissue homeostasis and liver homeostasis, although their precise role in an organ-related context is highly variable[6,36,96–98]. Further, NKT cells could play an important role in my Prf1$^{-/-}$ CD-HFD mice. However, I could only observe an increased glucose tolerance after 6 months of CD-HFD feeding, indicating a potential role of NKT cells in adipose tissue. In line, Lynch et al. reported that activation of adipose-resident NKT cells increased, in an FGF21-dependent manner, thermogenesis by browning of white adipose tissue[96]. One of my most robust findings is that no matter which animal model was put under NASH-inducing dietary conditions, after developing NASH, the NKT type I to type II ratio was always shifted to more type II NKT cells. This indicates that, on the one hand, there could be a selective loss of NKT type I[99], which could potentially on its own lead to hepatic steatosis and insulin resistance[100]. On the other hand, I observed an increase in type II NKT cells, which could be either driving the pathology or promoting hepatocarcinogenesis by promoting a Th2-polarized hepatic environment. Nevertheless, the role of NKT type I and type II could not be conclusively deciphered in the frame of this thesis - also with respect to the newly described innate lymphoid cells. One potential approach to define the role of NKT cells in NASH further could be either the activation of the NKT compartment by a-Gal treatment or a genetic increase of this compartment using CD4-Cre Vα14i$^{StopF/wt}$ [101]. However, the majority of non-significant differences between Jα18$^{-/-}$ or CD1d$^{-/-}$ with their respective control mice under CD-HFD, indicated a minor contribution of these cells in the investigated time points of NASH and advanced NASH states in the used NASH mouse model[98,102].

Thus, I focused on CD8-mediated mechanism in early NAFLD to NASH progression, as well as advanced NASH stages by antibody-mediated CD8 depletion and PD-1 blocking experiments. I reported a contribution of CD8$^+$ and PD-1-expressing cells depending on NASH pathology progression. When CD8$^+$ T-cells get depleted in established NASH, two studies report beneficial effects by reduced ALT, reduced liver triglycerides, reduced mRNA levels α-smooth muscle actin and collagen type 1 expression, as well as improved NAS[6,33]. Therefore, there are strong indications, that adaptive immune cells, especially CD8$^+$ T-cells in concert with

NKT, drive NAFLD development and NASH progression[103]. However, my CD8 depletion data from 4 to 6 months before manifestation of NASH, indicated, that probably subsets of the IFNy$^+$CD8$^+$ T-cells have not only a damage driving, but a protective role as well. Ablation of CD8$^+$ T-cells in the genetic MUP-uPA and the MCD mouse model indicated an anti-fibrotic role of CD8$^+$ correlating with IFNy levels as well[35]. Further, unpublished data from my collaborator indicated increased ALT because of CD8 depletion, too. If this increased damage upon CD8 depletion is a result of hepatic or peripheral mechanisms (e.g. adipose tissue inflammation, or loss of CD8$^+$ T-cell dependent intestinal barrier integrity[104,105]), remains up to date illusive.

However, upon CD8 depletion in advanced stages of NASH, I see less tumor burden, indicating CD8$^+$ T-cells drive liver pathology after NASH is established, similar to reports of Wolf et al. and Bhattacharjee et al., which both identified CD8$^+$ T-cells as drivers of liver damage[6,33]. To date, I have not identified a clear mechanism, by which ALT as a marker of liver damage is elevated in my CD8-depleted animals. I did not observe compensatory effects in the innate immune system, CD4$^+$ T-cell, NK or NKT compartment by flow cytometric phenotyping. In addition, double depletion of NK1.1 and CD8 T-cells did not result in lower liver damage or reduced NASH pathology, indicating a more complex driver of hepatic damage in advanced NASH. Potential mechanism could be increased levels of TNF-a[37], IL-1β[106], IL-6[107], IL-17[46] or metabolite-mediated lipotoxicity[31]. Further, potential dual roles of cytokines as either tumor-counteracting or tumor-promoting need to be analysed, for example IL-12, IFNy, high levels of GzmB, lymphotoxin α and β, as well as molecules of the M2 polarization like IL-10 and TGF-β[3]. Hepatocyte-intrinsic metabolic toxicity, ER stress and reactive oxygen species could also be responsible for the elevated ALT levels upon CD8 depletion in advanced NASH.

Nevertheless, when increasing the activity of PD-1-expressing cells in advanced NASH by clinically used doses of α-PD-1 blockade[108], I observed a significant increase in liver damage, liver pathology and tumor/nodule/lesion formation. Similar to my CD8 depletion experiments, the mechanisms promoting the observed liver damage and subsequent tumor/nodule/lesion formation have thus far been elusive. Similar to the CD8 depletion experiments, I observed no significant changes of damage-promoting or activation-associated mechanisms in the CD4$^+$ T-cell, NK or NKT compartment by flow cytometric phenotyping. This indicated α-PD-1-reactive CD8$^+$ T-cells and cells of the innate immune system are the main drivers of liver damage upon checkpoint inhibition. However, in-depth histopathological evaluation of the immune-related adverse events (irAEs) upon α-PD-1 treatment combined with in-depth characterization of the immune compartment by single cell RNA sequencing approaches could help to decipher my observed irAEs in more detail.

So far, the application of checkpoint inhibitiors (clinically used α-PD-1 inhibitors Nivolumab and Pembrolizumab) in hepatocellular carcinoma has been considered safe in clinical phase I/II[109] and II[110] studies. However, in general, 1-4% of patients receiving Nivolumab as anti-cancer

therapy developed hepatitis[111]. With the increasing number of studies using next generation checkpoint inhibitors (e.g. 34 studies with Nivolumab and status “active” or “recruiting”[112]; or 29 studies with Pembrolizumab and status “active” or “recruiting”[113]), it is of great importance for clinical management to understand the checkpoint inhibition-induced hepatotoxicity and irAEs[114–116]. For example, a study of mainly melanoma patients treated with Nivolumab (α-PD-1) or Ipilimumab (α-CTLA-4) reported irAEs by comparing checkpoint inhibitor induced hepatitis with drug-induced or autoimmune hepatitis[117]. Zen et al. reported that, as a result of checkpoint inhibitor treatment, higher numbers of liver-infiltrating $CD8^+$ T-cell were found without markers of classical autoimmune hepatitis, like zonal necrosis, anti-nuclear antibodies and elevated IgG levels[117]. However, irAEs can be even more severe. For example, a case study of a hepatitis virus-negative patient with advanced HCC plus bilateral pulmonary metastases who was unresponsive to first-line treatment with Sorafenib demonstrated that administration of Pembrolizumab led to acute liver failure and subsequent death[118].

As a consequence, in clinical practice, corticosteroids are recommended for treatment of irAEs induced by checkpoint inhibition[114]. However prolonged or high-dose corticosteroid therapy is known to induce hepatic steatosis, increased ALT and a liver pathology similar to NASH[119]. Thus, corticosteroid therapy for irAEs resulting from checkpoint inhibition as treatment of NASH-induced tumors could be detrimental[120]. Postow and Wolchok suggest TNF-a inhibitor Infliximab as a potential management option for irAEs in patients without elevated ALT levels[114]. TNF-a inhibiting agents like Infliximab have, on the one hand, been reported to cause hepatotoxicity and worsening of autoimmune-modulatory phenotypes[121] and, on the other hand, also to reduce steatosis and increase insulin signal transduction in animal models[122]. My CD8 depletion data implicating CD8 T-cells as the main drivers of disease with subsequent tumor development. Further, my unbiased analysis of our flow cytometric data set in which I in collaboration with Nicholas Nunez identified significantly enriched hepatic $PD\text{-}1^+TNF\text{-}a^+$ $CD8^+$ T-cells indicate that TNF-a inhibitors, like Infliximab, could potentially help to reduce irAEs upon checkpoint inhibition in the case of an underlying chronic liver diseases.

8.2 Aim 2: Platelet GPIbα is a mediator and potential interventional target for NASH and subsequent liver cancer

Adapted from my written and experimental contribution in Malehmir*, Pfister* et al.[9]: Further, in the frame of this PhD thesis, I report several findings that help to target or intervene with hepatic inflammation in NASH in an alternative way, without targeting potentially inflammation-driving immune cell populations like the hepatic $PD\text{-}1^+TNF\text{-}a^+$ $CD8^+$ T-cells described above. Platelets have been identified as a crucial factor mediating cytotoxic T-cell responses in virus-

induced liver inflammation, highlighting a potential direct interaction of platelet-CD8$^+$ T-cells in NASH development, NASH progression and NASH-induced hepatocarcinogenesis[64–66].

My data indicated that increased hepatic platelet numbers and aggregates and enhanced platelet activation are distinct features not of long-term HFD feeding-inducing NAFLD, but of long-term feeding of NASH-inducing diets like CD-HFD and WD-HTF. This finding was corroborated in mice with using different western-style diets (WD-non trans fats, or WD with fructose-supplemented drinking water), MCD, genetic models (hURI-tetOFF combined with HFD) but also in human patients[9]. Further, my data indicated that platelets in NASH diseased mice are activated and that manipulation of this platelet activation using Ticagrelor as APT is ameliorating or abrogating the progression of NASH pathology. Interestingly, fibrosis, which is detrimental for HCC induction, was also reduced upon therapeutic APT using the reversible $P2Y_{12}$ antagonists Ticagrelor[9]. Other groups using virus-associated hepatitis models report beneficial effects (e.g. prolonged survival) of APT, as well[67].

To understand the dynamics of intrahepatic platelet recruitment and attachment during the initial events of NASH development, I in collaboration with Moritz Peiseler, Bas Surewaard and Paul Kubes showed that platelets indeed home to the liver at the earliest time points of borderline NASH development[9]. Potential mechanisms could be increased physical and therefore potential receptor ligand interaction of platelets with other cell types in the blood flow. In collaboration with Suchira Gallage I showed an increase of hepatocyte size, decreased sinusoidal diameter and thus a potential local increase of blood flow pressure, potentially leading to a local environment of blood flow similar to arterial thrombosis in the background of atherosclerotic plaques[123]. However, my data indicated that there are specific platelet-KC interactions that lead to platelet attachment, recruitment and abundance in early phases of NASH development, as well as in NASH progression[9]. Further, my data indicated that there are specific platelet-CD44-hyaluronan-dependent mechanisms that lead to platelet attachment and recruitment in early phases NASH development[9]. Guidotti et al. reported similar findings on the importance of the CD44-hyaluronan axis for platelet adherence to the sinusoids in order to mediate docking of circulating CD8$^+$ T-cells in a model of HBV[66]. Although granulocytes are reported as being a cell type that homes to damaged tissue, mediating early inflammation[78], as well as interacting with the CD44-hyaluronan axis[124], I in collaboration with Caroline L. Wilson, Jack Leslie and Derek A. Mann could not observe significant effects on NASH development and NASH progression after 2 months of granulocyte depletion. Thus, granulocytes may play a minor role in the CD-HFD NASH mouse model. Thus, my data shed new light on intrahepatic platelet recruitment and attachment during the initial events of NASH development.

However, patients with established NASH with the risk of hepatocarcinogenesis are seen in the clinics; therefore, there is a great demand for targeting platelets with alternative strategies

besides APT, for example, with new druggable targets, which allow modifying platelet functions in a specific manner. Based on previous work[59], I could strengthen the hypothesis that GPIbα on platelets is important for platelet attachment, as well as platelet activation in NASH development, potentially in a platelet-KC-dependent manner. Langer et al. described a similar inflammation-promoting role of GPIbα in experimental autoimmune encephalomyelitis (EAE), in which platelet-derived, GPIbα mediated recruitment of immune cells to the inflamed central nervous system[9,125]. My data indicated in a genetic model that dysfunctional GPIbα correlated with NASH prevention[59] and therefore the livers lacked the pro-carcinogenic NASH-related environment in hIL4rα/GP1bα-Tg mice[59], which subsequently led to abrogated NASH-induced hepatocarcinogenesis[9]. Further, I could show, that therapeutic Fab-mediated blocking of GPIbα ameliorates NASH pathology and dampening fibrosis, highlighting the translational role of GPIbα as a potential interventional druggable target in NASH[9,59,60]. Of note, for clinical applications one has to consider that although the GPIbα receptor is left intact, interfering with platelet activation by antibody-mediated GPIbα blocking induces prolonged bleeding times in mice, but no spontaneous bleeding[9,126]. In conclusion, due to the lack of effective and safe treatment options targeting NASH specifically (e.g. Insulin-sensitizer pioglitazone, obeticholic acid or vitamin E), antibody-mediated GPIbα blocking could be a potentially safe new treatment against a metabolic disease like NASH, potentially in a combinatorial approach with additional anti-inflammatory or anti-fibrotic drugs[9,127,128].

As a result, my data presented in aim 2 (“Platelet GPIbα is a mediator and potential interventional target for NASH and subsequent liver cancer”) in the frame of this PhD thesis contributed significantly to a Nature Medicine publication, in which the role of APTs, KCs, platelet-related mechanisms and potential ligands of GPIbα (P-selectin, VWF and Mac-1) are investigated[9].

9 References

1. Singal, A. G. & El-Serag, H. B. Hepatocellular Carcinoma From Epidemiology to Prevention: Translating Knowledge into Practice. *Clin. Gastroenterol. Hepatol.* **13,** 2140–2151 (2015).
2. Margini, C. & Dufour, J. F. The story of HCC in NAFLD: From epidemiology, across pathogenesis, to prevention and treatment. *Liver Int.* **36,** 317–324 (2016).
3. Ringelhan, M., Pfister, D., O'Connor, T., Pikarsky, E. & Heikenwalder, M. The immunology of hepatocellular carcinoma. *Nat. Immunol.* **19,** (2018).
4. Michelotti, G. a, Machado, M. V & Diehl, A. M. NAFLD, NASH and liver cancer. *Nat. Rev. Gastroenterol. Hepatol.* **10,** 656–65 (2013).
5. Llovet, J. M., Villanueva, A., Lachenmayer, A. & Finn, R. S. Advances in targeted therapies for hepatocellular carcinoma in the genomic era. *Nat. Rev. Clin. Oncol.* **12,** 408–24 (2015).
6. Wolf, M. J. *et al.* Metabolic activation of intrahepatic CD8+ T cells and NKT cells causes nonalcoholic steatohepatitis and liver cancer via cross-talk with hepatocytes. *Cancer Cell* **26,** 549–64 (2014).
7. Nault, J.-C. The end of almost 10 years of negative RCTs in advanced hepatocellular carcinoma. *Lancet* **389,** 4–6 (2016).
8. Bruix, J. *et al.* Regorafenib for patients with hepatocellular carcinoma who progressed on sorafenib treatment (RESORCE): a randomised, double-blind, placebo-controlled, phase 3 trial. *Lancet* **389,** 56–66 (2016).
9. Malehmir, M. *et al.* Platelet GPIbα is a mediator and potential interventional target for NASH and subsequent liver cancer. *Nat. Med.* **25,** 641–655 (2019).
10. Arun J. Sanyal, Thomas D. Boyer, Norah A Terrault, K. D. L. *Zakim and Boyer's Hepatology*. (Elsevier, 2017).
11. Michalopoulos, G. K. & DeFrances, M. C. Liver Regeneration. *Science (80-.).* **276,** 60–66 (1997).
12. Ozakyol, A. Global Epidemiology of Hepatocellular Carcinoma (HCC Epidemiology). *J. Gastrointest. Cancer* **48,** 238–240 (2017).
13. Sun, B. & Karin, M. Obesity, inflammation, and liver cancer. *J. Hepatol.* **56,** 704–13 (2012).
14. El-Serag, H. B. Hepatocellular carcinoma. *Lancet* **380,** 469 (2012).

15. Harding, J. J., El Dika, I. & Abou-Alfa, G. K. Immunotherapy in hepatocellular carcinoma: Primed to make a difference? *Cancer* **122,** (2016).

16. Endig, J. *et al.* Dual Role of the Adaptive Immune System in Liver Injury and Hepatocellular Carcinoma Development. *Cancer Cell* 1–16 (2016). doi:10.1016/j.ccell.2016.06.009

17. Lees, C. W., Barrett, J. C., Parkes, M. & Satsangi, J. New IBD genetics: common pathways with other diseases. *Gut* **60,** 1739–1753 (2011).

18. Vernon, G., Baranova, a. & Younossi, Z. M. Systematic review: The epidemiology and natural history of non-alcoholic fatty liver disease and non-alcoholic steatohepatitis in adults. *Aliment. Pharmacol. Ther.* **34,** 274–285 (2011).

19. White, D. L., Kanwal, F. & El-Serag, H. B. Association Between Nonalcoholic Fatty Liver Disease and Risk for Hepatocellular Cancer, Based on Systematic Review. *Clin. Gastroenterol. Hepatol.* **10,** 1342–1359.e2 (2012).

20. Calle, E. E. & Kaaks, R. Overweight, obesity and cancer: epidemiological evidence and proposed mechanisms. *Nat. Rev. Cancer* **4,** 579–591 (2004).

21. Park, E. J. *et al.* Dietary and genetic obesity promote liver inflammation and tumorigenesis by enhancing IL-6 and TNF expression Eek. *Cell* **140,** 197–208 (2011).

22. Younes, R. & Bugianesi, E. A spotlight on pathogenesis, interactions and novel therapeutic options in NAFLD. *Nat. Rev. Gastroenterol. Hepatol.* **16,** 80–82 (2018).

23. Williams, R. *et al.* Addressing liver disease in the UK: A blueprint for attaining excellence in health care and reducing premature mortality from lifestyle issues of excess consumption of alcohol, obesity, and viral hepatitis. *Lancet* **384,** 1953–1997 (2014).

24. Jemal, A. *et al.* Global cancer statistics. *CA Cancer J Clin* **61,** 1,33-64 (2011).

25. Younossi, Z. *et al.* Global burden of NAFLD and NASH: trends, predictions, risk factors and prevention. *Nat. Rev. Gastroenterol. Hepatol.* **15,** 11–20 (2018).

26. Wattacheril, J., Issa, D. & Sanyal, A. Nonalcoholic Steatohepatitis (NASH) and Hepatic Fibrosis: Emerging Therapies. *Annu. Rev. Pharmacol. Toxicol. Vol 58* **58,** 649–662 (2018).

27. Perumpail, B. J. *et al.* Clinical epidemiology and disease burden of nonalcoholic fatty liver disease. *World J. Gastroenterol.* **23,** 8263–8276 (2017).

28. Loomba, R. & Sanyal, A. J. The global NAFLD epidemic. *Nat. Rev. Gastroenterol. Hepatol.* **10,** 686–690 (2013).

29. Ganz, M. & Szabo, G. Immune and inflammatory pathways in NASH. *Hepatol. Int.* **7**

Suppl 2, 771–81 (2013).

30. Magee, N., Zou, A. & Zhang, Y. Pathogenesis of Nonalcoholic Steatohepatitis: Interactions between Liver Parenchymal and Nonparenchymal Cells. *Biomed Res. Int.* **2016,** (2016).

31. Ma, C. *et al.* NAFLD causes selective CD4+ T lymphocyte loss and promotes hepatocarcinogenesis. *Nature* **531,** 253–257 (2016).

32. Kang, T.-W. *et al.* Senescence surveillance of pre-malignant hepatocytes limits liver cancer development. *Nature* **479,** 547–551 (2011).

33. Bhattacharjee, J. *et al.* Hepatic Natural Killer T-cell and CD8+ T-cell Signatures in Mice with Nonalcoholic Steatohepatitis. *Hepatol. Commun.* **1,** 299–310 (2017).

34. Liang, Q. *et al.* Intrahepatic T-Cell Receptor β Immune Repertoire Is Essential for Liver Regeneration. *Hepatology* **68,** 1977–1990 (2018).

35. Shalapour, S. *et al.* Inflammation-induced IgA + cells dismantle anti-liver cancer immunity. *Nat. Publ. Gr.* **551,** 340–345 (2017).

36. Michelet, X. *et al.* Metabolic reprogramming of natural killer cells in obesity limits antitumor responses. *Nat. Immunol.* **19,** 1330–1340 (2018).

37. Nakagawa, H. *et al.* ER Stress Cooperates with Hypernutrition to Trigger TNF-Dependent Spontaneous HCC Development. *Cancer Cell* **26,** 331–343 (2014).

38. Farrell, G. *et al.* Mouse models of nonalcoholic steatohepatitis Towards optimization of their relevance to human NASH. *Hepatology* **2,** 0–2 (2018).

39. Lau, J. K. C., Zhang, X. & Yu, J. Animal models of non-alcoholic fatty liver disease: current perspectives and recent advances. *J. Pathol.* **241,** 36–44 (2017).

40. Nakagawa, H. Recent advances in mouse models of obesityand nonalcoholic steatohepatitis-associated hepatocarcinogenesis. *World J. Hepatol.* **7,** 2110–2118 (2015).

41. Dannenberg, A. J. & Berger, N. A. *Obesity, Inflammation and Cancer*. (Springer-Verlag, 2013). doi:10.1007/978-1-4614-6819-6

42. Anstee, Q. M., Reeves, H. L., Kotsiliti, E., Govaere, O. & Heikenwalder, M. From NASH to HCC: Current concepts, future challenges. *Nat Rev Gastroenterol Hepatol* **acc. 04/19,** (2019).

43. Domitrović, R., Jakovac, H., Tomac, J. & Šain, I. Liver fibrosis in mice induced by carbon tetrachloride and its reversion by luteolin. *Toxicol. Appl. Pharmacol.* **241,** 311–321 (2009).

44. Thompson, K. J. *et al.* Obesity, but not ethanol, promotes tumor incidence and progression in a mouse model of hepatocellular carcinoma in vivo. *Surg. Endosc.* **27,** 2782–2791 (2013).

45. Friedman, J. M. & Halaas, J. L. Leptin and the regulation of body weight in mammals. *Nature* **395,** 763–770 (1998).

46. Gomes, A. L. *et al.* Metabolic Inflammation-Associated IL-17A Causes Non-alcoholic Steatohepatitis and Hepatocellular Carcinoma. *Cancer Cell* **30,** 161–175 (2016).

47. Clapper, J. R. *et al.* Diet-induced mouse model of fatty liver disease and nonalcoholic steatohepatitis reflecting clinical disease progression and methods of assessment. *AJP Gastrointest. Liver Physiol.* **305,** G483–G495 (2013).

48. Tsuchida, T. *et al.* A simple diet- and chemical-induced murine NASH model with rapid progression of steatohepatitis, fibrosis and liver cancer. *J. Hepatol.* **69,** 385–395 (2018).

49. Wang, Y., Ausman, L. M., Greenberg, A. S., Russell, R. M. & Wang, X.-D. Nonalcoholic steatohepatitis induced by a high-fat diet promotes diethylnitrosamine-initiated early hepatocarcinogenesis in rats. *Int. J. cancer* **124,** 540–6 (2009).

50. Iyer, S., Upadhyay, P. K., Majumdar, S. S. & Nagarajan, P. Animal Models Correlating Immune Cells for the Development of NAFLD/NASH. *J. Clin. Exp. Hepatol.* **5,** 239–245 (2015).

51. Shalapour, S. *et al.* Inflammation-induced IgA+ cells dismantle anti-liver cancer immunity. *Nature* **551,** 340–345 (2017).

52. Abbas, A. K., Lichtman, A. H. H. & Pillai, S. *Cellular and Molecular Immunology*. (Saunders, 2014).

53. Heymann, F. & Tacke, F. Immunology in the liver — from homeostasis to disease. *Nat. Publ. Gr.* **13,** 88–110 (2016).

54. Vantourout, P. & Hayday, A. Six-of-the-best: unique contributions of γδ T cells to immunology. *Nat. Rev. Immunol.* **13,** 88–100 (2013).

55. Smith-Garvin, J. E., Koretzky, G. A. & Jordan, M. S. T cell activation. *Annu. Rev. Immunol.* **27,** 591–619 (2009).

56. Wherry, E. J. T cell exhaustion. *Nat. Immunol.* **12,** 492–499 (2011).

57. Sun, C., Mezzadra, R. & Schumacher, T. N. Regulation and Function of the PD-L1 Checkpoint. *Immunity* **48,** 434–452 (2018).

58. Chen, L. & Flies, D. B. Molecular mechanisms of T cell co-stimulation and co-inhibition. *Nat. Rev. Immunol.* **13,** 227–242 (2013).

59. Malehmir, M. Anti-Platelet Therapy for Metabolically Induced Nonalcoholic Steatohepatitis and Hepatocellular Carcinoma. (2017).

60. Haemmerle, M., Stone, R. L., Menter, D. G., Afshar-Kharghan, V. & Sood, A. K. The Platelet Lifeline to Cancer: Challenges and Opportunities. *Cancer Cell* **33,** 965–983 (2018).

61. Chauhan, A., Adams, D. H., Watson, S. P. & Lalor, P. F. Platelets: No longer bystanders in liver disease. *Hepatology* **64,** 1774–1784 (2016).

62. Gawaz, M., Langer, H. & May, A. E. Platelets in inflammation and atherogenesis. *J. Clin. Invest.* **115,** 3378 (2005).

63. Jackson, S. P. Arterial thrombosis-insidious, unpredictable and deadly. *Nat. Med.* **17,** 1423–1436 (2011).

64. Iannacone, M. *et al.* Platelets mediate cytotoxic T lymphocyte–induced liver damage. *Nat. Med.* **11,** 1167–1169 (2005).

65. Iannacone, M., Sitia, G., Narvaiza, I., Ruggeri, Z. M. & Guidotti, L. G. Antiplatelet drug therapy moderates immune-mediated liver disease and inhibits viral clearance in mice infected with a replication-deficient adenovirus. *Clin. Vaccine Immunol.* **14,** 1532–5 (2007).

66. Guidotti, L. G. *et al.* Immunosurveillance of the Liver by Intravascular Effector CD8(+) T Cells. *Cell* **161,** 486–500 (2015).

67. Sitia, G. *et al.* Antiplatelet therapy prevents hepatocellular carcinoma and improves survival in a mouse model of chronic hepatitis B. *Proc. Natl. Acad. Sci. U. S. A.* **109,** E2165-72 (2012).

68. Gremmel, T., Frelinger, A. & Michelson, A. Platelet Physiology. *Semin. Thromb. Hemost.* **42,** 191–204 (2016).

69. Michelson, A. D. Antiplatelet therapies for the treatment of cardiovascular disease. *Nat. Rev. Drug Discov.* **9,** 154–169 (2010).

70. DRUG RECORD Aspirin. at <https://livertox.nlm.nih.gov/Aspirin.htm>

71. DRUG RECORD Clopidogrel. at <https://livertox.nlm.nih.gov/Clopidogrel.htm>

72. DRUG RECORD Ticagrelor. at <https://livertox.nlm.nih.gov/Ticagrelor.htm>

73. DRUG RECORD Prasugrel. at <https://livertox.nlm.nih.gov/Prasugrel.htm>

74. DRUG RECORD Cangrelor. at <https://livertox.nlm.nih.gov/Cangrelor.htm>

75. Krieg, C. *et al.* High-dimensional single-cell analysis predicts response to anti-PD-1

immunotherapy. *Nat. Med.* **24,** 144–153 (2018).

76. Raasch, J. *et al.* IkappaB kinase 2 determines oligodendrocyte loss by non-cell-autonomous activation of NF-kappaB in the central nervous system. *Brain* **134,** 1184–98 (2011).

77. Arvaniti, E. & Claassen, M. Sensitive detection of rare disease-associated cell subsets via representation learning. *Nat. Commun.* **8,** 14825 (2017).

78. Kim, N. D. & Luster, A. D. The role of tissue resident cells in neutrophil recruitment. *Trends Immunol.* **36,** 547–555 (2015).

79. Subramaniam, M. *et al.* Defects in hemostasis in P-selectin-deficient mice. *Blood* **87,** (1996).

80. Narayanan, S., Surette, F. a & Hahn, Y. S. The Immune Landscape in Nonalcoholic Steatohepatitis. *Immune Netw.* **16,** 147–58 (2016).

81. Inzaugarat, M. E. *et al.* Altered phenotype and functionality of circulating immune cells characterize adult patients with nonalcoholic steatohepatitis. *J. Clin. Immunol.* **31,** 1120–1130 (2011).

82. Ferreyra Solari, N. E. *et al.* The Role of Innate Cells Is Coupled to a Th1-Polarized Immune Response in Pediatric Nonalcoholic Steatohepatitis. *J. Clin. Immunol.* **32,** 611–621 (2012).

83. Wang, Z. *et al.* Paradoxical effects of obesity on T cell function during tumor progression and PD-1 checkpoint blockade. *Nat. Med.* 1 (2018). doi:10.1038/s41591-018-0221-5

84. Nishimura, S. *et al.* CD8+ effector T cells contribute to macrophage recruitment and adipose tissue inflammation in obesity. *Nat. Med.* **15,** 914–920 (2009).

85. Bird, L. Inflammation: Finding the T in fat. *Nat. Rev. Immunol. 2009 99* (2009).

86. Yang, H. *et al.* Obesity Increases the Production of Proinflammatory Mediators from Adipose Tissue T Cells and Compromises TCR Repertoire Diversity: Implications for Systemic Inflammation and Insulin Resistance. *J. Immunol.* **185,** 1836–1845 (2010).

87. McDonnell, W. J. *et al.* High CD8 T-Cell Receptor Clonality and Altered CDR3 Properties Are Associated With Elevated Isolevuglandins in Adipose Tissue During Diet-Induced Obesity. *Diabetes* **67,** 2361–2376 (2018).

88. Bhattacharjee, J. *et al.* Role of immunodeficient animal models in the development of fructose induced NAFLD. *J. Nutr. Biochem.* **25,** 219–226 (2014).

89. Kolachala, V. L. *et al.* Loss of L-selectin-guided CD8 + , but not CD4 + , cells protects against ischemia reperfusion injury in a steatotic liver. *Hepatology* **66,** 1258–1274

(2017).

90. Sato, K., Ohtsuka, K., Watanabe, H. & Asakura, H. Detailed characterization of γδT cells within the organs in mice: classification into three groups. *Immunology* **80,** 380–387 (1993).

91. Hammerich, L. & Tacke, F. Role of gamma-delta T cells in liver inflammation and fibrosis. *World J. Gastrointest. Pathophysiol.* **5,** 107–13 (2014).

92. Mauro, C. *et al.* Obesity-Induced Metabolic Stress Leads to Biased Effector Memory CD4+ T Cell Differentiation via PI3K p110δ-Akt-Mediated Signals. *Cell Metab.* **25,** 593–609 (2017).

93. Luk, C. T. *et al.* Perforin Is a Novel Immune Regulator of Obesity-Related Insulin Resistance. *Diabetes* **64,** 90–103 (2014).

94. Tanaka, M. *et al.* Macrophage-inducible C-type lectin underlies obesity-induced adipose tissue fibrosis. *Nat. Commun.* **5,** 4982 (2014).

95. Zlotnikov-Klionsky, Y. *et al.* Perforin-Positive Dendritic Cells Exhibit an Immuno-regulatory Role in Metabolic Syndrome and Autoimmunity. *Immunity* **43,** 776–787 (2015).

96. Lynch, L. *et al.* iNKT Cells Induce FGF21 for Thermogenesis and Are Required for Maximal Weight Loss in GLP1 Therapy. *Cell Metab.* **24,** 510–519 (2016).

97. Narayanan, S., Surette, F. A. & Hahn, Y. S. The Immune Landscape in Nonalcoholic Steatohepatitis. *Immune Netw.* **16,** 147–58 (2016).

98. Huh, J. Y., Park, Y. J., Ham, M. & Kim, J. B. Crosstalk between adipocytes and immune cells in adipose tissue inflammation and metabolic dysregulation in obesity. *Mol. Cells* **37,** 365–71 (2014).

99. Bandyopadhyay, K., Marrero, I. & Kumar, V. NKT cell subsets as key participants in liver physiology and pathology. *Cell Mol Immunol* **13,** 337–346 (2016).

100. Tajiri, K. & Shimizu, Y. Role of NKT Cells in the Pathogenesis of NAFLD. *Int. J. Hepatol.* **2012,** 1–6 (2012).

101. Vahl, J. C. *et al.* NKT Cell-TCR Expression Activates Conventional T Cells in Vivo, but Is Largely Dispensable for Mature NKT Cell Biology. *PLoS Biol.* **11,** (2013).

102. Kotas, M. E. *et al.* Impact of CD1d deficiency on metabolism. *PLoS One* **6,** (2011).

103. Sutti, S. *et al.* Is there a role for adaptive immunity in nonalcoholic steatohepatitis? *World J. Hepatol.* **7,** 1725–9 (2015).

104. Konjar, Š., Ferreira, C., Blankenhaus, B. & Veldhoen, M. Intestinal Barrier Interactions

with Specialized CD8 T Cells. *Front. Immunol.* **8,** 1281 (2017).

105. Winer, D. A., Luck, H., Tsai, S. & Winer, S. The intestinal immune system in obesity and insulin resistance. *Cell Metab.* **23,** 413–426 (2016).

106. Tak, K. H., Yu, G. I., Lee, M. Y. & Shin, D. H. Association Between Polymorphisms of Interleukin 1 Family Genes and Hepatocellular Carcinoma. *Med. Sci. Monit.* **24,** 3488–3495 (2018).

107. Park, E. J. *et al.* Dietary and Genetic Obesity Promote Liver Inflammation and Tumorigenesis by Enhancing IL-6 and TNF Expression. *Cell* **140,** 197–208 (2010).

108. El-Khoueiry, A. B. *et al.* Nivolumab in patients with advanced hepatocellular carcinoma (CheckMate 040): an open-label, non-comparative, phase 1/2 dose escalation and expansion trial. *Lancet* **6736,** 1–11 (2017).

109. El-Khoueiry, A. B. *et al.* Nivolumab in patients with advanced hepatocellular carcinoma (CheckMate 040): An open-label, non-comparative, phase 1/2 dose escalation and expansion trial. *Lancet* **6736,** 1–11 (2017).

110. Zhu, A. X. *et al.* Pembrolizumab in patients with advanced hepatocellular carcinoma previously treated with sorafenib (KEYNOTE-224): a non-randomised, open-label phase 2 trial. *Lancet Oncol.* **2045,** 1–13 (2018).

111. Colombo, M. & Lleo, A. Is Liver Injury an Affordable Risk of Immune Checkpoint Inhibitor Therapy for Cancer? *Gastroenterology* **155,** 2021–2023 (2018).

112. Clinical studies ongoing with Nivolumab and Hepatocellular Cancer. at <https://clinicaltrials.gov/ct2/results?term=Nivolumab&cond=Hepatocellular+Cancer&show_xprt=Y&Search=Apply&recrs=a&recrs=d&age_v=&gndr=&type=&rslt=>

113. Clinical studies ongoing with Pembrolizumab and Hepatocellular Cancer. at <https://clinicaltrials.gov/ct2/results?cond=Hepatocellular+Cancer&term=Pembrolizumab&cntry=&state=&city=&dist=&Search=Search&show_xprt=Y&recrs=a&recrs=d>

114. Postow, M. & Wolchok, J. Patient selection criteria and toxicities associated with checkpoint inhibitor immunotherapy. at <https://www.uptodate.com/contents/patient-selection-criteria-and-toxicities-associated-with-checkpoint-inhibitor-immunotherapy?search=immune checkpoint inhibitors&source=search_result&selectedTitle=1~150&usage_type=default&display_rank=1>

115. DRUG RECORD Nivolumab. at <https://livertox.nih.gov/Nivolumab.htm>

116. DRUG RECORD Pembrolizumab. at <https://livertox.nih.gov/Pembrolizumab.htm>

117. Zen, Y. & Yeh, M. M. Hepatotoxicity of immune checkpoint inhibitors: a histology study of seven cases in comparison with autoimmune hepatitis and idiosyncratic drug-induced liver injury. *Mod. Pathol.* **31,** 965–973 (2018).

118. Wu, Z., Lai, L., Li, M., Zhang, L. & Zhang, W. Acute liver failure caused by pembrolizumab in a patient with pulmonary metastatic liver cancer: A case report. *Medicine (Baltimore).* **96,** e9431 (2017).

119. DRUG RECORD Corticosteroids. at <https://livertox.nih.gov/Corticosteroids.htm#reference>

120. Weiler-Normann, C. & Lohse, A. W. Nonalcoholic Fatty Liver Disease in Patients with Autoimmune Hepatitis: Further Reason for Teeth GNASHing? *Dig. Dis. Sci.* **61,** 2462–2464 (2016).

121. DRUG RECORD Infliximab. at <https://livertox.nlm.nih.gov/Infliximab.htm>

122. Chao, C.-Y. *et al.* Co-existence of non-alcoholic fatty liver disease and inflammatory bowel disease: A review article. *World J. Gastroenterol.* **22,** 7727–34 (2016).

123. Jackson, S. P. Arterial thrombosis—insidious, unpredictable and deadly. *Nat. Med.* **17,** 1423–1436 (2011).

124. McDonald, B. *et al.* Interaction of CD44 and hyaluronan is the dominant mechanism for neutrophil sequestration in inflamed liver sinusoids. *J. Exp. Med.* **205,** 915–27 (2008).

125. Langer, H. F. *et al.* Platelets contribute to the pathogenesis of experimental autoimmune encephalomyelitis. *Circ. Res.* **110,** 1202–10 (2012).

126. Kleinschnitz, C. *et al.* Targeting platelets in acute experimental stroke: Impact of glycoprotein Ib, VI, and IIb/IIIa blockade on infarct size, functional outcome, and intracranial bleeding. *Circulation* **115,** 2323–2330 (2007).

127. Townsend†, S. A. & Philip N. Newsome†, ‡. Non-alcoholic fatty liver disease in 2016. *Br. Med. Bull.* 1–14 (2016). doi:10.1002/9781118556153.ch19

128. Neuschwander-Tetri, B. A. *et al.* Farnesoid X nuclear receptor ligand obeticholic acid for non-cirrhotic, non-alcoholic steatohepatitis (FLINT): a multicentre, randomised, placebo-controlled trial. *Lancet* **385,** 956–965 (2015).

129. Konukiewitz, B. *et al.* Somatostatin receptor expression related to TP53 and RB1 alterations in pancreatic and extrapancreatic neuroendocrine neoplasms with a Ki67-index above 20%. *Mod. Pathol.* **30,** 587–598 (2017).

10 Acknowledgements

I want to thank all the people who have guided and helped me over the last few years on this journey to my PhD degree. My grateful thanks belong to:

- Professor Dr. Mathias Heikenwälder, who trusted me in the beginning, starting as PhD student first in Munich and later in Heidelberg. I want to thank you, Mathias, for your open and direct communication; your direct and steady approach to solving problems; your helpful comments and discussions; your idea of a laboratory allowing fast-past and large-scale research. Lastly, I want to thank you for the guidance and the opportunity to grow personally, scientifically and communicatively during this time, forging me into the person I became.
- My first supervisor for both my thesis and defense, Professor Dr. Ralf Bartenschlager, who impressed me from the beginning by his calm, supportive and scientific demeanor. Thank you, Ralf, for guiding me along this long path and through my TAC meetings.
- My third TAC member, Professor Dr. Marc Schmidt-Supprian, who helped me greatly through discussions, mouse sharing, in TAC meetings and providing a helping hand countless times during my early stages of learning flow cytometry in Munich.
- My PhD examination committee Professor Dr. Viktor Umansky for his great insights on the role of MDSCs in the context of checkpoint inhibitor induced hepatic inflammation.
- My PhD examination committee Dr. Darjus Tschaharganeh for his huge help in tackling liver specific questions by genetic manipulations, as well as his open and direct approach of scientific problems.
- Eleni Kotsiliti, Dr. Tracy O´Connor and Valentina Leone, who took me by the hand in my first months of being a freshman and stayed in the closest and most direct feedback loop to develop my cultural, personal and scientific thinking over the whole time period of being a PhD. Further, I want to thank Tracy especially, who improved my German influenced style of writing English countless times.
- Dr. Marc Ringelhan, who challenged me extraordinarily scientifically by questions, by helping me keep my translational focus, and by trusting in my skills to write our review together. It was a remarkable and memorable experience.
- The technical team supporting me on nearly every step of my thesis, chronologically starting with Ruth Hillermann and Olga Seelbach, moving over to Heidelberg with Danijela Heide, Jenny Hetzer, Katharina Kessler, Corinna Gropp and Nathalie Klaumünzer, making the histological data in my thesis possible. Further, Sandra Prokosch and Florian Müller helped me with mice, flow cytometry and FACS. Ending with Ulrike Rothermel and Lena Beideck for the mouse work and genotyping. And last

but not least, the animal care takers Elke and Stefan for always helping me when I struggled with mice.

- Former lab members that helped me on my path, namely Monika Wolf, Arlind Adili, Bastian Seubert, Anna Lorentzen and Michael Meister, who opened my eyes for more than just liver research.
- All other members, co-authors and collaborators whose names would fill a thesis by themselves of the Institute of Virology, Helmholtz Zentrum München and the Department of Chronic Inflammation and Cancer, DKFZ Heidelberg
- All the collaborators who have helped me on this long path, sharing scientific discoveries with me.

Finally, I want to thank my whole family and loved ones for the great and extraordinary support, which gave me the opportunity to walk my path of nearly 10 years of studying Biochemistry and uncovering cancer-associated mechanisms. I will be grateful forever.

Sincerely,

Dominik Pfister

11 Appendix

Within this appendix I include published papers and articles with my written and experimental contribution during my PhD time.

Platelet GPIbα is a mediator and potential interventional target for NASH and subsequent liver cancer

Mohsen Malehmir[*], **Dominik Pfister**[*], Suchira Gallage[*], Marta Szydlowska[*], Donato Inverso[*], Elena Kotsiliti[£], Valentina Leone[£], Moritz Peiseler[£], Bas G.J. Surewaard[£], Dominik Rath, Adnan Ali, Monika Julia Wolf, Hannah Drescher, Marc E. Healy, Daniel Dauch, Daniela Kroy, Oliver Krenkel, Marlene Kohlhepp, Thomas Engleitner, Alexander Olkus, Tjeerd Sijmonsma, Julia Volz, Carsten Deppermann, David Stegner, Patrick Helbling, César Nombela-Arrieta, Anahita Rafiei, Martina Hinterleitner, Marcel Rall, Florian Baku, Oliver Borst, Caroline L. Wilson, Jack Leslie, Tracy O`Connor, Christopher J. Weston, David H. Adams, Lozan Sheriff, Ana Teijeiro, Marco Prinz, Ruzhica Bogeska, Natasha Anstee, Malte N. Bongers, Mike Notohamiprodjo, Tobias Geisler, Dominic J. Withers, Jerry Ware, Derek A. Mann, Hellmut G. Augustin, Alexandros Vegiopoulos, Michael D. Milsom, Adam J. Rose, Patricia F. Lalor, Josep M. Llovet, Roser Pinyol, Frank Tacke, Roland Rad, Matthias Matter, Nabil Djouder, Paul Kubes, Percy A. Knolle, Kristian Unger, Lars Zender, Bernhard Nieswandt, Meinrad Gawaz, Achim Weber[**] and Mathias Heikenwalder[**]

Nature Medicine | VOL 25 | APRIL 2019 | 641-655 |[9]

The immunology of hepatocellular carcinoma

Marc Ringelhan, **Dominik Pfister**, Tracy O'Connor, Eli Pikarsky and Mathias Heikenwalder

Nature Immunology | VOL 19 | MARCH 2018 | 222–232 |[3]

Somatostatin receptor expression related to TP53 and RB1 alterations in pancreatic and extra pancreatic neuroendocrine neoplasms with a Ki67-index above 20%

Björn Konukiewitz, Anna Melissa Schlitter, Moritz Jesinghaus, **Dominik Pfister**, Katja Steiger, Angela Segler, Abbas Agaimy, Bence Sipos, GiuseppeZamboni, Wilko Weichert, Irene Esposito, Nicole Pfarr and Günter Klöppel

Modern Pathology (2017) 30, 587–598[129]

11.1 Platelet GPIbα is a mediator and potential interventional target for NASH and subsequent liver cancer

Authors

Mohsen Malehmir[*], **Dominik Pfister**[*], Suchira Gallage[*], Marta Szydlowska[*], Donato Inverso[*], Elena Kotsiliti[£], Valentina Leone[£], Moritz Peiseler[£], Bas G.J. Surewaard[£], Dominik Rath, Adnan Ali, Monika Julia Wolf, Hannah Drescher, Marc E. Healy, Daniel Dauch, Daniela Kroy, Oliver Krenkel, Marlene Kohlhepp, Thomas Engleitner, Alexander Olkus, Tjeerd Sijmonsma, Julia Volz, Carsten Deppermann, David Stegner, Patrick Helbling, César Nombela-Arrieta, Anahita Rafiei, Martina Hinterleitner, Marcel Rall, Florian Baku, Oliver Borst, Caroline L. Wilson, Jack Leslie, Tracy O`Connor, Christopher J. Weston, David H. Adams, Lozan Sheriff, Ana Teijeiro, Marco Prinz, Ruzhica Bogeska, Natasha Anstee, Malte N. Bongers, Mike Notohamiprodjo, Tobias Geisler, Dominic J. Withers, Jerry Ware, Derek A. Mann, Hellmut G. Augustin, Alexandros Vegiopoulos, Michael D. Milsom, Adam J. Rose, Patricia F. Lalor, Josep M. Llovet, Roser Pinyol, Frank Tacke, Roland Rad, Matthias Matter, Nabil Djouder, Paul Kubes, Percy A. Knolle, Kristian Unger, Lars Zender, Bernhard Nieswandt, Meinrad Gawaz, Achim Weber[**] and Mathias Heikenwalder[**]

Journal

Nature Medicine | VOL 25 | APRIL 2019 | 641-655 |[9]

https://doi.org/10.1038/s41591-019-0379-5

nature medicine

ARTICLES

https://doi.org/10.1038/s41591-019-0379-5

Platelet GPIbα is a mediator and potential interventional target for NASH and subsequent liver cancer

Mohsen Malehmir[1,44], Dominik Pfister[2,44], Suchira Gallage[2,44], Marta Szydlowska[2,44], Donato Inverso[3,4,44], Elena Kotsiliti[2,5], Valentina Leone[2,6], Moritz Peiseler[7,8], Bas G. J. Surewaard[8,9,10], Dominik Rath[11], Adnan Ali[2], Monika Julia Wolf[1], Hannah Drescher[12], Marc E. Healy[1], Daniel Dauch[13,14], Daniela Kroy[12], Oliver Krenkel[12], Marlene Kohlhepp[12], Thomas Engleitner[15,16,17], Alexander Olkus[2,18], Tjeerd Sijmonsma[2], Julia Volz[19], Carsten Deppermann[19], David Stegner[19], Patrick Helbling[20], César Nombela-Arrieta[20], Anahita Rafiei[20], Martina Hinterleitner[13,14], Marcel Rall[11], Florian Baku[11], Oliver Borst[11], Caroline L. Wilson[21], Jack Leslie[21], Tracy O'Connor[5,22], Christopher J. Weston[23], David H. Adams[23,24], Lozan Sheriff[25], Ana Teijeiro[26], Marco Prinz[27,28,29], Ruzhica Bogeska[30,31], Natasha Anstee[30,31], Malte N. Bongers[32], Mike Notohamiprodjo[32], Tobias Geisler[33], Dominic J. Withers[34,35], Jerry Ware[36], Derek A. Mann[21], Hellmut G. Augustin[3,4], Alexandros Vegiopoulos[37], Michael D. Milsom[30,31], Adam J. Rose[38], Patricia F. Lalor[23], Josep M. Llovet[39,40,41], Roser Pinyol[40], Frank Tacke[12], Roland Rad[15,16,17], Matthias Matter[42], Nabil Djouder[26], Paul Kubes[7,8,9], Percy A. Knolle[22], Kristian Unger[6], Lars Zender[13,14,43], Bernhard Nieswandt[19], Meinrad Gawaz[11], Achim Weber[1,45*] and Mathias Heikenwalder[2,5,45*]

Non-alcoholic fatty liver disease ranges from steatosis to non-alcoholic steatohepatitis (NASH), potentially progressing to cirrhosis and hepatocellular carcinoma (HCC). Here, we show that platelet number, platelet activation and platelet aggregation are increased in NASH but not in steatosis or insulin resistance. Antiplatelet therapy (APT; aspirin/clopidogrel, ticagrelor) but not nonsteroidal anti-inflammatory drug (NSAID) treatment with sulindac prevented NASH and subsequent HCC development. Intravital microscopy showed that liver colonization by platelets depended primarily on Kupffer cells at early and late stages of NASH, involving hyaluronan-CD44 binding. APT reduced intrahepatic platelet accumulation and the frequency of platelet–immune cell interaction, thereby limiting hepatic immune cell trafficking. Consequently, intrahepatic cytokine and chemokine release, macrovesicular steatosis and liver damage were attenuated. Platelet cargo, platelet adhesion and platelet activation but not platelet aggregation were identified as pivotal for NASH and subsequent hepatocarcinogenesis. In particular, platelet-derived GPIbα proved critical for development of NASH and subsequent HCC, independent of its reported cognate ligands vWF, P-selectin or Mac-1, offering a potential target against NASH.

Non-alcoholic fatty liver disease (NAFLD) is the most common chronic liver disease in high-income countries[1] and is on trajectory to become the most common indication for liver transplantation in the United States[2,3]. NAFLD ranges from simple steatosis (non-alcoholic fatty liver (NAFL)) to NASH, which may progress to cirrhosis and ultimately to HCC[4,5]. HCC is the third most common cause of cancer-related death worldwide and is the fastest rising cancer in the United States and Europe[6–8]. Major risk factors for NASH include metabolic syndrome, abdominal obesity, insulin resistance, glucose intolerance or type 2 diabetes mellitus and dyslipidemia[4,5,9,10].

We previously developed a preclinical model of human metabolic syndrome, NASH and NASH-induced HCC[11]. In this model, intrahepatic influx of metabolically activated CD8$^+$ T cells and natural killer T (NKT) cells triggers metabolic reprogramming of hepatocytes, NASH and HCC development through cytokine-mediated cross-talk with hepatocytes. However, the mechanisms underlying immune cell recruitment during NASH and its consequences for NASH-to-HCC transition have remained unclear.

Platelets, produced by megakaryocytes in the bone marrow, play a fundamental role in hemostasis[12] but are also crucial in pathophysiological conditions like thrombosis, obesity, atherosclerosis, metastasis and stroke[13–15]. Additionally, a growing body of evidence highlights platelets as active players in liver disease and inflammation[13,16,17]. Notably, it has been reported that activated platelets contribute to cytotoxic T lymphocyte (CTL)-mediated liver damage in a model of viral hepatitis[18,19]. Moreover, blocking platelet activation and aggregation by aspirin-clopidogrel (Asp-Clo) abrogates hepatic T cell influx, subsequent liver damage and tumorigenesis

A full list of affiliations appears at the end of the paper.

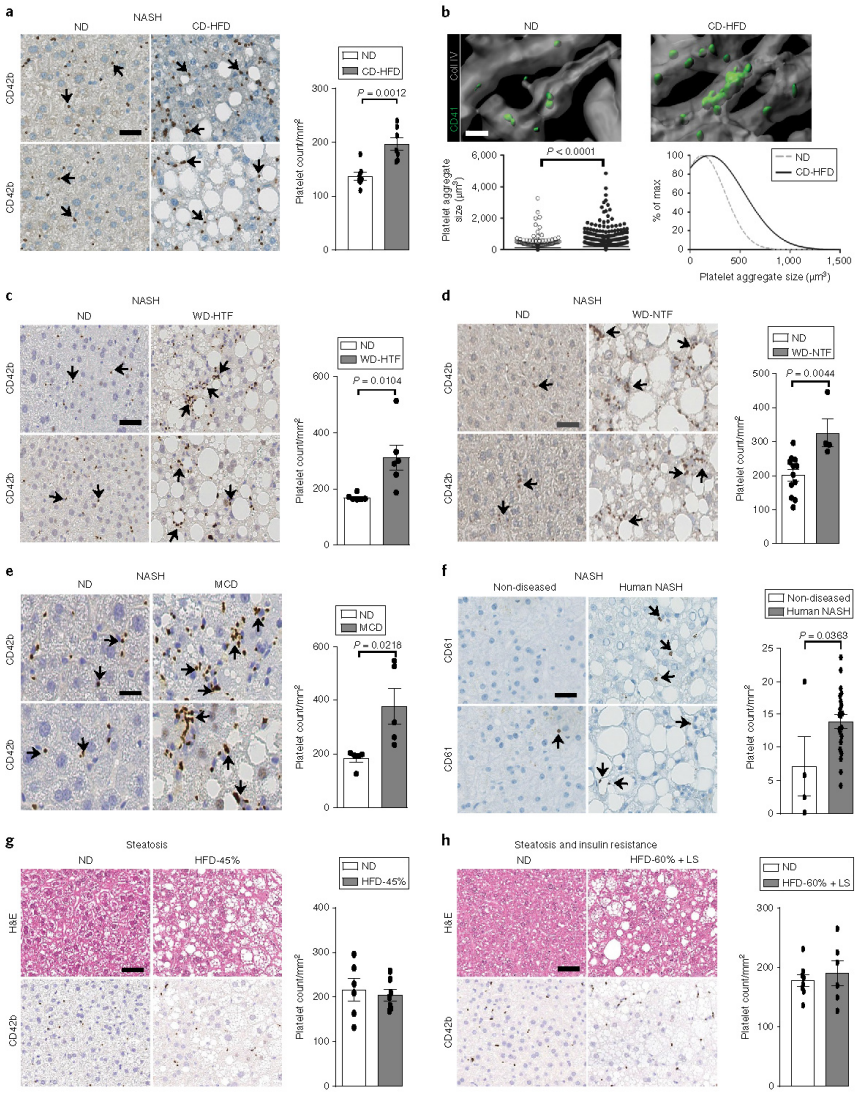

Fig. 1 | Increased platelet numbers and aggregates in liver sinusoids of murine and human NASH. a, CD42b staining and quantification of intrahepatic platelets (CD42b⁺) in 6-month ND-fed or CD-HFD-fed mice; arrows indicate platelets ($n=7$ mice/group). Scale bar, 50 µm. **b**, 3D confocal images of platelet (green)/liver endothelium (gray) interaction of 6-month ND-fed or CD-HFD-fed mice ($n=4$ mice/group). Scale bar, 20 µm. **c**,**d**, CD42b staining and quantification in 6-month (**c**) ND-fed and WD-HTF-fed ($n=6$ mice/group) or (**d**) WD-NTF-fed mice; arrows indicate platelets, (ND $n=12$ mice; WD-HTF $n=4$ mice). Scale bars, 50 µm. **e**, CD42b staining and quantification of intrahepatic platelets (CD42b⁺) in 2-month ND-fed or MCD-fed mice; arrows indicate platelets ($n=5$ mice/group). Scale bar, 50 µm. **f**, CD61 staining and quantification of platelets (CD61⁺) in human livers; arrows indicate platelets (non-diseased patients $n=4$; patients with NASH $n=21$). **g**, H&E staining, CD42b staining and quantification in 6-month ND-fed or HFD-45%-fed mice (ND $n=6$ mice; HFD-45% $n=7$ mice). Scale bar, 50 µm. **h**, H&E, CD42b staining and quantification in 6-month ND-fed or HFD-60%-fed (60% kcal and low sucrose (LS)) mice (ND $n=8$ mice; HFD $n=6$ mice). Scale bar, 50 µm. All data are shown as mean ± s.e.m. All data were analyzed using two-tailed Student's *t* test.

without affecting peripheral T cell function in viral hepatitis[19,20]. Additionally, in a recent study of NAFL (but not NASH) patients, APT lowered serum markers of obesity and liver damage[21].

There is an unmet need for efficacious, low-risk therapies against NASH and NASH-to-HCC transition. Although several drugs (e.g., those decreasing blood sugar levels) are in phase 2 and 3

development[22,23], currently no approved pharmacological therapies are available that can prevent NASH or related pathologies. Further, the role of platelets in NASH and HCC development is not well characterized. Thus, we investigated whether APT and molecules involved in platelet function might prevent NASH and NASH-induced HCC development.

Results

Hepatic accumulation of activated platelets in NASH. To test whether platelets contribute to NASH development, we investigated platelet number and distribution in livers of C57Bl/6 mice fed a choline-deficient, high-fat diet (CD-HFD). Platelet numbers (Fig. 1a) and aggregate size (Fig. 1b) were significantly increased compared with those of age-matched normal chow diet (ND)-fed controls (Fig. 1a), whereas platelet counts in peripheral blood remained normal (Supplementary Fig. 1a). Although fibrinogen levels and prothrombin time (PT) remained unchanged, activated partial thromboplastin time (aPTT) was significantly reduced (Supplementary Fig. 1a). Ex vivo analyses of circulating platelets revealed no significant differences in activation or aggregation responses in CD-HFD-fed mice compared with ND-fed mice (Supplementary Fig. 1b). We next analyzed other dietary and genetic murine NASH models (Fig. 1c–e and Supplementary Fig. 1c,d), including high-fat, high-fructose, high-cholesterol, 'Western-style' diets[24,25] with or without trans fat (WD-HTF; WD-NTF); a 'Western-style' diet with fructose (WD-FSDW)[26]; a methionine- and choline-deficient diet (MCD) and an inducible knock-in mouse expressing the human unconventional prefoldin RPB5 interactor (URI) in hepatocytes (hURI-tetOFFhep)[27]. All models induced NASH with varying NAFLD Activity Score (NAS) and degrees of fibrosis (Supplementary Fig. 2a,b), a primary determinant of outcome in NASH[28,29], and displayed a significant increase in intrahepatic platelet numbers compared to controls (Fig. 1a,c–e; Supplementary Fig. 1c,d). Further, human NAFLD/NASH patients displayed a significant increase in intrahepatic platelets in liver compared to healthy controls (Fig. 1f; Supplementary Table 1).

In contrast, mice fed a 45% kcal high-fat diet (HFD), displaying only steatosis, or mice fed a 60% kcal HFD with low sucrose (HFD-60%+LS) experiencing only simple steatosis and insulin resistance[30], lacked any significant increase in intrahepatic platelet numbers, despite increased body weight, NAS, liver damage and insulin resistance (Fig. 1g,h and Supplementary Fig. 3a–c). Intrahepatic platelet activation in NASH was confirmed by electron microscopy (EM) (Supplementary Fig. 3d). Thus, increased intrahepatic platelet number, platelet aggregation and platelet activation were specific to NASH.

Asp-Clo treatment is an APT currently used in several diseases (e.g., coronary stent thrombosis)[31]. We first addressed whether CD-HFD-fed mice would respond to APT. Compared with untreated CD-HFD-fed mice, Asp-Clo-treated mice displayed significantly lower intrahepatic platelet numbers (Supplementary Fig. 4a–c), as well as reduced platelet aggregation and activation (Supplementary Fig. 4d). To investigate the effects of APT on human NAFLD, we performed a pilot case study (German Clinical Trials Register (DRKS) 587/2016BO2) with patients at risk for NAFLD (body mass index >30 and/or diabetes mellitus type II) undergoing a heart catheter procedure. Depending on the outcome of the catheter procedure, one of three approaches was carried out: (1) patients received dual antiplatelet therapy (DAPT) for at least 6 months if a coronary stent was implanted; (2) ASA monotherapy was given for at least 6 months if coronary artery disease (CAD) was present but stent implantation was not indicated; (3) no anti-aggregation therapy was given if coronary artery disease was absent. None of the patients included received long-term treatment with ASA or P2Y12 before study inclusion (Supplementary Fig. 5a and Supplementary Table 2). In this pilot case study of 24 individual patients/observations, platelet function analyses revealed that patients generally responded well to APT (Supplementary Fig. 5b), although serum total cholesterol, LDL and HDL cholesterol remained unchanged (Supplementary Fig. 5b,c). For control, we investigated patients without APT (Supplementary Table 2). Patients with NAFLD underwent liver MRI, liver ultrasound and serum analysis at study inclusion and after 6 months of follow-up. APT-treated patients with NAFLD showed significantly reduced liver volume and liver fat mass (Supplementary Fig. 5d–f). Patients who received a new therapy with ASA or DAPT were diagnosed with CAD. The standard treatment in patients with CAD includes statins. Therefore, patients who received a new anti-aggregation therapy were usually treated with a new statin treatment if statins were not already administered on a regular basis and if contraindications were absent. Thus, statins might present a significant confounder in the actual pilot case study, which we tried to address by performing a linear regression analysis. Because the study collective was small, we included age, gender, anti-aggregation and new statin treatment in the regression analysis. For the course of liver fat, we found the strongest associations for anti-aggregation ($b=-0.334$, 95% CI −4.719, 1.197, $P=0.226$), whereas initiation of a new statin treatment showed weaker associations ($b=-0.095$, 95% CI −3.551, 2.526, $P=0.726$). For the course of liver volume, we found associations for anti-aggregation ($b=-0,454$, 95% CI −0.170, 0.006, $P=0.066$) that were stronger compared with

Fig. 2 | Asp-Clo treatment results in attenuation of steatosis, liver damage, NASH and NASH-associated conditions. a, Body weight development of 12-month ND-, CD-HFD- or CD-HFD/Asp-Clo-fed mice (ND $n=5$ mice; CD-HFD $n=5$ mice; CD-HFD/Asp-Clo $n=9$). Statistic: ND vs CD-HFD (black asterisks), ND vs CD-HFD/Asp-Clo (green asterisks). **b**, ALT of 6- and 12-month ND-, CD-HFD or CD-HFD/Asp-Clo-fed mice (6 months: ND $n=14$ mice; CD-HFD $n=11$ mice; CD-HFD/Asp-Clo $n=4$ mice; 12 months: ND $n=7$ mice; CD-HFD $n=12$ mice; CD-HFD/Asp-Clo $n=18$ mice). **c**, Intraperitoneal glucose tolerance test (IPGTT) of 6-month ND-, CD-HFD- or CD-HFD/Asp-Clo-fed mice ($n=5$ mice/group). Statistic: ND vs CD-HFD (black asterisks), ND vs CD-HFD/Asp-Clo (green asterisks). **d**,**e**, Liver triglyceride (6 months: ND $n=11$ mice; CD-HFD $n=15$ mice; CD-HFD/Asp-Clo $n=7$ mice; 12 months: ND $n=4$ mice; CD-HFD $n=9$ mice; CD-HFD/Asp-Clo $n=15$ mice) (**d**) and serum cholesterol (**e**) of 6- and 12-month ND-, CD-HFD- or CD-HFD/Asp-Clo-fed mice (6 months: ND $n=4$ mice; CD-HFD $n=7$ mice; CD-HFD/Asp-Clo $n=9$ mice; 12 months: ND $n=6$ mice; CD-HFD $n=17$ mice; CD-HFD/Asp-Clo $n=11$ mice). **f**, Real-time qPCR analysis for genes involved in lipid metabolism/β-oxidation of 6-month ND-, CD-HFD- or CD-HFD/Asp-Clo-fed mice (ND $n=4$ mice; CD-HFD $n=5$ mice; CD-HFD/Asp-Clo $n=7$ mice). Statistic: CD-HFD vs CD-HFD/Asp-Clo (green asterisks). **g**, Analysis of VO_2 and respiratory exchange ratio (RER) over time in 2-month ND-, CD-HFD- or CD-HFD/Asp-Clo-fed mice (ND $n=4$ mice; CD-HFD $n=8$ mice; CD-HFD/Asp-Clo $n=8$ mice). **h**, Analysis of food (g/mouse/day) and water intake (ml/mouse/day) (ND $n=4$ mice; CD-HFD $n=8$ mice; CD-HFD/Asp-Clo $n=6$ mice). **i**, MRI analyses in 6-month ND-, CD-HFD- or CD-HFD/Asp-Clo-fed mice ($n=3$ mice/group). T1 (fast low-angle shot (FLASH)) OUT phase: dark color indicative of steatosis. T2 TurboRare: an increase in subcutaneous and abdominal fat and hepatic lipid accumulation (bright regions). **j**,**k**, H&E staining (**j**) and NAS evaluation (**k**) of 6-month ND-, CD-HFD- or CD-HFD/Asp-Clo-fed mice (ND $n=9$ mice; CD-HFD $n=9$ mice; CD-HFD/Asp-Clo $n=6$ mice). Asterisks indicate damaged hepatocytes. Scale bars, 100 µm in 10×, 50 µm in 20×. All data are shown as mean ± s.e.m. Data in **a** and **c** were analyzed by two-way analysis of variance (ANOVA) with the post hoc Tukey's multiple comparison test; $^*P<0.05$, $^{**}P<0.01$, $^{***}P<0.001$, $^{****}P<0.0001$. Data in **b**, **d**, **e**, **g**, **h** and **k** were analyzed by one-way analysis of variance with the post hoc Tukey's multiple comparison test. Data in **f** were analyzed by two-tailed Mann–Whitney test; $^*P<0.05$, $^{**}P<0.01$.

initiation of a new statin treatment ($b = 0.047$, 95% CI −0.084, 0.101, $P = 0.847$). This finding indicated that effects of anti-aggregation were stronger than those of statin administration. Notably, $n = 4$ patients showed significant reductions in liver fat content and/or liver volume without new statin therapy. However, there was a trend toward effect of anti-aggregation without being statistically significant. Higher body mass index did not significantly affect liver fat or liver volume.

Asp-Clo treatment attenuates NASH and NASH-associated conditions. We next investigated whether Asp-Clo (adjusted to the body weight) affects NASH or HCC development in mice receiving ND, CD-HFD or CD-HFD with Asp-Clo for 12 months. Weight gain over time was significantly higher in CD-HFD and CD-HFD/Asp-Clo-fed mice compared with ND-fed controls (Fig. 2a). Similar to body weight, epididymal fat (eWAT) weight in CD-HFD/Asp-Clo-fed mice was not different from that in

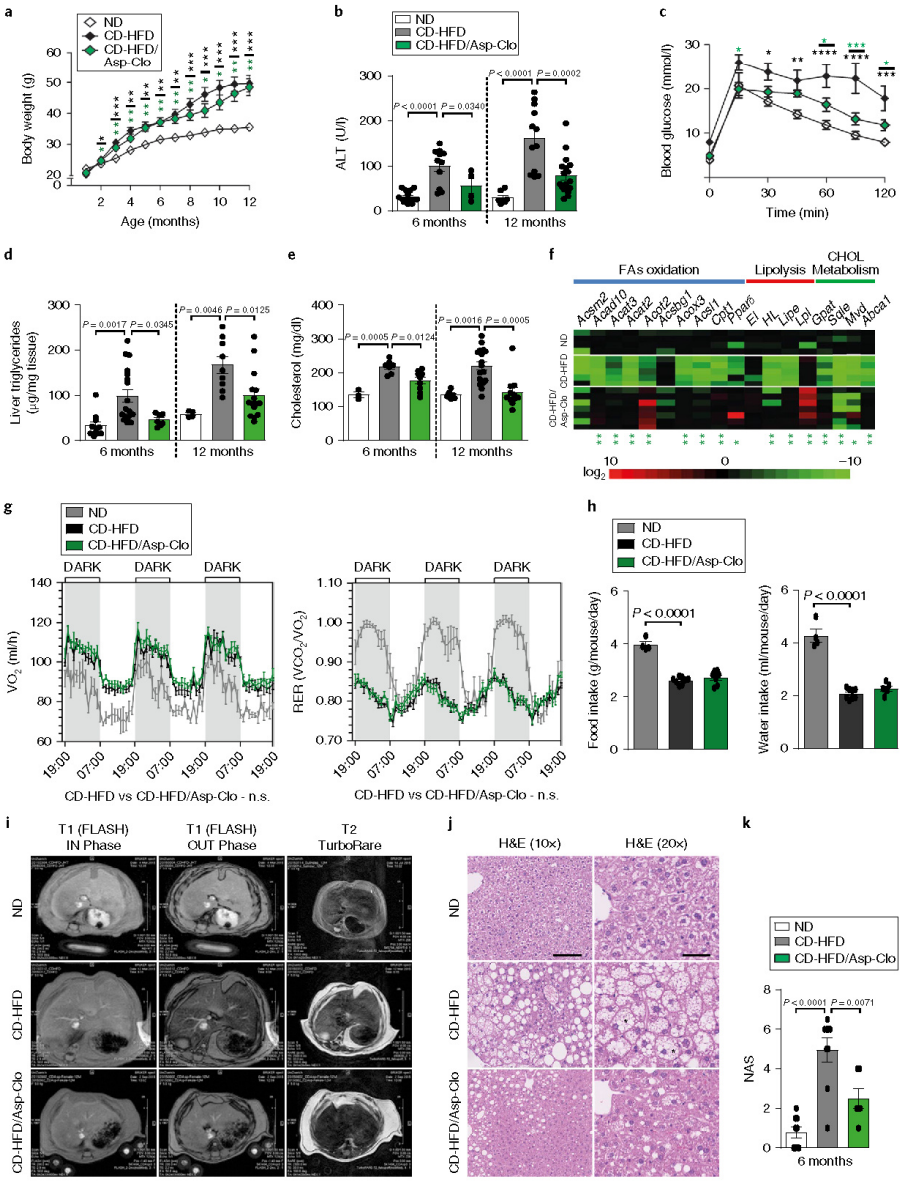

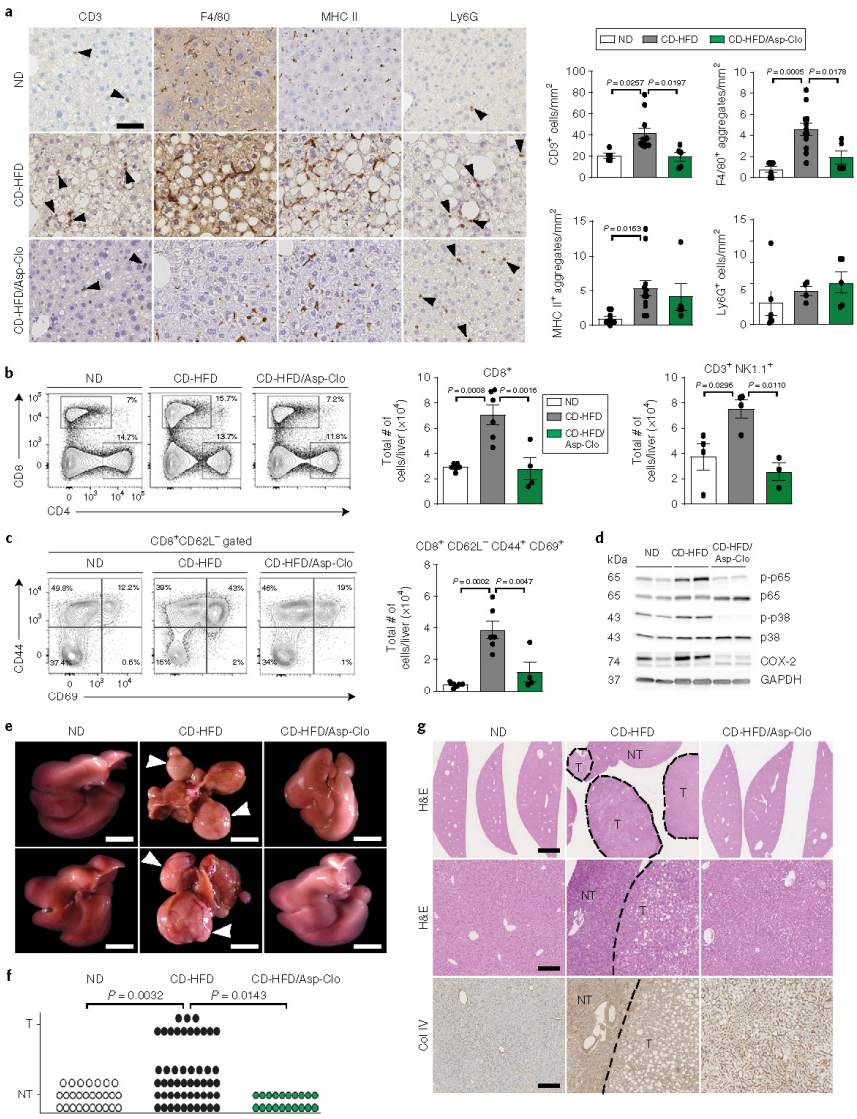

Fig. 3 | Antiplatelet treatment with Asp-Clo abrogates immune cell infiltration into the liver and prevents NASH-induced HCC development. a, CD3, F4/80, MHCII and Ly6G staining and quantification of 6-month ND-, CD-HFD- or CD-HFD/Asp-Clo-fed mice (CD3: ND $n=5$ mice; CD-HFD $n=11$ mice; CD-HFD/Asp-Clo $n=5$ mice; F4/80: ND $n=6$ mice; CD-HFD $n=12$ mice; CD-HFD/Asp-Clo $n=5$ mice; MHCII: ND $n=9$ mice; CD-HFD $n=12$ mice; CD-HFD/Asp-Clo $n=5$ mice), scale bar, 50 µm. **b**,**c**, Representative FACS plots and quantification of hepatic CD4/CD8 ratio and NKT cells (**b**) and activated CD8+cells of 6-month ND-, CD-HFD- or CD-HFD/Asp-Clo-fed mice (**c**) (CD8+: ND $n=6$ mice; CD-HFD $n=6$ mice; CD-HFD/Asp-Clo $n=4$ mice; CD3+NK1.1+: ND $n=4$ mice; CD-HFD $n=4$ mice; CD-HFD/Asp-Clo $n=3$ mice; CD8+CD62L-CD44+CD69+: ND $n=6$ mice; CD-HFD $n=6$ mice; CD-HFD/Asp-Clo $n=4$ mice). **d**, Western blot images of 6-month ND-, CD-HFD- or CD-HFD/Asp-Clo-fed mice ($n=2$ mice/group). **e**, Representative macroscopical images of livers from 12-month ND-, CD-HFD- or CD-HFD/Asp-Clo-fed mice (ND $n=0$ tumors in 27 mice; CD-HFD $n=13$ tumors in 51 mice; CD-HFD/Asp-Clo $n=0$ tumors in 20 mice). White arrowhead indicates HCC. Scale bar, 7.5 mm. **f**, HCC incidence of 12-month ND-, CD-HFD- or CD-HFD/Asp-Clo-fed mice. T, tumor; NT, non-tumor) (ND $n=0$ tumors in 27 mice; CD-HFD $n=13$ tumors in 52 mice; CD-HFD/Asp-Clo $n=0$ tumors in 20 mice). **g**, HCC characterization by H&E and collagen IV (Col IV) staining of 12-month ND-, CD-HFD- or CD-HFD/Asp-Clo-fed mice; dashed line indicates tumor (T) border. Scale bar, 2 mm (top H&E) and 200 µm (middle H&E; bottom Col IV). All data are shown as mean ± s.e.m. Data in **a**–**c** were analyzed by one-way ANOVA with the post hoc Tukey's multiple comparison test. Data in **f** were analyzed using two-sided Fisher's exact test.

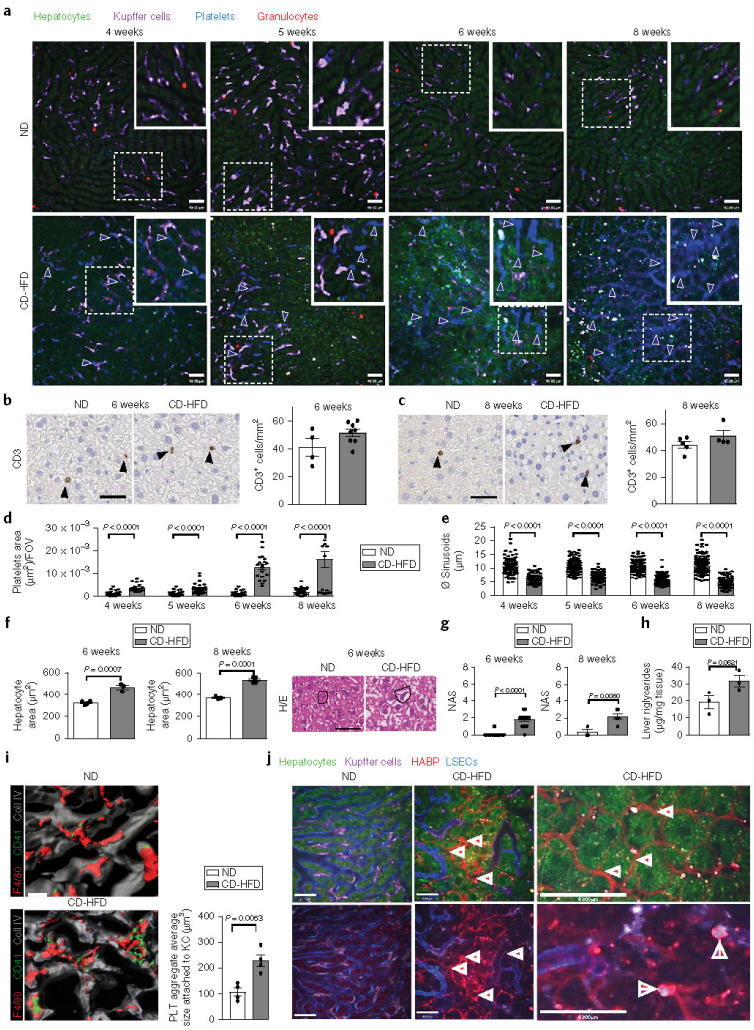

Fig. 4 | Platelets efficiently populate the liver early during fatty liver pathogenesis. a, Intravital microscopy of livers of 4, 5, 6 and 8 weeks ND- or CD-HFD-fed mice. Analysis of Kupffer cells (violet), platelets (blue) and granulocytes (red), (4 weeks: ND $n=2$ mice; CD-HFD $n=2$ mice; 5 weeks: ND $n=2$ mice; CD-HFD $n=2$ mice; 6 weeks: ND $n=4$ mice; CD-HFD $n=4$ mice; 8 weeks: ND $n=3$ mice; CD-HFD $n=3$ mice). Scale bars, 40 µm. **b**,**c**, CD3 staining and quantification of (**b**) 6-week (ND $n=4$ mice; CD-HFD $n=8$ mice) or (**c**) 8-week ND- or CD-HFD-fed mice (ND $n=5$ mice; CD-HFD $n=4$ mice). Scale bar, 50 µm. **d**, Quantification of platelet area by intravital microscopy of mice shown in **a** (ND: 4 weeks $n=2$ mice and 40 FOV; 5 weeks $n=2$ mice and 40 FOV; 6 weeks $n=4$ mice and 40 FOV; 8 weeks $n=2$ mice and 40 FOV; CD-HFD: 4 weeks $n=2$ mice and 20 FOV; 5 weeks $n=2$ mice and 20 FOV; 6 weeks $n=4$ mice and 30 FOV; 8 weeks $n=2$ mice and 19 FOV). **e**, Analysis of liver sinusoid diameter by intravital microscopy of mice shown in **a** (ND: 4 weeks $n=2$ mice and 101 sinusoids; 5 weeks $n=2$ mice and 150 sinusoids; 6 weeks $n=4$ mice and 100 sinusoids; 8 weeks $n=2$ mice and 150 sinusoids; CD-HFD: 4 weeks $n=2$ mice and 100 sinusoids; 5 weeks $n=2$ mice and 150 sinusoids; 6 weeks $n=4$ mice and 100 sinusoids; 8 weeks $n=2$ mice and 100 sinusoids). **f**, Hepatocyte swelling measurement by H&E of mice shown in **b** and **c** (6 weeks: ND $n=4$ mice; CD-HFD $n=3$ mice; 8 weeks: ND $n=3$ mice; CD-HFD $n=4$ mice). **g**, NAS evaluation of 6- or 8-week ND- or CD-HFD-fed mice (6 weeks: ND $n=19$ mice; CD-HFD $n=18$ mice; 8 weeks: ND $n=3$ mice; CD-HFD $n=6$ mice). **h**, Liver triglycerides of 6-week ND- or CD-HFD-fed mice ($n=3$ mice/group). **i**, 3D confocal images and quantification of platelet (green)/Kupffer cells (red) interaction of 6-month ND- or CD-HFD-fed mice ($n=4$ mice/group). Liver endothelium (gray). Scale bar, 20 µm. **j**, Left, representative images of intravital microscopy of 6-week ND- or CD-HFD-fed mice. Analysis of Kupffer cells (violet, violet arrowhead), hyaluronan binding protein (HABP) (red, red arrowhead) and LSECs (blue). Scale bar, 43 µm. Right, representative high-magnification images of intravital microscopy of mice shown in **i**, analysis of Kupffer cells (violet, violet arrowhead), HABP (red, red arrowhead) and LSECs (blue), (ND $n=4$ mice; CD-HFD $n=4$ mice). Scale bar, 43 µm. All data are shown as mean ± s.e.m. All data were analyzed using two-tailed Student's t test.

CD-HFD-fed mice (Supplementary Fig. 6a). Low platelet numbers were found in eWAT and remained unaltered (Supplementary Fig. 6b). CD3$^+$ T cell infiltration was significantly reduced by Asp-Clo (Supplementary Fig. 6c). RNA-seq analysis of eWAT from ND- and CD-HFD-fed mice revealed a different gene expression pattern resulting in spatial separation in the principal component analysis plot. Analysis of the most differentially expressed genes between diets showed upregulation of pathways involved in immune signaling, cell-cell interactions and extracellular matrix regulation in eWAT from CD-HFD-fed mice. In contrast, eWAT of CD-HFD-fed mice showed a significant downregulation in pathways involved in metabolism and antioxidant response (Supplementary Fig. 6d). ALT, AST, liver/body weight ratio, platelet numbers and aggregation state were significantly lower in livers of mice fed CD-HFD/Asp-Clo for 6 and 12 months (Fig. 2b, Supplementary Fig. 4a–d, Supplementary Fig. 7a,b). Asp-Clo significantly improved glucose tolerance (Fig. 2c), reduced liver triglycerides (Fig. 2d) and attenuated serum total cholesterol, LDL and HDL cholesterol (Fig. 2e and Supplementary Fig. 7c,d). Several genes involved in fatty acid β-oxidation, lipolysis and cholesterol metabolism are dysregulated during NASH development[11]. Asp-Clo treatment prevented downregulation of genes from all three groups (Fig. 2f). CD-HFD/Asp-Clo-fed mice lacked statistically significant changes in oxygen consumption, respiratory exchange ratio (RER), physical activity or in food and water intake compared with CD-HFD-fed mice (Fig. 2g,h and Supplementary Fig. 7e). These data were corroborated in WD-HTF-fed mice (Supplementary Fig. 7f,g).

To analyze platelet activation, P-selectin, a marker of α-granule release, and integrin αIIbβ3 activation were analyzed by means of flow cytometry. In Asp-Clo-treated CD-HFD-fed mice, circulating platelets showed markedly reduced integrin αIIbβ3 activation and P-selectin exposure compared with platelets in ND-fed and CD-HFD-fed mice in response to all tested agonists (Supplementary Fig. 8a), suggesting that Asp-Clo treatment effectively reduced platelet activation. Levels of major platelet surface glycoproteins were unchanged (Supplementary Fig. 8b).

MRI analysis revealed subcutaneous/abdominal fat accumulation in CD-HFD-fed and CD-HFD/Asp-Clo-treated mice, but not in ND-fed controls (Fig. 2i). However, liver steatosis was strongly ameliorated by Asp-Clo treatment in CD-HFD-fed mice (Fig. 2i). In contrast, untreated CD-HFD-fed mice displayed histopathological features of NASH, including liver fat deposition (Sudan red$^+$ areas), fibrosis, damaged hepatocytes and lobular inflammation, including satellitosis (Figs. 2j,k and Supplementary Fig. 8c,d). We concluded that Asp-Clo treatment effectively prevented NASH development.

Asp-Clo treatment abrogates intrahepatic immune cell infiltration and inhibits NASH-induced HCC. In addition to hepatic infiltration of CD3$^+$CD8$^+$ T cells, CD11b$^+$ MHCII$^+$ myeloid cells and Ly6G$^+$ granulocytes are increased in CD-HFD-fed mice, similar to human patients with NASH[11]. Immune cell infiltration was reduced in 6-month CD-HFD/Asp-Clo-treated mice (Fig. 3a). Flow cytometry analysis showed strong reduction in total number, effector differentiation (CD8$^+$CD62L$^-$CD44$^+$CD69$^+$) and proportion of CD4$^+$/CD8$^+$ and NKT cells (Fig. 3b,c). B cells remained unchanged in 6-month ND-, CD-HFD- or CD-HFD/Asp-Clo-fed mice (Supplementary Fig. 9a,b).

Analyses of several potentially carcinogenic inflammatory signaling pathways activated under CD-HFD were dampened by Asp-Clo (Fig. 3d and Supplementary Fig. 9c). Asp-Clo significantly reduced CD11b+F4/80^{hi} Kupffer cells in livers of WD-HTF-fed mice (Supplementary Fig. 10a–d). An unbiased *t*-distributed stochastic neighbor embedding (t-SNE)-based clustering approach identified nine myeloid sub-clusters (Supplementary Fig. 11a,b and Supplementary Table 3). Asp-Clo significantly reduced the abundance of cluster 6, characterized by a high expression of CD11b, F4/80 and Gr1, closely resembling CD11b$^+$F4/80$^+$ monocyte-derived macrophages (MoMFs). Further, a multiplex gene expression analysis for FACS-isolated Ly6C$^+$ MoMFs, Ly6C$^-$ MoMFs and Kupffer cells was performed. Principal component analysis of 561 genes revealed similar Ly6C$^+$ MoMFs and Ly6C$^-$ MoMFs in NASH-diet-fed mice with and without Asp/Clo treatment. However, Kupffer cells from WD-HTF/Asp-Clo livers clustered more closely to ND Kupffer cells than those of WD-HTF-fed mice (Supplementary Fig. 11a–d). This finding indicates that Asp-Clo influences the Kupffer cell compartment. Taken together, these data suggest that Asp-Clo treatment attenuated Kupffer cell activation, alongside reduced inflammatory myeloid cell infiltration in the injured liver. Altogether, Asp-Clo prevented NASH, reduced intrahepatic immune cell influx and dampened pathways potentially supporting hepatocarcinogenesis[32].

Next, we studied the effects of Asp-Clo treatment on CD-HFD-induced HCC[11]. Thirteen of 51 CD-HFD livers (~25%) displayed macroscopically visible tumors by 12 months (Fig. 3e–g). In contrast,

Fig. 5 | Intrahepatic platelet accumulation depends on Kupffer cells, hyaluronan and cargo function. a, Representative images of intravital microscopy after treatment (clodronate liposomes (CLL) or hyaluronidase (HYAL)) in 6-week ND-, CD-HFD-, CD-HFD + CLL- or CD-HFD + HYAL-fed mice. Analysis of Kupffer cells (violet), platelets (blue, blue arrowhead), and granulocytes (red), ($n = 4$ mice/group). Scale bar, 40 µm. **b**, H&E and F4/80 staining with quantification and NAS evaluation after treatment in 6-week ND-, CD-HFD-, CD-HFD + CLL- or CD-HFD + HYAL-fed mice (H&E: ND $n = 10$ mice; CD-HFD $n = 14$ mice; CD-HFD + CLL $n = 9$ mice; CD-HFD + HYAL $n = 8$ mice; F4/80: ND $n = 7$ mice; CD-HFD $n = 10$ mice; CD-HFD + CLL $n = 4$ mice; CD-HFD + HYAL $n = 5$ mice). Scale bar: 50 µm. **c**, Quantification of platelet area by intravital microscopy of mice shown in **a** (ND $n = 4$ mice and 40 FOV; CD-HFD $n = 4$ mice and 30 FOV; CD-HFD + CLL $n = 4$ mice and 40 FOV; CD-HFD + HYAL $n = 4$ mice and 30 FOV). **d**, ALT levels of mice shown in **b** (ND $n = 17$ mice; CD-I IFD $n = 13$; CD-I IFD + CLL $n = 7$ mice; CD-I IFD + I IYAL $n = 8$ mice). **e**–**g**, I I&E histology (**e**), ALT levels (**f**) and NAS evaluation (**g**) after anti-CD44 antibody treatment (anti-CD44 antibody blocking (KM81) or non-blocking (IM7) HA-binding site) in 6-week ND-, CD-HFD-, CD-HFD + IM7 (non-HA blocking)-or CD-HFD + KM81 (HA-blocking)-fed mice (ALT: ND $n = 16$ mice; CD-HFD $n = 12$ mice; CD-HFD + IM7 $n = 4$ mice; CD-HFD + KM81 $n = 4$ mice; H&E and NAS: ND $n = 19$ mice; CD-HFD $n = 15$ mice; CD-HFD + IM7 $n = 4$ mice; CD-HFD + KM81 $n = 4$ mice). Scale bars, 50 µm. **h**,**i**, Representative H&E and CD42b staining (**h**) and NAS evaluation and platelet quantification (**i**) after CLL treatment in 6-month CD-HFD -or CD-HFD + CLL-fed mice (H&E and NAS: CD42b: CD-HFD $n = 5$ mice; CD-HFD + CLL $n = 3$ mice; CD42b: CD-HFD $n = 5$ mice; CD-HFD + CLL $n = 3$). **j**, Body weight development of 6-month ND-fed, CD-HFD-fed or CD-HFD/Nbeal2$^{-/-}$ mice (ND $n = 6$ mice; CD-HFD $n = 6$ mice; CD-HFD/Nbeal2$^{-/-}$ $n = 4$ mice). Statistic: ND vs CD-HFD (black asterisks), CD-HFD vs CD-HFD/Nbeal2$^{-/-}$ (blue asterisks). **k**–**m**, ALT, AST levels (**k**) liver triglycerides (**l**) and serum cholesterol (**m**) of mice shown in **i** (ALT: ND $n = 7$ mice; CD-HFD $n = 18$ mice; CD-HFD/Nbeal2$^{-/-}$ $n = 4$ mice; AST: ND $n = 4$ mice; CD-HFD $n = 8$ mice; CD-HFD/Nbeal2$^{-/-}$ $n = 3$ mice; liver triglycerides: ND $n = 5$ mice; CD-HFD $n = 7$ mice; CD-HFD/Nbeal2$^{-/-}$ $n = 4$ mice; serum cholesterol: ND $n = 4$ mice; CD-HFD $n = 11$ mice; CD-HFD/Nbeal2$^{-/-}$ $n = 3$ mice;). **n**, Representative H&E of mice shown in **i** (CD-HFD n = 9 mice; CD-HFD/Nbeal2$^{-/-}$ $n = 10$ mice), damaged hepatocytes (asterisks) are indicated. Scale bar, 50 µm. **o**, Fat quantification by Sudan red staining of mice shown in **i** (ND $n = 4$ mice and 17 fields; CD-HFD $n = 4$ mice and 14 fields; CD-HFD/Nbeal2$^{-/-}$ $n = 4$ mice and 35 fields). Scale bar, 100 µm. All data are shown as mean ± s.e.m. Data in **b**–**d**,**f**,**g**,**k**–**m**,**o** were analyzed by one-way ANOVA with the post hoc Tukey's multiple comparison test. Data in **i** were analyzed using two-tailed Student's *t* test. Data in **j** were analyzed using two-way analysis of variance with the post hoc Tukey's multiple comparison test. *$P < 0.05$, **$P < 0.01$, ***$P < 0.001$, ****$P < 0.0001$.

CD-HFD/Asp-Clo-treated mice lacked macro- and microscopically visible liver tumors (Fig. 3e–g and Supplementary Fig. 12a). CD-HFD-fed mice treated with a lower dose of Asp-Clo (according to the initial body weight and not further adjusted to diet or age-related weight gain) developed significantly fewer HCC (3/52) compared with untreated CD-HFD-fed mice (13/51) (Supplementary Fig. 12b). Therefore, continuously adjusting the dose of Asp-Clo to body weight is critical to fully prevent HCC.

Asp/Clo dampens hepatic cytokine expression, platelet–liver endothelium and platelet–immune cell interactions. Gene expression and signaling pathway analyses of ND, CD-HFD and WD-HTF

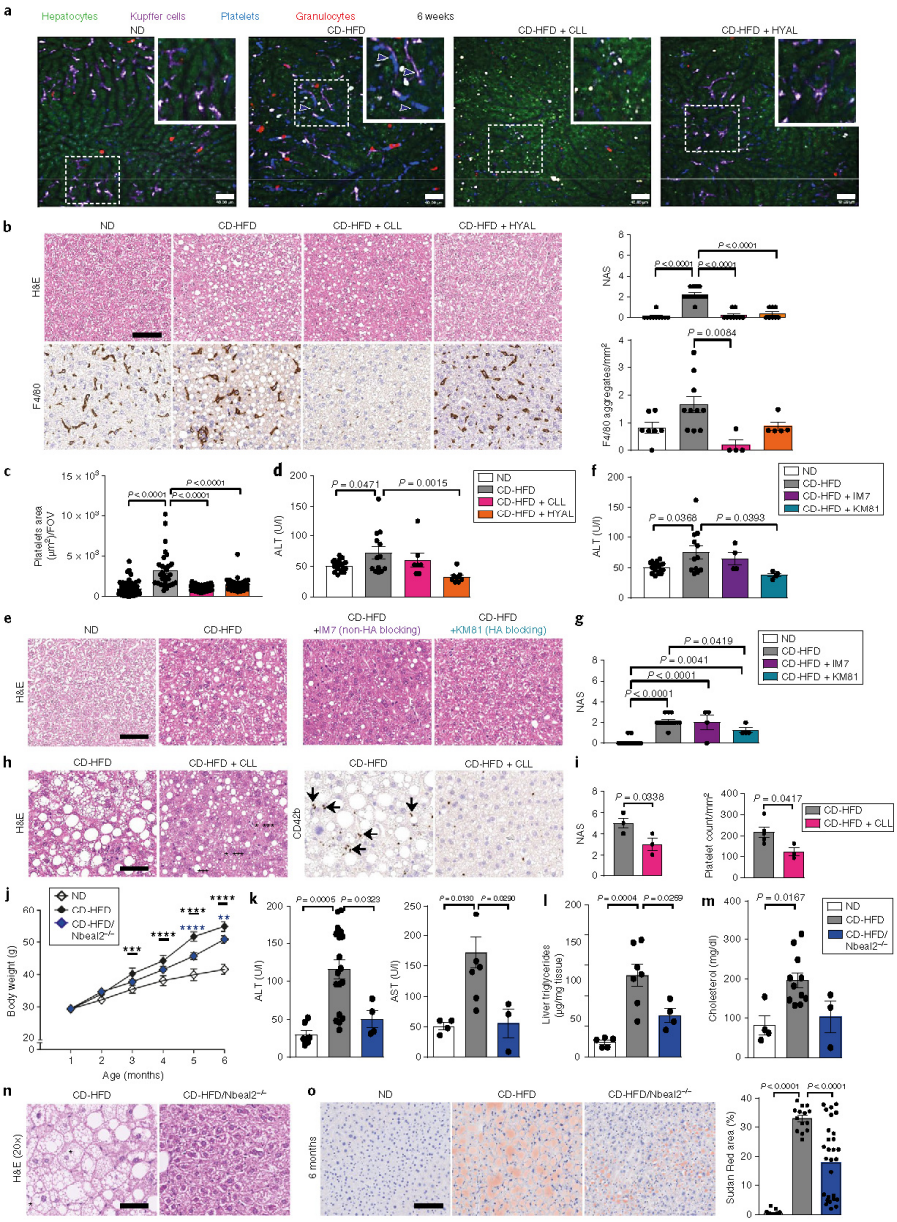

livers revealed a significant induction in gene expression profiles involved in platelet activation, aggregation and degranulation (Extended Data Fig. 1a–i). Moreover, NASH-related enrichment of genes was associated with expression of TNF superfamily members, cytokine and chemokine production and chemotaxis[11,27] (Extended Data Fig. 1a–i). Asp-Clo treatment significantly attenuated the latter, some of which are also released from activated platelets (e.g., CCL5, TGFβ)[33] (Supplementary Fig. 13a).

Coupling high-resolution confocal microscopy and 3D reconstruction of liver sinusoids enabled visualization and quantification of platelet interactions with the liver endothelium and immune cells. Asp-Clo reduced NASH-related increase of platelet interaction with the liver endothelium, T cells and innate immune cells (Supplementary Fig. 13b–f and 14a,b).

To exclude COX2-dependent effects of Asp-Clo, we used another NSAID/COX1/2 inhibitor, sulindac. CD-HFD/sulindac-treated mice exhibit obesity; no significant changes in liver/body weight ratio, hepatic triglycerides and glucose tolerance; no significant alteration in gene expression involved in metabolism; severe steatosis; and increased liver damage comparable to that of CD-HFD-fed mice (Extended Data Fig. 2a–f). Thus, Asp/Clo-mediated effects on NASH are COX independent.

To corroborate our results with another platelet inhibitor, CD-HFD-fed mice were treated with ticagrelor (CD-HFD/ticagrelor), an FDA-approved direct and reversible antagonist of the platelet P2Y12 receptor[34] for coronary artery disease used in the clinic (e.g., with ASA after coronary stent implantation in patients presenting with an acute coronary syndrome without increased bleeding risk)[35]. Intrahepatic platelet number, platelet/liver endothelium coverage, platelet aggregation, liver damage, liver triglycerides and serum cholesterol were significantly reduced in ticagrelor-treated mice, whereas very-low-density lipoprotein secretion was not affected (Extended Data Fig. 3a–h). Expression of genes involved in cholesterol metabolism, 'de novo' lipogenesis and lipid storage were unchanged by the treatment, whereas downregulation of several genes involved in fatty acid oxidation and lipolysis that occurs in CD-HFD-fed mice (Extended Data Fig. 3i,j) and in histopathological features of NASH were prevented by ticagrelor (Supplementary Fig. 15a–c). Total numbers, activation and proportion of $CD4^+$/$CD8^+$, $CD8^+CD62L^-CD44^+CD69^+$ and $CD3^+NK1.1^+$ cells were also reduced (Supplementary Fig. 15d,e). In contrast to liver tissues, increased expression of genes involved in inflammation and fibrosis was found in eWAT from CD-HFD- and WD-HTF-fed mice receiving Asp-Clo or ticagrelor (Supplementary Fig. 15f). This finding indicates that APT is beneficial specifically to the liver, affecting intrahepatic platelets and immune cell infiltration and improving hepatic steatosis by maintaining normal expression of genes involved in lipid catabolism.

We next investigated whether ticagrelor would affect NASH-to-HCC transition. Compared with that in untreated CD-HFD-fed mice, ticagrelor treatment significantly reduced HCC development. One tumor was detected in 29 livers of CD-HFD/ticagrelor-treated mice (Supplementary Fig. 16a). The therapeutic potential of ticagrelor was tested in CD-HFD-fed mice with fully established NASH (4-month CD-HFD), followed by 8 weeks of ticagrelor treatment with CD-HFD. Intrahepatic platelet numbers, NAS and liver damage were reduced, but no difference in glucose tolerance was found (Supplementary Fig. 17a,b), and no effect on the blood immune cell populations was observed (Supplementary Fig. 17c). Similar results were obtained with therapeutic ticagrelor treatment in the context of a WD-HTF and of fibrosis; no difference in whole-body metabolism was found upon ticagrelor treatment in CD-HFD or WD-HTF mice (Supplementary Figs. 17d,e and 18a,b).

Early platelet recruitment in fatty liver correlates with liver damage, hepatocyte swelling and reduced sinusoidal diameter. To understand the dynamics of intrahepatic platelet recruitment and attachment during the initial events of NAFL preceding NASH, we performed intravital microscopy in CD-HFD or WD-HTF-fed mice over 4, 5, 6 and 8 weeks post diet induction (Fig. 4a and Supplementary Fig. 19a–c). Platelets were the first non-resident cell type to populate the liver at ≤4 weeks post diet induction in both CD-HFD- and WD-HTF-fed mice (Fig. 4a–d and Supplementary

Fig. 6 | Anti-GPIbα antibody treatment as well as genetic dysfunction of GPIbα reduces NASH, fibrosis and HCC development. a, Representative 3D confocal images of GPIbα (green, green arrowheads) and Kupffer cells (red, red arrowheads) interaction of 6-month ND- or CD-HFD-fed mice (ND $n=4$ mice; CD-HFD $n=4$ mice). Liver endothelium (gray), scale bar, 30 µm. **b**, High-magnification 3D confocal images and quantification of GPIbα (green)/Kupffer cells (red) and GPIbα (green)/LSECs (gray) interaction in 6-month ND- or CD-HFD-fed mice (ND $n=4$ mice and 2 FOV/mouse; CD-HFD $n=4$ mice and 2 FOV/mouse) Scale bar, 3 µm. For visualization of intravascular events, the transparency of the sinusoidal rendering was set to 50%. **c**, Representative H&E and CD42b staining after 5 weeks of GPIbα blocking or control Fab in 6-month CD-HFD-fed mice; scale bar, 50 µm. Platelets are indicated by arrows. **d**–**h**, Platelet quantification (**d**), NAS evaluation (**e**), ALT levels (**f**), liver triglycerides (**g**) and quantification of Sirius red–positive areas (**h**) of mice shown in **c** (CD42b staining and platelet quantification: CD-HFD + control Fab $n=8$ mice; CD-HFD + GPIbα blocking Fab $n=8$ mice; H&E, NAS and ALT: CD-HFD + control Fab $n=5$ mice; CD-HFD + GPIbα blocking Fab $n=4$ mice; liver triglycerides: CD-HFD + control Fab $n=4$ mice; CD-HFD + GPIbα blocking Fab $n=4$ mice; Fibrosis: CD-HFD + control Fab $n=5$ mice; CD-HFD + GPIbα blocking Fab $n=4$ mice). **i**,**j**, Serum cholesterol, liver triglycerides (**i**) and ALT levels (**j**) of 6-month ND, CD-HFD- or CD-HFD/*hIL4rα/GPIbα*-Tg mice (serum cholesterol: ND $n=4$ mice; CD-HFD $n=5$ mice; CD-HFD/*hIL4rα/GPIbα*-Tg $n=4$ mice; liver triglycerides: ND $n=6$ mice; CD-HFD $n=5$ mice; CD-HFD/*hIL4rα/GPIbα*-Tg $n=4$ mice; ALT: ND $n=4$ mice; CD-HFD $n=3$ mice; CD-HFD/*hIL4rα/GPIbα*-Tg $n=4$ mice). **k**, Quantification by flow cytometry of intrahepatic immune cells (CD8+ T cells (left), activated $CD8^+$ T cells (middle), NKT cells (right)) of mice shown in **i** ($CD8^+$, activated $CD8^+$ and NKT cells: ND $n=3$ mice; CD-HFD $n=3$ mice; CD-HFD/*hIL4rα/GPIbα*-Tg $n=4$ mice). **l**, Representative H&E staining of mice shown in **i**, indications of damaged hepatocytes (asterisks) and satellitosis (arrows); scale bars, 100 µm in 10× and 25 µm in 40×. **m**–**o**, Sudan red staining (**m**) and quantification of Sudan red–positive areas (**n**), NAS evaluation (**o**) of 6-month ND, CD-HFD or CD-HFD/*hIL4rα/GPIbα*-Tg mice (H&E and NAS: ND $n=7$ mice; CD-HFD $n=13$ mice; CD-HFD/*hIL4rα/GPIbα*-Tg $n=8$ mice; Sudan red staining and quantification: $n=5$ mice/group). **p**,**q**, Fibrosis quantification (**p**) and Sirius red staining (**q**) of 12-month ND, CD-HFD or CD-HFD/*hIL4rα/GPIbα*-Tg mice (H&E and NAS: ND $n=7$ mice; CD-HFD $n=13$ mice; CD-HFD/*hIL4rα/GPIbα*-Tg $n=8$ mice; Sudan red: $n=5$ mice/group; fibrosis and Sirius red: ND $n=4$ mice; CD-HFD $n=9$ mice; CD-HFD/*hIL4rα/GPIbα*-Tg $n=10$ mice). **r**, ALT levels of 12-month ND, CD-HFD or CD-HFD/*hIL4rα/GPIbα*-Tg mice (ND $n=12$ mice; CD-HFD $n=16$ mice; CD-HFD/*hIL4rα/GPIbα*-Tg $n=9$ mice). **s**, Macroscopical images of tumors of mice shown in **r**; tumor nodules are indicated by arrowhead) (CD-HFD: $n=13$ tumors in 52 mice; CD-HFD/*hIL4rα/GPIbα*-Tg: $n=0$ tumors in 24 mice); scale bar, 750 µm. **t**, HCC characterization by CD44v6, Collagen IV (Coll IV) and Ki67 staining form mice shown in **r**. Arrowheads indicate positive hepatocytes, dashed line indicates tumor (T) border; scale bar, 200 µm (CD44v6 and Coll IV), 50 µm (Ki67). **u**, HCC incidence (T = HCC; NT = non-tumor) from 12-month CD-HFD-fed or CD-HFD/*hIL4rα/GPIbα*-Tg mice, CD-HFD: $n=13$ tumors in 52 mice; CD-HFD/*hIL4rα/GPIbα*-Tg: $n=0$ tumors in 24 mice). All data are shown as mean ± s.e.m. Data in **b**,**d**–**h** were analyzed by two-tailed Student's *t* test. Data in **i**–**k**,**n**–**p**,**r** were analyzed by one-way ANOVA with the post hoc Tukey's multiple comparison test. Data in **u** were analyzed by two-sided Fisher's exact test.

Fig. 19a–c). Platelets progressively aggregated and increased in number in liver sinusoids over 8 weeks in the absence of significantly elevated CD3$^+$ T cells or Ly6G$^+$ granulocytes (Fig. 4a–d and Supplementary Fig. 19a–c). Even at this early stage, mild steatosis, reduced sinusoidal diameter and hepatocyte swelling were observed (Fig. 4e,f and Supplementary Fig. 19e). NAS and liver triglycerides were increased in CD-HFD- and WD-HTF-fed mice (Fig. 4g,h and Supplementary Fig. 19d–f). Platelets interacted primarily with Kupffer cells, as determined by 3D high-resolution reconstruction (Fig. 4i). Although intrahepatic granulocyte numbers remained unaltered in the first 8 weeks post diet induction, granulocytes might still support intrahepatic platelet recruitment and NAFL and NASH induction. Administration of anti-Ly6G antibodies via osmotic pumps for 8 weeks to CD-HFD-fed mice did not reduce intrahepatic platelet numbers but successfully reduced granulocytes. Experiments revealed no significant role of granulocytes in the early development of NAFL and borderline NASH (Supplementary Fig. 20a–e).

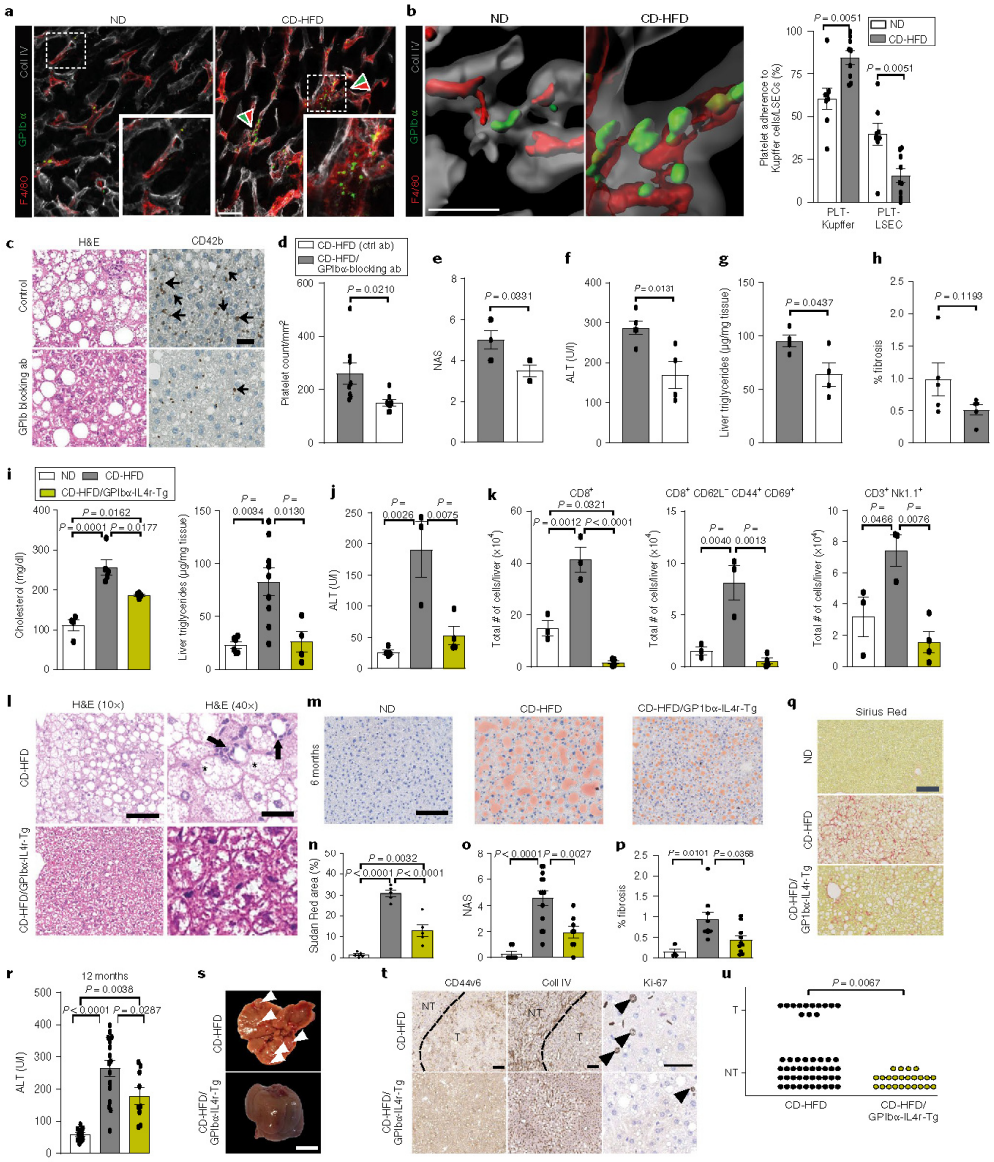

We next screened for possible adhesion molecules and danger markers responsible for early platelet attachment and recruitment. We found progressive induction of the extracellular matrix component hyaluronan colocalizing with hepatocytes, Kupffer cells and, to a lesser degree, on liver sinusoidal endothelial cells (LSECs) (Fig. 4j).

Kupffer cell-dependent platelet recruitment involving hyaluronan-CD44 binding supports early and advanced stages of NAFL including NASH. To investigate the functional role of Kupffer cells and molecules involved in platelet–LSEC and platelet–immune cell interaction (e.g., hyaluronan, CD44) in borderline NASH, CD-HFD- or WD-HTF-fed mice were treated with clodronate liposomes (CLL), control liposomes (CL), hyaluronidase (HYAL), HYAL/CLL (double treatment), CD44-binding/HA-blocking AB (clone KM81) or CD44-binding/HA-non-blocking AB (clone IM7), for control (Fig. 5a and Supplementary Fig. 21a,b). Treatment with CLL and CLL/HYAL, but not CL reduced Kupffer cell numbers in CD-HFD- and WD-HTF-fed mice (Fig. 5b and Supplementary Fig. 21c,d). CLL and HYAL reduced NAS significantly in CD-HFD- and WD-HTF-fed mice (Fig. 5b and Supplementary Fig. 21d). CLL and HYAL treatments significantly reduced intrahepatic platelets (Fig. 5c); a significant reduction in liver damage was found following HYAL but not CLL (Fig. 5d). Combined treatment with both CLL and HYAL did not result in a further decrease of platelet numbers (Supplementary Fig. 21f,g). Similar data (platelet reduction and NAS reduction) with CLL treatment were obtained using WD-HTF-fed mice, although ALT levels remained elevated (Supplementary Fig. 21d,e). Also, treatment with a CD44-binding/HA-blocking, but not with a CD44-binding/HA non-blocking antibody led to a reduction in NAS and liver damage (Fig. 5e–g).

Notably, significantly reduced NAS, platelet accumulation, triglycerides, and liver damage by CLL treatment in mice fed CD-HFD for 6 months demonstrate a potential therapeutic effect of CLL even in a short treatment scheme (Fig. 5h,i and Supplementary Fig. 22). These data imply that Kupffer cells, hyaluronan and CD44 are important players in the early and advanced stages of NAFL, including NASH.

Platelet cargo is indispensable for NASH development. Platelets release bioactive factors from intracellular granules in response to cellular activation. During thrombo-inflammatory reactions, the mostly proteinous components of α-granules are essential for immune cell recruitment and tissue damage[36]. Nbeal2-knockout mice (*Nbeal2*$^{-/-}$), which lack α-granules in platelets and are thus protected from thrombosis and thrombo-inflammatory tissue damage[37–39] were on a CD-HFD for 6 months. CD-HFD-fed *Nbeal2*$^{-/-}$ mice displayed no significant difference in intrahepatic platelet number or aggregation and gained weight similarly to CD-HFD-fed controls (Fig. 5j and Supplementary Fig. 23a). Still, significantly lower serum ALT and AST levels were found in CD-HFD-fed *Nbeal2*$^{-/-}$ mice compared with those in CD-HFD-fed mice (Fig. 5k). This finding was paralleled by a significant decrease in liver triglycerides, lower serum cholesterol (Fig. 5l,m), and improved glucose tolerance in CD-HFD-fed *Nbeal2*$^{-/-}$ mice (Supplementary Fig. 23b). Deregulation of lipid metabolism genes found in CD-HFD livers was partially prevented in CD-HFD-fed *Nbeal2*$^{-/-}$ mice (Supplementary Fig. 23c). CD-HFD *Nbeal2*$^{-/-}$ livers lacked steatosis and NASH and displayed a lower NAS (Fig. 5n and Supplementary Fig. 23d). Suppression of NASH in *Nbeal2*$^{-/-}$ mice on CD-HFD was corroborated by significant diminution of lipid content (Fig. 5o). Decreased T cell infiltration, neutrophil accumulation and macrophage activation were found in *Nbeal2*$^{-/-}$ mice on CD-HFD (Supplementary Fig. 23e). Together, these results indicated that platelet α-granule components contribute to NASH.

CD-HFD-induced NASH could not be rescued in mice lacking the GPIIb subunit of the platelet fibrinogen receptor GPIIb/IIIa (integrin α2β3; *Itga2b*$^{-/-}$ mice) which harbors activatable platelets unable to aggregate (Extended Data Fig. 4). This is in agreement with a recent study indicating that deletion of the platelet integrin α2β3 binding motif of fibrinogen did not alter NASH[40].

Moreover, mice lacking the activating platelet collagen receptor glycoprotein VI (GPVI; *Gp6*$^{-/-}$)[41], the platelet-derived C-type lectin-like receptor 2 (*Clec-2*$^{-/-}$) or the hematopoietic cell–specific podoplanin (*Pdpn*$^{-/-}$) all developed NASH and NASH-associated conditions upon CD-HFD feeding (Extended Data Figs. 5–6).

Mucosal vascular addressin cell adhesion molecule 1 (MAdCAM-1) was recently discovered as an important player in NASH[42]. Animals with genetic depletion of MAdCAM-1 presented lower NAS and less liver damage after 6-month of WD-HTF[42]. We analyzed livers of WD-HTF-fed mice lacking MAdCAM-1 (*MAdCAM-1*$^{-/-}$), L-selectin (*L-sel*$^{-/-}$), integrin beta7 (*β7*$^{-/-}$) and both L-selectin and integrin beta7 (*L-sel/β7*$^{-/-}$). *MAdCAM-1*$^{-/-}$ mice displayed significantly reduced intrahepatic platelet numbers correlating with a partial protection from NASH (Extended Data Fig. 7a,b). In contrast, deletion of MAdCAM-1 ligands integrin beta7, L-selectin and L-selectin/integrin beta7 did not affect intrahepatic platelet numbers or platelet aggregation and did not prevent, or only partially prevented, NASH (Extended Data Fig. 7a, b).

Platelet GPIbα and α-granules are required to induce NASH. Our data demonstrate that intrahepatic interaction of platelets with Kupffer cells, involving hyaluronan/CD44 binding and platelet cargo function, but not platelet aggregation contribute to NASH. Platelet-derived GPIbα has been implicated in platelet attachment and activation[43].

We thus hypothesized that GPIbα might mediate early platelet-trafficking/activation in NASH livers[43]. We first analyzed the interaction of GPIbα with parenchymal and non-parenchymal liver cells (LSECs; Kupffer cells, etc.) in NASH. 3D reconstruction revealed that the most abundant interactions of GPIbα^{+} platelets were with Kupffer cells and less so with LSECs in mouse and human NASH samples (Fig. 6a,b; Supplementary Fig. 24a).

Thus, we blocked the major ligand binding domain of GPIbα in 6-month CD-HFD-fed mice therapeutically using antigen-binding fragments (Fab) of the anti-GPIbα antibody pop/B[44] for 5 weeks. Notably, this short therapeutic treatment significantly reduced intrahepatic platelet accumulation in the presence of CD-HFD (Fig. 6c,d). Consequently, steatosis, NAS, liver damage, liver triglycerides and intrahepatic immune cell infiltration were reduced; fibrosis was dampened (Fig. 6c–h and Supplementary Fig. 24b–d). Additionally, anti-GPIbα antibody treatment reduced intrahepatic protein expression of several pro-inflammatory and homeostatic cytokines and chemokines, including CCL5, CCL6, ICAM-1, P-selectin and CD40, linking intrahepatic platelet activation and Nbeal2-dependent cargo release with mediators of inflammation (Supplementary Fig. 24e).

We next tested whether therapeutic anti-GPIbα antibody treatment would prevent fatty liver-to-NASH transition in early disease progression (e.g., after 6-week CD-HFD; Fig. 4). However, these treatments did not ameliorate NAFL/ borderline NASH, most likely due to lack or low expression of yet unidentified GPIbα ligands at early disease stages (Supplementary Fig. 24f,g). These data highlight distinct mechanisms of platelet recruitment in early versus established NAFL/borderline NASH—still involving Kupffer cells at both disease stages.

To corroborate the above data in a genetic model, we fed transgenic mice expressing an IL-4rα/GPIbα fusion-protein in a *GPIbα*$^{-/-}$ background[45] in which the ligand-binding ectodomain of GPIbα is replaced by the α-subunit of the human IL-4 receptor (*hIL4rα/GPIbα*-Tg)[45] with a CD-HFD for 6 months. Remarkably, platelet aggregate size, platelet area and platelet–liver endothelium coverage were significantly lower in CD-HFD-fed *hIL4Rα/GPIbα*-Tg

mice compared with those off CD-HFD-fed C57Bl/6 controls (Supplementary Fig. 25a–c). Both *hIL4rα/GPIbα*-Tg and C57Bl/6 mice gained weight similarly when fed a CD-HFD (Supplementary Fig. 25d). Serum cholesterol, liver triglycerides, serum ALT and AST levels were significantly lower in CD-HFD/*hIL4rα/GPIbα*-Tg mice (Fig. 6i,j; Supplementary Fig. 25e), accompanied by less LDL and HDL cholesterol (Supplementary Fig. 25e). Similarly, dysregulated mRNA expression of lipid metabolism-related genes in livers of CD-HFD-fed C57BL/6 mice was prevented in livers of CD-HFD/*hIL4rα/GPIbα*-Tg mice (Supplementary Fig. 25f). We also observed strong and significant reductions in intrahepatic $CD8^+$ T and NKT cells by flow cytometry analysis (Fig. 6k). Reduced $CD3^+$ and reduced macrophage influx and activation were observed using immunohistochemistry (Supplementary Fig. 25g,h). CD-HFD/*hIL4rα/GPIbα*-Tg mice showed lower intrahepatic protein expression of several pro-inflammatory and homeostatic cytokines and chemokines, including CCL5, CD40 and TNFRSF11B (Supplementary Fig. 25i), mechanistically linking platelet attachment and activation and cytokine and chemokine expression to efficient intrahepatic immune cell attraction. CD-HFD/*hIL4rα/GPIbα*-Tg mice lacked histological features of NASH, paralleled by a reduction in lipid accumulation and absence of macrovesicular steatosis analyzed by H&E and Sudan red staining (Fig. 6l–o).

Notably, mice lacking the major platelet adhesion receptors P-selectin ($Selp^{-/-}$)[46], von-Willebrand-factor ($vWF^{-/-}$)[47] or Mac-1 ($Mac\text{-}1^{-/-}$)[48], the known ligands of GPIbα, displayed full-blown NASH after 6 months of CD-HFD (Extended Data Figs. 8–10).

Finally, we investigated whether *hIL4rα/GPIbα*-Tg mice would develop HCC upon long-term CD-HFD. Of note, *hIL4rα/GPIbα*-Tg mice receiving CD-HFD for 12 months displayed significantly lower fibrosis and serum ALT, and lacked any macro- or microscopic evidence of HCC (Fig. 6p–u).

Discussion

It is becoming increasingly clear that beyond their central role in hemostasis and wound repair after vascular injury[49], platelets are key players in multiple pathophysiological conditions[16–18,20], including cytotoxic T lymphocyte–mediated liver damage and associated pathologies[18]. Here, we identified Kupffer cells as key players in intrahepatic platelet recruitment in early and advanced stages of NAFL, borderline NASH and NASH. In early NAFL and borderline NASH, hyaluronan and CD44 binding are also involved. In late NASH, GPIbα expressed by platelets appears to be primarily involved in the interaction of platelets with Kupffer cells and in the maintenance of NASH. Thus, Kupffer cells play distinct roles in intrahepatic platelet recruitment at different NAFLD stages.

We found no evidence for a role of platelet-derived GPIIb/IIIa ($Itga2b^{-/-}$ mice) in NASH, suggesting that platelet activation and adhesion are important, whereas platelet aggregation is dispensable.

What is the function of platelets recruited to the liver? Our results indicate a major contribution of the platelet cargo function (α-granule components) in NASH progression, exemplified by the marked protection of $Nbeal2^{-/-}$ mice. The exact nature of platelet-derived α-granule constituents is currently unclear. However, several chemokines and cytokines were reduced upon therapeutic anti-GPIbα antibody treatment in the liver, suggesting that the number and activation state of intrahepatic platelets directly or indirectly correlate with an increase in immune cell–attracting chemokines and cytokines.

The key role of GPIbα in NASH identified in this study parallels a similarly vital function of this receptor in the development of experimental autoimmune encephalomyelitis (EAE), where it orchestrates the recruitment of leukocytes to the inflamed CNS[50]. Our results, similar to those of the EAE study, argue against a key role of the three known cognate interaction partners of GPIbα: P-selectin, vWF and Mac-1 (refs. [48,51,52]) and point to a GPIbα-activation-dependent proinflammatory function of α-granules in intrahepatic immune cell attraction.

Selectins have also been shown to be dispensable for leukocyte recruitment in inflamed liver microvasculature[53]. Other interaction partners might be involved (e.g., coagulation factors XI, XII). It is also conceivable that GPIbα exerts its function in disease development independent of an ectopic ligand[54]. Moreover, due to the complex pathogenesis underlying NASH, it is plausible that GPIbα is not the only molecule involved. Mice lacking MAdCAM-1 ($MAdCAM\text{-}1^{-/-}$) also showed significantly reduced intrahepatic platelet infiltration, but the exact mechanisms by which this occurs is unknown.

Cholesterol also plays a pivotal role during NASH pathogenesis by inducing hepatic lipotoxicity[55]. Notably, different Western diets (e.g., HTF and NTF) with high cholesterol recapitulated platelet-dependent phenotypes (increased intrahepatic platelets and responsiveness to therapeutic APT) described in the CD-HFD, but with a more pronounced NASH phenotype with higher NAS and fibrosis.

Of note, platelets and platelet-derived GPIbα are potential therapeutic targets of NASH and subsequent HCC development. Although GPIbα-antibody treatment induces prolonged bleeding time, it does not induce spontaneous bleeding[44], as only one GPIbα epitope is blocked, leaving receptor function largely intact. Thus, GPIbα antibody is a potentially safe new treatment modality against a metabolic disease of major public health burden[4,9]. So far, there is no drug treatment available specifically targeting NASH. The use of pioglitazone (most promising drug so far, off-label outside type II diabetes mellitus because of side effects) or vitamin E (better safety and tolerability in the short term) or combination thereof could be used for NASH treatment[4,56]. Other agents such as obeticholic acid have also improved histological features of NASH, although data with respect to their long-term benefits are still awaited[57]. Combined therapies for NASH treatment are currently being pursued, as only a subset of patients respond well to monotherapies[5]. This might be overcome by stratifying more responsive patients to a given monotherapy or by utilizing multitarget drugs. A viable approach might be a metabolic target in combination with an anti-inflammatory or anti-fibrotic drug, such as APT and statins, as described in our pilot case study. Nevertheless, given that APT and anti-GPIbα treatment attenuated metabolic dysfunction, inflammation and fibrosis, these modalities constitute potential monotherapies against NASH. Although a risk for bleeding cannot be excluded for both, which warrants careful monitoring, a single-substance therapy is expected to harbor a lower risk of side effects compared with combined therapies.

Given that only a proportion of patients with NAFLD progress to NASH and HCC, the question remains at which stage of NAFLD such treatments should be initiated. Future studies are needed not only to identify novel druggable targets for NASH and HCC, but also to identify non-invasive biomarkers for detection of early NAFLD and NASH, when it is still amenable to therapeutic intervention. It was recently demonstrated that higher serum ALT correlated with HCC development not only in a mouse model of chronic liver cell damage, but also in patients with chronic liver disease of diverse etiology including NASH[11,58].

Prophylactic APT, commonly used for acute and long-term treatment of coronary artery disease[59], and ticagrelor attenuate NASH and NASH-induced HCC[16]. In contrast, sulindac did not prevent NASH in mice. Thus, rather than NSAIDs in general, therapies that specifically block intrahepatic platelet accumulation or platelet function seem to be required to prevent NASH and NASH-associated conditions.

For NASH, we also observed a therapeutic effect of APT in preventing NASH-triggered HCC (although potential therapeutic effects of APT in the context of pre-existing HCC was not tested)[60]. Similarly, we have observed a therapeutic anti-NASH effect of

anti-GPIbα antibody treatment. Remarkably, in both cases, therapeutic treatment partially dampened fibrosis.

Furthermore, in a small prospective human cohort study, APT reduced liver volume and liver fat accumulation in patients with NAFLD, thus supporting the results of our murine in vivo experiments. The results of this pilot case study, being a starting point for further studies, have to be interpreted with caution as it is currently underpowered. Although a multivariate analysis on a small patient cohort inherently warrants careful interpretation, our data have shown that effects of anti-aggregation were stronger than those of statin administration.

In our study, NASH prevention (e.g., by two distinct APTs, ticagrelor and Asp/Clo, in hIL4rα/GP1bα-Tg mice) ultimately suppressed subsequent HCC formation, mostly because the pro-carcinogenic NASH-related environment (e.g., intrahepatic inflammation, signaling, hepatocyte damage) was lacking. Moreover, treatment with anti-GPIbα antibody or depletion of Kupffer cells abrogated NASH therapeutically. These approaches might have an important impact for chemo-preventive strategies, which are still lacking in NASH treatment. Thus, our findings provide a rationale for APT, P2Y12 antagonists or reagents directly blocking platelet-derived GPIbα or related pathways as possible therapeutic approaches for patients with NASH, not only to prevent or revert NASH but also to prevent NASH-to-HCC transition.

Online content

Any methods, additional references, Nature Research reporting summaries, source data, statements of data availability and associated accession codes are available at https://doi.org/10.1038/s41591-019-0379-5.

Received: 14 September 2017; Accepted: 28 January 2019;
Published online: 1 April 2019

References

1. Fleet, S. E., Lefkowitch, J. H. & Lavine, J. E. Current concepts in pediatric nonalcoholic fatty liver disease. *Gastroenterol. Clin. North Am.* **46**, 217–231 (2017).
2. European Association for the Study of the Liver, European Association for the Study of Diabetes & European Association for the Study of Obesity. EASL-EASD-EASO Clinical Practice Guidelines for the management of non-alcoholic fatty liver disease. *J. Hepatol.* **64**, 1388–1402 (2016).
3. Younossi, Z. et al. Global perspectives on non-alcoholic fatty liver disease and non-alcoholic steatohepatitis. *Hepatology* https://doi.org/10.1002/hep.30251 (2018).
4. Brunt, E. M. et al. Nonalcoholic fatty liver disease. *Nat. Rev. Dis. Primers* **1**, 15080 (2015).
5. Friedman, S. L., Neuschwander-Tetri, B. A., Rinella, M. & Sanyal, A. J. Mechanisms of NAFLD development and therapeutic strategies. *Nat. Med.* **24**, 908–922 (2018).
6. El-Serag, H. B. & Kanwal, F. Epidemiology of hepatocellular carcinoma in the United States: where are we? Where do we go? *Hepatology* **60**, 1767–1775 (2014).
7. Torre, L. A. et al. Global cancer statistics, 2012. *CA Cancer J. Clin.* **65**, 87–108 (2015).
8. Ozakyol, A. Global epidemiology of hepatocellular carcinoma (HCC epidemiology). *J. Gastrointest. Cancer* **48**, 238–240 (2017).
9. Ashfin, A. et al. Health effects of overweight and obesity in 195 countries over 25 years. *N. Engl. J. Med.* **377**, 13–27 (2017).
10. Ringelhan, M., Pfister, D., O'Connor, T., Pikarsky, E. & Heikenwalder, M. The immunology of hepatocellular carcinoma. *Nat. Immunol.* **19**, 222–232 (2018).
11. Wolf, M. J. et al. Metabolic activation of intrahepatic CD8+ T cells and NKT cells causes nonalcoholic steatohepatitis and liver cancer via cross-talk with hepatocytes. *Cancer Cell.* **26**, 549–564 (2014).
12. Michelson, A. D. How platelets work: platelet function and dysfunction. *J. Thromb. Thrombolysis* **16**, 7–12 (2003).
13. Chauhan, A., Adams, D. H., Watson, S. P. & Lalor, P. F. Platelets: no longer bystanders in liver disease. *Hepatology* **64**, 1774–1784 (2016).
14. Gawaz, M., Langer, H. & May, A. E. Platelets in inflammation and atherogenesis. *J. Clin. Invest.* **115**, 3378–3384 (2005).
15. Jackson, S. P. Arterial thrombosis—insidious, unpredictable and deadly. *Nat. Med.* **17**, 1423–1436 (2011).
16. Fujita, K. et al. Effectiveness of antiplatelet drugs against experimental non-alcoholic fatty liver disease. *Gut* **57**, 1583–1591 (2008).
17. Lang, P. A. et al. Aggravation of viral hepatitis by platelet-derived serotonin. *Nat. Med.* **14**, 756–761 (2008).
18. Iannacone, M. et al. Platelets mediate cytotoxic T lymphocyte-induced liver damage. *Nat. Med.* **11**, 1167–1169 (2005).
19. Iannacone, M., Sitia, G., Narvaiza, I., Ruggeri, Z. M. & Guidotti, L. G. Antiplatelet drug therapy moderates immune-mediated liver disease and inhibits viral clearance in mice infected with a replication-deficient adenovirus. *Clin. Vaccine Immunol.* **14**, 1532–1535 (2007).
20. Sitia, G. et al. Antiplatelet therapy prevents hepatocellular carcinoma and improves survival in a mouse model of chronic hepatitis B. *Proc. Natl Acad. Sci. USA* **109**, E2165–E2172 (2012).
21. Shen, H., Shahzad, G., Jawairia, M., Bostick, R. M. & Mustacchia, P. Association between aspirin use and the prevalence of nonalcoholic fatty liver disease: a cross-sectional study from the third national health and nutrition examination survey. *Aliment. Pharmacol. Ther.* **40**, 1066–1073 (2014).
22. Musso, G., Cassader, M., Rosina, F. & Gambino, R. Impact of current treatments on liver disease, glucose metabolism and cardiovascular risk in non-alcoholic fatty liver disease (NAFLD): a systematic review and meta-analysis of randomised trials. *Diabetologia* **55**, 885–904 (2012).
23. Wong, V. W. et al. Pathogenesis and novel treatment options for non-alcoholic steatohepatitis. *Lancet Gastroenterol. Hepatol.* **1**, 56–67 (2016).
24. Clapper, J. R. et al. Diet-induced mouse model of fatty liver disease and nonalcoholic steatohepatitis reflecting clinical disease progression and methods of assessment. *Am. J. Physiol. Gastrointest. Liver Physiol.* **305**, G483–G495 (2013).
25. Wang, B. et al. Intestinal phospholipid remodeling is required for dietary-lipid uptake and survival on a high-fat diet. *Cell. Metab.* **23**, 492–504 (2016).
26. Weston, C. J. et al. Vascular adhesion protein-1 promotes liver inflammation and drives hepatic fibrosis. *J. Clin. Invest.* **125**, 501–520 (2015).
27. Gomes, A. L. et al. Metabolic inflammation-associated il-17a causes non-alcoholic steatohepatitis and hepatocellular carcinoma. *Cancer Cell.* **30**, 161–175 (2016).
28. Angulo, P. et al. Liver fibrosis, but no other histologic features, is associated with long-term outcomes of patients with nonalcoholic fatty liver disease. *Gastroenterology* **149**, 389–397 e310 (2015).
29. Dulai, P. S. et al. Increased risk of mortality by fibrosis stage in nonalcoholic fatty liver disease: Systematic review and meta-analysis. *Hepatology* **65**, 1557–1565 (2017).
30. Bayindir-Buchhalter, I. et al. Cited4 is a sex-biased mediator of the antidiabetic glitazone response in adipocyte progenitors. *EMBO Mol. Med.* **10**, e8613 (2018).
31. Mauri, L. et al. Twelve or 30 months of dual antiplatelet therapy after drug-eluting stents. *N. Engl. J. Med.* **371**, 2155–2166 (2014).
32. He, G. & Karin, M. NF-kappaB and STAT3—key players in liver inflammation and cancer. *Cell Res.* **21**, 159–168 (2011).
33. Kral, J. B., Schrottmaier, W. C., Salzmann, M. & Assinger, A. Platelet interaction with innate immune cells. *Transfus. Med. Hemother.* **43**, 78–88 (2016).
34. Husted, S. & van Giezen, J. J. Ticagrelor: the first reversibly binding oral P2Y12 receptor antagonist. *Cardiovasc. Ther.* **27**, 259–274 (2009).
35. Wallentin, L. et al. Ticagrelor versus clopidogrel in patients with acute coronary syndromes. *N. Engl. J. Med.* **361**, 1045–1057 (2009).
36. Deppermann, C. et al. Gray platelet syndrome and defective thrombo-inflammation in *Nbeal2*-deficient mice. *J. Clin. Invest.* **123**, 3331–3342 (2013).
37. Albers, C. A. et al. Exome sequencing identifies NBEAL2 as the causative gene for gray platelet syndrome. *Nat. Genet.* **43**, 735–737 (2011).
38. Kahr, W. H. et al. Mutations in NBEAL2, encoding a BEACH protein, cause gray platelet syndrome. *Nat. Genet.* **43**, 738–740 (2011).
39. Gunay-Aygun, M. et al. NBEAL2 is mutated in gray platelet syndrome and is required for biogenesis of platelet alpha-granules. *Nat. Genet.* **43**, 732–734 (2011).
40. Kopec, A. K. et al. Thrombin promotes diet-induced obesity through fibrin-driven inflammation. *J. Clin. Invest.* **127**, 3152–3166 (2017).
41. Jandrot-Perrus, M. et al. Cloning, characterization, and functional studies of human and mouse glycoprotein VI: a platelet-specific collagen receptor from the immunoglobulin superfamily. *Blood* **96**, 1798–1807 (2000).
42. Drescher, H. K. et al. beta7-Integrin and MAdCAM-1 play opposing roles during the development of non-alcoholic steatohepatitis. *J. Hepatol.* **66**, 1251–1264 (2017).
43. Haemmerle, M., Stone, R. L., Menter, D. G., Afshar-Kharghan, V. & Sood, A. K. The platelet lifeline to cancer: challenges and opportunities. *Cancer Cell.* **33**, 965–983 (2018).
44. Kleinschnitz, C. et al. Targeting platelets in acute experimental stroke: impact of glycoprotein Ib, VI, and IIb/IIIa blockade on infarct size, functional outcome, and intracranial bleeding. *Circulation* **115**, 2323–2330 (2007).
45. Kanaji, T., Russell, S. & Ware, J. Amelioration of the macrothrombocytopenia associated with the murine Bernard-Soulier syndrome. *Blood* **100**, 2102–2107 (2002).

46. Subramaniam, M. et al. Defects in hemostasis in P-selectin-deficient mice. *Blood* **87**, 1238–1242 (1996).
47. Blenner, M. A., Dong, X. & Springer, T. A. Structural basis of regulation of von Willebrand factor binding to glycoprotein Ib. *J. Biol. Chem.* **289**, 5565–5579 (2014).
48. Wang, Y. et al. Leukocyte integrin Mac-1 regulates thrombosis via interaction with platelet GPIbalpha. *Nat. Commun.* **8**, 15559 (2017).
49. George, J. N. Platelets. *Lancet* **355**, 1531–1539 (2000).
50. Langer, H. F. et al. Platelets contribute to the pathogenesis of experimental autoimmune encephalomyelitis. *Circ. Res.* **110**, 1202–1210 (2012).
51. Romo, G. M. et al. The glycoprotein Ib-IX-V complex is a platelet counterreceptor for P-selectin. *J. Exp. Med.* **190**, 803–814 (1999).
52. Kroll, M. H., Harris, T. S., Moake, J. L., Handin, R. I. & Schafer, A. I. von Willebrand factor binding to platelet GpIb initiates signals for platelet activation. *J. Clin. Invest.* **88**, 1568–1573 (1991).
53. Wong, J. et al. A minimal role for selectins in the recruitment of leukocytes into the inflamed liver microvasculature. *J. Clin. Invest.* **99**, 2782–2790 (1997).
54. Dutting, S. et al. A Cdc42/RhoA regulatory circuit downstream of glycoprotein Ib guides transendothelial platelet biogenesis. *Nat. Commun.* **8**, 15838 (2017).
55. Min, H. K. et al. Increased hepatic synthesis and dysregulation of cholesterol metabolism is associated with the severity of nonalcoholic fatty liver disease. *Cell Metab.* **15**, 665–674 (2012).
56. Townsend, S. A. & Newsome, P. N. Non-alcoholic fatty liver disease in 2016. *Br. Med. Bull.* **119**, 143–156 (2016).
57. Neuschwander-Tetri, B. A. et al. Farnesoid X nuclear receptor ligand obeticholic acid for non-cirrhotic, non-alcoholic steatohepatitis (FLINT): a multicentre, randomised, placebo-controlled trial. *Lancet* **385**, 956–965 (2015).
58. Boege, Y. et al. A dual role of caspase-8 in triggering and sensing proliferation-associated dna damage, a key determinant of liver cancer development. *Cancer Cell.* **32**, 342–359 e310 (2017).
59. Franchi, F., Rollini, F. & Angiolillo, D. J. Antithrombotic therapy for patients with STEMI undergoing primary PCI. *Nat. Rev. Cardiol.* **14**, 361–379 (2017).
60. Margetts, J. et al. Neutrophils: driving progression and poor prognosis in hepatocellular carcinoma? *Br. J. Cancer* **118**, 248–257 (2018).

Acknowledgements

We thank D. Heide, I. Hetzer, R. Hillermann, C. Gropp, F. Müller, S. Prokosch, D. Kull, R. Dunkl, O. Seelbach, M. Bawohl, R. Maire, M. Bieri, C. Mittmann, H. Honcharova-Biletska, A. Fitsche, A. Adili, P. Münzer, T. Nussbaumer, F. Prutek, G. Dharmalingam and I. Singh for excellent technical assistance. We thank K. Nikolaou for the help with the human cohort recruitment and analysis. M. Malehmir was partially supported by grants from the University Zurich (Zurich Integrative Human Physiology (ZHIP) Sprint Fellowship) and from the Hartmann Müller Stiftung, Zurich. A.W. was supported by a grant from the Swiss National Science Foundation (320030_182764/1). M. Heikenwaelder was supported by an ERC Consolidator grant (HepatoMetaboPath), an EOS grant, SFBTR 209, SFBTR179, Research Foundation Flanders (FWO) under grant 30826052 (EOS Convention MODEL-IDI), Deutsche Krebshilfe projects 70113166 and 70113167, and the Helmholtz-Gemeinschaft, Zukunftsthema 'Immunology and Inflammation' (ZT-0027). This project has received funding from the European Union's Horizon 2020 research and innovation program under grant agreement 667273 and the DFG (SFB/TR 240 (project 374031971) to B.N. and D.S.), ERC Consolidator grant 'CholangioConcept' (to L.Z.), and the German Research Foundation (DFG): grants FOR2314, SFB685 and the Gottfried Wilhelm Leibniz Program (to L.Z.). Further funding was provided by the German Ministry for Education and Research (BMBF) (eMed/Multiscale HCC), the German Universities Excellence Initiative (third funding line: 'future concept'), the German Center for Translational Cancer Research (DKTK) and the German-Israeli Cooperation in Cancer Research (DKFZ-MOST) (to L.Z. and M. Heikenwaelder). D.I. was supported by an EMBO Long-term Fellowship. J.M.L. is supported by Asociación Española Contra el Cáncer (Accelerator award: HUNTER), Spanish National Health Institute (SAF2013–41027), Generalitat de Catalunya (SGR 1162 and AGAUR, SGR-1358), the Samuel Waxman Cancer Research Foundation, the US Department of Defense (CA150272P3), the European Commission Horizon 2020 Program (HEPCAR, proposal number 667273-2), and the National Cancer Institute (P30 CA196521). D.A.M. is supported by CRUK grant C18342/A23390 and MRC grant MR/K001949/1. M.P. is supported by the German Research Foundation (DFG). M.G., T.G. and D.R. was supported by grants from the German Research Foundation (KFO274 and SFB/TR240 (project 374031971)). D.J.W. received a Wellcome Trust Strategic Award (098565/Z/12/Z) and funding from the Medical Research Council (MC-A654-5QB40). C.L.W. was funded by CRUK project Cancer Research UK Programme Grant C18342/A23390. H.G.A. has been supported by the Deutsche Forschungsgemeinschaft (SFB-TR209 'Liver Cancer').

Author contributions

M. Malehmir, D.P., S.G., M.S. and D.I. contributed equally as first authors. E.K., V.L., M.P. and B.G.J.S. contributed equally as second authors. Design of the study: M. Malehmir, M.J.W., D.R., A.W., B.N., M.G. and M. Heikenwaelder. M. Malehmir, E.K., D.P., V.L., M.J.W. and C.D. performed breeding and housing of mice. M. Malehmir, S.G., M.S., E.K., D.P., V.L., D.I., A.A., M.P., B.G.J.S., A.O., C.D., J.V., D.S., D.D., C.L.W., P.H., A.R., A.T., H.D., O.K., M.K., C.J.W., R.B., N.A., M.E.H., L.S. and M. Hinterleitner performed experiments. D.R., M.R., F.B., T.G., M.N.B., O.B., M.N. and M.G. designed and performed the clinical case study. J.W., R.P., N.D., L.Z., D.J.W, H.G.A, H.D., D.K., F.T., P.F.L., T.O., D.J.W., A.V., M.D.M., A.J.R., R.R., P.K., P.A.K., B.N., A.W, J.M.L, M. Matter, D.A.M., T.S., M.P., L.S., D.H.A., C.N.-A. and J.L. provided tissue samples or mouse strains and/or scientific input. K.U. and T.E. performed biostatistical analyses. All authors analyzed data. M. Malehmir, M.E.H., D.P., S.G., M.S., P.K., B.N., M.G., O.K., T.O., A.W., and M. Heikenwaelder wrote the manuscript, and all authors contributed to writing and provided feedback.

Competing interests

J.M.L. receives consulting fees from Bayer HealthCare Pharmaceuticals, Eli Lilly, Bristol-Myers Squibb, Merck, Eisai Inc, Celsion Corporation, Exelixis, Merck, Ipsen, Glycotest, Navigant, Leerink Swann LLC, Midatech Ltd, Fortress Biotech, Sprink Pharmaceuticals and Nucleix and research support from Bayer HealthCare Pharmaceuticals, Eisai Inc, Bristol-Myers Squibb and Ipsen. This article presents independent research supported in part by the National Institute for Health Research (NIHR) Birmingham Biomedical Research Centre. The views expressed are those of the author(s) and not necessarily those of the National Health Service, the NIHR, or the Department of Health.

Additional information

Extended data is available for this paper at https://doi.org/10.1038/s41591-019-0379-5.

Supplementary information is available for this paper at https://doi.org/10.1038/s41591-019-0379-5.

Reprints and permissions information is available at www.nature.com/reprints.

Correspondence and requests for materials should be addressed to A.W. or M.H.

Publisher's note: Springer Nature remains neutral with regard to jurisdictional claims in published maps and institutional affiliations.

[1]Department of Pathology and Molecular Pathology, University and University Hospital Zurich, Zurich, Switzerland. [2]Division of Chronic Inflammation and Cancer, German Cancer Research Center Heidelberg (DKFZ), Heidelberg, Germany. [3]Division of Vascular Oncology and Metastasis, German Cancer Research Center Heidelberg (DKFZ-ZMBH Alliance), Heidelberg, Germany. [4]European Center of Angioscience (ECAS), Medical Faculty Mannheim, Heidelberg University, Mannheim, Germany. [5]Institute for Virology, Technische Universität München/Helmholtz Zentrum München, Munich, Germany. [6]Research Unit of Radiation Cytogenetics, Helmholtz Zentrum München, Neuherberg, Germany. [7]Calvin Phoebe & Joan Snyder Institute for Chronic Diseases, Cumming School of Medicine, University of Calgary, Calgary, Alberta, Canada. [8]Department of Physiology and Pharmacology, Cumming School of Medicine, University of Calgary, Calgary, Alberta, Canada. [9]Department of Microbiology, Immunology & Infectious Diseases, Cumming School of Medicine, University of Calgary, Calgary, Alberta, Canada. [10]Department of Medical Microbiology, University Medical Center, Utrmeecht, the Netherlands. [11]Department of Cardiology and Circulatory Diseases, Internal Medicine Clinic III, Eberhard Karls University Tübingen, Tübingen, Germany. [12]Department of Medicine III, University Hospital RWTH Aachen, Aachen, Germany. [13]Department of Internal Medicine VIII, University Hospital Tübingen, Tübingen, Germany. [14]Department of Physiology I, Institute of Physiology, Eberhard Karls University Tübingen, Tübingen, Germany. [15]Center for Translational Cancer Research (TranslaTUM), Technische Universität München, Munich, Germany. [16]Department of Medicine II, Klinikum Rechts der Isar, Technische Universität München, Munich, Germany. [17]German Cancer Consortium (DKTK), German Cancer Research Center (DKFZ), Heidelberg, Germany. [18]Medical Faculty, University of Heidelberg, Heidelberg, Germany. [19]Institute of Experimental Biomedicine, University Hospital and Rudolf Virchow Center, University of Würzburg, Würzburg, Germany. [20]Hematology, University Hospital and University of Zurich, Zurich, Switzerland. [21]Newcastle Fibrosis Research Group, Institute of Cellular Medicine, Newcastle University, Newcastle Upon Tyne, UK. [22]Institute of Molecular Immunology and Experimental Oncology, Technical University of Munich, Munich, Germany. [23]Centre for Liver Research and National Institute for Health Research (NIHR) Birmingham

Liver Biomedical Research Unit, Birmingham, UK. [24]Liver Unit, University Hospitals Birmingham NHS Trust, Birmingham, UK. [25]Institute for Cardiovascular Sciences, University of Birmingham, Birmingham, UK. [26]Cancer Cell Biology Programme, Growth Factors, Nutrients and Cancer Group, Spanish National Cancer Research Centre, CNIO, Madrid, Spain. [27]Institute of Neuropathology, Medical Faculty, University of Freiburg, Freiburg, Germany. [28]Signalling Research Centres BIOSS and CIBSS, University of Freiburg, Freiburg, Germany. [29]Center for NeuroModulation, Faculty of Medicine, University of Freiburg, Freiburg, Germany. [30]Division of Experimental Hematology, Deutsches Krebsforschungszentrum (DKFZ), Heidelberg, Germany. [31]DKFZ-ZMBH Alliance, Heidelberg Institute for Stem Cell Technology and Experimental Medicine (HI-STEM gGmbH) Deutsches Krebsforschungszentrum (DKFZ), Heidelberg, Germany. [32]Department of Diagnostic and Interventional Radiology, University Hospital of Tübingen, Tübingen, Germany. [33]Department of Cardiovascular Medicine, University Hospital, Eberhard Karls University of Tübingen, Tübingen, Germany. [34]Metabolic Signalling Group, MRC London Institute of Medical Sciences, London, UK. [35]Institute of Clinical Sciences, Faculty of Medicine, Imperial College London, London, UK. [36]Department of Physiology and Biophysics, University of Arkansas for Medical Sciences, Little Rock, AR, USA. [37]DKFZ Junior Group Metabolism and Stem Cell Plasticity, German Cancer Research Center (DKFZ), Heidelberg, Germany. [38]Nutrient Metabolism and Signalling Lab, Department of Biochemistry and Molecular Biology, School of Biomedical Sciences, and Metabolism, Diabetes and Obesity Program, Biomedicine Discovery Institute, Monash University, Clayton, Australia. [39]Mount Sinai Liver Cancer Program (Divisions of Liver Diseases, Department of Medicine, Department of Pathology, Recanati Miller Transplantation Institute), Tisch Cancer Institute, Icahn School of Medicine at Mount Sinai, New York, NY, USA. [40]Liver Cancer Translational Research Laboratory, IDIBAPS, Liver Unit, Hospital Clinic, University of Barcelona, Barcelona, Catalonia, Spain. [41]Institució Catalana de Recerca i Estudis Avançats (ICREA), Barcelona, Catalonia, Spain. [42]Institute of Pathology, University Hospital of Basel, Basel, Switzerland. [43]Translational Gastrointestinal Oncology Group, German Consortium for Translational Cancer Research (DKTK), German Cancer Research Center (DKFZ), Heidelberg, Germany. [44]These authors contributed equally: Mohsen Malehmir, Dominik Pfister, Suchira Gallage, Marta Szydlowska, Donato Inverso. [45]These authors jointly supervised this work: Achim Weber, Mathias Heikenwalder. *e-mail: achim.weber@usz.ch; heikenwaelder@helmholtz-muenchen.de

Methods

Mice, diets and treatments. Mice 4 to 5 weeks old (C57BL/6 JOlaHsd) were purchased from ENVIGO. P-selectin knockout mice (*Selp*$^{-/-}$) and MAC-1 knockout mice were purchased from Jackson Laboratories (mouse strains 002289 and 003991). Knockout mice for *Nbeal2*$^{-/-}$, GPVI (*Gp6*$^{-/-}$)[61], GPIIb/IIIa (*GpIIb*$^{-/-}$; *Itga2b*$^{-/-}$), von Willebrand factor (*vWF*$^{-/-}$) and transgenic mice, lacking functional GPIbα, hIL4rα/GPIbα-Tg, all on the background of C57Bl/6J were kindly provided by B. Nieswandt and J. Ware (University Hospital and Rudolf Virchow Center, University of Würzburg, Würzburg, Germany; Department of Physiology and Biophysics, University of Arkansas for Medical Sciences, Little Rock, AR, USA). Tissues from inducible knock-in mice expressing the human unconventional prefoldin RPB5 interactor (URI) in hepatocytes (hURI-tetOFFhep) were received from N. Djouder, CNIO, Madrid. *Pdpn*$^{fl/fl}$ x Vav1-iCre mice (obtained from Jackson Laboratories) and *Clec1b*$^{fl/fl}$ x Pf4-Cre mice are described elsewhere[62]. All strains of genetically altered mice were on a C57BL/6J background. Control mice were negative for Cre recombinase and matched by genetic background, age and sex. Mice were housed at the University Hospital Zurich (USZ), the Technical University Munich/Helmholtz Zentrum Munich, the Biomedical Services Unit at University of Birmingham or University of Newcastle, the University of Calgary, RWTH Aachen University and the German Cancer Research Center (DKFZ). All animal work was conducted under the approval of the Swiss Veterinary Office (136/2014), according to German Law (G7/17, 55.2-1-54-2532-39-2015, G-91/14 and AZ:84-02.04.2014.A010), the UK Animals Scientific Procedures Act of 1986, with project license approval granted by the UK Home Office, the local biomedical research ethics committee approval, the Newcastle Ethical Review Committee under UK Home Office project license P3F79C606 and the University of Calgary Animal Care Committee (protocol AC16-0148) in accordance with the Canadian Council for Animal Care Guidelines. Animals were maintained under specific-pathogen-free conditions and experiments were performed in accordance with the guidelines of the respective institution and were in accordance with ethical regulations and humane endpoints.

Five-week-old mice were fed ad libitum: a normal diet (ND) (Provimi Kliba) or a choline-deficient high-fat diet (CD-HFD) (Research Diets; D05010402) for 6 or 12 months; a Western diet with trans-fat (WD-HTF) (Research Diets; D09100301: 40 kcal % fat (Primex shortening), 20 kcal % fructose, 2% cholesterol) for 6 or 7.5 months; or a methionine-choline-deficient diet (MCD) (MP Biomedicals) for 4 weeks; and control mice were fed a calorifically matched control diet, a Western diet with fructose in drinking water (WD-FSDW) (Custom Research Diet TD.06303; Harlan Laboratories in conjunction with fructose-supplemented drinking water: 55% fructose, 45% glucose by weight at a concentration of 42 g/l) ad libitum for 6 and 9 months. Control animals received ND and non-supplemented drinking water.

Cohorts of mice fed CD-HFD or WD-HTF were in addition treated with either aspirin (through food pellets containing 7.5 mg per kg of food) in combination with clopidrogel high (40 μg/ml drinking water; ~3 mg/kg/day) or low dose (20 μg/ml drinking water; ~1.5 mg/kg/day), with sulindac (200 μg/ml drinking water; ~20 mg/kg/day) or with ticagrelor (40 μg/ ml drinking water; ~3 mg/kg/day).

For interventional studies 5-week-old male mice were fed a normal diet (ND), a choline-deficient high-fat diet (CD-HFD) (Research Diets; D05010402) or a Western diet containing trans-fat (WD-HTF) (Research Diets, D09100301) for 3.5 weeks and then treatment started for 2.5 weeks, twice per week intravenously in 100 μl PBS of either 20 μg/mouse anti-CD44 antibody (clone KM81, Cedarlane, CL8944AP), 100 μg/mouse anti-CD44 (clone IM7, Bioxcell, BE0039), 100 μl/mouse Clodrosome (liposomal clodronate), 100 μl/mouse Encapsome (Control Liposomes), 100 μg/mouse anti-GPIbα or 100 μg/mouse Fab-Rat IgG (kindly provided by B.N., University Hospital and Rudolf Virchow Center, University of Würzburg, Würzburg, Germany) or intraperitoneally 20 U/g murine hyaluronidase (HYAL). In late treatment regimes, mice were fed CD-HFD for 6 months and treated with the same protocol for indicated time points.

For the osmotic pump experiment, 5-week-old male mice were fed a choline-deficient high-fat diet (CD-HFD) (Research Diets; D05010402) for 12 weeks. Four weeks after the diet, mini pumps (Alzet, model 2004) were implanted subcutaneously into the mice to deliver 30 μg per day of Ly6G (clone 1A8, Bioxcell, BP0075) neutrophil-depleting antibody or Rat IgG2a (clone 2A3, Bioxcell, BE0089) for 8 more weeks. At the end of the experiment, animals were culled, and the liver, fat and serum were harvested for analysis.

Human material. Specimens were obtained from formalin-fixed, paraffin-embedded non-diseased NAFLD- or NASH-diagnosed human liver tissue, retrieved from the archives and the biobank of the Department of Pathology and Molecular Pathology, University Hospital Zurich, University Hospital Würzburg and in the setting of the HEP-CAR consortium (Institute for Research in Biomedicine (IRB) Barcelona). Tissues were examined by certified liver pathologists (A.W., J.M.L.). These studies were approved by the local ethics committee ('Kantonale Ethikkommission Zürich', application numbers StV26/2005 and KEK-ZH-Nr. 2013-0382) or the Institute for Research in Biomedicine (IRB) Barcelona, Hospital Clinic HCB/2015/0789. In line with the regulation of KEK, individual informed consent from all patients was not required for this kind of retrospective analysis on patients' material.

The prospective clinical trial has been listed at the German Clinical Trials Register (DRKS), evaluated and accepted by the local ethical authorities (Ethik-Kommission Universitätsklinikum Tübingen) with the ID 587/2016BO2, under the name 'Platelet inhibition to recues formation of non-alcoholic steatohepatitis in cardiovascular patients' (Prometheus—prospective, monocenter, observational study).

Prospective trial, ethics, MRI and ultrasound analyses. The case study of 24 individual observations prospective trial was approved by the institutional ethics committee (587/2016BO2) and complies with the declaration of Helsinki and the good clinical practice guidelines[63–66].

For the prospective, ongoing case study, we have included only patients ($n = 23$) with diabetes mellitus type II and/or body mass index > 30, two risk factors, that are highly correlated with development of NAFLD or NASH. All patients underwent cardiac catheretization due to suspected coronary artery disease (CAD). Patients received no antiplatelet treatment if CAD was excluded. Patients received antiplatelet therapy with 100 mg acetylsalicylic acid (ASA) once daily if CAD was present but coronary stent implantation was not indicated. Patients received dual antiplatelet therapy with ASA 100 mg once daily and P2Y12 inhibitor (clopidogrel 75 mg once daily, ticagrelor 90 mg twice daily or prasugrel 10 mg once daily) depending on acuity and severity of CAD (e.g., myocardial infarction versus stable CAD). None of the patients included received long-term treatment with ASA or P2Y12 before study inclusion.

All patients remained on the respective treatment regimens until follow-up. All patients underwent liver MRI and liver ultrasound at baseline (within 4 weeks after hospital discharge) and after 6 months of follow-up. The serum from all patients was analyzed for classic liver damage parameters like AST, ALT, bilirubin, GGT, etc. Additional measurements were performed to exclude reasons other than NAFLD for liver damage, e.g., immune hepatitis, viral hepatitis and AFLD. All patients underwent the Michigan Alcoholism Screening Test to evaluate drinking habits. Patients with left ventricular ejection fraction <45% or severe valve diseases were not included in the study due to the risk of liver congestion.

The hepatic lipid accumulation was quantified by 3T MRI (Skyra, Siemens Healthcare, Erlangen, Germany) at the Department of Diagnostic and Interventional Radiology of the University Hospital of Tübingen, Germany. A commercially available multi-echo Dixon sequence (LiverLab, Siemens Healthcare, Erlangen, Germany) was used, allowing the computation of proton density fat fraction maps and inline segmentation of the liver. Ultrasound examinations in patients were performed twice, at the time of patient recruitment and 6 months after patient recruitment. In order to identify patients presenting with signs of liver steatosis or with signs of liver cirrhosis, bright hepatic echos, increased hepatorenal echogenicity, presence of nodular liver morphology and signs of portal hypertension (e.g., splenomegaly, ascites or intra-abdominal varices) were analyzed using an Aplio 500/T1 (Toshiba)/Ultrasonic transducer 3–5 MHz.

The multivariate analysis (age, gender, anti-aggregation and new statin treatment) to identify statin administration as a possible confounder of the observed effects, patients were differentiated into groups, that received statin treatment prior to hospital admission and those that received new statin treatment at hospital discharge prior to the first MRI examination. We performed a linear regression analysis.

For further details regarding the human samples, please refer to Supplementary Tables 1a,b and 2.

Cholesterol measurements. Hyperlipidemia is defined as baseline LDL cholesterol ≥ 160 mg/dl and triglycerides ≥ 200 mg/dl. Interestingly, only three of the patients of the prospective cohort had triglyceride values ≥ 200 mg/dl. However, all patients of the prospective cohort showed significantly elevated liver fat accumulation, indicating that patients might not need elevated serum lipid levels to develop fatty liver disease. According to our measurements, only three patients of the prospective trial fulfill the diagnosis hyperlipidemia. However, we decided to include patients with pre-existing conditions, e.g., diagnosis by family doctor, because serum lipid undergoes dynamic regulations. This explains the discrepancy between hyperlipidemia and measured lipid levels in baseline Table 2.

Isolation of liver leukocytes for in-depth myeloid characterization. Livers were perfused once with PBS, then digested via collagenase at 37 °C for 40 minutes (collagenase type IV, Worthington, UK). Additionally, 0.1 mg/ml DNase I was added after 20 min. Single-cell suspension was obtained by filtering the digested liver through a 70-μm mesh. Hepatocytes were removed by low-speed centrifugation (50 r.c.f., 1 min), and density gradient centrifugation was performed using 18% Nycodenz dissolved in Gey's Balanced Salt Solution (GBSS) as previously described[67].

Cells were then stained for CD206 (C068C2, 141708), CX3CR1 (SA011F11, 149031), CD3 (17A2, 100218), MHCII (M5/114.15.2, 107632) (all BioLegend); CD11b (M1/70, 48-0112-82), F4/80 (BM8, 25-4801-82) (all Invitrogen); CD86 (GL-1, eBioscience, 12-0862-82); CD45 (30-F11, 557659), Ly6G (RB6-8C5, 566218), Ly6C (1A8, 562737) CD11c (HL3, 562949), CD31 (MEC13.3, 565097), NK1.1 (PK136, 557391), TIM-4 (RMT4-54, 564147) (all BD Bioscience), and then multicolor flow cytometry was run using an LSR Fortessa (BD Biosciences). Analysis was done using FlowLogic (v7.2, Inivai, Australia) and FlowJo (v10.4,

BD Biosciences). Additionally, liver MoMF and Kupffer cells were sorted for NanoString gene expression analysis using an Aria-II (BD Biosciences).

For details regarding the definitions of violin plot elements of Supplementary Fig. 3i, refer to Supplementary Table 3.

t-distributed stochastic neighbor embedding (t-SNE). Liver leukocytes were pregated for living (7-AAD-), $CD45^+$, $Ly6G^-$, $CD31^-$, $F4/80^+$ cells by using FlowJo (v10.4, BD Biosciences), then t-SNE-based clustering was done as described previously[68], using the Rtsne package for R. Clusters were identified by hierarchical clustering and projected onto the two-dimensional t-SNE plot, while relative protein expression was displayed for each cluster by violin plots using R (v3.5.1).

nCounter gene expression analysis. Gene expression analysis of 561 selected gene targets of liver MoMF and Kupffer cells was performed using NanoString assays (nCounter Mouse Immunology Kit, NanoString Technologies). Analysis was done using the nSolver Software (v2.0, NanoString Technologies). PCA was done using the prcomp package for R (v3.5.1).

Measurement of serum parameters. Serum was isolated from mice and liver enzymes AST and ALT were quantified using the Roche Modular System (Roche Diagnostics) with a commercially available automated colorimetric system at the Institute of Clinical Chemistry at the University Hospital Zurich using a Hitachi P-Modul (Roche). Total cholesterol was measured in a 96-well format using CHOL or TG GPO-PAP substrates (Roche Diagnostics).

Measurement of liver triglycerides. Liver-specific triglyceride levels were analyzed from snap frozen liver tissue samples. Liver tissue samples were homogenized in sodium chloride (0.9 % NaCl), and liver-resident lipids were precipitated using ethanolic potassium hydroxide (0.5 M KOH) and solubilized in magnesium sulphate (0.15 M $MgSO_4$). The concentration of hepatic triglycerides was then measured using triglycerides GPO-PAP from Roche Diagnostics on a spectrophotometer at 505 nm.

Intraperitoneal glucose tolerance test. Intraperitoneal glucose tolerance tests were carried out on mice fasted overnight for 16 h. Basal blood glucose concentrations were determined for each mouse prior to glucose (2 mg/g body weight) administration using a hand-held glucose analyzer (FreeStyle Freedom Lite; Abbott). Each mouse then received glucose via intraperitoneal injection, and blood glucose concentrations were subsequently remeasured 15, 30, 60 and 120 min post glucose administration.

Intraperitoneal insulin tolerance test and fasting insulin determination. Intraperitoneal insulin tolerance tests were carried out on mice mild fasted for 6 h. Basal blood glucose concentrations were determined for each mouse prior to insulin (1U/g lean mass determined by EchoMRI analysis) administration using a hand-held glucose analyzer (FreeStyle Freedom Lite; Abbott). Each mouse then received Insulin via intraperitoneal injection and blood glucose concentrations were subsequently re-measured 15, 30, 60 and 120 min post glucose administration. Fasted insulin levels were measured in mildly fasted (8 h) mice using the ALPCO mouse insulin ELISA kit.

Immunoblot analysis. Liver homogenates were prepared in a pH 7.4 lysis buffer containing 1% NP-40 (Sigma-Aldrich, Gillingham, UK), 50 mmol/L Tris, 10% glycerol, 0.02% NaN3, 150 mmol/L NaCl, and a cocktail of phosphatase and protease inhibitors (Sigma-Aldrich), and protein concentration was determined using the Pierce BCA Protein Assay Kit (Thermo Scientific) according to the manufacturer's manual. Liver homogenates were prepared using a homogenizer. Tissue preparation was performed with gentleMACS Octo Dissociator (Miltenyi Biotec). 20–80 µg of proteins were separated under reducing conditions (2.5% β-mercaptoethanol) by gel electrophoresis (Mini Protean Gels, Bio Rad) and blotted by semi-dry blotting (Trans-Blot Turbo Transfer, Bio Rad) onto nitrocellulose membranes (Bio Rad). Membranes were blocked in 5% milk/PBS-T for at least 1 h at RT. Primary antibodies against P-p38MAPK ((Thr180/Tyr182) D3F9, 4511), p38 MAPK (D13E1, 8690), P-p65 (Ser536, 3033), p65 (D14E12, 8242), COX2 (D5H5, 12282), GAPDH (14C10, 2118) (all Cell Signaling) were incubated at 4 °C overnight under shaking conditions. Incubation with the secondary antibody (HRP-anti-rabbit IgG, 1:5000; Promega, W4011) was performed under shaking conditions for 1 h. Detection was achieved using Clarity Western ECL Substrate (Bio Rad) with the Stella 3200 imaging system (Raytech).

Flow cytometry. For flow cytometry analysis, antibodies against CD8-α (53-6.7, 100734), CD3-ε (500A2, 152314), CD19 (6D5, 115530), NK1.1 (PK136, 108710), were purchased from BioLegend. Antibodies against CD4 (RM4-5, 11-0042-82) and Foxp3 (FJK-16s, 17-5773-82) were purchased from eBioscience. Viability was assessed by LIVE/DEAD Fixable Aqua or ZombieDyeNIR (Life Technologies). TA99 was labeled with an Alexa Fluor 647 NHS Ester (Life Technologies, MA1-25303) to generate TA99–647. Further antibodies that were used include CD44 (clone IM7, BioLegend, diluted 1:200, 103012), CD69 (clone H1.2F3, BioLegend, diluted 1:200, 104508), CD62L(clone MEL-14, BioLegend, diluted 1:200, 104448). Intracellular cytokine staining (ICS) was performed as described previously[21]. Peptides used for restimulation were 10 µg/ml of the relevant antigen: Trp2180–188 (SVYDFFVWL), Her2/Neu66–74 (TYVPANASL), Tyrp-1455–463native (TAPDNLGYA), or gp10025–33native (EGSRNQDWL). Cells were analyzed using BD FACS LSR II, BD FACS LSR Fortessa, BD FACSCanto, and Sony spectral analyzer SP6800 flow cytometers, and data were analyzed using FlowJo.

Histology, immunohistochemistry, scanning and automated analysis. Liver samples were fixed in 4% paraformaldehyde and paraffin-embedded at the University Hospital Zürich, Department of Pathology and Molecular Pathology Core, at the Technical University of Munich (TUM), or at the DKFZ, Department of Chronic Inflammation and Cancer (Heidelberg) as described[11]. Briefly, 2 µm sections from FFPE and cryo-preserved tissues were prepared and stained with Hematoxylin/Eosin or IHC antibodies. Incubation in Ventana buffer and staining was performed on a NEXES immunohistochemistry robot (Ventana Instruments) using an IVIEW DAB Detection Kit (Ventana) or on a Bond MAX (Leica). For Sudan Red staining, cryo sections (5 µm) were cut and stained with Sudan Red (0.25% Sudan IV in ethanolic solution). Slides were scanned with a Nano Zoomer (Hamamatsu, Japan).

Antibodies that were used included anti-MHCII, rat, 1:500 (clone M5/114.15.2, NBP1-43312); anti-CD3, rabbit, 1:250 (clone SP7, Abcam, ab16669); and anti-F4/80, rat, 1:50 (BioLegend, BM8, cat. no. 123105). Further antibodies used included collagen IV, rabbit 1:50 (Cedarlane, clone CL50451AP-1, 007CL50451AP); Ki67, rabbit 1:200 (Thermo Scientific, clone RM-9106-S1, RM-9106-S1); B220, rat 1:3000 (BD, clone RA3-6B2, 553084); Ly6G rat 1:600 (BD, clone 1A8, 551459), PERK1/2, rabbit, 1:400 (Cell Signaling, clone D13.14.4E, 4370); glutamine synthethase (GS) rabbit 1:500 (Abcam, ab16802); PSTAT3, rabbit, 1:100 (Cell Signaling clone D3A7, 9145); and CD42b, rabbit, 1:200 (Abcam, clone SP219, ab183345).

For quantification of stains, slides were scanned using a SCN400 slide scanner (Leica) and analyzed using Tissue IA image analysis software (4.0.6 Slidepath, Leica). For quantification of platelet staining on human (CD61) and mouse (CD42b) tissue, software-based analysis and counting at the screen (CD42b; 100 high-power fields; 40×) were performed.

For Sudan red^+ liver area, data are presented as Sudan red–positive area in percent of total tissue area. Three random liver tissue areas of approximately 6–8 mm^2 (87,000 μm^2) were selected in DIH (digital image hub, Leica), submitted to analysis and merged.

NAFLD activity score (NAS) was applied to murine livers.

Electron microcopy. For electron microscopy, sections from epon-embedded, glutaraldehyde-fixed liver samples were cut and stained with toluidine blue. The tissue was trimmed, and ultrathin cross sections of the liver were cut and treated with uranyl acetate and lead citrate as described previously[69]. Electron micrographs were analyzed for cell composition and localization using the analySIS Docu System (Soft Imaging System).

Preparation of mouse platelets. Blood was obtained from the tail of each mouse and drawn into citrate tubes at a 1:10 ratio. Platelet-rich plasma (PRP) was obtained by centrifugation at 260*g* for 5 min. Afterward, platelet-rich plasma was centrifuged at 640*g* for 5 min to pellet the platelets. After two washing steps, the pellet of washed platelets was resuspended in modified Tyrode-HEPES buffer (pH 7.4, supplemented with 1 mM $CaCl_2$).

Platelet aggregometry. Washed platelets were adjusted to a concentration of 150×10^3 platelets/µl in Tyrode-HEPES buffer (pH 7.4 supplemented with 1 mM $CaCl_2$). Aggregation was estimated from light transmission determined with a luminoaggregometer model 700 (ChronoLog, Havertown, PA, USA). Following calibration, agonists including adenosine 5′-diphosphate (ADP), U46619 (U46), thrombin (Thr), collagen-related peptide (CRP), rhodocytin (RC) were added at the indicated concentrations, and aggregation was measured for 10 min with a stir speed of 1,000 r.p.m. at 37 °C. Afterward, analysis was performed using the aggrolink8 software (ChronoLog).

Analysis of platelets and flow cytometry of platelets. Mice were bled under isoflurane anesthesia. Blood was collected in a tube containing 20 U/ml heparin, and PRP was obtained by two cycles of centrifugation at 300*g* for 6 min at room temperature. For preparation of washed platelets, PRP was washed twice at 800*g* for 5 min at RT, and the pellet was resuspended in modified Tyrodes-HEPES (N-2-hydroxyethyl-piperazone-N′2-ethanesulfonic acid) buffer (134 mM NaCl, 0.34 mM Na_2HPO_4, 2.9 mM KCl, 12 mM $NaHCO_3$, 5 mM HEPES, 1 mM $MgCl_2$, 5 mM glucose, 0.35% BSA, pH 7.4) in the presence of prostacyclin (0.1 µg/ml) and apyrase (0.02 U/ml).

Apyrase grade III (Sigma-Aldrich), prostacyclin (PGI2), ADP (Sigma-Aldrich), U-46619 (Enzo Life Sciences), thrombin (Roche), rabbit anti-human VWF (DAKO), rabbit anti-human fibrinogen (DAKO) were purchased as indicated. CRP and rhodocytin were generated and isolated as previously described[56]. The antibody against the activated form of integrin αIIbβ3 (JON/A-PE) was from Emfret Analytics. Other antibodies we received, listed below, were generated in the laboratory of B.N.

Antibody	Clone	Isotype	Antigen	Reference
JON/A	4H5	IgG2b	αgG2be	70
WUG 1.9	5C8	IgG1	P-selectin	71
JAQ1	98A3	IgG2a	GPVI	72
LEN1	12C6	IgG2b	α2	73
ULF1	96H10	IgG2a	CD9	74
p0p4	15E2	IgG2b	GPIb	74
p0p6	56F8	IgG2b	GPIX	74
JON2	14A3	IgG2b	αIIbβ3	74
DOM2	89H11	IgG2a	GPV	74
INU1	11E9	IgG1	CLEC-2	75

RNA isolation and quantitative real-time PCR. Total RNA was isolated from snap frozen liver tissues according to the manufacturer's protocol using RNeasy Mini Kit (Qiagen). The quantity and quality of the RNA were determined spectroscopically using a Nanodrop analyzer (Thermo Scientific). 1 µg of purified RNA was subsequently transcribed into cDNA using Quantitect Reverse Transcription Kit (Qiagen) according to the manufacturer's protocol. Quantitative RT-PCR was performed using Fast Start SYBR Green Master Rox (Roche). Primers were custom made by Microsynth as previously described[11]. For mRNA expression analysis, quantitative real-time PCR was performed in duplicates in 384-well plates using Fast Start SYBR Green Master Rox (Roche) on a 7900 HT qRT-PCR system (Applied Biosystems, Life Technologies Darmstadt, Germany). Relative mRNA levels were calculated according to the $\Delta\Delta C_t$ relative quantification method and were normalized to levels of a housekeeping gene (GAPDH or ROTH2). The data were normalized to the expression of the housekeeping gene and analyzed using GraphPad Prism software version 7.03 (GraphPad Software). For the analysis of whole liver homogenates by microarray (Agilent), the following genes were selected, analyzed and shown. For a list of all used primers for RT-qPCRs, refer to Supplementary Table 4.

Gene expression profiling. Transcriptional profiling was performed using SurePrint G3 Mouse Gene Expression 8×60 k microarrays (Agilent Technologies, AMADID 28005) according to the manufacturer's protocol. 75 ng of total RNA was used in labeling using the Low Input Quick Amp Labeling Kit (one-color, Agilent Technologies). Raw gene expression data were extracted as text files with the Feature Extraction software 11.0.1.1 (Agilent Technologies). The expression microarray data were uploaded to ArrayExpress (www.ebi.ac.uk/arrayexpress/), and the data set is available under the accession number E-MTAB-6073, entitled 'Transcriptomic differences in livers of mice fed with normal diet and choline-deficient high-fat diet'.

All data analysis was conducted using the R statistical platform (version 3.2.2, www.r-project.org). Data quality assessment, filtering, preprocessing, normalization, batch correction based on nucleic acid labeling batches and data analyses were carried out with the Bioconductor R-packages limma, Agi4x44PreProcess and the ComBat function of the sva R-package. All quality control, filtering, preprocessing and normalization thresholds were set to the same values as suggested in Agi4x44PreProcess R-package user guide. Only HGNC annotated genes were used in the analysis. GSEA was conducted on calculated $\log_2$-expression values of all array probes using the 'GSEA Pre-ranked' function with default settings[76].

RNA sequencing. Library preparation for bulk 3′-sequencing of poly(A)-RNA was done as described previously[77]. Briefly, barcoded cDNA of each sample was generated with a Maxima RT polymerase (ThermoFisher) using oligo-dT primer containing barcodes, unique molecular identifiers (UMIs) and an adapter. 5′ ends of the cDNAs were extended by a template switch oligo (TSO); after pooling of all samples, full-length cDNA was amplified with primers binding to the TSO-site and the adapter. cDNA was tagmented with the Nextera XT kit (Illumina) and 3′-end-fragments finally amplified using primers with Illumina P5 and P7 overhangs. In comparison to Parekh et al.[77], the P5 and P7 sites were exchanged to allow sequencing of the cDNA in read1 and barcodes and UMIs in read2 to achieve a better cluster recognition. The library was sequenced on a NextSeq 500 (Illumina) with 75 cycles for the cDNA in read1 and 16 cycles for the barcodes and UMIs in read2.

RNA sequencing analysis. Gencode gene annotations version M18 and the mouse reference genome GRCm38.p6 were derived from the Gencode homepage (https://www.gencodegenes.org/). Dropseq tools v1.12 (ref. [78]) was used for mapping the raw sequencing data to the reference genome. The resulting UMI filtered countmatrix was imported into R v3.4.4. Prior differential expression analysis with DESeq2 1.18.1 (ref. [79]), dispersion of the data was estimated with a parametric fit including the dietary status of the mice as explanatory variable in the model. The Wald test was used for determining differentially regulated genes between the high-fat and normal diet group and shrunken $\log_2$ fold changes were calculated afterward, with setting the type argument of the lfcShrink function to 'normal'. A gene was determined to be differentially regulated if the absolute $\log_2$ fold change was greater than 1 and the adjusted P value was below 0.05. Gene set enrichment analysis was conducted with EnrichR[80] within the Reactome database. Raw sequencing data are available under the accession number MTAB-7625.

MRI analysis for mice. Steatosis was analyzed in 6-month-old B6 mice fed with ND, CD-HFD or CD-HFD/Asp-Clop treated groups. A Pharmascan 7 T MRI (Bruker) with Paravision 5.1 software was used in FLASH scan mode without fat suppression using an echo-time of 2.2 ms for out-phase and 2.9 ms for in-phase based on previous reports[81,82].

Calorimetric TSE analysis. Mice were individually housed for indirect calorimetry in PhenoMaster (TSE systems). Mice were allowed to acclimate to the new environment for at least 2–3 d, then metabolic parameters were measured, such as food and water intake, O_2 consumption, CO_2 production, respiratory exchange ratio and total activity. All parameters were measured for at least 4 consecutive d with five measurement values every hour. Analysis of covariance (ANCOVA) was first conducted to ensure that body weight does not play a significant effect on the measured parameters.

Immunofluorescence microscopy of liver sections. To achieve rapid fixation after euthanasia, livers were fixed with paraformaldehyde–lysine–periodate (PLP) for 4–8 h, rehydrated in 30% sucrose solution for 48 h and snap frozen in OCT (Cell Path). Thick (5 µm) cryosections were obtained using a Leica Cryostat and the Cryojane tape transfer system (Leica Microsystems).

Generation of liver slices for confocal microscopy. The generation of the liver slices for microscopy was performed and adapted from a previously described protocol[83]. Briefly, livers were collected and processed as described above. OCT-embedded frozen livers were iteratively sectioned using a cryostat. Samples were then reversed and the procedure was repeated on the opposite face of the liver until a 30-µm-thick slice of liver was obtained. OCT freezing medium covering the sample was removed, and slices were washed with PBS and blocked overnight at 4°C in blocking solution (0.2% Triton/1%BSA/10% donkey serum/PBS). Liver slices were stained with rat anti-CD41, goat anti-CD105, rabbit anti-Col IV and rabbit anti-CD8 for 3 d in blocking solution, washed overnight in PBS and stained with DyLight488 donkey anti-rabbit IgG and DyLight549 or DyLight649 donkey anti-rat IgG. Stained slices were then washed in PBS and incubated overnight in FocusClear (CelExplorer Lab). For observation under the confocal microscope, liver slices were embedded in FocusClear and mounted on glass slides.

Immunofluorescence staining. Livers were perfused with PBS through inferior vena cava, harvested and fixed in 4% paraformaldehyde for 16 h, then dehydrated in 30% sucrose prior to embedding in OCT freezing media (Sakura). 25-µm sections were cut on a HM550 cryostat (ThermoFisher) and adhered to Superfrost Plus slides (Thermo Scientific). Sections were then permeabilized and blocked in PBS containing 0.3% Triton X-100 (Sigma-Aldrich) and 10% FBS, then stained in the same blocking buffer. The following primary antibodies were used for staining: rabbit anti-collagen IV (1:200 Abcam, 10808); CD41 PE (1:100 MWReg-30 BioLegend, 133906), rat anti-F4/80 APC (1:100 BM8 ThermoFisher, 17-4801-82), rabbit anti-CD3 (1:100 DAKO A0445229-2), B220 AF 647 (1:100 RA3-6B2 BioLegend, 103226), CD11b APC (1:100 M1/70 BioLegend, 101212). Stained slides were mounted with fluorescence mounting medium (DAKO), and images were acquired on an inverted Leica microscope (TCS STED CW SP5, Leica Microsystems) with a motorized stage for tiled imaging.

To minimize fluorophore spectral spillover, we used the Leica sequential laser excitation and detection modality. The bleed-through among sequential fluorophore emission was removed by applying simple compensation correction algorithms to the acquired images. The semiautomatic surface-rendering module in Imaris (Bitplane) was used to create 3D volumetric surface objects corresponding either to individual cells or to the liver sinusoids. Signal thresholds were determined using the Imaris Surface Creation module, which provides automatic threshold identification and value-based visual surface thresholding around the positively stained objects.

For the semi-quantitative analysis of platelet adhesion to liver sinusoids, high-resolution confocal x–y–z stacks of 30 x–y sections (1,024×1,024 pixels) sampled with 0.5 µm z spacing were acquired to provide image volumes of 388×388×30 µm^3. The confocal z stacks were imported into Imaris software (Bitplane), and platelets were reconstructed as 3D volumes by means of the semiautomatic surface-rendering module with a seed point diameter of 2.08 µm (the mean platelet diameter[84,85]). The split touching objects option of the module supports the separation of two or more objects that are identified as one, enabling the splitting of aggregates into single components. All analysis was performed at least on 12 random fields of view (FOV).

Confocal imaging analysis. For platelet aggregate size analysis, the surface and volume of each single platelet aggregate (containing more than two single platelets)

from at least 12 different FOV was automatically obtained from the surface-rendering module (imaris, Bitplane); The PLT/endothelium coverage was derived from the same FOV as percentage of the total sinusoidal surface (calculated in each FOV) covered by PLT.

For quantification of the immune cell–PLT interaction, the immune cells ($CD3^+$, $CD11b^+$ and $B220^+$) adjacent and non-adjacent to PLT were manually counted in 12 FOV. The interaction was expressed as total number of adjacent cells as well as percentage of cells adjacent to PLT over the total number of cells.

The $CD3^+$ cells/PLT interaction was further analyzed by calculating, for each cell, the contact surface area between them.

Multiplex ELISA. Cytokines and chemokines in whole liver of ND, CD-HFD and Asp-Clo-treated CD-HFD mice (12 months old) were evaluated using a laser bead technology–based Mouse Cytokine Array Chemokine Array 31-Plex (MD31) by Eve Tech (Eve Technologies, Calgary, AB, Canada).

Cytokine profiler. Cytokines and chemokines in whole liver of ND, CD-HFD/ctrl ab and CD-HFD/anti-GPIbα antibody mice (6 months old) or in CD-HFD and CD-HFD/*hIL4Rα/GPIbα*-Tg mice (12 months old) were assessed using the Mouse XL Cytokine Array Kit by R&D Systems.

Spinning-disc microscopy. All imaging experiments were performed using 7- to 12-week-old male mice. All mice were co-housed and bred in a specific-pathogen-free facility at the University of Calgary with a 12h light/dark cycle and access to food and water ad libitum.

Preparation for intravital Microscopy. Multichannel spinning-disk confocal microscopy was used to image the liver as previously described (Surewaard and Kubes 2017). Briefly, mice were anesthetized by intraperitoneal injection of ketamine (200 mg/kg body weight; Bayer Animal Health) and xylazine (10 mg/kg body weight; Bimeda-MTC). A catheter was inserted into the tail vein to allow administration of fluorescently conjugated antibodies, proteins and additional anesthetics. A midline and lateral abdominal incision were made, and the abdominal wall was partly removed to access the liver. The mouse was placed in a right lateral position on a heating plate to maintain body temperature at 37°C. The liver was exteriorized onto a glass coverslip and covered with moisturized laboratory tissues to restrict movement and breathing artefacts. Abdominal organs were covered with saline-soaked gauze to prevent dehydration.

Intravital microscopy. Image acquisition of the liver was performed using an inverted spinning-disk confocal microscope (IX81; Olympus), equipped with a focus drive (Olympus) and a motorized stage (Applied Scientific Instrumentation). The microscope was fitted with a motorized objective turret equipped with 4/3/0.16 UPLANSAPO, 10/3/0.40 UPLANSAPO, and 20/3/0.70 UPLANSAPO objective lenses. The microscope was linked with a confocal light path (WaveFx; Quorum Technologies) based on a modified CSU-10 head (Yokogawa Electric Corporation). Cells of interest were visualized using fluorescently conjugated antibodies. Volocity software (Perkin Elmer) was used to drive the confocal microscope and for acquisition and analysis of images.

Antibodies for intravital imaging. Antibodies for intravital imaging were as follows: Alexa Fluor (AF) 750–conjugated anti-mouse F4/80 (2 μg/mouse; clone BM8; AbLab, custom made), Alexa Fluor (AF) 647–conjugated anti-mouse CD49b (3 μg/mouse; clone HMa2; BioLegend, 103511), PE-conjugated anti-mouse Ly6G (3 μg/mouse; clone 1A8; BioLegend, 127607) and FITC-conjugated anti-mouse CD3e (2 μg(mouse; clone 145-2c11; eBioscience, 11-0031-82). HAPB (Sigma-Aldrich) was fluorescently (Alexa Fluor 555; Invitrogen) conjugated and injected intravenously to detect intrahepatic HA.

In vivo treatments. Kupffer cell depletion was performed by intravenous injection of 100 μl Clodronate (17 mM) twice a week for 2 weeks. Hyaluronidase (Sigma-Aldrich) was given by intraperitoneal injection twice a week at a dose of 20U/g per mouse for 2 weeks. The last dose was given 3h before intravital imaging.

In vivo image analysis. All videos and images were acquired and processed using Volocity software (PerkinElmer). Quantification of platelet aggregation, Kupffer cell and neutrophil numbers and sinusoid diameters were also performed using Volocity software. For each mouse, ten FOV were randomly selected and assessed. Platelet aggregation was measured using the 'find objects' function in Volocity software and the highest background was subtracted as described (Surewaard et al 2018). Kupffer cell and neutrophil numbers were manually counted in ten randomly selected FOV. For measurement of sinusoidal diameter, images were exported from Volocity software as.jpg files. ImageJ software (NIH) was used to measure sinusoid diameters. For each mouse, we measured ten randomly selected sinusoids in five FOV.

Statistical analyses. Mouse data are presented as the mean ± s.e.m. Pilot experiments and previously published results were used to estimate the sample size such that appropriate statistical tests could yield significant results. Statistical analysis was performed using GraphPad Prism software version 7.03 (GraphPad Software). Data of three or more groups were analyzed by analysis of variance with the post hoc Tukey's or Bonferroni multiple comparison test. Data for the three groups over time were analyzed by two-way analysis of variance with the post hoc Tukey's multiple comparison test. Analysis of two samples was performed with two-tailed Student's *t* test and the Mann–Whitney *t* test, and statistics for HCC incidence were calculated using two-tailed Fisher's exact test. Statistical significance is indicated either as exact *P* value or as follows: $^*P < 0.05$, $^{**}P < 0.01$, $^{***}P < 0.001$, and $^{****}P < 0.0001$; 'n.s.' indicates not significant.

Moreover, the data that support the findings of this study are available from the corresponding authors upon reasonable request. If not stated otherwise, the authors declare that all other data supporting the findings of this study are available within the paper and its supplementary information files.

Fig. 6a and Supplementary Fig. 12 have associated source data that are uploaded to ArrayExpress (www.ebi.ac.uk/arrayexpress/) and the data set is available under the accession number E-MTAB-6073, entitled 'Transcriptomic differences in livers of mice fed with normal diet and choline-deficient high-fat diet'.

Reporting Summary. Further information on research design is available in the Nature Research Reporting Summary linked to this article.

Data availability

Data that support the findings of this study have been uploaded to ArrayExpress (www.ebi.ac.uk/arrayexpress/) and the data set is available under the accession number E-MTAB-6073, entitled 'Transcriptomic differences in livers of mice fed with normal diet and choline-deficient high-fat diet'.

References

61. Bender, M., Hagedorn, I. & Nieswandt, B. Genetic and antibody-induced glycoprotein VI deficiency equally protects mice from mechanically and $FeCl_3$-induced thrombosis. *J. Thromb. Haemost.* **9**, 1423–1426 (2011).
62. Tiedt, R., Schomber, T., Hao-Shen, H. & Skoda, R. C. Pf4-Cre transgenic mice allow the generation of lineage-restricted gene knockouts for studying megakaryocyte and platelet function in vivo. *Blood* **109**, 1503–1506 (2007).
63. World Medical Association Declaration of Helsinki. Recommendations guiding physicians in biomedical research involving human subjects. *Cardiovasc. Res.* **35**, 2–3 (1997).
64. International Conference on Harmonisation of Technical Requirements for Registration of Pharmaceuticals for Human Use. ICH harmonized tripartite guideline: guideline for good clinical practice. *J. Postgrad. Med.* **47**, 45–50 (2001).
65. European Commission. Directive 2001/20/EC of the European Parliament and of the Council of 4 April 2001 on the approximation of the laws, regulations and administrative provisions of the member states relating to the implementation of good clinical practice in the conduct of clinical trials on medicinal products for human use. *Med Etika Bioet.* **9**, 12–19 (2002).
66. Grundy, S. M. et al. Implications of recent clinical trials for the national cholesterol education program adult treatment panel III guidelines. *Circulation* **110**, 227–239 (2004).
67. Werner, M. et al. All-In-One: advanced preparation of human parenchymal and non-parenchymal liver cells. *PLoS One* **10**, e0138655 (2015).
68. Maaten, L. J. Pvd & Hinton, G. E. Visualizing high-dimensional data using t-SNE. *J Mach Learn Res.* **9**, 2579–2605 (2008).
69. Raasch, J. et al. IkappaB kinase 2 determines oligodendrocyte loss by non-cell-autonomous activation of NF-kappaB in the central nervous system. *Brain* **134**, 1184–1198 (2011).
70. Bergmeier, W. et al. Flow cytometric detection of activated mouse integrin alphaIIbbeta3 with a novel monoclonal antibody. *Cytometry* **48**, 80–86 (2002).
71. Schulte, V. et al. Targeting of the collagen-binding site on glycoprotein VI is not essential for in vivo depletion of the receptor. *Blood* **101**, 3948–3952 (2003).
72. Nieswandt, B. et al. Long-term antithrombotic protection by in vivo depletion of platelet glycoprotein VI in mice. *J. Exp. Med.* **193**, 459–469 (2001).
73. Gruner, S. et al. Multiple integrin-ligand interactions synergize in shear-resistant platelet adhesion at sites of arterial injury in vivo. *Blood* **102**, 4021–4027 (2003).
74. Nieswandt, B., Bergmeier, W., Rackebrandt, K., Gessner, J. E. & Zirngibl, H. Identification of critical antigen-specific mechanisms in the development of immune thrombocytopenic purpura in mice. *Blood* **96**, 2520–2527 (2000).
75. May, F. et al. CLEC-2 is an essential platelet-activating receptor in hemostasis and thrombosis. *Blood* **114**, 3464–3472 (2009).
76. Subramanian, A. et al. Gene set enrichment analysis: a knowledge-based approach for interpreting genome-wide expression profiles. *Proc. Natl Acad. Sci. USA* **102**, 15545–15550 (2005).
77. Parekh, S., Ziegenhain, C., Vieth, B., Enard, W. & Hellmann, I. The impact of amplification on differential expression analyses by RNA-seq. *Sci. Rep.* **6**, 25533 (2016).

78. Macosko, E. Z. et al. Highly parallel genome-wide expression profiling of individual cells using nanoliter droplets. *Cell* **161**, 1202–1214 (2015).
79. Love, M. I., Huber, W. & Anders, S. Moderated estimation of fold change and dispersion for RNA-seq data with DESeq2. *Genome Biol.* **15**, 550 (2014).
80. Kuleshov, M. V. et al. Enrichr: a comprehensive gene set enrichment analysis web server 2016 update. *Nucleic Acids Res.* **44**, W90–W97 (2016).
81. Levin, Y. S. et al. Effect of echo-sampling strategy on the accuracy of out-of-phase and in-phase multiecho gradient-echo MRI hepatic fat fraction estimation. *J. Magn. Reson. Imaging* **39**, 567–575 (2014).
82. Merkle, E. M. & Nelson, R. C. Dual gradient-echo in-phase and opposed-phase hepatic MR imaging: a useful tool for evaluating more than fatty infiltration or fatty sparing. *Radiographics* **26**, 1409–1418 (2006).
83. Nombela-Arrieta, C. et al. Quantitative imaging of haematopoietic stem and progenitor cell localization and hypoxic status in the bone marrow microenvironment. *Nat. Cell Biol.* **15**, 533–543 (2013).
84. Thon, J. N. & Italiano, J. E. Platelets: production, morphology and ultrastructure. *Handb. Exp. Pharmacol.* **210**, 3–22 (2012).
85. Thon, J. N. & Italiano, J. E. Jr. Does size matter in platelet production? *Blood* **120**, 1552–1561 (2012).

11.2 The immunology of hepatocellular carcinoma

Authors

Marc Ringelhan, **Dominik Pfister**, Tracy O'Connor, Eli Pikarsky and Mathias Heikenwalder

Journal

Nature Immunology | VOL 19 | MARCH 2018 | 222–232 |[3]

https://doi.org/10.1038/s41590-018-0044-z

REVIEW ARTICLE
https://doi.org/10.1038/s41590-018-0044-z

nature immunology

The immunology of hepatocellular carcinoma

Marc Ringelhan[1,2,3], Dominik Pfister[4], Tracy O'Connor[2,5], Eli Pikarsky[6] and Mathias Heikenwalder[4,5]*

In contrast to most other malignancies, hepatocellular carcinoma (HCC), which accounts for approximately 90% of primary liver cancers, arises almost exclusively in the setting of chronic inflammation. Irrespective of etiology, a typical sequence of chronic necroinflammation, compensatory liver regeneration, induction of liver fibrosis and subsequent cirrhosis often precedes hepatocarcinogenesis. The liver is a central immunomodulator that ensures organ and systemic protection while maintaining immunotolerance. Deregulation of this tightly controlled liver immunological network is a hallmark of chronic liver disease and HCC. Notably, immunotherapies have raised hope for the successful treatment of advanced HCC. Here we summarize the roles of specific immune cell subsets in chronic liver disease, with a focus on non-alcoholic steatohepatitis and HCC. We review new advances in immunotherapeutic approaches for the treatment of HCC and discuss the challenges posed by the immunotolerant hepatic environment and the dual roles of adaptive and innate immune cells in HCC.

Responsible globally for approximately 800,000 deaths each year, primary liver cancer is the second leading cause of cancer-related death and the fifth-most-common cancer worldwide[1]. Primary liver cancer comprises a heterogeneous group of malignant tumors that do not include metastases to the liver from other sites. Liver carcinogenesis is a multifactorial process, and predisposing factors for the various liver cancer subtypes differ. Hepatocellular carcinoma (HCC) is the most prevalent primary liver cancer, accounting for 80–90% of cases, with major geographical differences in prevalence[2]. Intrahepatic cholangiocarcinoma and extrahepatic bile-duct carcinoma (perihilar or distal cholangiocarcinoma) account for 6–15% of liver cancers. A distinction between intrahepatic cholangiocarcinoma and extrahepatic bile-duct carcinoma is important, as inflammatory risk factors for intrahepatic cholangiocarcinoma have been found to be similar to those known for HCC[2,3]. Thus, in the development of intrahepatic cholangiocarcinoma as well as that of HCC, geographical differences in incidence probably reflect differences in genetic, environmental and infectious risk factors[2,3]. Other liver cancers include rare non-epithelial tumors and pediatric hepatoblastoma[4].

Known causes of chronic liver disease (CLD) and HCC include alcohol abuse and rare disorders such as α-1 antitrypsin deficiency and hemochromatosis[2]. HCC is less common in liver cirrhosis caused by autoimmune hepatitis, Wilson disease or cholestatic liver disorder[2] (Table 1). However, chronic infection with hepatitis B virus (HBV)[5] remains the leading cause of HCC worldwide, and chronic infection with hepatitis C virus (HCV) is currently the leading cause of end-stage liver disease and HCC in the Western world[6,7].

The incidence of liver cancer, including HCC, has risen in areas with historically low rates, including Western Europe and North America[6]. This might be due in part to the rising prevalence of metabolic syndrome and non-alcoholic steatohepatitis (NASH)[8–10]. Non-alcoholic fatty liver disease (NAFLD), characterized by increased intrahepatic lipid storage and a non-symptomatic diminished ability of the liver to metabolize several substrates, is on the rise[8]. NAFLD can progress to NASH, in which metabolic stress within hepatocytes initiates the death of liver cells, the production of damage-associated molecules (DAMPs) and the influx of activated immune cells (i.e., 'sterile' chronic inflammation)[9,10]. Thus, not only in chronic viral hepatitis but also in alcoholic or metabolic liver disease, chronic inflammation and an altered immune response are associated with the development of HCC[2,11,12].

HCC: an inflammation-driven disease in which chronicity matters

90% of HCCs develop due to underlying chronic liver inflammation, the induction of fibrosis and/or subsequent cirrhosis[2]. The liver is unique in its considerable ability to repair itself after acute damage. Differentiated hepatocytes are able to re-enter the cell cycle and serve as their own main source of replacement[13]. However, in chronic 'necroinflammation', constant cell death, compensatory regeneration and activation of non-parenchymal cells, together with an altered immune response, promote liver fibrosis and tumorigenesis[2,11]. Altered survival and proliferation signals during necroinflammation, cellular stress, epigenetic modifications, mitochondrial alterations and senescence promote tumorigenesis[2,12]. Necroinflammation also induces proliferation-associated replication stress, DNA damage and genetic instability, which is detectable before neoplastic changes occur[14] (Fig. 1).

Mouse models have helped in the identification of molecular and cellular mechanisms yet only partially recapitulate human disease. This might be due in part to missing 'oncogene addiction' loops in human HCC and the distinct, heterogenous types of liver cancer[2,15–17] (Box 1). Proinflammatory cytokines, such as IL-6 and TNF, which activate the transcription factors STAT3 and NF-κB, respectively, have been reported to be important for the development and progression of HCC[18,19], and hepatocyte-specific inhibition of STAT3 has been shown to inhibit HCC in a mouse model of chemically induced HCC[20]. Similarly, inflammation-associated NF-κB signaling has been identified as a central factor in the development of HCC. However, different mouse models have shown

[1]Department of Internal Medicine II, University Hospital rechts der Isar, Technical University of Munich, Munich, Germany. [2]Institute of Virology, Technical University of Munich/Helmholtz Zentrum Munich, Munich, Germany. [3]German Center for Infection Research (DZIF), partner site Munich, Munich, Germany. [4]Division of Chronic Inflammation and Cancer, German Cancer Research Center, Heidelberg, Germany. [5]Institute of Molecular Immunology and Experimental Oncology, Technical University of Munich, Munich, Germany. [6]The Lautenberg Center for Immunology and Cancer Research, Institute for Medical Research Israel Canada and Department of Pathology, Hebrew University-Hadassah Medical School, Jerusalem, Israel.
*e-mail: m.heikenwaelder@dkfz.de

Table 1 | Roles of various immune cell subsets in NAFLD, NASH and HCC

Cell type	NAFLD, NASH, fibrosis	HCC
CD8$^+$ T cells	↑	↑↓
CD4$^+$ effector T cells	↑↓	↑↓
T_{reg} cells	↓	↑
B cells	?	↑↓
KCs or monocytes	↑	↑
NKT cells	↑	↓
NK cells	↓	↓
HSCs	↑	↑
DCs	Sub-type dependent?	↑
Neutrophils	↑	↑

↑, exacerbation; ↓, amelioration.

both pro-tumorigenic functions and anti-tumorigenic functions for NF-kB signaling[21,22]. For example, expression of lymphotoxin-α and lymphotoxin-β in hepatocytes is sufficient for the development of HCC[23]. In contrast, proliferation of damaged hepatocytes and HCC are reportedly increased in mouse models of chemical- and HBV surface antigen–driven hepatocarcinogenesis after inhibition of NF-κB[22,24]. Thus, inhibition of NF-κB remains a challenging approach, as NF-κB is involved in multiple processes and has opposing functions in the development of HCC.

Studies of mouse models have also shown that liver tumors driven by the same oncogenes can have different transcriptomes depending on the level of inflammation and the tumor microenvironment[25,26]. Moreover, the innate and adaptive immune systems are important for the detection and elimination of transformed cells[27]. Thus, understanding the immunological network of the liver and alterations to the microenvironment in CLD is vital for liver cancer research.

The liver as a central player in immunoregulation

The liver has a unique blood supply that flows through a specific microarchitecture known as the 'liver sinusoids', which serve to slow the blood flow and enable optimal exchange of molecules for metabolic functions and form a platform for the central immunological functions of the liver[27]. In addition to nutrients, a large and diverse spectrum of microbes, microbe-associated molecular patterns (MAMPs) and DAMPs continuously reach the liver from the gut. The liver has a large capacity to remove gut-derived microbial compounds (for example, lipopolysaccharide) and pathogens from the circulation. The concentration of MAMPs in portal blood is up to 100-fold higher than that in peripheral blood[28]. Moreover, the liver is centrally involved in the detection and clearance of blood-borne infectious organisms[27]. This is reflected by the multitude of innate and adaptive immune cells in the liver. The liver has the largest population of resident macrophages (Kupffer cells (KCs)) in the body and a high density of natural killer cells (NK cells), natural killer T cells (NKT cells), γδ T cells and liver-transiting and/or resident lymphocytes, with a greater ratio of CD8$^+$ T cells to CD4$^+$ T cells than that in the periphery[27]. Hepatic innate lymphocytes such as NK cells can respond to an array of cell-surface ligands expressed by infected, damaged or transformed cells and influence innate and adaptive immune responses through potent cytokine production[29]. NKT cells actively patrol the liver, directly kill target cells and act as immunological modulators by producing a wide spectrum of pro- and anti-inflammatory molecules (for example, IFN-γ, IL-4 and IL-17)[29,30]. Additionally, liver sinusoidal endothelial cells (LSECs), hepatic stellate cells (HSCs) and hepatocytes are also involved in the detection and capture of pathogens, antigen presentation, cytokine production and maintaining the balance between immunotolerance and activation of the immune system[27,31,32]. The liver serves a key immunoregulatory role through its ability to maintain immunotolerance to non-pathological or constant inflammatory stimuli. This prevents liver damage and induces systemic tolerance[31,32]. Liver immunotolerance results from complex interactions between liver-resident cells (for example, KCs, LSECs, dendritic cells (DCs) and hepatocytes) and peripheral leukocytes. This immunosuppressive environment is maintained by a complex cytokine milieu that includes basal proinflammatory cytokines (IL-2, IL-7, IL-12, IL-15 and IFN-γ) counter-balanced by anti-inflammatory cytokines (IL-10, IL-13 and TGF-β)[32].

Continuous antigen presentation in the liver in the absence of co-stimulatory molecules and CD4$^+$ cells induces T cell tolerance, and KC-derived IL-10 expands regulatory T cell (T_{reg} cell) populations, which induces antigen-specific tolerance[33]. KCs constitute ~90% of all tissue macrophages and are central to pathogen capture, as they clear bacteremia and recruit immune cells to the liver[34]. KCs express an array of scavenger receptors, Toll-like receptors (TLRs), and complement and antibody receptors, which allows the internalization of pathogens and activation of KCs. They are highly plastic and are able to adapt their phenotype in response to signals from the microenvironment[35]. KCs induce hepatic tolerance by producing anti-inflammatory cytokines in response to bacterial endotoxins. This leads to the downregulation of co-stimulatory molecules on antigen-presenting cells, which prevents the activation of T cells[36]. KCs weakly stimulate T cells under basal conditions. However, certain MAMPs induce KCs, via TLR3 and TLR9, to become potent antigen-presenting cells and thereby override T cell tolerance and induce robust T cell responses[37]. While granulocytic cells are mostly absent from the quiescent liver, other myeloid cell populations, including immature myeloid and plasmacytoid DCs, are present[38]. Potent proinflammatory CD141$^+$ myeloid DCs can stimulate strong T cell responses via IFN-γ and IL-17, and chronically inflamed livers are depleted of these DCs[39]. The liver also contains myeloid-derived suppressor cells, which are powerful producers of IL-10, TGF-β and arginase that suppress the activation of T cells[32] and undergo population expansion during chronic infection with HBV[40]. In addition to professional antigen-presenting cells, LSECs, hepatocytes and possibly HSCs can also directly present antigens to T cells[27]. LSECs express a wide variety of pattern-recognition receptors and costimulatory and adhesion molecules and are important sentinels of the immune system[41,42]. LSECs efficiently cross-present blood-derived antigens via major histocompatibility complex class I and class II, and recognition by cognate T cells results in reciprocal signaling in LSECs, with the induction of high levels of the checkpoint ligand PD-L1 and T cell tolerance[43,44]. Furthermore, constant low-level activation of LSECs by some MAMPs (for example, lipopolysaccharide) and KC-derived IL-10 downregulate major histocompatibility complex and costimulatory molecules and thereby facilitate T cell tolerance[27,36]. The accumulation of activated and memory CD8$^+$ T cells in the healthy liver is associated with T cell apoptosis[45].

Deregulation of the tightly controlled immunological network described above inevitably leads to liver disease, including chronic infection, autoimmunity and tumor development[31]. Chronic infection (for example, infection with HBV or HCV), accumulation of fat (in NASH) or DAMPs due to toxic liver damage (in alcoholic liver disease) or liver damage in hereditary disease (for example, hemochromatosis) persistently upregulate inflammatory signals (e.g., cytokines) and cause the breakdown of proper tolerance[27]. The reasons for this shift toward deregulation of the immune system are still incompletely understood, and identifying the factors that contribute to specific liver diseases might pave the way for novel therapeutic interventions.

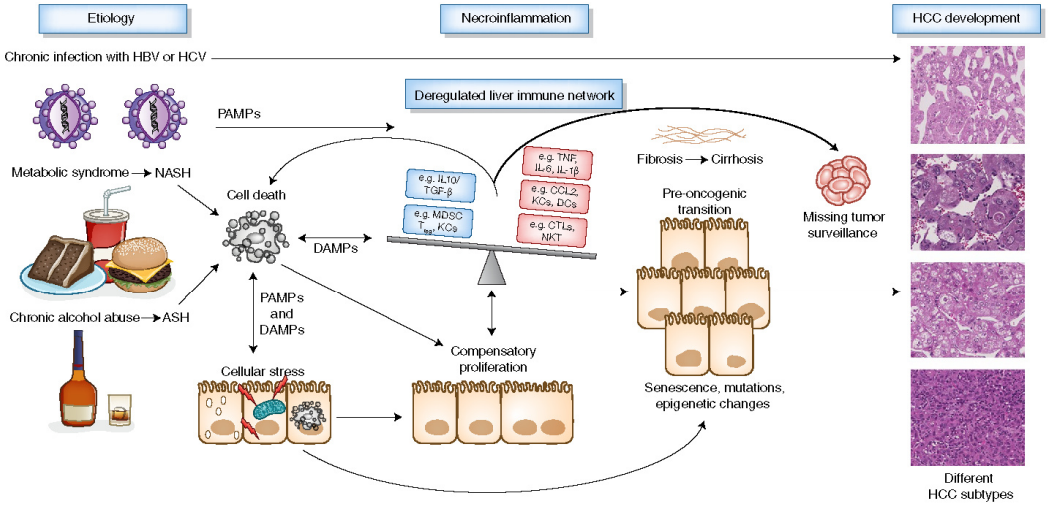

Fig. 1 | Role of necroinflammation in CLD and the development of HCC. The liver continuously removes a large and diverse spectrum of pathogens, MAMPs and DAMPs from the circulation while ensuring organ protection by maintaining immunotolerance. In CLD, this immunological network is deregulated. Persistent infection (for example, with HBV or HCV), accumulation of fat (in NASH) or DAMPs due to toxic liver damage (in alcoholic liver disease) or liver damage due to hereditary disease (for example, hemochromatosis) upregulates proinflammatory signals (IL-2, IL-7, IL-12, IL-15 and IFN-γ) and breaks tolerance. This necroinflammation leads to the activation of non-parenchymal liver cells, altered survival and proliferation signals, cellular stress, epigenetic modifications, mitochondrial alterations and DNA damage, senescence and chromosomal aberrations. This leads to continual cell death, compensatory regeneration and liver fibrosis, which collectively induce tumorigenesis. Moreover, the innate and adaptive immune systems are important for the detection and elimination of transformed cells. However, this surveillance of aberrant cells by the immune system is also dysregulated in necroinflammation. Here, anti-inflammatory cytokines (IL-10, IL-13 and TGF-β) additionally lead to the suppression of effective anti-tumor immune responses. PAMP, pathogen-associated molecular pattern. Credit: Marina Corral Spence/Springer Nature.

Chronic viral liver infection and HCC

In chronic viral hepatitis, the natural history and risk for the development of HCC is linked to the degree of liver inflammation[46].

Box 1 | Clinicopathological features of HCC

HCC is usually derived from malignant, transformed hepatocytes[13] and exists as a spectrum of various tumor subtypes with distinct molecular phenotypes[15]. Classical histomorphological features of HCC include arterial vascularization, cytological atypia, mitotic activity, vascular invasion and loss of the reticulin network. Descriptive histological growth patterns (i.e., a trabecular, pseudoglandular, acinar or solid pattern) are used. Hematogenous extrahepatic metastasis correlate with grading and tumor diameter and travel most often to the lungs, followed by the adrenals and bone[128]. Whole-exome sequencing has provided a complex picture of the main drivers of HCC[125,126], with a mean of ~40 somatic alterations present in coding regions[126]. Mutations in the promoter of the gene encoding telomere reverse transcriptase are common[125] in all major etiologies[129]. The frequency of other mutations, including those in the genes encoding the tumor suppressor p53 and cell-cycle regulators, as well as molecules involved in WNT–β-catenin signaling, epigenetic modification, oxidative-stress pathways, and the RAS–RAF–MAPK and PI(3)K–AKT–mTOR pathways[6,125,126], depends on underlying risk factors. Evidence of genetic predisposition to HCC also exists[6]. However, thus far, molecular characterization of HCC has not helped to identify biomarkers or stratify patients.

Both HBV and HCV are non-cytopathic, and liver damage is induced mainly by immune responses to the virus[31,47]. Immune reactions during persistent infection with HBV or HCV are insufficient to clear the virus, which leads to progressive liver damage. Although the mechanisms by which these infections persist are still incompletely understood, multiple mechanisms for evading the immune system have been described that inhibit the effector function of virus-specific T cells[31,48]. During infection with HBV, the strength of the anti-viral $CD8^+$ T cell response to HBV surface and core antigens correlates with the clearance of HBV[47]. The development of chronicity is due to T cell exhaustion from the substantial load of circulating HBV antigens[49], as well as to tolerogenic factors in the liver that weaken specific immunity[40,50]. HCV evades detection by the immune system by high replication and mutation rates[51], and through viral factors, which counteract the sensors RIG-I, MDA5 and TLR3[52–54]. Interestingly, a memory-like virus-specific $CD8^+$ T cell subset with features of T cell exhaustion has been reported during chronic infection with HCV; this subset was maintained even after chronic antigen stimulation ceased[55]. However, T cell exhaustion in such hepatotropic infections is still incompletely understood. Nevertheless, HBV can directly induce hepatocyte damage under certain conditions[24]. In addition, HCV activates the NLRP3 inflammasome in macrophages and monocytes without inducing type I interferons[56]. Furthermore, DAMPs from ongoing hepatocyte death might induce activation of the innate immune system and contribute to chronic necroinflammation, the elevation of proinflammatory cytokines and the subsequent development of HCC[57].

Alcoholic liver disease and alcoholic steatohepatitis

Prolonged or excessive exposure to alcohol induces hepatic steatosis and CLD, which leads to hepatocyte death, accumulation of DAMPs, activated innate immunity and inflammation; this results in end-stage liver disease and the risk of HCC[58]. In some cases, alcohol abuse leads to acute alcoholic steatohepatitis (ASH), which is associated with high mortality regardless of treatment with corticosteroids[58]. Ongoing toxic stress induced by chronic alcohol consumption and the resulting inflammation (activation of monocytes and macrophages, neutrophilia and increased TNF, IL-1β and IL-18) critically influence the progression of alcoholic liver disease. A major feature of this prototypical type of 'sterile inflammation' is activation of the NLRP3 inflammasome, which amplifies proinflammatory signals[57]. Experimental data support the importance of the activation of inflammasomes by DAMPs (for example, uric acid and ATP or HMGB1 from hepatocytes) in ASH[59,60], and inhibition of inflammasomes attenuates ethanol-induced liver injury[59,60]. Nonetheless, the specific role of these sterile signals in alcohol-induced liver damage is debatable, and data also support the possibility of a role for gut-derived MAMPs[57].

NAFLD and NASH: emerging HCC etiologies

NAFLD and NASH are on the rise, and patients with these disorders are at increased risk of developing HCC[10]. Although NASH shares histopathological features with ASH, the immunological pathogenic factors involved are apparently different[61]. Insulin resistance and metabolic syndrome have been linked to the development of NASH, but the role of the inflammasomes, as well as that of other ligands and immune cell subsets, is only partially understood. The activation of TLRs via MAMPs and DAMPs from the gut microbiota and damaged hepatocytes (HMGB1, saturated fatty acids, cholesterol esters and reactive oxygen species (ROS)) has been suggested[57]. However, an important difference in the 'sterile inflammation' of NASH is that the activation of inflammasomes occurs not only in macrophages but also in hepatocytes and other immune cells[57]. Moreover, adaptive immune cells also seem to have a pivotal role in NASH. This is highlighted by experimental data obtained with a mouse model, in which mice are fed a choline-deficient high-fat diet, that recapitulates NASH-induced HCC. Antibody-mediated depletion of $CD8^+$ T cells in established NASH abolishes liver damage, which indicates that metabolically activated intrahepatic $CD8^+$ T cells are the main drivers of liver damage[62]. At the same time, inflammation-induced suppression of the activation of cytotoxic $CD8^+$ T lymphocytes by IgA^+ cells has been identified as a tumor-promoting mechanism[63].

Adaptive and innate lymphocytes in NASH and HCC

$CD8^+$ T cells serve opposing roles in promoting a chronic proinflammatory microenvironment and in anti-tumor surveillance. $CD8^+$ cytotoxic T lymphocytes (CTLs) kill their target cells by direct contact and by lysing them via perforin, granzyme A and granzyme B in concert with signaling via the cell-surface receptor Fas and its ligand, FasL[64,65], as well as via secretion of IFN-γ and TNF[66]. Activated T cells produce HCC-inducing lymphotoxin-α and lymphotoxin-β[23], as well as other mitogenic cytokines. This is consistent with a general role for lymphotoxin-expressing T cells in chronic inflammation-induced tissue damage and autoimmune diseases[67]. Moreover, lymphotoxins have been linked to the promotion of HCC by ectopic lymphoid structures, which are associated with a worse prognosis in HCC[68] (Box 2).

Depletion of $CD8^+$ T cells and a decrease in lymphotoxin-β delay tumor development in an HCC model driven by repeated fumarylacetoacetate-induced flares of hepatitis in mice with homozygous deficiency in the gene encoding fumarylacetoacetate hydrolase (*Fah*$^{-/-}$ mice)[69]. The effects of therapeutic depletion of $CD8^+$ T cells on NASH have indicated an increased incidence of HCC in such mice[63]. On the other hand, $CD8^+$ T cells are the main subset of tumor-infiltrating lymphocytes (TILs) that perform anti-tumor effector functions[70]. The surveillance of pre-malignant, senescent hepatocytes was shown to be dependent on helper T cells by hepatic expression of NRas oncogene–induced senescence in a mouse model using mice deficient in CTLs or NKT cells or by using $CD4^+$ T cell–depleting antibodies[71]. Accordingly, large numbers of $CD8^+$ TILs in human HCC correlate with improved overall survival, longer relapse-free survival and diminished disease progression[69,72]. In HCC, the main cytotoxic interactions seem to be mediated by IFN-γ-secreting $CD8^+$ T cells and $CD57^+$ NK cells[72]. Accordingly, an increased abundance of T_{reg} cells in HBV^+ patients is associated with the progression of HCC disease[73]. Further studies are needed to delineate the seemingly opposing roles of $CD8^+$ T cells in different stages of HCC pathogenesis, and such studies might reveal distinct subsets of $CD8^+$ T cells (Fig. 2).

$CD4^+$ T cells also have opposing roles in CLD and HCC that range from effector cell function to regulatory cell function. In a model of NASH and HCC using hepatocyte-specific overexpression of the proto-oncoprotein c-Myc and a diet deficient in methionine and choline, depletion of $CD4^+$ T cells led to accelerated growth of HCC. In that study, dysregulated lipid metabolism induced ROS-mediated selective loss of $CD4^+$ T cells but not of $CD8^+$ T cells[77]. That is consistent with dysregulated T cell metabolism and impaired immunity in chronic infection and cancer and excessive T cell activity in autoimmune and inflammatory pathologies[78]. On the other hand, $CD8^+$ T cell responses mediated by the T_H1 subset of helper T cells in viral or sterile hepatitis are proinflammatory and pro-tumorigenic[62,69]. Furthermore, the anti-inflammatory functions of particular $CD4^+$ T cell subtypes have also been reported to be pro-tumorigenic. A pro-tumorigenic role for T_H17 cells was identified in a mouse model system of overexpression of the transcriptional repressor URI. Systemic IL-17A caused the infiltration of neutrophils into adipose tissue; this generated a feed-forward mechanism that aggravated NASH via the release of fatty acids and induction of DNA damage in hepatocytes, which led to HCC[79]. In humans, impaired $CD4^+$ follicular helper T cells have been reported to influence the development of HBV-associated HCC and have been proposed as a potential prognostic marker[80]. Both circulating $CD4^+$ CTLs and tumor-infiltrating $CD4^+$ CTLs have been shown to be independent predictors of disease-free survival and overall survival after resection of HCC[73]. A progressive lack of $CD4^+$ T cells has been shown in a large study of patients with HCC, and an increased

Box 2 | Ectopic lymphoid structures, HCC and prognosis

During chronic inflammatory conditions, infiltrating immune cells can form distinct aggregates. Certain MAMPs have been shown to induce intrahepatic aggregates of myeloid cells via TLR3 and TLR9, which enables local proliferation and licensing of $CD8^+$ T cells. These aggregates, composed of inflammatory monocyte–derived $CD11b^+$ cells, as well as signaling via TNF-induced formation of intrahepatic myeloid-cell aggregates for T cell population expansion, facilitate the OX40-dependent population expansion of CTLs[57]. Other lymphoid structures that show enrichment for $CD20^+$ B cells or $CD8^+$ T cells, called 'ectopic lymphoid structures' (ELSs), have also been described in the context of liver tumorigenesis[68]. ELSs are thought to be beneficial in many tumor types due to their ability to foster an effective local anti-tumor response[74–76]. ELSs seem to provide a local niche in which HCC progenitors can proliferate until they gain independence, leave ELSs and disseminate into liver parenchyma[68]. The exact role of these complex structures in the shift from anti-tumor immunity to liver cancer development, relative to that of their single-cell counterparts, remains under investigation.

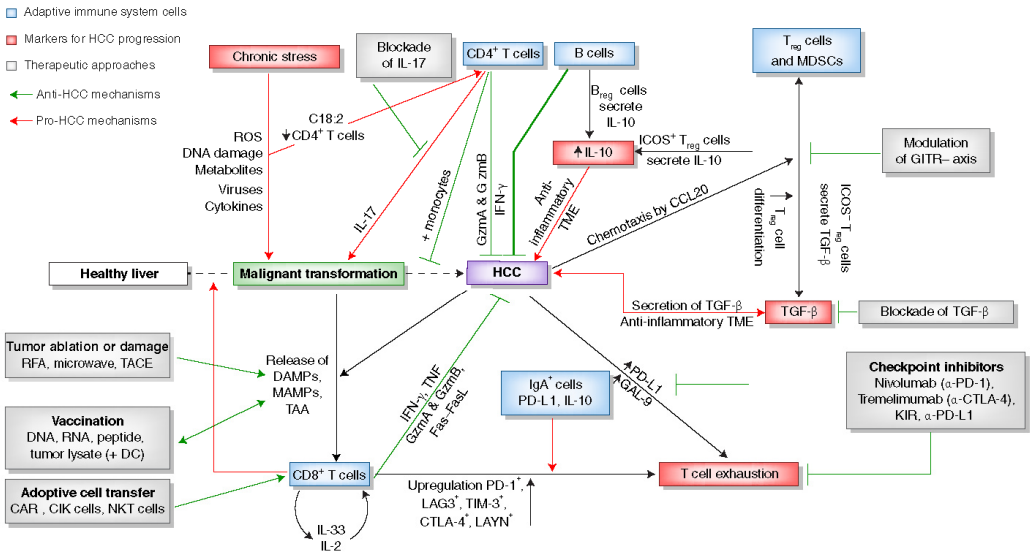

Fig. 2 | The dual role of the adaptive immune system in hepatocarcinogenesis and HCC surveillance. In chronic necroinflammation, adaptive immune cells fulfil seemingly opposing functions. Activated adaptive immune cells in necroinflammation are part of a proinflammatory environment, which leads to DNA damage, cellular stress, epigenetic modifications, mitochondrial alterations, senescence and chromosomal aberrations in liver cells. At the same time, exhaustion and tolerance of adaptive immune cells diminish the important role of these cells in the detection and elimination of transformed cells. Cytotoxic T cells not only cause liver damage but also are needed for the surveillance of pre-malignant cells in the liver. CD4+ T cells, in cooperation with monocytes, mediate anti-senescence responses, whereas T_H17 cells are involved in NASH-induced hepatocarcinogenesis. This dual role also functions in established HCC. TILs in HCC express markers of exhaustion (PD-1, LAG-3, TIM-3, CTLA-4 and layilin) and show increased IL-10, TGF-β and CCL20. The recruitment of T_{reg} cells diminishes the effectiveness of T cell–mediated tumor surveillance. Overcoming the exhaustion of effector cells promises to be a powerful therapeutic strategy in HCC (via antibodies to PD-1, PD-L1 and CTLA-4). TAA, tumor-associated antigen; RFA, radiofrequency ablation; CAR, chimeric antigen receptor; CIK cells, chemokine-induced killer cells; Gzm, granzyme; B_{reg} cells, regulatory B cells; TME, tumor microenvironment; GITRL, ligand for GITR; α-, antibody to.

abundance of T_{reg} cells is correlated with poor survival and high recurrence rates in patients with HCC[73].

The role of B lymphocytes in the development of HCC and of tumor-infiltrating B cells remains controversial. There are weaknesses in the existing mouse models used to investigate the role of B cells, due to the influence of B cell depletion on other immune cells in these mice. Experimental data using mice deficient in B cells (the μMT strain), as well as data on the expression of mRNA from human HCC, suggest that T cells prevent initial tumor formation, while B cells critically limit the growth of established tumors[81]. Furthermore, the number of tumor-infiltrating B cells in HCC is reported to correlate with T cell–activation markers. The close proximity of tumor-infiltrating T cells and B cells indicates a functional interaction that might contribute to a better prognosis[72]. In contrast, a greater abundance of IL-10-expressing B cells has been found in patients with HCC, and this negatively correlates with activated CD4+ T cells[82]. The suppression of anti-tumor cytotoxic CD8+T cells through the accumulation of liver-resident IgA+ regulatory B cells in NASH has been reported in an experimental study. Experimental ablation of T cells accelerates HCC, and the IgA+ cells, which express PD-L1 and IL-10, directly suppress cytotoxic CD8+ T cells in the liver as a tumor-promoting mechanism[63] (Fig. 2). Future experiments should reveal whether B cells in different compartments (for example, the liver and secondary lymphoid organs) represent a possible therapeutic target.

The number of NKT cells is increased in human NASH and cirrhosis[62,83,84], and experimental evidence suggests they might have an adverse effect on the course of this disease. NKT cells can directly activate HSCs via the signaling protein hedgehog and osteopontin, and NKT cell–deficient mice are protected from fibrosis[83]. Moreover, NKT cells contribute to steatosis and macrovesicular steatosis by promoting the uptake of lipids by hepatocytes through signaling via the lymphotoxin-like inducible protein LIGHT[62]. The liver in HCC also seems to show enrichment for NKT cells[30,62]. Whether these ultimately have a beneficial role or a negative role in the progression of HCC has not been investigated extensively. However, one group has reported a protective role for type I NKT cells against β-catenin-induced HCC in mice[85]. Those findings and the known increase in NKT cells in CLD indicate a possible important role for NKT cells in the development of HCC and anti-tumor surveillance. However, some studies claim that NKT cells promote fibrosis[62,83,84].

Liver NK cells target activated HSCs and are thus considered anti-fibrotic[86]. NK cells have well-documented anti-tumor functions. However, NK cell function seems to be diminished during the development of HCC. Various explanations for this exist, including STAT3-mediated upregulation of IL-10 and TGF-β[87], NK cell exhaustion[88] and infiltration of the liver with inactive or immature peripheral NK cells[89]. Boosting endogenous NK cell–like cytolytic activity via ex vivo stimulation of 'cytokine-induced killer cells' is being pursued as a therapeutic strategy for HCC[90]. In human patients with NAFLD or NASH, transcriptional markers of

NK cells are elevated[91]. Unlike many other innate immune cells, NK cells seem to have a beneficial role during NAFLD and NASH. The anti-fibrotic property of NK cells has been attributed to their ability to influence macrophage polarity rather than to their cytolytic activity[92].

Innate immune cells in NASH and HCC

In vivo studies suggest that prolonged activation of KCs and inflammatory monocytes is pathological in the context of chronic liver inflammation and liver regeneration. Targeting signaling via the chemokine CCL2 and its receptor CCR2 appears to be protective against HCC[93]; this might be due in part to the ability of inflammatory monocytes to promote angiogenesis[94]. However, CCR2 deficiency in mice suffering from NASH has no effect on the incidence of HCC[62]. Cross-talk between KCs and hepatocytes, including KC-derived inflammatory signaling, is important for chemical carcinogen–induced liver cancer[22]. At later stages of disease, the intracellular components of dying hepatocytes might release DAMPs, such as hepatocyte DNA[95], which trigger the activation of KCs via TLRs. It has been reported that hypoxic conditions in the liver might activate KCs via upregulation of the transcription factor HIF-1α[96]. However, due to the lack of animal models that allow selective and distinct inhibition of KCs without inducing liver toxicity or disrupting the physiological function of KCs[97], it is difficult to determine the role of KCs in liver pathologies experimentally. Considerable research has been devoted to identifying the triggers that promote the activation of KCs in NASH. Changes in the gut microbiota that might influence the immunological profile of the liver are one main avenue of investigation. In addition, altered metabolism might diminish glucocorticoid signaling in KCs[98] or induce epigenetic changes that maintain KCs in a proinflammatory state[99]. Inhibition of $CD163^+$ macrophages[100], depletion of macrophages via clodronate[101] and antagonizing CCL2–CCR2 signaling[102] all ameliorate experimental NASH. The activation of inflammasomes by KCs can promote NASH; accordingly, pharmacological inhibition of NLRP3 ameliorates NASH in rodent models[57]. The activation of NLRP3 produces IL-1β and IL-18, which trigger an inflammatory cascade, including the production of IL-6, which has a mitogenic effect on hepatocytes. Hence, IL-6 produced by KCs promotes HCC[103]. Another mechanism by which activated KCs promote NASH and the development of HCC is through the production of ROS[104,105]. However, the activation of KCs can promote other types of liver malignancies as well. For example, it has been discovered that in the context of severe damage to hepatocytes, activation of KCs and a large abundance of TNF leads to cholangiocellular overgrowth and malignant transformation of biliary cells. This pathological process is also very much dependent on the production of ROS[26].

However, the function of KCs might be impaired in the tumor microenvironment of HCC due to the presence of myeloid-derived suppressor cells[106]. The recruitment and maturation of $CCR2^+$ myeloid cells by hepatocyte senescence–associated cytokines might accelerate the growth of fully established HCC[107]. The multifaceted role of myeloid-derived suppressor cells in HCC has been discussed extensively elsewhere[38].

Existing experimental data on the role of DCs in NASH are conflicting[108–111]. However, the use of DCs to boost anti-tumor immunity has been widely pursued as a therapeutic approach for HCC[112]. Interestingly, human studies[113,114] and mouse studies investigating the role of endogenous DCs in the pathogenesis of HCC have identified an exacerbating role as well for this cell type, due to its ability to promote immunotolerance by a variety of mechanisms[115,116] (Fig. 3).

A large number of neutrophils in patients with HCC is predictive of a poorer outcome[117,118]. Neutrophils can promote tumorigenesis by enhancing cell growth, angiogenesis and metastasis through production of the growth factors HGF and VEGF or the proteinase MMP9 and closely interact with KCs[119]. Neutrophils are considered a hallmark of ASH. Likewise, an increase in neutrophils has been reported in both mouse NASH and human NASH[62]. In addition, a large number of circulating neutrophils or neutrophil elastase is indicative of NASH in patients[120]. Mechanistically, neutrophils seem to contribute to the development of fibrosis directly through the activation of HSCs[121]. In HCC, tumor-associated neutrophils recruit macrophages and T_{reg} cells and promote resistance to the tyrosine-kinase inhibitor sorafenib[122]. The exact role of neutrophils in HCC remains controversial and is poorly understood.

HCC: a therapeutic challenge

HCC is a chemotherapy-resistant tumor that is most frequently diagnosed at advanced stages with limited treatment options (Box 1) and is thus associated with a high mortality rate. Potentially curative therapy (i.e., surgical resection, liver transplantation and/or local ablation) is feasible only at early stages of HCC. Some patients at intermediate stages benefit from transcatheter arterial chemoembolization (TACE)[123] or selective internal radiation therapy. However, the only treatment available for advanced HCC is sorafenib or, as a second-line option, the mulit-kinase inhibitor regorafenib, each of which extends median survival by only a few weeks. Moreover, more than 100 trials testing other substances or treatment approaches have thus far failed to show survival advantages in advanced HCC[124], which might at least partially be due to missing biomarkers and the considerable molecular heterogeneity of HCC[125,126]. Intratumor immune cell infiltrates in HCC also show a heterogeneous immunological profile. It has been reported that ~25% of HCCs robustly express inflammatory response markers and have fewer chromosomal aberrations (i.e., 'the immune class'). This includes HCC with markers of an adaptive T cell response, as well as HCC with markers of an exhausted immune response[127], which has important implications for prognosis as well as for patient stratification for novel therapeutic approaches.

Immunotherapy: a possible future for HCC treatment?

Tumor-associated antigens have been identified for HCV-associated HCC, and engineering T cells that express specific T cell antigen receptors for HCV has been proposed as a therapeutic option[130]. Vaccination with tumor-associated antigens (α-fetoprotein, glypican-3 and the multidrug resistance–associated protein MRP3) has produced T cell response rates of >70%, but vaccination with these antigens has shown no advantage for overall survival[131,132]. Other HCC-derived antigens produce lower T cell response rates and similarly fail to elicit clinical responses[132,133]. These approaches must be intensively personalized and are a major challenge in the immunotolerant liver environment[134]. Thus, no vaccination strategies for HCC have progressed to phase III clinical trials so far. Eliciting an optimal antigen response mediated by the interaction of major histocompatibility complex molecules with the T cell antigen receptor might require secondary receptor interactions (for example, interactions between the following receptors and their ligands: CD28–CD80 (or CD86); ICOS–B7RP1; CD137–CD137L; OX40–OX40L; and CD27-CD70)[135]. Interestingly, the alarmin IL-33 is reported to be a marker of prolonged patient survival in HCC with the ability to induce clonal expansion of CTLs and thus offers the potential to prolong the responses of tumor-associated antigens[136].

Combating T cell exhaustion

In established HCC, impaired secretion of IFN-γ, TNF, granzyme A and granzyme B by CTLs has been reported; this correlates with an exhausted effector-cell phenotype, including upregulation of inhibitory receptors, such as PD-1, CTLA-4, TIM-3, LAG3, Gal-9 and HVEM, and leads to a poor prognosis[137,138]. Single-cell RNA-sequencing analysis has identified a previously unknown exhaustion marker, layilin, on tumor-infiltrating $CD8^+$ T cells and T_{reg} cells

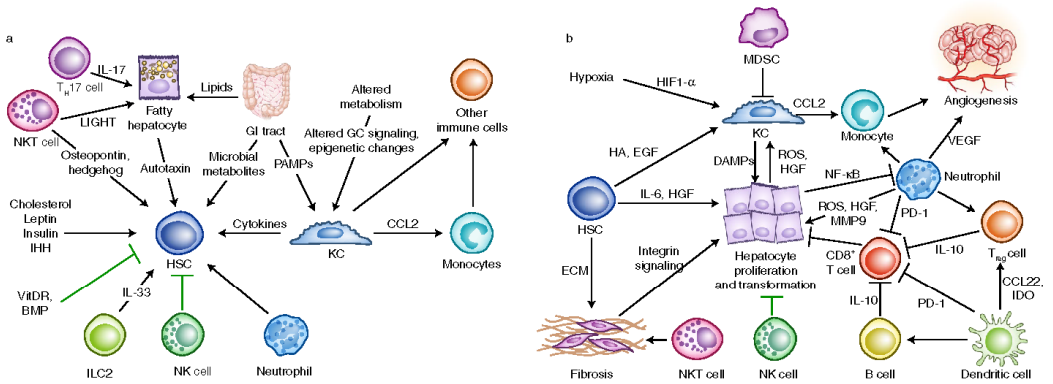

Fig. 3 | Innate and adaptive immune cell subsets in NAFLD, NASH and NASH-induced HCC. a, During NAFLD and NASH, an altered gut microbiome and/or enhanced gut permeability leads to the release of MAMPs and microbial metabolites in the liver, which activate HSCs and KCs. In addition, increased lipids, as well as LIGHT secreted from NKT cells, enhance lipid uptake by hepatocytes. An altered metabolic environment might directly lead to the activation of KCs. Activated KCs release cytokines, such as CCL2, which recruit inflammatory monocytes and other immune cells and activate HSCs. IHH, indian hedgehog; VitDR, vitamin D receptor; BMP, bone-morphogenic protein; GI, gastrointestinal; GC, glucocorticoid; ILC2, group 2 innate lymphoid cell. **b**, During the transition from NASH to fibrosis and HCC, various factors, including ROS and hepatocyte growth factors (HGF), are released by activated innate immune cells, which has a pro-proliferative effect on hepatocytes or promotes metastatic activity. Activated HSCs deposit excessive components of the extracellular matrix (ECM), which eventually leads to fibrosis. Fibrosis has a mitogenic effect on hepatocytes, possibly through enhanced integrin signaling. The activation of NKT cells also promotes fibrosis. These pro-proliferative effects on hepatocytes are counteracted by the activity of NK cells and $CD8^+$ T cells. In addition, neutrophils and DCs indirectly promote the proliferation of transformed hepatocytes through their multitude of inhibitory effects on $CD8^+$ T cells. Finally, monocytes and neutrophils directly promote angiogenesis. Green lines indicate a positive effect. HA, hyaluronic acid; EGF, epidermal growth factor; IDO, indoleamine 2,3-dioxygenase. Credit: Marina Corral Spence/Springer Nature

but not on $CD4^+$ cytolytic T cells. Overexpression of layilin on $CD8^+$ T cells is correlated with a poor prognosis, reduced production of IFN-γ and exhausted FoxP3$^+$ $CD8^+$ cells[139]. Interestingly, absent or low tumor expression of PD-L1, Gal-9 and HVEM in HCC seems to be associated with even poorer survival. Infiltrating $CD8^+$ TILs induce PD-L1 expression via IFN-γ[140]. Higher expression of Gal-9 and PD-L1 might indicate an increased number of $CD8^+$ TILs and thus active immunosurveillance of the tumor[141]. In a cohort of 956 patients with HCC, 25% had high expression of PD-L1 and PD-1. This group could be stratified into two subtypes characterized by either markers of adaptive T cell response or an exhausted immune response and genes regulated by TGF-β[127], which indicates that a subset of patients with HCC might respond well to immunotherapies that target markers of T cell exhaustion.

Immunological checkpoint inhibitors

Immunological checkpoint receptors control immune reactions and prevent autoimmune responses. Blocking these receptors enhances T cell responses directed against tumors. However, the efficacy of this approach has been variable between cancer types and patients[142,143]. A non-comparative phase I study has reported a 20% response rate to treatment with nivolumab, a monoclonal antibody to PD-1[144]. A phase I trial with tremelimumab, a monoclonal antibody to CTLA-4, has shown a partial response rate of 17.6% and stable disease in 76.4% of the subjects[145]. It is thus likely that immunological biomarkers could assist with immunomodulatory treatment of HCC[146]. Substantial phosphorylation of the kinase ERK in HCC has been found to correspond to a favorable response to sorafenib, whereas little phosphorylation of ERK is associated with considerable infiltration of PD-1$^+$$CD8^+$ T cells[137]. Adding a secondary stimulus, such as surgical treatment, ablation, TACE or radiation to boost the immune response, might maximize the effect of checkpoint inhibitors. Combining TACE or radiation with tremelimumab is feasible and holds promise for improved therapeutic responses[147], while combining TACE with sorafenib does not increase overall survival[123].

However, immunological checkpoint therapies can induce serious autoimmune reactions, the severity of which might be exacerbated by combination therapies[142]. Given the underlying liver disease in most HCC, the side effects of these drugs on the liver, such as checkpoint-induced hepatitis, put such patients at high risk for liver failure and death. Thus, using these therapies requires early recognition and treatment of side effects, as well as biomarker-based stratification of patients who are likely to respond favorably.

Circumventing T_{reg} cells

The potent inhibitory function of T_{reg} cells is a major obstacle to the generation of an effective anti-tumor response in HCC. HCC-infiltrating T_{reg} cells can be further subdivided into an ICOS$^+$, mainly IL-10-secreting subset and an ICOS$^-$ subset with abundant secretion of TGF-β, which are probably attracted by signaling via interaction between the chemokine CCL20 and its receptor CCR6. T_{reg} cells, along with other immunosuppressive cells such as regulatory B cells, lead to increased expression of IL-10 in HBV-associated HCC[72]. An increased number of T_{reg} cells correlates with diminished patient survival and resurgence-free time[72,82]. In a mouse model of diethylnitrosamine-induced HCC, TGF-β promoted T_{reg} cell differentiation, and this was identified as a key inhibitory mechanism of $CD8^+$ T cells[148]. Accordingly, the TGF-β inhibitor SM-16 decreased the frequency of T_{reg} cells and delayed the progression of HCC, and a correlation was found between a TGF-β$^+$ phenotype and a FoxP3$^+$ phenotype (T_{reg} cell) in tumor cells[149]. Such results make TGF-β an attractive therapeutic target[138]. Other combinations, such as lirilumab (a monoclonal antibody to the killer immunoglobulin-like receptor KIR) plus nivolumab, are being tested in clinical trials. Furthermore, the ligand for the glucocorticoid-induced TNF

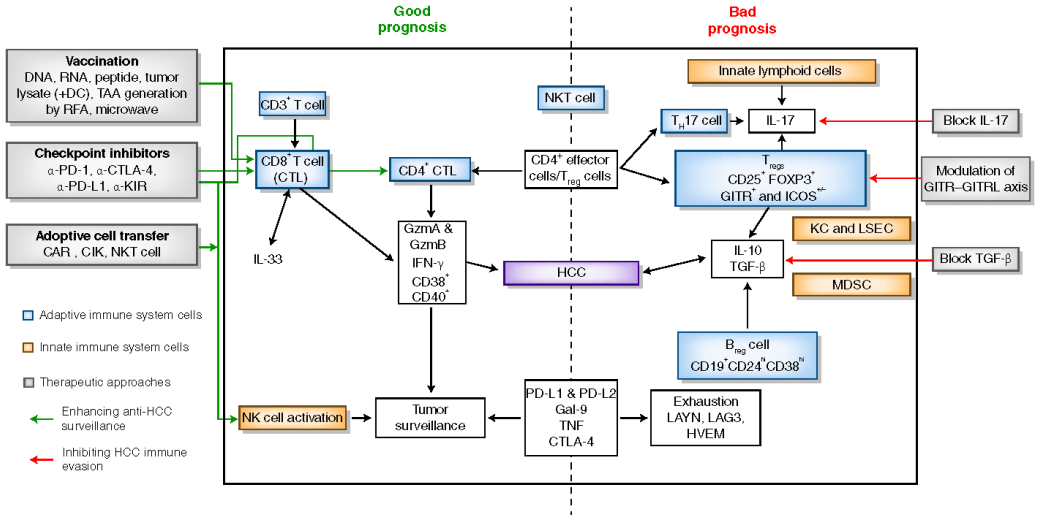

Fig. 4 | Immunological prognostic markers in HCC and possible patient stratification. Immunological status in HCC is characterized by immune responses that lead to anti-tumor immunity or immunotolerance, which promotes tumor cell growth. A shift in the immune response toward tumor immunotolerance is associated with carcinogenesis and disease progression. This includes the following: the release of inhibitory cytokines by KCs and LSECs, and the upregulation of immunological checkpoint molecules (PD-1, PD-L1 and CTLA-4), T_{reg} cells and regulatory B cells. Furthermore, a role for innate lymphoid cells via IL-17 has been reported. These factors protect the liver from autoimmune damage by blocking the activation of effector T cells but also allow escape from the immune system by HCC. In HCC, a good prognosis can be assumed if there is substantial activation of CTLs, sometimes correlated with an increased number of intratumoral CD8+ and CD4+ CTLs. However, strong intratumoral CTL activity is associated with increased expression of PD-L1 or other inhibitory signals. Thus, the number of NKT cells and CD4+ T cells and the expression of PD-L1/2, Gal-9 or TNF do not always correlate with a poor prognosis (immunotolerance) but correlate with an enhanced CTL response directed against HCC and a good prognosis. The identification of immunological checkpoint inhibitors that oppose evasion of the immune system by HCC has raised hope for successful therapy of advanced HCC in clinical trials. Other strategies (vaccination, adoptive cell transfer, and blockade of TGF-β, IL-17, GITRL or IL-33) and combination strategies might help to shift this balance in certain patients.

receptor GITR might also help to shift the T_{reg} cell–effector cell balance and restore robust anti-tumor immunity[150] (Fig. 4).

Conclusions

HCC is a pervasive liver pathology, and it is well accepted that chronic inflammation is a key driver of disease progression in the prototypical etiologies of HCC. The liver continuously removes a large and diverse spectrum of pathogens, MAMPs and DAMPs from the circulation, which ensures organ protection while maintaining immunotolerance. Deregulation of this tightly controlled immunological network inevitably leads to liver disease, including chronic infection, autoimmunity and tumor development. Persistent upregulation of inflammatory signals due to chronic liver damage leads to necroinflammation (activation of immune cells, altered immunological, survival and proliferation signals and promotion of liver fibrosis) and, subsequently, the induction of tumorigenesis. The roles of various microbial and danger signals, loss of immunotolerance mechanisms and immune cell subsets involved in the progression of CLD are being elucidated. However, most facets of this are still incompletely understood, and experimental data sometimes seem to be contradictory. Various immune cells seem to change their phenotype during the disease course. The innate and adaptive immune systems are undoubtedly important for the detection and elimination of transformed cells. However, this process is dysregulated in necroinflammation, and anti-inflammatory cytokines (e.g., IL-10 and TGF-β) suppress proper anti-tumor immune responses. Further elucidation of these mechanisms is crucial, as early and sustained elimination of the underlying chronic liver damage is key to reducing the risk of HCC and end-stage liver disease. Furthermore, the highly immunotolerant environment and tightly controlled protective mechanisms in the liver make the development of effective immunotherapies for HCC challenging. The identification and validation of previously unknown (for example, immunological) biomarkers in HCC and the stratification of patients will be vital for the generation of favorable responses to emerging immunotherapies.

Received: 6 August 2017; Accepted: 29 November 2017;
Published online: 29 January 2018

References

1. Ferlay, J. et al. Cancer incidence and mortality worldwide: sources, methods and major patterns in GLOBOCAN 2012. *Int. J. Cancer* **136**, E359–E386 (2015).
2. Llovet, J. M.et al Hepatocellular carcinoma. *Nat. Rev. Dis. Prim.* **2**, 16018 (2016).
3. Bridgewater, J. et al. Guidelines for the diagnosis and management of intrahepatic cholangiocarcinoma. *J. Hepatol.* **60**, 1268–1289 (2014).
4. Bosman, F. T., Carneiro, F., Hruban, R. H. & Theise, N. D. *WHO Classification of Tumours of The Digestive System*. (World Health Organization, Geneva, 2010.
5. Liu, J. et al. Spontaneous seroclearance of hepatitis B seromarkers and subsequent risk of hepatocellular carcinoma. *Gut* **63**, 1648–1657 (2014).
6. Torre, L. A. et al. Global cancer statistics, 2012. *CA Cancer J. Clin.* **65**, 87–108 (2015).
7. Levrero, M. & Zucman-Rossi, J. Mechanisms of HBV-induced hepatocellular carcinoma. *J. Hepatol.* **64**(Suppl), S84–S101 (2016).

8. Wong, V. W. et al. Pathogenesis and novel treatment options for non-alcoholic steatohepatitis. *Lancet Gastroenterol. Hepatol.* **1**, 56–67 (2016).
9. Nakagawa, H. et al. ER stress cooperates with hypernutrition to trigger TNF-dependent spontaneous HCC development. *Cancer Cell.* **26**, 331–343 (2014).
10. Loomba, R. & Sanyal, A. J. The global NAFLD epidemic. *Nat. Rev. Gastroenterol. Hepatol.* **10**, 686–690 (2013).
11. Hernandez-Gea, V., Toffanin, S., Friedman, S. L. & Llovet, J. M. Role of the microenvironment in the pathogenesis and treatment of hepatocellular carcinoma. *Gastroenterology* **144**, 512–527 (2013).
12. Fattovich, G., Stroffolini, T., Zagni, I. & Donato, F. Hepatocellular carcinoma in cirrhosis: incidence and risk factors. *Gastroenterology* **127**, S35–S50 (2004).
13. Jörs, S. et al. Lineage fate of ductular reactions in liver injury and carcinogenesis. *J. Clin. Invest.* **125**, 2445–2457 (2015).
14. Boege, Y. et al. A dual role of caspase-8 in triggering and sensing proliferation-associated DNA damage, a key determinant of liver cancer development. *Cancer Cell.* **32**, 342–359 (2017).
15. Sia, D., Villanueva, A., Friedman, S. L. & Llovet, J. M. Liver cancer cell of origin, molecular class, and effects on patient prognosis. *Gastroenterology* **152**, 745–761 (2017).
16. Zucman-Rossi, J., Villanueva, A., Nault, J. C. & Llovet, J. M. Genetic landscape and biomarkers of hepatocellular carcinoma. *Gastroenterology* **149**, 1226–1239 (2015). e1224.
17. Villanueva, A., Hernandez-Gea, V. & Llovet, J. M. Medical therapies for hepatocellular carcinoma: a critical view of the evidence. *Nat. Rev. Gastroenterol. Hepatol.* **10**, 34–42 (2013).
18. Naugler, W. E. et al. Gender disparity in liver cancer due to sex differences in MyD88-dependent IL-6 production. *Science* **317**, 121–124 (2007).
19. Subramaniam, A. et al. Potential role of signal transducer and activator of transcription (STAT)3 signaling pathway in inflammation, survival, proliferation and invasion of hepatocellular carcinoma. *Biochim. Biophys. Acta* **1835**, 46–60 (2013).
20. He, G. et al. Hepatocyte IKKβ/NF-κB inhibits tumor promotion and progression by preventing oxidative stress-driven STAT3 activation. *Cancer Cell.* **17**, 286–297 (2010).
21. Pikarsky, E. et al. NF-κB functions as a tumour promoter in inflammation-associated cancer. *Nature* **431**, 461–466 (2004).
22. Maeda, S., Kamata, H., Luo, J. L., Leffert, H. & Karin, M. IKKβ couples hepatocyte death to cytokine-driven compensatory proliferation that promotes chemical hepatocarcinogenesis. *Cell* **121**, 977–990 (2005).
23. Haybaeck, J. et al. A lymphotoxin-driven pathway to hepatocellular carcinoma. *Cancer Cell.* **16**, 295–308 (2009).
24. Sunami, Y. et al. Canonical NF-κB signaling in hepatocytes acts as a tumor-suppressor in hepatitis B virus surface antigen-driven hepatocellular carcinoma by controlling the unfolded protein response. *Hepatology* **63**, 1592–1607 (2016).
25. Matter, M. S. et al. Oncogenic driver genes and the inflammatory microenvironment dictate liver tumor phenotype. *Hepatology* **63**, 1888–1899 (2016).
26. Yuan, D. et al. Kupffer cell-derived TNF triggers cholangiocellular tumorigenesis through JNK due to chronic mitochondrial dysfunction and ROS. *Cancer Cell.* **31**, 771–789 (2017).
27. Jenne, C. N. & Kubes, P. Immune surveillance by the liver. *Nat. Immunol.* **14**, 996–1006 (2013).
28. Lumsden, A. B., Henderson, J. M. & Kutner, M. H. Endotoxin levels measured by a chromogenic assay in portal, hepatic and peripheral venous blood in patients with cirrhosis. *Hepatology* **8**, 232–236 (1988).
29. Notas, G., Kisseleva, T. & Brenner, D. NK and NKT cells in liver injury and fibrosis. *Clin. Immunol.* **130**, 16–26 (2009).
30. Bricard, G. et al. Enrichment of human CD4$^+$ $V_\alpha 24/V_\beta 11$ invariant NKT cells in intrahepatic malignant tumors. *J. Immunol.* **182**, 5140–5151 (2009).
31. Protzer, U., Maini, M. K. & Knolle, P. A. Living in the liver: hepatic infections. *Nat. Rev. Immunol.* **12**, 201–213 (2012).
32. Robinson, M. W., Harmon, C. & O'Farrelly, C. Liver immunology and its role in inflammation and homeostasis. *Cell. Mol. Immunol.* **13**, 267–276 (2016).
33. Heymann, F. et al. Liver inflammation abrogates immunological tolerance induced by Kupffer cells. *Hepatology* **62**, 279–291 (2015).
34. Helmy, K. Y. et al. CRIg: a macrophage complement receptor required for phagocytosis of circulating pathogens. *Cell* **124**, 915–927 (2006).
35. Tacke, F. Targeting hepatic macrophages to treat liver diseases. *J. Hepatol.* **66**, 1300–1312 (2017).
36. Knolle, P. A. et al. Endotoxin down-regulates T cell activation by antigen-presenting liver sinusoidal endothelial cells. *J. Immunol.* **162**, 1401–1407 (1999).
37. Huang, L. R. et al. Intrahepatic myeloid-cell aggregates enable local proliferation of CD8$^+$ T cells and successful immunotherapy against chronic viral liver infection. *Nat. Immunol.* **14**, 574–583 (2013).
38. Medina-Echeverz, J., Eggert, T., Han, M. & Greten, T. F. Hepatic myeloid-derived suppressor cells in cancer. *Cancer Immunol. Immunother.* **64**, 931–940 (2015).
39. Kelly, A. et al. CD141$^+$ myeloid dendritic cells are enriched in healthy human liver. *J. Hepatol.* **60**, 135–142 (2014).
40. Pallett, L. J. et al. Metabolic regulation of hepatitis B immunopathology by myeloid-derived suppressor cells. *Nat. Med.* **21**, 591–600 (2015).
41. Knolle, P. A. et al. Interleukin-10 expression is autoregulated at the transcriptional level in human and murine Kupffer cells. *Hepatology* **27**, 93–99 (1998).
42. Wu, J. et al. Toll-like receptor-induced innate immune responses in non-parenchymal liver cells are cell type-specific. *Immunology* **129**, 363–374 (2010).
43. Diehl, L. et al. Tolerogenic maturation of liver sinusoidal endothelial cells promotes B7-homolog 1-dependent CD8$^+$ T cell tolerance. *Hepatology* **47**, 296–305 (2008).
44. Limmer, A. et al. Efficient presentation of exogenous antigen by liver endothelial cells to CD8$^+$ T cells results in antigen-specific T-cell tolerance. *Nat. Med.* **6**, 1348–1354 (2000).
45. Huang, L., Soldevila, G., Leeker, M., Flavell, R. & Crispe, I. N. The liver eliminates T cells undergoing antigen-triggered apoptosis in vivo. *Immunity* **1**, 741–749 (1994).
46. Ringelhan, M., McKeating, J. A. & Protzer, U. Viral hepatitis and liver cancer. *Phil. Trans. R. Soc. Lond. B* https://doi.org/10.1098/rstb.2016.0274 (2017).
47. Knolle, P. A. & Thimme, R. Hepatic immune regulation and its involvement in viral hepatitis infection. *Gastroenterology* **146**, 1193–1207 (2014).
48. Wieland, D., Hofmann, M. & Thimme, R. Overcoming CD8$^+$ T-cell exhaustion in viral hepatitis: lessons from the mouse model and clinical perspectives. *Dig. Dis.* **35**, 334–338 (2017).
49. Lopes, A. R. et al. Bim-mediated deletion of antigen-specific CD8 T cells in patients unable to control HBV infection. *J. Clin. Invest.* **118**, 1835–1845 (2008).
50. Das, A. et al. Functional skewing of the global CD8 T cell population in chronic hepatitis B virus infection. *J. Exp. Med.* **205**, 2111–2124 (2008).
51. Hedegaard, D. L. et al. High resolution sequencing of hepatitis C virus reveals limited intra-hepatic compartmentalization in end-stage liver disease. *J. Hepatol.* **66**, 28–38 (2017).
52. Li, X. D., Sun, L., Seth, R. B., Pineda, G. & Chen, Z. J. Hepatitis C virus protease NS3/4A cleaves mitochondrial antiviral signaling protein off the mitochondria to evade innate immunity. *Proc. Natl Acad. Sci. USA* **102**, 17717–17722 (2005).
53. Meylan, E. et al. Cardif is an adaptor protein in the RIG-I antiviral pathway and is targeted by hepatitis C virus. *Nature* **437**, 1167–1172 (2005).
54. Ahlén, G. et al. Cleavage of the IPS-1/Cardif/MAVS/VISA does not inhibit T cell-mediated elimination of hepatitis C virus non-structural 3/4A-expressing hepatocytes. *Gut* **58**, 560–569 (2009).
55. Wieland, D. et al. TCF1$^+$ hepatitis C virus-specific CD8$^+$ T cells are maintained after cessation of chronic antigen stimulation. *Nat. Commun.* **8**, 15050 (2017).
56. Chattergoon, M. A. et al. HIV and HCV activate the inflammasome in monocytes and macrophages via endosomal Toll-like receptors without induction of type 1 interferon. *PLoS. Pathog.* **10**, e1004082 (2014).
57. Szabo, G. & Petrasek, J. Inflammasome activation and function in liver disease. *Nat. Rev. Gastroenterol. Hepatol.* **12**, 387–400 (2015).
58. European Association for the Study of Liver. EASL clinical practical guidelines: management of alcoholic liver disease. *J. Hepatol.* **57**, 399–420 (2012).
59. Iracheta-Vellve, A. et al. Inhibition of sterile danger signals, uric acid and ATP, prevents inflammasome activation and protects from alcoholic steatohepatitis in mice. *J. Hepatol.* **63**, 1147–1155 (2015).
60. Ge, X. et al. High mobility group box-1 (HMGB1) participates in the pathogenesis of alcoholic liver disease (ALD). *J. Biol. Chem.* **289**, 22672–22691 (2014).
61. Petrasek, J., Csak, T., Ganz, M. & Szabo, G. Differences in innate immune signaling between alcoholic and non-alcoholic steatohepatitis. *J. Gastroenterol. Hepatol.* **28** (Suppl 1), 93–98 (2013).
62. Wolf, M. J. et al. Metabolic activation of intrahepatic CD8$^+$ T cells and NKT cells causes nonalcoholic steatohepatitis and liver cancer via cross-talk with hepatocytes. *Cancer Cell.* **26**, 549–564 (2014).
63. Shalapour, S. et al. Inflammation-induced IgA$^+$ cells dismantle anti-liver cancer immunity. *Nature* **551**, 340–345 (2017).
64. Hassin, D., Garber, O. G., Meiraz, A., Schiffenbauer, Y. S. & Berke, G. Cytotoxic T lymphocyte perforin and Fas ligand working in concert even when Fas ligand lytic action is still not detectable. *Immunology* **133**, 190–196 (2011).
65. Guidotti, L. G. et al. Immunosurveillance of the liver by intravascular effector CD8$^+$ T cells. *Cell* **161**, 486–500 (2015).
66. Lucifora, J. et al. Specific and nonhepatotoxic degradation of nuclear hepatitis B virus cccDNA. *Science* **343**, 1221–1228 (2014).

67. Chiang, E. Y. et al. Targeted depletion of lymphotoxin-α-expressing T_H1 and T_H17 cells inhibits autoimmune disease. *Nat. Med.* **15**, 766–773 (2009).
68. Finkin, S. et al. Ectopic lymphoid structures function as microniches for tumor progenitor cells in hepatocellular carcinoma. *Nat. Immunol.* **16**, 1235–1244 (2015).
69. Endig, J. et al. Dual role of the adaptive immune system in liver injury and hepatocellular carcinoma development. *Cancer Cell.* **30**, 308–323 (2016).
70. Flecken, T. et al. Immunodominance and functional alterations of tumor-associated antigen-specific CD8+ T-cell responses in hepatocellular carcinoma. *Hepatology* **59**, 1415–1426 (2014).
71. Kang, T. W. et al. Senescence surveillance of pre-malignant hepatocytes limits liver cancer development. *Nature* **479**, 547–551 (2011).
72. Garnelo, M. et al. Interaction between tumour-infiltrating B cells and T cells controls the progression of hepatocellular carcinoma. *Gut* **66**, 342–351 (2017).
73. Fu, J. et al. Impairment of CD4+ cytotoxic T cells predicts poor survival and high recurrence rates in patients with hepatocellular carcinoma. *Hepatology* **58**, 139–149 (2013).
74. Sautès-Fridman, C.et al Tertiary Lymphoid structures in cancers: prognostic value, regulation, and manipulation for therapeutic intervention. *Front. Immunol.* 7, 407 (2016)..
75. Coppola, D. et al. Unique ectopic lymph node-like structures present in human primary colorectal carcinoma are identified by immune gene array profiling. *Am. J. Pathol.* **179**, 37–45 (2011).
76. Messina, J. L. et al. 12-Chemokine gene signature identifies lymph node-like structures in melanoma: potential for patient selection for immunotherapy? *Sci. Rep.* **2**, 765 (2012).
77. Ma, C. et al. NAFLD causes selective CD4+ T lymphocyte loss and promotes hepatocarcinogenesis. *Nature* **531**, 253–257 (2016).
78. Dimeloe, S., Burgener, A. V., Grählert, J. & Hess, C. T-cell metabolism governing activation, proliferation and differentiation; a modular view. *Immunology* **150**, 35–44 (2017).
79. Gomes, A. L. et al. Metabolic inflammation-associated IL-17A causes non-alcoholic steatohepatitis and hepatocellular carcinoma. *Cancer Cell.* **30**, 161–175 (2016).
80. Jia, Y. et al. Impaired function of CD4+ T follicular helper (Tfh) cells associated with hepatocellular carcinoma progression. *PLoS. One* **10**, e0117458 (2015).
81. Schneider, C. et al. Adaptive immunity suppresses formation and progression of diethylnitrosamine-induced liver cancer. *Gut* **61**, 1733–1743 (2012).
82. Xue, H. et al. Overrepresentation of IL-10-expressing b cells suppresses cytotoxic CD4+ T cell activity in HBV-induced hepatocellular carcinoma. *PLoS. One* **11**, e0154815 (2016).
83. Syn, W. K. et al. NKT-associated hedgehog and osteopontin drive fibrogenesis in non-alcoholic fatty liver disease. *Gut* **61**, 1323–1329 (2012).
84. Syn, W. K. et al. Accumulation of natural killer T cells in progressive nonalcoholic fatty liver disease. *Hepatology* **51**, 1998–2007 (2010).
85. Anson, M. et al. Oncogenic β-catenin triggers an inflammatory response that determines the aggressiveness of hepatocellular carcinoma in mice. *J. Clin. Invest.* **122**, 586–599 (2012).
86. Gur, C. et al. NKp46-mediated killing of human and mouse hepatic stellate cells attenuates liver fibrosis. *Gut* **61**, 885–893 (2012).
87. Sui, Q. et al. NK cells are the crucial antitumor mediators when STAT3-mediated immunosuppression is blocked in hepatocellular carcinoma. *J. Immunol.* **193**, 2016–2023 (2014).
88. Sun, C. et al. High NKG2A expression contributes to NK cell exhaustion and predicts a poor prognosis of patients with liver cancer. *OncoImmunology* **6**, e1264562 (2016).
89. Zhang, Q. F. et al. Liver-infiltrating $CD11b^{-}CD27^{-}$ NK subsets account for NK-cell dysfunction in patients with hepatocellular carcinoma and are associated with tumor progression. *Cell. Mol. Immunol.* **14**, 819 829 (2017).
90. Lee, J. H. et al. Adjuvant immunotherapy with autologous cytokine-induced killer cells for hepatocellular carcinoma. *Gastroenterology* **148**, 1383–1391 (2015).
91. Kahraman, A. et al. Major histocompatibility complex class I-related chains A and B (MIC A/B): a novel role in nonalcoholic steatohepatitis. *Hepatology* **51**, 92–102 (2010).
92. Tosello-Trampont, A. C. et al. NKp46+ natural killer cells attenuate metabolism-induced hepatic fibrosis by regulating macrophage activation in mice. *Hepatology* **63**, 799–812 (2016).
93. Li, X. et al. Targeting of tumour-infiltrating macrophages via CCL2/CCR2 signalling as a therapeutic strategy against hepatocellular carcinoma. *Gut* **66**, 157–167 (2017).
94. Ehling, J. et al. CCL2-dependent infiltrating macrophages promote angiogenesis in progressive liver fibrosis. *Gut* **63**, 1960–1971 (2014).
95. Garcia-Martinez, I. et al. Hepatocyte mitochondrial DNA drives nonalcoholic steatohepatitis by activation of TLR9. *J. Clin. Invest* **126**, 859–864 (2016).
96. Koh, M. Y. et al. A new HIF-1α/RANTES-driven pathway to hepatocellular carcinoma mediated by germline haploinsufficiency of SART1/HAF in mice. *Hepatology* **63**, 1576–1591 (2016).
97. Greten, F. R. et al. NF-κB is a negative regulator of IL-1β secretion as revealed by genetic and pharmacological inhibition of IKKβ. *Cell* **130**, 918–931 (2007).
98. Robert, O. et al. Decreased expression of the glucocorticoid receptor-GILZ pathway in Kupffer cells promotes liver inflammation in obese mice. *J. Hepatol.* **64**, 916–924 (2016).
99. Fan, Z. et al. The histone methyltransferase Suv39h2 contributes to nonalcoholic steatohepatitis in mice. *Hepatology* **65**, 1904–1919 (2017).
100. Svendsen, P. et al. Antibody-directed glucocorticoid targeting to CD163 in M2-type macrophages attenuates fructose-induced liver inflammatory changes. *Mol. Ther. Methods Clin. Dev.* **4**, 50–61 (2016).
101. Reid, D. T. et al. Kupffer cells undergo fundamental changes during the development of experimental NASH and are critical in initiating liver damage and inflammation. *PLoS. One* **11**, e0159524 (2016).
102. Baeck, C. et al. Pharmacological inhibition of the chemokine CCL2 (MCP-1) diminishes liver macrophage infiltration and steatohepatitis in chronic hepatic injury. *Gut* **61**, 416–426 (2012).
103. Kong, L.et al Deletion of interleukin-6 in monocytes/macrophages suppresses the initiation of hepatocellular carcinoma in mice. *J. Exp. Clin. Cancer Res.* **35**, 131 (2016)..
104. Sun, K. et al. Autophagy-deficient Kupffer cells promote tumorigenesis by enhancing mtROS-NF-κB-IL1α/β-dependent inflammation and fibrosis during the preneoplastic stage of hepatocarcinogenesis. *Cancer Lett.* **388**, 198–207 (2017).
105. Kessoku, T. et al. Resveratrol ameliorates fibrosis and inflammation in a mouse model of nonalcoholic steatohepatitis. *Sci. Rep.* **6**, 22251 (2016).
106. Lacotte, S. et al. Impact of myeloid-derived suppressor cell on Kupffer cells from mouse livers with hepatocellular carcinoma. *OncoImmunology* 5, e1234565 (2016).
107. Eggert, T. et al. Distinct functions of senescence-associated immune responses in liver tumor surveillance and tumor progression. *Cancer Cell.* **30**, 533–547 (2016).
108. Connolly, M. K. et al. In liver fibrosis, dendritic cells govern hepatic inflammation in mice via TNF-alpha. *J. Clin. Invest.* **119**, 3213–3225 (2009).
109. Henning, J. R. et al. Dendritic cells limit fibroinflammatory injury in nonalcoholic steatohepatitis in mice. *Hepatology* **58**, 589–602 (2013).
110. Sutti, S. et al. CX3CR1-expressing inflammatory dendritic cells contribute to the progression of steatohepatitis. *Clin. Sci.* **129**, 797–808 (2015).
111. Heier, E. C. et al. Murine $CD103^{+}$ dendritic cells protect against steatosis progression towards steatohepatitis. *J. Hepatol.* **66**, 1241–1250 (2017).
112. Rai, V. et al. Cellular and molecular targets for the immunotherapy of hepatocellular carcinoma. *Mol. Cell. Biochem.* **437**, 13–36 (2017).
113. Cheng, J. T. et al. Hepatic carcinoma-associated fibroblasts induce IDO-producing regulatory dendritic cells through IL-6-mediated STAT3 activation. *Oncogenesis* **5**, e198 (2016).
114. Pedroza-Gonzalez, A. et al. Tumor-infiltrating plasmacytoid dendritic cells promote immunosuppression by Tr1 cells in human liver tumors. *OncoImmunology* **4**, e1008355 (2015).
115. Ouyang, F. Z. et al. Dendritic cell-elicited B-cell activation fosters immune privilege via IL-10 signals in hepatocellular carcinoma. *Nat. Commun.* **7**, 13453 (2016).
116. Wiedemann, G. M. et al. Cancer cell-derived IL-1α induces CCL22 and the recruitment of regulatory T cells. *OncoImmunology* **5**, e1175794 (2016).
117. Li, X. et al. Neutrophil count is associated with myeloid derived suppressor cell level and presents prognostic value of for hepatocellular carcinoma patients. *Oncotarget* **8**, 24380–24388 (2017).
118. Personeni, N. et al. Prognostic value of the neutrophil-to-lymphocyte ratio in the ARQ 197-215 second-line study for advanced hepatocellular carcinoma. *Oncotarget* **8**, 14408–14415 (2017).
119. Xu, R., Huang, H., Zhang, Z. & Wang, F. S. The role of neutrophils in the development of liver diseases. *Cell. Mol. Immunol.* **11**, 224–231 (2014).
120. Zang, S. et al. Increased ratio of neutrophil elastase to α1-antitrypsin is closely associated with liver inflammation in patients with nonalcoholic steatohepatitis. *Clin. Exp. Pharmacol. Physiol.* **43**, 13–21 (2016).
121. Ibusuki, R. et al. Transgenic expression of human neutrophil peptide-1 enhances hepatic fibrosis in mice fed a choline-deficient, L-amino acid-defined diet. *Liver Int.* **33**, 1549–1556 (2013).
122. Zhou, S. L. et al. Tumor-associated neutrophils recruit macrophages and T-regulatory cells to promote progression of hepatocellular carcinoma and resistance to sorafenib. *Gastroenterology* **150**, 1646–1658 (2016).
123. Meyer, T. et al. Sorafenib in combination with transarterial chemoembolisation in patients with unresectable hepatocellular carcinoma (TACE 2): a randomised placebo-controlled, double-blind, phase 3 trial. *Lancet Gastroenterol. Hepatol.* **2**, 565–575 (2017).
124. Llovet, J. M. & Hernandez-Gea, V. Hepatocellular carcinoma: reasons for phase III failure and novel perspectives on trial design. *Clin. Cancer Res.* **20**, 2072–2079 (2014).

125. Totoki, Y. et al. Trans-ancestry mutational landscape of hepatocellular carcinoma genomes. *Nat. Genet.* **46**, 1267–1273 (2014).
126. Schulze, K. et al. Exome sequencing of hepatocellular carcinomas identifies new mutational signatures and potential therapeutic targets. *Nat. Genet.* **47**, 505–511 (2015).
127. Sia, D. et al. Identification of an immune-specific class of hepatocellular carcinoma, based on molecular features. *Gastroenterology* **153**, 812–826 (2017).
128. Schlageter, M. et al. Clinicopathological features and metastatic pattern of hepatocellular carcinoma: an autopsy study of 398 patients. *Pathobiology* **83**, 301–307 (2016).
129. Nault, J. C. & Zucman-Rossi, J. TERT promoter mutations in primary liver tumors. *Clin. Res. Hepatol. Gastroenterol.* **40**, 9–14 (2016).
130. Spear, T. T. et al. TCR gene-modified T cells can efficiently treat established hepatitis C-associated hepatocellular carcinoma tumors. *Cancer Immunol. Immunother.* **65**, 293–304 (2016).
131. Hiroishi, K. et al. Strong CD8$^+$ T-cell responses against tumor-associated antigens prolong the recurrence-free interval after tumor treatment in patients with hepatocellular carcinoma. *J. Gastroenterol.* **45**, 451–458 (2010).
132. Sun, Z. et al. Status of and prospects for cancer vaccines against hepatocellular carcinoma in clinical trials. *Biosci. Trends* **10**, 85–91 (2016).
133. Mizukoshi, E. et al. Enhancement of tumor-associated antigen-specific T cell responses by radiofrequency ablation of hepatocellular carcinoma. *Hepatology* **57**, 1448–1457 (2013).
134. Rosenberg, S. A. & Restifo, N. P. Adoptive cell transfer as personalized immunotherapy for human cancer. *Science* **348**, 62–68 (2015).
135. Pardoll, D. M. The blockade of immune checkpoints in cancer immunotherapy. *Nat. Rev. Cancer* **12**, 252–264 (2012).
136. Brunner, S. M. et al. Tumor-infiltrating, interleukin-33-producing effector-memory CD8$^+$ T cells in resected hepatocellular carcinoma prolong patient survival. *Hepatology* **61**, 1957–1967 (2015).
137. Chen, J. et al. Sorafenib-resistant hepatocellular carcinoma stratified by phosphorylated ERK activates PD-1 immune checkpoint. *Oncotarget* **7**, 41274–41284 (2016).
138. Harding, J. J., El Dika, I. & Abou-Alfa, G. K. Immunotherapy in hepatocellular carcinoma: primed to make a difference? *Cancer* **122**, 367–377 (2016).
139. Zheng, C. et al. Landscape of infiltrating T cells in liver cancer revealed by single-cell sequencing. *Cell* **169**, 1342–1356 (2017).
140. Xie, Q. K. et al. Programmed death ligand 1 as an indicator of pre-existing adaptive immune responses in human hepatocellular carcinoma. *OncoImmunology* **5**, e1181252 (2016).
141. Sideras, K. et al. PD-L1, Galectin-9 and CD8$^+$ tumor-infiltrating lymphocytes are associated with survival in hepatocellular carcinoma. *OncoImmunology* **6**, e1273309 (2017).
142. Topalian, S. L., Drake, C. G. & Pardoll, D. M. Immune checkpoint blockade: a common denominator approach to cancer therapy. *Cancer Cell.* **27**, 450–461 (2015).
143. Okazaki, T., Chikuma, S., Iwai, Y., Fagarasan, S. & Honjo, T. A rheostat for immune responses: the unique properties of PD-1 and their advantages for clinical application. *Nat. Immunol.* **14**, 1212–1218 (2013).
144. El-Khoueiry, A. B. et al. Nivolumab in patients with advanced hepatocellular carcinoma (CheckMate 040): an open-label, non-comparative, phase 1/2 dose escalation and expansion trial. *Lancet* **389**, 2492–2502 (2017).
145. Sangro, B. et al. A clinical trial of CTLA-4 blockade with tremelimumab in patients with hepatocellular carcinoma and chronic hepatitis C. *J. Hepatol.* **59**, 81–88 (2013).
146. Nault, J. C. The end of almost 10 years of negative RCTs in advanced hepatocellular carcinoma. *Lancet* **389**, 4–6 (2017).
147. Duffy, A. G. et al. Tremelimumab in combination with ablation in patients with advanced hepatocellular carcinoma. *J. Hepatol.* **66**, 545–551 (2017).
148. Shen, Y. et al. TGF-β regulates hepatocellular carcinoma progression by inducing Treg cell polarization. *Cell. Physiol. Biochem.* **35**, 1623–1632 (2015).
149. Wang, Y. et al. Hepatocellular carcinoma cells induce regulatory T cells and lead to poor prognosis via production of transforming growth factor-β1. *Cell. Physiol. Biochem.* **38**, 306–318 (2016).
150. Knee, D. A., Hewes, B. & Brogdon, J. L. Rationale for anti-GITR cancer immunotherapy. *Eur. J. Cancer* **67**, 1–10 (2016).

Acknowledgements

Supported by Else-Kröner-Stiftung (M.R., as a member of the Else-Kröner-Forschungskolleg München "Microbial triggers in disease development"), Deutsche Forschungsgemeinschaft (5892/5-1 to T.O.) and the European Research Council (consolidator grant HepatoMetaboPath to M.H.; SFBTR36, SFBTR179 and SFBTR209 to M.H.; and the European Union's Horizon 2020 research and innovation programme (under grant agreement 667273), for M.H.).

Competing interests

The authors declare no competing financial interests.

Additional information

Correspondence and requests for materials should be addressed to M.H.

11.3 Somatostatin receptor expression related to TP53 and RB1 alterations in pancreatic and extra pancreatic neuroendocrine neoplasms with a Ki67-index above 20%

Authors

Björn Konukiewitz, Anna Melissa Schlitter, Moritz Jesinghaus, **Dominik Pfister**, Katja Steiger, Angela Segler, Abbas Agaimy, Bence Sipos, GiuseppeZamboni, Wilko Weichert, Irene Esposito, Nicole Pfarr and Günter Klöppel

Journal

Modern Pathology (2017) 30, 587–598[129]

https://doi.org/10.1038/modpathol.2016.217

Modern Pathology (2017) 30, 587–598

Somatostatin receptor expression related to *TP53* and *RB1* alterations in pancreatic and extrapancreatic neuroendocrine neoplasms with a Ki67-index above 20%

Björn Konukiewitz[1], Anna Melissa Schlitter[1], Moritz Jesinghaus[1], Dominik Pfister[2], Katja Steiger[1], Angela Segler[1], Abbas Agaimy[3], Bence Sipos[4], Giuseppe Zamboni[5], Wilko Weichert[1], Irene Esposito[6], Nicole Pfarr[1] and Günter Klöppel[1]

[1]Institute of Pathology, Technical University of Munich, Munich, Germany; [2]Division of Chronic Inflammation and Cancer, German Cancer Research Center (DKFZ), Heidelberg, Germany; [3]Institute of Pathology, Friedrich-Alexander University Erlangen-Nuremberg, University Hospital, Erlangen, Germany; [4]Institute of Pathology, University Hospital of Tuebingen, Tuebingen, Germany; [5]Institute of Pathology, Sacro Cuore Hospital of Negrar, Verona, Italy and [6]Institute of Pathology, Heinrich-Heine-University, Düsseldorf, Germany

Somatostatin receptor 2A expression is a feature of well-differentiated neuroendocrine neoplasms and is important for their diagnosis and therapy. Little is known about somatostatin receptor 2A expression in poorly differentiated neuroendocrine neoplasms in relation to *TP53* and *RB1* status and how these features may contribute to the separation of well from poorly differentiated neuroendocrine neoplasms with a proliferation index above 20%. This study investigates the expression of somatostatin receptors, p53 and Rb1, and *TP53* alterations in pancreatic and extrapancreatic well and poorly differentiated neuroendocrine neoplasms (Ki67-index >20%). Thirty-seven poorly differentiated neuroendocrine neoplasms of pancreatic ($n=12$) and extrapancreatic origin ($n=25$) as well as 10 well-differentiated neuroendocrine neoplasms of the pancreas ($n=9$) and rectum ($n=1$) with a Ki67-index >20% were immunostained for synaptophysin, chromogranin A, Ki67, CD56, p53, Rb1, ATRX, DAXX, progesterone receptor, somatostatin receptor 2A, somatostatin receptor 5, and cytokeratin 20, and sequenced for *TP53*, exons 5–9. Somatostatin receptor 2A was positive in 6/37 of poorly differentiated and in 8/10 of well-differentiated neuroendocrine neoplasms. One well-differentiated and two poorly differentiated neuroendocrine neoplasms expressed somatostatin receptor 5. Abnormal nuclear p53 and Rb1 staining was found in 29/37 and 22/37 poorly differentiated neuroendocrine neoplasms, respectively, whereas all well-differentiated neuroendocrine neoplasms showed normal p53 and Rb1 expression. *TP53* gene alterations were restricted to poorly differentiated neuroendocrine neoplasms (24/34) and correlated well with p53 expression. All cases were progesterone receptor negative. Somatostatin receptor 2A expression is not limited to well-differentiated neuroendocrine neoplasms but also occurs in 16% of poorly differentiated neuroendocrine neoplasms from various sites. Most poorly differentiated neuroendocrine neoplasms are characterized by *TP53* alterations and Rb1 loss, usually in the absence of somatostatin receptor 2A expression. In the pancreas, these criteria contribute to separate well-differentiated neuroendocrine neoplasms with a Ki67-index above 20% from poorly differentiated neuroendocrine neoplasms.
Modern Pathology (2017) **30**, 587–598; doi:10.1038/modpathol.2016.217; published online 6 January 2017

Correspondence: Dr B Konukiewitz, MD, Institute of Pathology, Technical University of Munich, Trogerstr. 18, 81675 Munich, Germany.
E-mail: b.konukiewitz@tum.de
Received 3 June 2016; revised 8 November 2016; accepted 10 November 2016; published online 6 January 2017

www.modernpathology.org

The 2010 World Health Organization tumor classification of the gastroenteropancreatic system for neuroendocrine neoplasms defines the tumors with well-differentiated histology and a Ki67-index below 20% as neuroendocrine tumors. In contrast, poorly

differentiated neuroendocrine neoplasms that are called neuroendocrine carcinomas have a Ki67-index greater than 20%. Arguments in favor of this distinction are profound differences in tumor progression (slow *vs* fast), hormone production (expression *vs* no expression), hormonal syndromes (syndromes *vs* no syndromes), association with hereditary endocrine tumor syndromes (such as multiple endocrine neoplasia type 1, von Hippel Lindau or neurofibromatosis type 1 *vs* no association), and genetic profiles (*MEN1, DAXX/ARTX, TSC2, PTEN, PIK3CA* and *VHL* gene alterations *vs TP53* and *RB1* gene alterations).[1–5] This subdivision of the neuroendocrine neoplasms into well and poorly differentiated groups probably also applies to the respective neoplasms outside the gastroenteropancreatic organ system as for instance in the lung (typical and atypical carcinoids *vs* poorly differentiated neuroendocrine carcinomas), head and neck area or the urinary bladder.

The subdivision of the neuroendocrine neoplasms into two biologically distinct groups is crucial for the treatment of these tumors.[6,7] Neuroendocrine tumors are initially treated by surgery that is usually followed by various bioresponse modifiers such as somatostatin analogs, chemotherapy with streptozotocin, temozolomid and/or peptide radio receptor therapy, if the tumors pursue a malignant course.[1] Poorly differentiated neuroendocrine neoplasms are rarely resected, but treated with platinum-based chemotherapy.[6] In recent years, peptide radio receptor therapy has gained increasing importance as an effective treatment option for neuroendocrine tumors, provided that the tumors express somatostatin receptors, as the ligand consists of a somatostatin analog coupled to a radioisotope such as yttrium or lutetium.[8,9] Strong membranous immunohistochemical expression highly correlates with somatostatin receptor imaging.[10–13] Somatostatin analogs are well established in the treatment of neuroendocrine tumors due to their inhibition of hormonal symptoms and their anti-proliferative effect.[14] The progression free survival rate in a subset of metastatic G1 and G2 enteropancreatic neuroendocrine tumors is longer when treated with somatostatin analogs.[15]

The majority of gastroenteropancreatic neuroendocrine tumors express somatostatin receptor subtypes 1–5 that can be detected by real time polymerase chain reaction and/or immunohistochemistry.[16–18] Especially somatostatin receptor 2 A is highly expressed in these tumors, whereas the other somatostatin receptors, for instance somatostatin receptor 5, have been less often demonstrated.[16,19] Somatostatin receptor 2 A has also been found to be expressed in neuroendocrine tumors/carcinoids and neuroendocrine carcinomas outside the gastroenteropancreatic system, such as in the lung and in the urinary bladder.[19–23] In contrast to neuroendocrine tumors, the poorly differentiated gastroenteropancreatic neuroendocrine neoplasms do rarely express somatostatin receptor 2 A, thereby usually excluding these neoplasms from the benefits of peptide radio receptor therapy. However, as exceptions from this general notion occur, it is of interest to get a more precise overview of the ability of poorly differentiated neuroendocrine neoplasms of the gastroenteropancreatic system and beyond to express somatostatin receptor 2 A or somatostatin receptor 5, in particular regarding the predictability of the expression related to criteria such as morphology, proliferative activity, and tumor localization.

Recently, the distinction of well from poorly differentiated neuroendocrine neoplasms by applying the World Health Organization 2010 classification[3] has become difficult for those few well-differentiated neuroendocrine neoplasms whose Ki67-index exceeds 20%. Although they have retained their well-differentiated neuroendocrine growth pattern, their Ki67-index greater than 20% gives them a grade G3 that shifts them into the poorly differentiated neuroendocrine neoplasm category.[24] Neoplasms of this type most often originate in the pancreas and increase their proliferative activity when developing liver metastases in the course of the disease. As their behavior is still better than that of the poorly differentiated neuroendocrine neoplasms, and also their treatment response to first-line platinum-based chemotherapy, as used for poorly differentiated neuroendocrine neoplasms, is often poor, there is a need to distinguish these 'neuroendocrine tumors G3' clearly from poorly differentiated neuroendocrine neoplasms.[25,26] In case the histological pattern is ambiguous, surrogate markers could facilitate the differential diagnosis. Recent studies have shown that poorly differentiated neuroendocrine neoplasms of the pancreas often overexpress p53, show *TP53* mutations and loose the expression of Rb1, whereas pancreatic neuroendocrine tumors lack these changes but show instead mutations in the *MEN1* gene, *DAXX/ATRX* genes, genes belonging to the mTOR pathway and von Hippel Lindau related genes.[2,27,28]

However, little is known whether neuroendocrine tumors G3 retain the features of the neuroendocrine tumors G1 and G2 with intact *TP53* and *RB1* function or if these tumors assume an intermediate status between neuroendocrine tumors and poorly differentiated neuroendocrine neoplasms. In addition, it is not clear so far whether they also retain the ability to express somatostatin receptor 2 A and thus may respond to peptide radio receptor therapy.

In this study, we therefore addressed three questions. Firstly, do poorly differentiated neuroendocrine neoplasms from various sites including the pancreas, the colorectum, the urinary bladder, the parotid gland, and the skin (ie, Merkel cell carcinomas) lack the immunohistochemical expression of somatostatin receptor 2 A and 5? Secondly, how does the *TP53* and *RB1* status relate to the expression of somatostatin receptor 2 A and 5 in poorly differentiated neuroendocrine neoplasms? Thirdly, how helpful are the *TP53, RB1, ATRX*, and *DAXX*

mutational status and somatostatin receptor 2 A/5 expression patterns in discriminating neuroendocrine tumors G3 from poorly differentiated neuroendocrine neoplasms in the pancreas? The answers to these questions reveal somatostatin receptor 2 A expression in association with intact *TP53* and *RB1* status as diagnostically valuable neuroendocrine tumor G3 features. P53 and Rb1 have a high discriminative power and are helpful markers to distinguish well from poorly differentiated neuroendocrine neoplasms.

Materials and methods

Patients and Tissues

Formalin-fixed and paraffin-embedded tissue blocks from 47 surgical resection specimens of primary neuroendocrine neoplasms with a Ki67-index >20% were retrieved from the Institute of Pathology and the Consultation Center of Pancreatic and Endocrine Tumors, Institute of Pathology, Technical University Munich, Munich, Germany, including 21 neoplasms of pancreatic ($n=20$) and ampullary origin ($n=1$) and 26 neoplasms of extrapancreatic origin (colorectum, $n=10$; urinary bladder, $n=8$; parotid gland, $n=5$; Merkel cell carcinoma of the skin, $n=3$). The study was approved by the ethics committee of the Technical University of Munich, Germany (document no. 129/16 S).

Histological Analysis

Three micrometer-thick slides were cut from each block and stained with hematoxylin and eosin. The tumors were histologically classified according to World Health Organization recommendations as well-differentiated neuroendocrine neoplasms, when presenting with typical neuroendocrine growth pattern (diffuse, nested, trabecular, glandular, and so on) and low-grade cytological atypia. Poorly differentiated neoplasms of the pancreas, the colorectum, the urinary bladder, the parotid gland, and the skin were subclassified into neoplasms from small cell, large cell, and Merkel cell type, based on cytological criteria. Small-cell-type neoplasms consist of small neoplastic cells with a high nucleus to cytoplasm ratio and dense chromatin. Large-cell-type neoplasms are defined by larger nuclei with vesicular chromatin and large nucleoli.[3,29]

Immunohistochemistry

Immunohistochemistry was performed on 3 µm-thick paraffin sections using a fully automated slide preparation system 'Benchmark XT System' (Ventana Medical Systems, Tucson, Arizona, USA). All reagents and buffers were retrieved from Ventana Medical Systems. Immunohistochemical analysis was performed using antibodies against synaptophysin (Ventana Medical Systems, Tucson, Arizona, USA; 1:1), chromogranin A (Boehringer, Mannheim, Germany; 1:5000), Ki67 (DakoCytomation, Glostrup, Denmark; 1:50), CD56 (Cell Marque, Rocklin, California, USA; 1:4), p53 (DakoCytomation, Glostrup, Denmark; 1:200), progesterone receptor (DCS, Hamburg, Germany; 1:50), somatostatin receptor 2 A (ZYTOMED Systems, Berlin, Germany; 1:100), somatostatin receptor 5 (ZYTOMED Systems, Berlin, Germany; 1:25), cytokeratin 20 (PROGEN Biotechnik GmbH, Heidelberg, Germany; 1:60), and Rb1 (BD Biosciences, Heidelberg, Germany; 1:200). In addition, ATRX (Sigma-Aldrich, Munich, Germany, 1:250) and DAXX (Sigma-Aldrich, Munich, Germany, 1:100) immunostainings were performed in pancreatic neuroendocrine neoplasms. Nuclear (Ki67, p53, progesterone receptor, Rb1, ATRX, and DAXX), cytoplasmic (synaptophysin, chromogranin A, cytokeratin 20), and membranous (CD56, somatostatin receptor 2 A, somatostatin receptor 5) staining were scored as specific. The grading of the neoplasms was based on the Ki67-index. In poorly differentiated neuroendocrine neoplasms with a Ki67-index >50% a minimum of 250–500 neoplastic cells were counted in hot-spot areas by two observers (GK and BK). In cases of well-differentiated neuroendocrine neoplasms and poorly differentiated neuroendocrine neoplasms with Ki67-index <50%, Ki67-positive cells were manually counted on prints of photographs containing >500 cells and including hot-spot areas.[30] P53 expression was scored as abnormal in cases of moderate to strong nuclear positivity in more than 20% of neoplastic cells or in cases of complete absence. The loss of nuclear Rb1, ATRX, and DAXX expression in >90% of neoplastic cells was considered as abnormal. The staining of somatostatin receptors was evaluated using a three tired scoring system (using the established HER2 scoring system of the breast, adapted to the somatostatin receptor 2 A expression patterns in the pancreas). Score 0 (no staining, weakly membranous staining in <10% of neoplastic cells) and score 1+ (weakly membranous staining in >10% of neoplastic cells) were recorded as negative, score 2+ (moderate membranous staining in >10% of neoplastic cells), and score 3+ (strong membranous staining in >10% of neoplastic cells) were recorded as positive.[31,32]

Molecular Sequencing

Neoplastic tissue was microdissected from representative formalin-fixed and paraffin-embedded tissue blocks. Genomic DNA was extracted using the FFPE Tissue Kit (Qiagen). Exon 5–9 of the *TP53* gene locus were amplified by polymerase chain reaction using the following primers: 5′-atc tgt tca ctt gtg ccc tg-3′ (exon 5 forward), 5′-aac cag ccc tgt cgt ctc tc-3′ (exon 5 reverse), 5′-agg gtc ccc agg cct ctg at-3′ (exon 6 forward), 5′-cac cct taa ccc ctc ctc cc-3′ (exon 6 reverse),

5′-cca agg cgc act ggc ctc atc-3′ (exon 7 forward), 5′-cag agg ctg ggg cac agc agg-3′ (exon 7 reverse), 5′-ttc ctt act gcc tct tgc tt-3′ (exon 8 forward), 5′-tgt cct gct tgc tta cct cg-3′ (exon 8 reverse), 5′-aag caa gca gga caa gaa gc-3′ (exon 9 forward), 5′-cca ctt gat aag agg tcc ca-3′ (exon 9 reverse). The polymerase chain reaction products were directly Sanger sequenced (forward and reverse). Selected cases were additionally analyzed by massive parallel sequencing using a panel of 409 genes including all coding regions of *TP53, RB1, KRAS, CDKN2A/p16, SMAD4, RET, MEN1, ATRX, DAXX,* and *BRAF* amongst others on an Ion Torrent S5XL platform.

Statistical Analysis

Statistical analysis was done using SPSS 23.0 statistical software (SPSS, Chicago, IL, USA). Histological analysis was correlated with immunohistochemical findings and *TP53* molecular pathology using the Chi-square and Fisher's exact test. Significance was considered if the *P*-value was < 0.05.

Results

A total of 47 primary neuroendocrine neoplasms with Ki67-index exceeding 20% were examined. The mean age of the patients at diagnosis was 62 years (range 16–89 years). 57% of the patients were women and 43% were men (27:20).

Histological Features

Twelve of 21 (57%) pancreatic neuroendocrine neoplasms (including one ampullary neuroendocrine neoplasm) and 25/26 (96%) extrapancreatic neuroendocrine neoplasms (9 from the colorectum, 8 from the urinary bladder, 5 from the parotid gland, 3 from the skin (ie, Merkel cell carcinomas)) were classified as poorly differentiated neuroendocrine neoplasms. Small-cell-type poorly differentiated neuroendocrine neoplasms were found in the pancreas (4/12) and particularly in the urinary bladder (7/8). Large-cell-type poorly differentiated neuroendocrine neoplasms were seen in the pancreas (8/12) and in the colorectum (7/9). The pancreatic large cell neuroendocrine neoplasm with the lowest proliferation (Ki67-index 21%; case 5 on Table 2) showed a diffuse non-organoid growth pattern (see also Discussion). All neuroendocrine neoplasms of the skin and the parotid gland were classified as Merkel cell- and/or Merkel cell-like carcinomas.[29] Three poorly differentiated neuroendocrine neoplasms from the pancreas ($n=2$) and the rectum ($n=1$) had a glandular component, two poorly differentiated neuroendocrine neoplasms (one from the parotid gland, one from the urinary bladder) had a squamoid cell component and one poorly differentiated neuroendocrine neoplasm (urinary bladder) had a transitional cell component, exceeding 30% of the tumor cells, and were therefore classified as mixed carcinomas.

Ten of the 47 neuroendocrine neoplasms (nine from the pancreas, one from the rectum) presented with well-differentiated neuroendocrine growth patterns, mainly with a trabecular arrangement, and were classified as well-differentiated neuroendocrine neoplasms or neuroendocrine tumors G3. There was no neuroendocrine tumor G3 that in addition to the well-differentiated component included poorly differentiated areas.

Immunohistochemical Data in Poorly Differentiated Neuroendocrine Neoplasms

All neoplasms were synaptophysin positive. Chromogranin A was expressed in 24 of 37 cases. CD56 was expressed in 9/12 pancreatic and in 24/25 of extrapancreatic poorly differentiated neuroendocrine neoplasms with a focal/weak (10/33) or diffuse/strong (23/33) expression pattern. Cytokeratin 20 was detected in 27/37 neoplasms. The Ki67-index ranged from 21% to 90%.

Around 16% (6/37, pancreas, colon, rectum, urinary bladder, parotid gland) of poorly differentiated neuroendocrine neoplasms were somatostatin receptor 2 A positive (score 2+, 5/6; score 3+ 1/6). And, 32% of the somatostatin receptor 2 A negative cases (10/31) showed a weak membranous staining in more than 10% of neoplastic cells, corresponding to a score of 1+. Somatostatin receptor 5 was expressed in two cases (score 2+, pancreas, colon). Abnormal p53 immunolabeling was seen in 75% (9/12) of pancreatic and in 80% (20/25) of extrapancreatic cases. Loss of nuclear Rb1 expression was more frequent in extrapancreatic (68%, 17/25) than in pancreatic neoplasms (42%, 5/12). All cases of the urinary bladder (100%, 8/8) showed an abnormal Rb1 status, followed by the skin (67%, 2/3), the parotid gland (60%, 3/5), and the colorectum (44%, 4/9). All cases were progesterone receptor negative. All poorly differentiated pancreatic neuroendocrine neoplasms showed a normal nuclear ATRX and DAXX staining (both 100%, 11/11).

Immunohistochemical Data in Well-Differentiated Neuroendocrine Neoplasms with a Ki67-Index Greater than 20% (Neuroendocrine Tumors G3)

All neoplasms were synaptophysin and chromogranin A positive. The Ki67-index ranged from 21% to 36%. Eight of ten neuroendocrine tumors G3 were somatostatin receptor 2 A positive (score 2+, 6/8; score 3+, 2/8). Somatostatin receptor 5 (score 2+) was expressed in a single pancreatic neuroendocrine tumor G3. No abnormal immunostaining of p53 and Rb1 was detected. CD56 and cytokeratin 20 were expressed in all neuroendocrine tumors G3. All cases were progesterone receptor negative. Nuclear

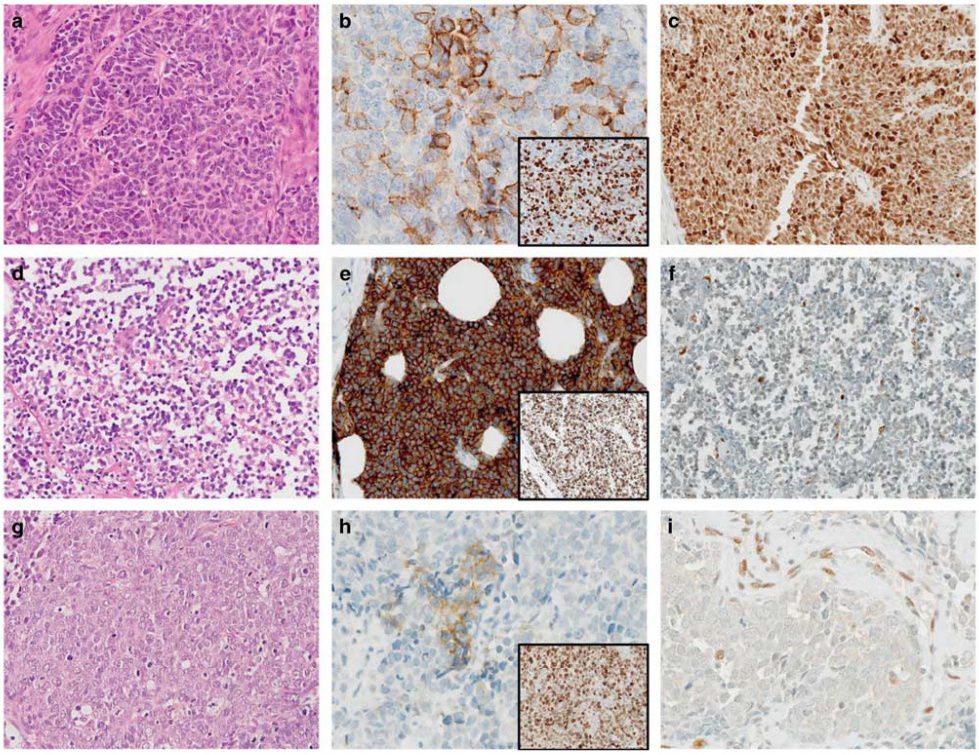

Figure 1 Immunohistochemistry of extrapancreatic poorly differentiated neuroendocrine carcinomas: (**a–c**) large cell neuroendocrine carcinoma of the colon (**a**) with expression of somatostatin receptor 2 A (**b**, score 2+), a Ki67-index of 60% (**b**, inset) and normal nuclear expression of Rb1 (**c**); (**d–f**) small cell neuroendocrine carcinoma of the urinary bladder (**d**) with expression of somatostatin receptor 2 A (**e**, score 3+), a Ki67-index of 90% (**e**, inset) and nuclear loss of Rb1 (**f**); (**g–i**) Merkel cell type neuroendocrine carcinoma of the parotid gland (**g**) with a somatostatin receptor 2 A score 1+ (**h**), a Ki67-index of 90% (**h**, inset) and nuclear loss of Rb1 (**i**).

ATRX and DAXX losses were seen in 1/9 and in 3/9 pancreatic neuroendocrine tumors G3, respectively.

Figures 1 and 2 show the histological and immunohistochemical stainings for somatostatin receptor 2 A, Ki67, and Rb1 of extrapancreatic poorly differentiated neuroendocrine neoplasms and pancreatic neuroendocrine neoplasms with a Ki67-index >20%, respectively. Figure 3 shows the ATRX and DAXX immunohistochemistry in pancreatic neuroendocrine carcinomas and neuroendocrine tumors G3.

Molecular TP53 Status

Molecular analysis of exons 5–9 of the *TP53* gene was performed in 44/47 cases (three cases of poorly differentiated neuroendocrine neoplasms of the urinary bladder were not available for molecular analysis). 71% (24/34) of poorly differentiated neuroendocrine neoplasms harbored *TP53* mutations. Exon 5 was altered in 38% (9/24), exon 6 in 8% (2/24), exon 7 in 25% (6/24), exon 8 in 25% (6/24), and exon 9 in 13% (3/24) of the cases. One parotid gland neuroendocrine carcinoma and one Merkel cell carcinoma showed mutations both in exons 5 and 9, and in exons 6 and 8, respectively. Most mutations were missense mutations (58%, 15/26), followed by nonsense mutations (15%, 4/26), splice site defects (12%, 3/26) and frameshift mutations (12%, 3/26) as well as deletions (4%, 1/26). 64% (7/11) of pancreatic poorly differentiated neuroendocrine neoplasms were *TP53* mutated, either in exon 5 (4/7) or exon 7 (3/7). The ampullary poorly differentiated neuroendocrine neoplasm showed a mutation in exon 8. Amongst extrapancreatic poorly differentiated neuroendocrine neoplasms, 73% (16/22) of them were *TP53* mutated (2/5 of the parotid gland, 2/3 Merkel cell carcinomas,

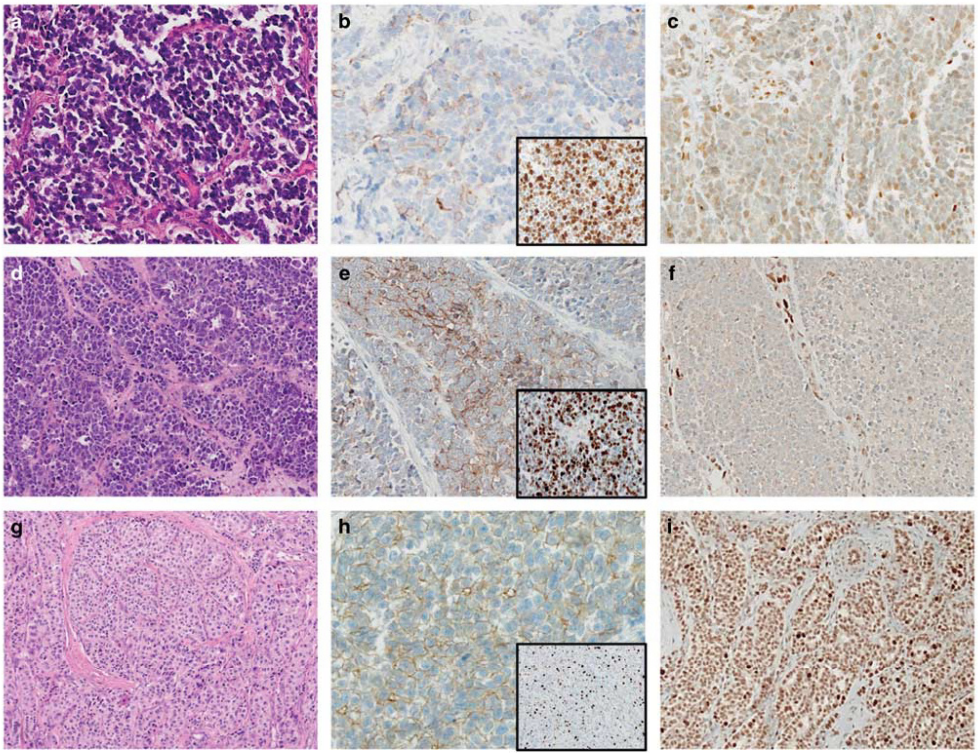

Figure 2 Immunohistochemistry of pancreatic neuroendocrine neoplasms with a Ki67-index above 20%: (**a–c**) small cell neuroendocrine carcinoma (**a**) with a somatostatin receptor 2 A score 1+ (**b**), a Ki67-index of 55% (**b**, inset) and normal nuclear expression of Rb1 (**c**); (**d–f**) large cell neuroendocrine carcinoma (**d**) with expression of somatostatin receptor 2 A (**e**, score 2+), a Ki67-index of 70% (**e**, inset) and nuclear loss of Rb1 (**f**); (**g–i**) neuroendocrine tumor G3 (**g**) with expression of somatostatin receptor 2 A (**h**, score 2+), a Ki67-index of 21% (**h**, inset) and normal nuclear expression of Rb1 (**i**).

8/9 of the colorectum, 4/5 of the urinary bladder). All neuroendocrine tumors G3 were *TP53* wild type.

Table 1 summarizes immunohistochemical and molecular findings in poorly differentiated neuroendocrine neoplasms of pancreatic and extrapancreatic origin. Table 2 summarizes the clinicopathological data including immunohistochemistry and molecular analysis of poorly differentiated neuroendocrine neoplasms and neuroendocrine tumors G3 of the pancreas. Three neuroendocrine carcinomas showed a *TP53* wild-type status and a normal immunohistochemistry for p53 and Rb1, while their histology was compatible with neuroendocrine carcinoma features (case numbers 1, 3, 5; Table 2). Deep sequencing confirmed the wild-type status of *TP53* and *RB1*, but revealed mutations in case 1, affecting *NF1, CSMD3, EP300, KDM5C, AKT3, CDH5, ERBB2*, and *BIRC5*. Case 5, which had a Ki67-index of 21% despite its diffuse non-organoid histology (see also discussion and Figure 5) and a somatostatin receptor 2 A 1+ score, and case 3 had no mutation in any of the genes included in our panel (data not shown).

Correlation Between Somatostatin Receptor 2 A, p53, Rb1, and TP53 Status

Neuroendocrine tumors G3 were significantly more often somatostatin receptor 2 A positive than their poorly differentiated counterparts (*P*-value: 0.0001) and showed a normal p53 expression (*P*-value: 0.0001). *TP53* wild-type status was significantly associated with well-differentiated morphology (*P*-value: 0.0001). Somatostatin receptor 2 A positive poorly differentiated neuroendocrine neoplasms harbored *TP53* mutations in four of six cases. Abnormal p53 immunolabeling was an indicator for *TP53* gene alterations (23/26 cases, 88%, *P*-value: 0.0001) and often occurred in combination with nuclear Rb1 loss (*P*-value: 0.001). Loss of nuclear

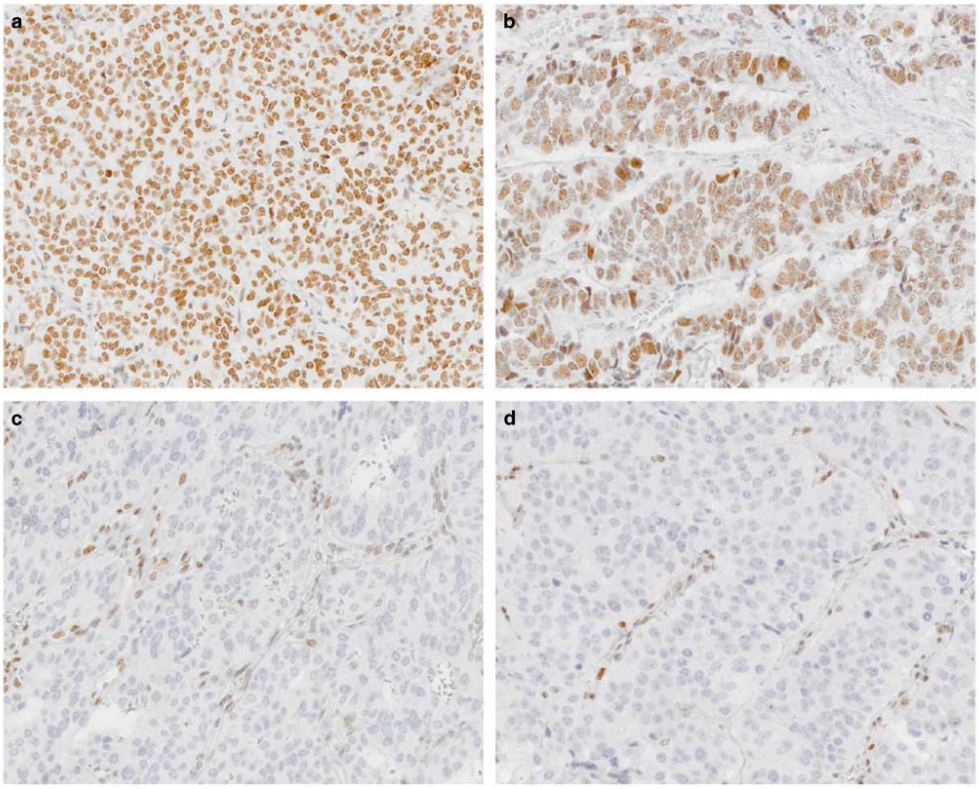

Figure 3 Immunohistochemistry of ATRX and DAXX in pancreatic neuroendocrine neoplasms with a Ki67-index above 20%: (**a** and **b**) large cell neuroendocrine carcinomas of the pancreas with normal nuclear expression of ATRX (**a**) and DAXX (**b**); (**c** and **d**) neuroendocrine tumors G3 with nuclear loss of ATRX (**c**) and DAXX (**d**), endothelial cells served as positive internal controls.

Table 1 Immunohistochemical expression (Ki67, somatostatin receptor 2 A, somatostatin receptor 5, Rb1, and p53) and *TP53* status in poorly differentiated neuroendocrine neoplasms of pancreatic and extrapancreatic origin

Organ	*Diagnosis*	n	*Ki67-range*	*SSTR2A*[a]	*SSTR5*[a]	*Rb1*[b]	*p53*[c]	*TP53*[d]
Pancreas	Neuroendocrine carcinoma	12	21–90%	8% (1/12)	8% (1/12)	42% (5/12)	75% (9/12)	67% (8/12)
Colorectum	Neuroendocrine carcinoma	9	30–90%	22% (2/9)	11% (1/9)	44% (4/9)	89% (8/9)	89% (8/9)
Urinary bladder	Neuroendocrine carcinoma	8	40–90%	25% (2/8)	0% (0/8)	100% (8/8)	100% (8/8)	80% (4/5)
Parotid gland	Neuroendocrine carcinoma	5	30–90%	20% (1/5)	0% (0/5)	60% (3/5)	40% (2/5)	40% (2/5)
Skin	Merkel cell carcinoma	3	50–80%	0% (0/3)	0% (0/3)	67% (2/3)	67% (2/3)	67% (2/3)

Abbreviation: SSTR, somatostatin receptor.
[a]Score 2+ and 3+.
[b]Loss of nuclear positivity in >90% of cells.
[c]Nuclear positivity in >20% of cells or complete loss.
[d]Mutations in exons 5–9.

Rb1 was not present in neuroendocrine tumors G3, but was frequently found in neuroendocrine neoplasms with poorly differentiated morphology (*P*-value: 0.001). Figure 4 shows normal and abnormal nuclear p53 stainings and *TP53* mutations.

Discussion

There is increasing evidence that the low proliferative well-differentiated neuroendocrine neoplasms (G1–2) and the high proliferative poorly differentiated

Table 2 Clinicopathological data in poorly (NEC) and well-differentiated (NET) neuroendocrine neoplasms of the pancreas[a]

Case	*Diagnosis*	*Age*	*Sex*	*Immunohistochemistry*								*Molecular pathology*
				Syn	*CG*	*Ki67*	*SSTR2A*	*SSTR5*	*ATRX*	*DAXX*	*Rb1*	*p53*	*TP53, exons 5–9*
Poorly differentiated neuroendocrine neoplasms													
1	NEC, sc	56	F	Pos	Neg	60%	Neg (0)	Neg (1+)	N	N	N	N	WT
2	NEC, sc	62	F	Pos	Pos[b]	55%	Neg (1+)	Neg (0)	N	N	N	A	Exon 7; c.742C>G; p.R248G
3	NEC, sc	16	F	Pos	Pos	50%	Neg (0)	Neg (0)	N	N	N	N	WT
4	NEC, sc[c]	75	M	Pos	Pos	60%	Neg (0)	Neg (0)	NA	NA	A	A	Exon 8; c.800G>A; p.R267Q
5	NEC, lc	43	F	Pos	Pos	21%	Neg (1+)	Neg (0)	N	N	N	N	WT
6	NEC, lc	56	F	Pos	Pos	30%	Neg (1+)	Neg (1+)	N	N	A	A	Exon 5; c.524G>A; p.R175H
7	NEC, lc	76	F	Pos	Pos	60%	Neg (0)	Pos (2+)	N	N	N	A	Exon 5; c.454C>A; p.P152T
8	NEC, lc[c]	64	M	Pos	Pos[b]	35%	Neg (0)	Neg (1+)	N	N	N	A	Exon 7; c.769_770insAC; p.L257fs
9	NEC, lc	32	F	Pos	Pos[b]	70%	Pos (2+)	Neg (0)	N	N	A	A	WT
10	NEC, lc	64	M	Pos	Pos[b]	40%	Neg (1+)	Neg (1+)	N	N	A	A	Exon 5; c.488 A>G; p.Y163C
11	NEC, lc	74	M	Pos	Pos	90%	Neg (0)	Neg (1+)	N	N	A	A	Exon 7; c.723delC; p.S241fs
12	NEC, lc	51	F	Pos	Neg	55%	Neg (0)	Neg (0)	N	N	N	A	Exon 5; c.524G>A; p.R175H
Neuroendocrine tumors G3													
13	NET, G3	78	F	Pos	Pos[b]	28%	Pos (3+)	Neg (0)	N	A	N	N	WT
14	NET, G3	53	F	Pos	Pos	21%	Pos (2+)	Neg (1+)	N	N	N	N	WT
15	NET, G3	58	F	Pos	pos[b]	25%	Pos (2+)	Neg (1+)	A	N	N	N	WT
16	NET, G3	57	F	Pos	Pos	23%	Pos (2+)	Neg (0)	N	A	N	N	WT
17	NET, G3	44	F	Pos	Pos	32%	Pos (2+)	Pos (2+)	N	N	N	N	WT
18	NET, G3	47	F	Pos	Pos	36%	Neg (0)	Neg (0)	N	N	N	N	WT
19	NET, G3	72	F	Pos	Pos	26%	Pos (3+)	Neg (1+)	N	A	N	N	WT
20	NET, G3	69	F	Pos	Pos[b]	25%	Pos (2+)	Neg (1+)	N	N	N	N	WT
21	NET, G3	25	M	Pos	Pos	27%	Neg (0)	Neg (0)	N	N	N	N	WT

Abbreviations: A, abnormal; CG, chromogranin A; lc, large cell type; N, normal; NA, not available; Neg, negative; Pos, positive ; sc, small cell type; SSTR, somatostatin receptor; Syn, synaptophysin; WT, wild type.
[a]Including one ampullary NEC.
[b]Focal expression of chromogranin.
[c]Mixed adenoneuroendocrine carcinoma.

neuroendocrine neoplasms (G3) belong to two biologically different entities of neuroendocrine neoplasms.[2] The results of our study confirm and extend this notion. We show that the majority of poorly differentiated neuroendocrine neoplasms, pancreatic as well as extrapancreatic, lack significant somatostatin receptor 2 A expression, a key finding in well-differentiated neuroendocrine neoplasms, and, at the same time, have *TP53* and *RB1* gene alterations. This dichotomy also applies to those neuroendocrine neoplasms that maintain their well-differentiated histology although their Ki67-index exceeds 20%. Accordingly, these neuroendocrine neoplasms have been provisionally termed 'neuroendocrine tumors G3'. They are mainly of pancreatic and only rarely of extrapancreatic origin.[24,33,34]

The membranous expression of somatostatin receptor 2 A is a typical feature of well-differentiated neuroendocrine tumors of different origin.[18] In contrast, somatostatin receptor 2 A expression in highly proliferative neuroendocrine neoplasms has only been demonstrated in a fraction of tumors from various sites.[16,19,35] In Kaemmerer's study investigating somatostatin receptor 2 A expression in gastroenteropancreatic neuroendocrine neoplasms (together with the CXCR4 chemokine receptor), 23% of the tumors regarded to be G3 were strongly somatostatin receptor 2 A positive.[16] Using the established HER2 scoring system of the breast and adapting it to the somatostatin receptor 2 A expression patterns in the pancreas,[31,32] our data in poorly differentiated neuroendocrine neoplasms of pancreatic and extrapancreatic origin demonstrated that somatostatin receptor 2 A, scored 2+ and 3+, was positive in 16% of these neoplasms including one in the pancreas and in the parotid gland, as well as two cases each in the colon and the urinary bladder. The positive tumors belonged to the small or large cell category and showed a range between 50% and 90% of proliferative activity. For example, the three pancreatic poorly differentiated neuroendocrine neoplasms with the lowest Ki67-index (between 21% and 35%) were all somatostatin receptor 2 A negative.

Low expression levels of somatostatin receptor 2 A (score 1+) were found in ten poorly differentiated neuroendocrine neoplasms. Miederer showed that few neuroendocrine neoplasms detected by somatostatin receptor imaging were somatostatin receptor 2 A negative.[12] This discrepancy between imaging and immunohistochemistry is most likely due to tumor heterogeneity regarding somatostatin receptor 2 A expression which effects imaging, as a large scale method, much less than immunohistochemical examination that screens only a small tumor area.

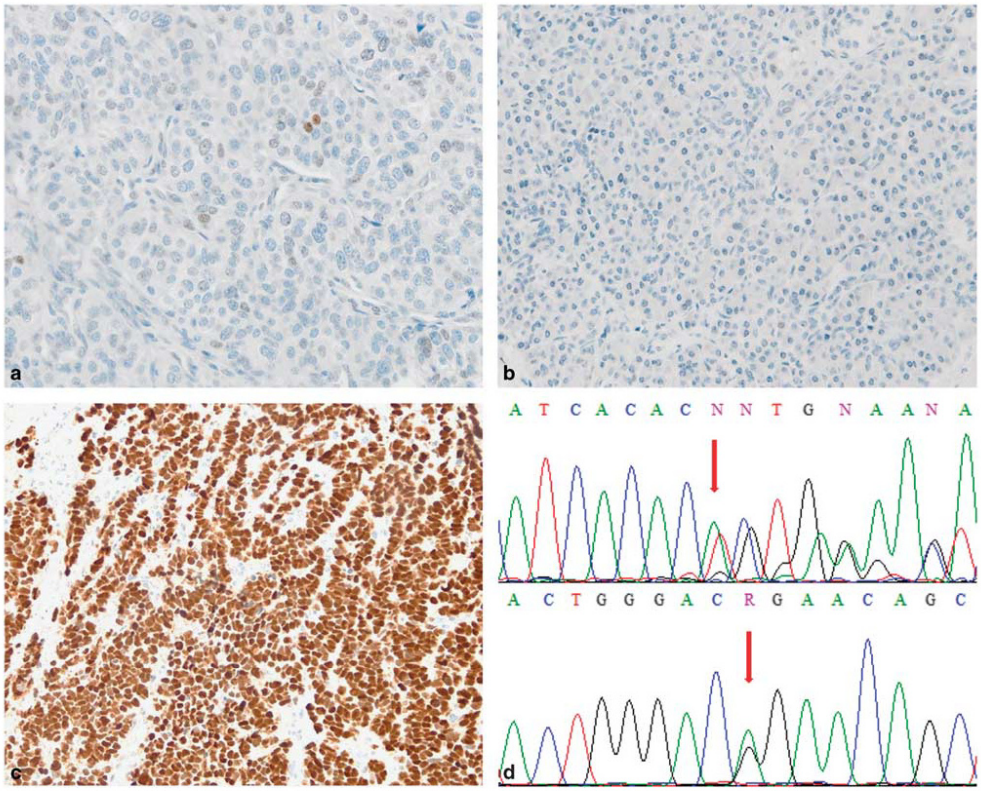

Figure 4 P53 and *TP53* in pancreatic neuroendocrine neoplasms: normal nuclear expression of p53 in <20% of the cells of a neuroendocrine tumor G3 (**a**); abnormal expression of p53 with complete loss of nuclear staining in a large cell type neuroendocrine carcinoma (**b**); nuclear overexpression of p53 in a small cell type neuroendocrine carcinoma (**c**); Sanger sequences of *TP53* mutated cases with a frameshift (upper row) and a point mutation (lower row) (**d**).

It is therefore possible that among our score 1+ somatostatin receptor 2A positive poorly differentiated neuroendocrine neoplasms are some tumors that might be detected by imaging.

Somatostatin receptor 5, which shares the membranous expression with somatostatin receptor 2A, was only found to be expressed in three cases, including two poorly differentiated neuroendocrine neoplasms and one neuroendocrine tumor G3. Somatostatin receptor 5 expression was neither correlated to somatostatin receptor 2A positivity nor to any of the above mentioned tumor criteria. These data suggest that somatostatin receptor 5 probably does not play any significant functional role in neuroendocrine neoplasms, neither in those with well nor with poorly differentiated histology.

As to tumor localization, it appears from our data and those in other studies that somatostatin receptor 2A may be present in poorly differentiated neuroendocrine neoplasms from various sites of the body, including the pancreas, stomach, colorectum, urinary bladder, lung, breast, and prostate.[16,19–21,35] Whether Merkel cell carcinomas of the skin may be an exception in this regard, as our data might suggest, remains to be clarified in a larger series of cases.

In order to find out whether there is any correlation between the somatostatin receptor 2A expression with the *TP53* and *RB1* status, we investigated p53 and Rb1 expression or loss, and *TP53* mutation in our tumor series. In confirming a recent genetic analysis of poorly differentiated small cell and large cell neuroendocrine neoplasms of the pancreas,[2] we found *TP53* mutated in 71% of poorly differentiated neuroendocrine neoplasms and abnormally expressed in 78% of the cases. Rb1 was lost in 59% of the cases (Table 1). Abnormal p53 immunolabeling (ie, overexpression as well as total loss)

matched with *TP53* gene alterations in 92% of our cases. Correlation of the *TP53* data with that of somatostatin receptor 2 A expression revealed no relationship between the two markers.

Histologically, the differential diagnosis of neuroendocrine tumors G3 and poorly differentiated neuroendocrine neoplasms, particularly of the large cell subtype, may sometimes be difficult. In these cases it would be helpful to have immunohistochemical and/or molecular markers available to identify these tumors. The comparison of the results in a series of nine primary pancreatic neuroendocrine tumors G3 with those in twelve pancreatic poorly differentiated neuroendocrine neoplasms shows that the application of somatostatin receptor 2 A, p53, Rb1, ATRX, and DAXX together with a high Ki67-index can solve the problem in most cases. Exceptionally, as observed in case 5 (Table 2; Figure 5), classification as poorly differentiated neuroendocrine neoplasm may remain difficult, if it is only based on histology (showing a diffuse non-organoid growth pattern) and low level somatostatin receptor 2 A expression, and not on *TP53* and *RB1* alterations or a high Ki67-index. Progesterone receptor expression, which was also tested, was of no use, as it was negative in all cases. The discriminative power in separating neuroendocrine tumors G3 from poorly differentiated neuroendocrine neoplasms was greatest for p53, which, in case of abnormal expression, was associated with poorly differentiated neuroendocrine neoplasms in almost 78% of the neoplasms, and, in case of negativity, with all neuroendocrine tumors G3. A similar but less sensitive distinction was also seen for Rb1. Somatostatin receptor 2 A, with its 80% positivity in neuroendocrine tumors G3, was less discriminative in poorly differentiated neuroendocrine neoplasms than p53 and Rb1, as it was found to be positive in six of the latter neoplasms. However, when somatostatin receptor 2 A was combined with p53 and Rb1, it usually solved the differential diagnosis between pancreatic neuroendocrine tumors G3 and poorly differentiated neuroendocrine neoplasms in most of the cases.

In summary, we showed that the expression of somatostatin receptor 2 A is not restricted to the group of well-differentiated neuroendocrine neoplasms but may also be detected in a small fraction of poorly differentiated neuroendocrine neoplasms of pancreatic and extrapancreatic origin. This makes these neuroendocrine neoplasms potentially amenable to treatment with somatostatin analogs and peptide radio receptor therapy. Morphological criteria that predict somatostatin receptor 2 A positivity in poorly differentiated neuroendocrine neoplasms could not be identified so far. The distinction of neuroendocrine tumors from poorly differentiated neuroendocrine neoplasms, that may be especially difficult in the neuroendocrine tumors G3 of pancreatic origin, can be very much improved by the application of p53 in combination with Rb1 and somatostatin receptor 2 A. ATRX and DAXX are less important as their discriminative power is much lower than that of aforementioned markers. The fact that p53, Rb1 and somatostatin receptor 2 A have such a high differential expression in well and poorly differentiated neuroendocrine neoplasms further supports the concept of two basically different groups among the neuroendocrine neoplasms.[5,34]

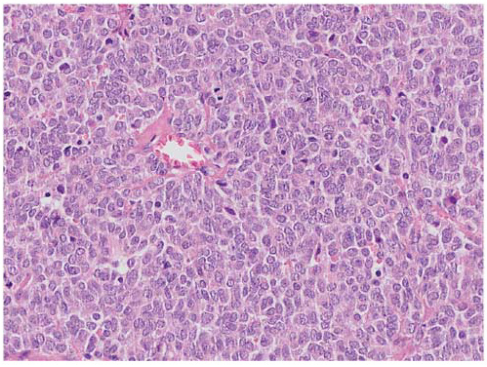

Figure 5 Poorly differentiated large cell neuroendocrine neoplasm of the pancreas with a diffuse non-organoid growth pattern and a Ki67-index of 21%.

Acknowledgments

We are grateful to Petra Meyer, Daniela Angermeier and Dennis Thiele for excellent technical assistance. We thank Professor Anne Hoorens, Gent, Belgium, Dr Diana Karimi, Munich, Germany, Dr Gratiana Hermann, Zerifin, Israel and Professor Yersu Kapran, Istanbul, Turkey, who supported this study by contributing cases. This study has been supported by a fund from Novartis Pharma GmbH, Germany. KS is funded by DFG (SFB824, Z2).

Disclosure/conflict of interest

The authors declare no conflict of interest.

References

1 Shi C, Klimstra DS. Pancreatic neuroendocrine tumors: pathologic and molecular characteristics. Semin Diagn Pathol 2014;31:498–511.
2 Yachida S, Vakiani E, White CM, *et al.* Small cell and large cell neuroendocrine carcinomas of the pancreas are genetically similar and distinct from well-differentiated pancreatic neuroendocrine tumors. Am J Surg Pathol 2012;36:173–184.
3 Rindi G, Arnold R, Bosman FT, *et al.* Nomenclature and classification of neuroendocrine neoplasms of the

digestive system In: Bosman FT, Carneiro F, Hruban RH, Theise ND (eds). WHO Classification of Tumours of the Digestive System, 4th edn. WHO Press: IARC Lyon, 2010, pp 13–14.
4 Esposito I, Segler A, Steiger K, *et al.* Pathology, genetics and precursors of human and experimental pancreatic neoplasms: an update. Pancreatology 2015;15:598–610.
5 Klöppel G. Classification and pathology of gastroenteropancreatic neuroendocrine neoplasms. Endocr Relat Cancer 2011;18:S1–16.
6 Sorbye H, Welin S, Langer SW, *et al.* Predictive and prognostic factors for treatment and survival in 305 patients with advanced gastrointestinal neuroendocrine carcinoma (WHO G3): the NORDIC NEC study. Ann Oncol 2013;24:152–160.
7 Frilling A, Akerstrom G, Falconi M, *et al.* Neuroendocrine tumor disease: an evolving landscape. Endocr Relat Cancer 2012;19:R163–R185.
8 van Essen M, Krenning EP, Kam BL, *et al.* Peptide-receptor radionuclide therapy for endocrine tumors. Nat Rev Endocrinol 2009;5:382–393.
9 Kwekkeboom DJ, de Herder WW, Kam BL, *et al.* Treatment with the radiolabeled somatostatin analog [177 Lu-DOTA 0,Tyr3]octreotate: toxicity, efficacy, and survival. J Clin Oncol 2008;26:2124–2130.
10 Volante M, Brizzi MP, Faggiano A, *et al.* Somatostatin receptor type 2 A immunohistochemistry in neuroendocrine tumors: a proposal of scoring system correlated with somatostatin receptor scintigraphy. Mod Pathol 2007;20:1172–1182.
11 Kaemmerer D, Peter L, Lupp A, *et al.* Molecular imaging with (6)(8)Ga-SSTR PET/CT and correlation to immunohistochemistry of somatostatin receptors in neuroendocrine tumours. Eur J Nucl Med Mol Imaging 2011;38:1659–1668.
12 Miederer M, Seidl S, Buck A, *et al.* Correlation of immunohistopathological expression of somatostatin receptor 2 with standardised uptake values in 68Ga-DOTATOC PET/CT. Eur J Nucl Med Mol Imaging 2009;36:48–52.
13 Korner M, Waser B, Schonbrunn A, *et al.* Somatostatin receptor subtype 2 A immunohistochemistry using a new monoclonal antibody selects tumors suitable for *in vivo* somatostatin receptor targeting. Am J Surg Pathol 2012;36:242–252.
14 Rinke A, Muller HH, Schade-Brittinger C, *et al.* Placebo-controlled, double-blind, prospective, randomized study on the effect of octreotide LAR in the control of tumor growth in patients with metastatic neuroendocrine midgut tumors: a report from the PROMID Study Group. J Clin Oncol 2009;27:4656–4663.
15 Caplin ME, Pavel M, Cwikla JB, *et al.* Lanreotide in metastatic enteropancreatic neuroendocrine tumors. N Engl J Med 2014;371:224–233.
16 Kaemmerer D, Trager T, Hoffmeister M, *et al.* Inverse expression of somatostatin and CXCR4 chemokine receptors in gastroenteropancreatic neuroendocrine neoplasms of different malignancy. Oncotarget 2015;6:27566–27579.
17 Nakayama Y, Wada R, Yajima N, *et al.* Profiling of somatostatin receptor subtype expression by quantitative PCR and correlation with clinicopathological features in pancreatic endocrine tumors. Pancreas 2010;39:1147–1154.
18 Papotti M, Bongiovanni M, Volante M, *et al.* Expression of somatostatin receptor types 1-5 in 81 cases of gastrointestinal and pancreatic endocrine tumors. A correlative immunohistochemical and reverse-transcriptase polymerase chain reaction analysis. Virchows Arch 2002;440:461–475.
19 Mizutani G, Nakanishi Y, Watanabe N, *et al.* Expression of Somatostatin Receptor (SSTR) Subtypes (SSTR-1, 2 A, 3, 4 and 5) in Neuroendocrine Tumors Using Real-time RT-PCR Method and Immunohistochemistry. Acta Histochem Cytochem 2012;45:167–176.
20 Nese N, Kumbaraci BS, Baydar DE, *et al.* Small cell carcinomas of the bladder highly express somatostatin receptor type 2 A: impact on prognosis and treatment-A multicenter study of Urooncology Society, Turkey. Appl Immunohistochem Mol Morphol 2016;24:253–260.
21 Lapa C, Hanscheid H, Wild V, *et al.* Somatostatin receptor expression in small cell lung cancer as a prognostic marker and a target for peptide receptor radionuclide therapy. Oncotarget 2016;7:20033–20040.
22 Kanakis G, Grimelius L, Spathis A, *et al.* Expression of somatostatin receptors 1-5 and dopamine receptor 2 in lung carcinoids: implications for a therapeutic role. Neuroendocrinology 2015;101:211–222.
23 Righi L, Volante M, Tavaglione V, *et al.* Somatostatin receptor tissue distribution in lung neuroendocrine tumours: a clinicopathologic and immunohistochemical study of 218 'clinically aggressive' cases. Ann Oncol 2010;21:548–555.
24 Basturk O, Yang Z, Tang LH, *et al.* The high-grade (WHO G3) pancreatic neuroendocrine tumor category is morphologically and biologically heterogenous and includes both well differentiated and poorly differentiated neoplasms. Am J Surg Pathol 2015;39:683–690.
25 Sorbye H, Strosberg J, Baudin E, *et al.* Gastroenteropancreatic high-grade neuroendocrine carcinoma. Cancer 2014;120:2814–2823.
26 Velayoudom-Cephise FL, Duvillard P, Foucan L, *et al.* Are G3 ENETS neuroendocrine neoplasms heterogeneous? Endocr Relat Cancer 2013;20:649–657.
27 Jiao Y, Shi C, Edil BH, *et al.* DAXX/ATRX, MEN1, and mTOR pathway genes are frequently altered in pancreatic neuroendocrine tumors. Science 2011;331:1199–1203.
28 Tang LH, Basturk O, Sue JJ, Klimstra DS. A practical approach to the classification of WHO grade 3 (G3) well-differentiated neuroendocrine tumor (WD-NET) and poorly differentiated neuroendocrine carcinoma (PD-NEC) of the pancreas. Am J Surg Pathol 2016;40:1192–1202.
29 Kohler S, Kerl H. Merkel cell carcinoma. In: LeBoit PE, Burg G, Weedon D, Sarasin A (eds). World Health Organization Classification of Tumours. Skin Tumours 1st edn. WHO Press: IARC Lyon, 2006, pp 272–273.
30 Reid MD, Bagci P, Ohike N, *et al.* Calculation of the Ki67 index in pancreatic neuroendocrine tumors: a comparative analysis of four counting methodologies. Mod Pathol 2015;28:686–694.
31 Kaemmerer D, Peter L, Lupp A, *et al.* Comparing of IRS and Her2 as immunohistochemical scoring schemes in gastroenteropancreatic neuroendocrine tumors. Int J Clin Exp Pathol 2012;5:187–194.

32 Wolff AC, Hammond ME, Hicks DG, *et al*. Recommendations for human epidermal growth factor receptor 2 testing in breast cancer: American Society of Clinical Oncology/College of American Pathologists clinical practice guideline update. J Clin Oncol 2013;31:3997–4013.
33 Garcia-Carbonero R, Sorbye H, Baudin E, *et al*. ENETS Consensus Guidelines for high-grade gastroenteropancreatic neuroendocrine tumors and neuroendocrine carcinomas. Neuroendocrinology 2016;103:186–194.
34 Tang LH, Untch BR, Reidy DL, *et al*. Well-differentiated neuroendocrine tumors with a morphologically apparent high-grade component: a pathway distinct from poorly differentiated neuroendocrine carcinomas. Clin Cancer Res 2016;22:1011–1017.
35 Zamora V, Cabanne A, Salanova R, *et al*. Immunohistochemical expression of somatostatin receptors in digestive endocrine tumours. Dig Liver Dis 2010;42:220–225.